NIRS－M－79

特別研究「重粒子線によるがん治療法に関する調査研究」　論文集

第　1　集

（平成元年４月－平成２年３月）

放射線医学総合研究所

Collected Papers of Project Research
"Cancer Treatment and its Modalities using Accelerated Heavy Ions"

No. 1

(April 1989 — March 1990)

March, 1991

National Institute of Radiological Sciences
9-1, Anagawa 4-chome, Chiba-shi, 260 Japan

序

重粒子線治療臨床トライアルは平成５年度に始まる予定である。特別研究「重粒子線によるがん治療法に関する調査研究」は、重粒子線治療に必要な線量の評価、標的容積の診断法と治療システムを臨床トライアルの開始に合わせて確立し、整備するために平成元年度からの５カ年計画のもとに実施されることになった。

一方、重粒子線がん治療装置、ＨＩＭＡＣ、の製作と建屋の工事を準調に進む状況のもとで、重粒子線治療の医療体制の整備が緊急を要する課題となった。そのため、平成元年５月には重粒子線医療準備チームが設けられ、約１年間にわたる討議を経て、その成果は「重粒子線がん治療臨床試行体制整備に関する検討報告書」としてまとめられた。この１年間にわたる討議によって掘り起こされた内容は、重粒子線治療施設の計画に大きな寄与となったと考えている。

重粒子線治療の実施体制については、平成２年度から始まる重粒子線治療ネットワーク会議により全国的な視野のもとで具体的な姿が着実に浮かび上がってくるものと期待している。

重粒子線治療に関する前臨床研究を行う本特別研究の役割は重く、その発展を願うものである。

特研班長　　恒　元　　博

目　次

Energy Spectra and Depth-Dose Curves for 70 MeV Protons

HANS BICHSEL
1211 22nd Avenue East, Seattle, Washington 98112-3534

T. HIRAOKA
National Institute of Radiological Sciences, Chiba 260 Japan

Abstract

In cancer therapy with fast charged particles, the energy deposition ("dose") near the end of the range of the particles must be determined with an error of less than 2%. The dose is strongly influenced by straggling and multiple scattering effects. Calculations of straggling have been made in which spectra of protons with an initial energy of 70 MeV were obtained for successive layers of water. An average multiple scattering correction was made in each layer. The ionization in a thin gas layer as a function of absorber thickness was determined. It agrees quite well with measured ionization curves.

Introduction

At the National Institute of Radiological Sciences, 70 MeV protons are used for cancer therapy. In water or tissues, these protons travel a distance of about 4 cm. During the traversal of the absorber they lose their energy steadily, but at an increasing rate in greater depths. A general description of their motion can be found in Table I. Actually, protons lose their energy in random collisions: the average energy loss per collision is about 70 eV, depending on particle speed v, but the most probable energy loss is only about 20 eV [1], thus their energies will spread more and more with increasing depth ("straggling").

For cancer therapy, the dose D (energy deposited by the protons in a tissue per unit mass) should be known with an uncertainty of no more than 2%. For a parallel beam of protons with a spectrum of energies, the dose (in MeV/g) is given by [2]

$$D = N \int f(T) S(T)\, dT \tag{1}$$

where $f(T)$ is the fluence spectrum [the number of protons with an energy between T and $T + dT$ is given by $Nf(T)\, dT$, where N is the total number of protons/cm^2], and $S(T)$ is the stopping power in units of MeV cm^2/g. In order to completely define the fluence spectrum f for an arbitrary beam, it would be necessary to give the coordinates of the point at which f is observed and also the directions of the particles, in addition to their energies. In order to simplify the notation for this paper, only the variables of immediate concern are listed. In particular, $f(t, T)$ shall mean the spectrum of energies T at a depth t in an absorber. In order to apply

International Journal of Quantum Chemistry: Quantum Chemistry Symposium 23, 565–574 (1989)

CCC 0020-7608/89/230565-10$04.00

TABLE I. Change in energy of initially monoenergetic protons traversing water, obtained with the continuous-slowing-down approximation (CSDA).

s	T_c	$S(T_c)$	σ(MeV)
0	70	9.56	0
0.5	65.1	10.11	0.227
1	59.9	10.79	0.332
1.5	54.31	11.65	0.427
2	48.23	12.8	0.528
2.5	41.47	14.45	0.646
3	33.67	17.08	0.799
3.5	24.01	22.46	1.097
3.6	21.68	24.4	1.19
3.7	19.12	27.02	1.34
3.8	17.25	29.38	1.46
3.9	13.9	35	1.75
4	8.6	51.51	—
4.094	0.1	793	—

Note: The calculation is done with Eqs. (2) and (4), with an I value of 75 eV. In CSDA it is assumed that all the protons lose exactly the same energy. After the protons have traveled a path length s (in cm, density of water ρ = 0.997 g/cm^3, at 20 C), their residual energy is T_c (MeV). Their energy loss per unit path length is given by the stopping power $S(T_c)$ [MeV/(g/cm^2)]. Equivalent tables are available for any other absorber. If straggling is taken into account, the energies of the protons at pathlength s have a spectral distribution $f(T_1)$, Figure 2, with a mean value $\langle T_1 \rangle = T_c$. The standard deviation of $f(T_1)$ is σ and was obtained from Tschalär [18]. It is smaller than the values given in Fig. 2 (which include a spread in energy of the initial beam).

Eq. (1), it is necessary to know the stopping power for many human tissues (e.g., muscle, brain, lung, bone) or materials similar to them with an uncertainty of much less than 2%. Therefore the penetration of charged particles in matter must be studied accurately.

The Bethe-Bloch theory with the Barkas correction is a reliable method to calculate the energy dependence of $S(T)$:

$$S(T) = \frac{0.30708}{\beta^2} \frac{z^2 Z}{A} L \tag{2}$$

where $L = L_0(\beta) + L_1(\beta) + L_2(\beta)$, z is the particle charge, and

$$L_0(\beta) = \ln\left[\frac{2mc^2\beta^2}{1-\beta^2}\right] - \beta^2 - \ln I - \frac{C(\beta)}{Z}$$

is the Bethe stopping number, L_1 is the Barkas correction term, and L_2 is the Bloch

term. $S(T)$ is in units of MeV cm^2/g. Expressions for L_1, L_2, and $C(\beta)$ are given in Bichsel and Porter [3]. For light elements and their compounds, and energies above about 4 MeV, the shell corrections $C(\beta)$, L_1, and L_2 amount to only a few percent of L and will be similar for most compounds. Thus the most important parameter in the theory is the mean excitation energy I. In general, I values are obtained from experimental stopping power data, except for some gases [4] and for aluminum, where I was obtained from optical data [5]. Frequently, the Bragg additivity approximation is used to calculate I values for compounds from those for the separate elements [6], but differences exceeding 10% have been found between experimental values and those calculated with the Bragg approximation [7,8]. Therefore it is advisable to measure the stopping power for the compounds needed in cancer therapy and extract I values from the experimental data.

For the experiments discussed here, it is necessary to use the range-energy relation. Using the continuous slowing down approximation (CSDA), the range is

$$R(T) = \int_0^T \frac{dT'}{S(T')} \tag{3}$$

where $S(T)$ is the stopping power.

Since absolute measurements of stopping power are difficult (e.g., Refs. 9 and 10), methods determining relative values of S have been used frequently (e.g., Refs. 11–13). The general idea of the methods is the following: particle beams with initial kinetic energy T_0 are sent through absorbers of thickness t. The residual mean energy of the particles leaving the absorber is $\langle T_1 \rangle$. Various methods are used to measure $\langle T_1 \rangle$ (e.g., Ref. 7). For the present measurements, $\langle T_1 \rangle$ was obtained by measuring the corresponding residual range in water, R_1, with the apparatus shown in Figure 1. It has the advantage of great simplicity, using equipment available in medical radiation departments, and short measuring times. The theoretical evaluation of the data is quite complex, though.

The Ionization Chamber

In traversing the ionization chamber, each proton will lose an energy $\Delta = g \cdot S(T_2)$ in the gas, Figure 1, and will produce a number n of ion pairs, $n = \Delta/w$, where w is the mean energy required to produce an ion pair ($w \approx 30$ eV [14]). By applying an electric field across the gas, the ions will be collected, and their charge $q = n \cdot e$ can be measured. For N protons, the total charge $j = Nq = Neg\, S(T_2)/w$ will be obtained. Here, j is called "the ionization." Since j is proportional to the stopping power, it will also be proportional to the dose D of Eq. (1). Therefore, measuring the function $j(x)$ will be equivalent to measuring $D(x)$, and $D(x)$ is called a depth-dose curve.

Simple Evaluation of the Measurements

In the situation given in Figure 1, the relative measurement is made by placing an absorber of measured thickness t in the first position. The thickness of water, t_w, giving the same residual energy as the absorber, is measured. Then, if the stopping

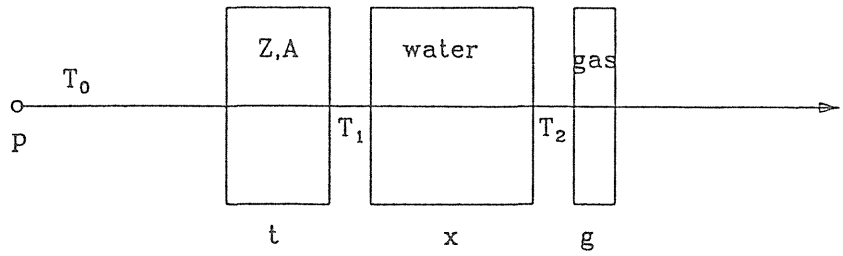

Figure 1. Schematic drawing of apparatus used for energy loss measurements. The proton beam p with initial energy T_0 = 70 MeV traverses an arbitrary absorber (atomic number Z, atomic weight A) of thickness t. It emerges from the absorber with an energy spectrum $f(t, T_1)$ (usually, $T_1 \approx 35$ MeV) and then enters a water absorber with variable thickness x, whence it emerges with an energy spectrum $f(t + x, T_2)$, and then ionizes the gas of thickness g (which is contained in an ionization chamber with very thin walls). In the experiment, there is no space between the absorbers. In the absence of straggling and multiple scattering, the energies would be given by the range energy relation of Table I, and all protons would have the same energy $T_2(x)$ at the face of the ionization chamber, and the ionization curve would be strictly proportional to the stopping power $S(T_2)$. Thus if the ionization in the gas is measured as a function of increasing thickness of the water absorber, the ionization current $j(x)$ increases to a maximum value and then decreases rapidly toward zero. Measurements were made with a thin (g = 4.8 mm) ionization chamber filled with nitrogen [19]. The beam extended over a square area 4 cm to a side, while the ionization chamber had a diameter of only 1.2 cm. Since the lateral displacement due to multiple scattering is only a few mm, the fluences across the center of the beam are not changed by it: as many particles are scattered into this area as are scattered out of it.

power for water is known, the stopping power for the absorber Z can be calculated. Neglecting straggling and multiple scattering, the evaluation of experimental data is simple. We measure the distance x_1 at which the ionization $j(x_1)$ is equal to zero. We call x_1 the residual range $R_w(T_1)$ in water for the energy T_1. From the range energy table for water, we have

$$x_1 = R_w(T_1) = \int_0^{T_1} \frac{dT}{S_w(T)} \tag{3a}$$

where $S_w(T)$ is the stopping power for water. Given x_1, we interpolate in the table to find T_1. We can also find the thickness of water which would reduce the energy from T_0 to T_1:

$$t_w = \int_{T_1}^{T_0} \frac{dT}{S_w(T)} \tag{4}$$

and the total range of the protons with energy T_0 is $R_w(T_0) = (t_w + R_w(T_1)$. If the I value I_a for the absorber is unknown, we calculate the following integral for several values of I_a:

$$t_a = \int_{T_1}^{T_0} \frac{dT}{S_a(T)} \tag{5}$$

until we obtain a value t_a which is equal to the measured absorber thickness t. Thus we have determined I_a.

An approximate method which does not require explicit integrations is to rewrite the integrals of Eqs. (4) and (5) with the mean value theorem:

$$t = \int_{T_0}^{T_1} \frac{dT}{S(T)} \equiv \frac{T_0 - T_1}{S(T_m)} \tag{6}$$

where T_m thereby is defined, and $T_1 < T_m < T_0$. A first approximation is $T_m \approx (T_0 + T_1)/2$. Now we can consider the ratio of the experimental thicknesses $r \equiv t/t_w$. Since $T_0 - T_1$ is the same for both absorbers, we substitute Eq. (6) and obtain

$$r = \frac{S_w(T_m)}{S_a(T'_m)} \quad \text{or} \quad S_a(T'_m) = \frac{S_w(T_m)}{r} \tag{7}$$

where r and $S_w(T_m)$ are known, and $S_a(T'_m)$ thus is determined from the experiment. Now $S_a(T'_m)$ can be used in Eq. (2) to solve for I_a. It must be noted, though, that T_m differs for different absorbers. If, for example, $T_0 = 70$ MeV, $T_1 = 30$ MeV, with a lead absorber we have ${}_L T_m = 49.596$ MeV, for water, ${}_w T_m = 49.651$ MeV. To appreciate the sensitivity of the ratio r, it is useful to calculate it for water and lead at two energies: it is 2.1873 at 50 MeV, 2.1911 at 49 MeV (using the range energy tables in Bichsel [15]). Next, approaches are described in which straggling and multiple scattering are included.

Evaluation of Experiment with the Range Straggling Method

Mather and Segre [16] used the experimental method of Fig. 1 to measure the ranges of 340 MeV protons. They used a simple and plausible method to calculate the ionization curves: they convoluted a Gaussian range straggling curve with the ionization function calculated for the residual energy, T_2, based on the residual range. Bichsel and Uehling [17] also included multiple scattering (also see Berger and Seltzer [18]). Here, a further modification was added to this approach: the range straggling function was assumed to be skewed and was determined by the two free parameters σ and γ_3 mentioned below. The best fit ionization curve calculated with this approach is shown as the dashed-dotted line in Figure 3. The calculation does not simulate the actual events in the absorbers closely, and a more complex method is described next.

Evaluation of Measurements with the Energy Straggling Method

Straggling and multiple scattering both change with the absorber [17]. In principle, a calculation could be made which follows in detail the penetration of the proton beam through the absorbers, considering successive thin layers and calculating the modification of the proton spectrum by each layer, using the Blunck-Leisegang straggling function [1], until the protons have lost all their energy. This approach consumes large amounts of computer time. Therefore a somewhat simpler approach has been used here. It consists of two parts: using the method given by Tschalär [19] for the reduction in energy from 70 to 20 MeV, then using the thin slice approximation for the rest of the energy loss.

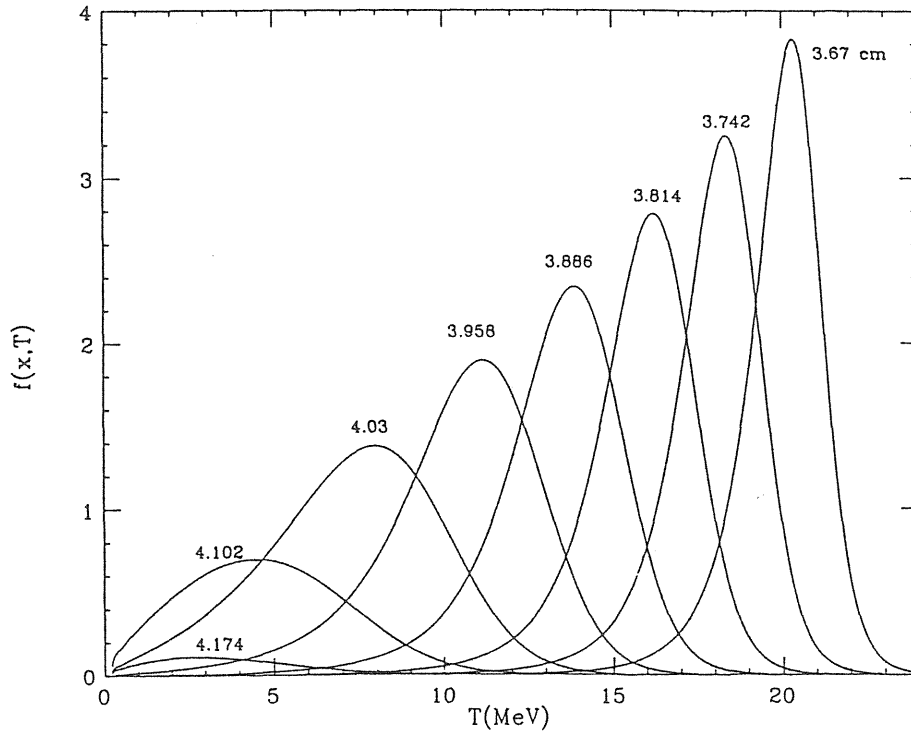

Figure 2. Energy spectra $f(x, T)$ of 70 MeV protons after traversing thicknesses x (cm) of water, calculated with the method described in Evaluation of Measurements with the Energy Straggling Method. The mean range of the protons is 4.094 cm (Table I). The abscissa represents the proton energy, T, the ordinate the spectrum $f(x, T)$, in arbitrary units, but the area under the curves is equal to the number of protons, N, in the beam. The absorber thickness x is the parameter given next to the curves. The functions are asymmetric, with more protons at lower energies except for the largest x. The spectra can be characterized with the following parameters: N = proton fluence, T_M = most probable energy, $\langle T_1 \rangle$ = mean energy, σ = standard deviation, γ_3 = skewness parameter:

x (cm)	N (%)	T_M (MeV)	$\langle T_1 \rangle$ (MeV)	σ (MeV)	γ_3
3.67	100	20.35	19.87	1.35	−1.27
3.742	100	18.35	17.89	1.54	−1.22
3.814	100	16.25	15.71	1.77	−1.17
3.886	99.7	13.85	13.25	2.06	−1.03
3.958	98.2	11.15	10.42	2.39	−0.72
4.03	87.6	7.95	7.28	2.58	−0.21
4.102	44	4.5	4.75	2.34	+0.37
4.174	6	2.8	3.69	2.12	+0.8

Note the reversal in the skewness of the curves for the last two thicknesses. This occurs because protons with the lowest energies have disappeared from the beam.

In a detailed study of straggling in thick absorbers, Tschalär [19] found that straggling can be calculated reliably (using moment theory) for mean energy losses up to about 80%. For the 70 MeV protons, this is 14 MeV. For larger losses, protons are lost from the beam because they have reached energy 0, and the method becomes unreliable (see Table I). Tschalär did not include multiple scattering in his calculation.

A computer program which approximates the experimental energy loss processes and produces ionization curves (numerical values are given for water) includes the following steps. In steps 1 to 3, the fluence spectrum $f(t + x_0, T_1)$ is calculated for a thickness x_0 at which $\langle T_1 \rangle = 20$ MeV. In step 4, the protons are transported through successive layers of water until their energy is zero. In step 5, the ionization in the thin chamber is calculated.

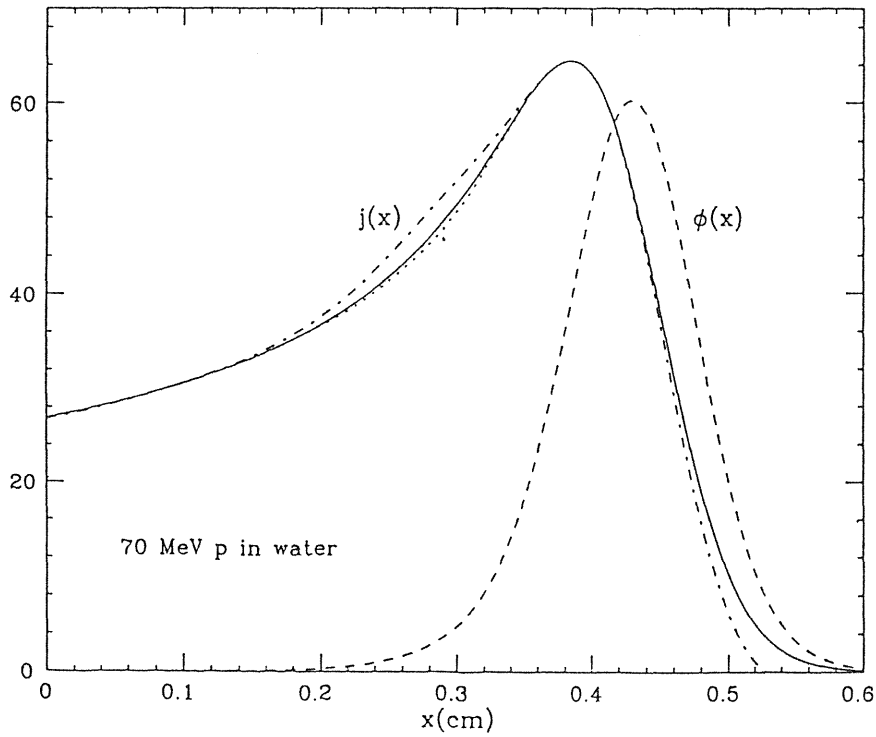

Figure 3. Ionization curves $j(x)$ calculated with the methods in Evaluation of Measurements with the Energy Straggling Method (solid line) and Results (dashed-dotted line); the average measured function agrees with the solid line except where a dotted line is shown. The stochastic errors of the experimental curve are about thrice the width of the line, though. The total distance traveled by the protons is $t + x = (3.667 + x)$ cm. The distance x (cm) is measured from the plane at which the mean residual energy $\langle T_1 \rangle$ of the protons is 20 MeV. The projected residual mean range of the beam is 0.4256 cm (the total multiple scattering path length correction is 0.0018 cm). The range straggling curve is given by the broken curve, $\phi(x)$. It represents the relative number of protons stopping in the layer between x and $x + dx$. The standard deviation of this function is $\sigma = 0.0566$ cm, or 1.4% of the mean range. This is about 20% larger than the value calculated with the CSDA approximation (Figs. 8d–10 in Bichsel [14]). The curve is asymmetric; the area under the curve represents the number of protons in the beam.

(1) **Calculation of the energy spectrum at a reduced energy.** The transport of the protons through the materials from the original energy, $T_0 = 70$ MeV, to a mean energy $\langle T_1 \rangle = 20$ MeV (Table I) is calculated with Tschalär's [19] theory. This theory assumes that all the protons have traveled the same distance s given by the range difference calculated with the continuous slowing down approximation, $s = R(70\ \text{MeV}) - R(20\ \text{MeV}) = 3.667$ cm (Table I), but due to energy loss straggling, the protons have a distribution of energies, $f(s, T_1)$, centered around 20 MeV (see Fig. 2). For monoenergetic incident particles, Tschalär provided graphs giving the parameters σ (for the width of the spectrum) and γ_3 (giving the skewness of the spectrum) needed to calculate the energy spectrum $f(s, T_1)$ of the protons at s.

(2) **Modification of $f(s, T_1)$ for spread in energy of 70 MeV beam.** Since the protons from the accelerator have an unknown energy spectrum, it is necessary to assume parameters σ and γ_3 for the spectrum $f(s, T_1)$ of step 1 somewhat larger than the parameters given by Tschalär. In practice, σ and γ_3 are assumed to be adjustable parameters (within reasonable limits), and calculations are repeated until calculated and experimental ionization curves agree approximately. With this choice of parameters, the influence of inhomogeneities of the absorber foils is included in the energy loss spectrum.

(3) **Modification of $f(s, T_1)$ for multiple scattering.** Since Tschalär's theory neglects multiple scattering, an approximate correction for this effect must be made. Because of multiple scattering, the protons will travel along crooked paths with length s, but the distance projected along the initial direction is shorter than s. For the protons to arrive at the absorber thickness t, they must travel an additional distance $\delta = c \cdot \Delta_{BU}$ ($c \approx 1.1$). An approximation for δ is given in Bichsel and Uehling [17]. In traversing δ, the protons lose additional energy given by $\Delta = \delta \cdot S(T_1) = S(T_1) \cdot c \cdot \Delta_{BU}$. The energy spectrum calculated in steps 1 and 2 thus is changed to lower energies and shall be designated as $f_M(t, T_1)$ to indicate that it has been calculated for an absorber of thickness t, is modified for multiple scattering (subscript M), and is a function of proton energy T_1 (the reduction Δ at $T_1 = 20$ MeV is about 0.08 MeV for water and about 0.6 MeV for the lead absorber).

At this point, the protons also have an angular spread, but this only influences the distances traveled (see step 4), and not the fluence (Fig. 1).

(4) **Transport of protons through further layers of water.** The protons penetrate successive thin layers of water (each of thickness $\Delta x = 0.0009$ cm). The energy losses in these layers are calculated for the entire spectrum $f_M(T_1, t)$, giving a new spectrum $f_M(T_1, t + \Delta x)$. Rather than calculating the energy loss as a function of multiple scattering angle for each energy, the assumption is made that all the protons of a given energy T_1 will traverse the layer Δx at a mean angle θ. This angle is given by multiple scattering theory for the total absorber thickness t traversed so far [17]. The energy loss then is given by $\Delta = S(T_1) \cdot \Delta x / \cos\theta$, where $S(T_1)$ is the stopping power at energy T_1. The protons are assigned to a spectrum $f_M(T_1 - \Delta, t + \Delta x)$ appropriate for the thickness $t + \Delta x$ and the reduced energy $T_1 - \Delta$. In the calculation, the energy bins ΔT are 0.1 MeV wide, and therefore, straggling in the layer Δx is neglected since the width of the Vavilov straggling function for Δx is only about 0.01 MeV. An energy spectrum $f_M(t + \Delta x, T_1)$ is thus obtained.

This process is repeated for further layers Δx, giving spectra $f(t + x, T_1)$ until all the protons have lost all their energy. About 700 layers are needed to achieve this. The number of protons reaching a residual energy $T_1 = 0$ is recorded and results in the range straggling spectrum $\phi(x)$.

(5) Ionization curve. After each layer, the ionization j is calculated with

$$j(x) = \int f_M(t + x, T_1)[S_t(T_1)/\cos\theta]\, dT_1$$

where $S_t(T_1)$ is the stopping power of the gas in the ionization chamber, at energy T_1. $j(x)$ should agree with the experimental ionization curve. By fitting the ionization curves to the experimental data for different absorbers, T_1 can be found, and the method described in Simple Evaluation of the Measurements is used to find I_a.

Results

The changes in the energy spectra $f_M(t + x, T_1)$ as a function of x are shown in Figure 2 and described in the caption. Calculated and experimental ionization curves are compared in Figure 3. The agreement between the function calculated in the previous section and the experiment is quite close. Further investigations must show whether the small differences at x between 0.2 and 0.3 cm are due to problems with the experiments or with the theoretical calculations. The range straggling curve $\phi(x)$ obtained in the previous section is also given.

The calculation made with the method described in Evaluation of Experiment with the Range Straggling Method differs from the experimental data but might still be useful for the evaluation of the experiments. Evaluations of measurements for different absorbers will be presented later.

Bibliography

[1] H. Bichsel, Rev. Mod. Phys. 60, 663 (1988).
[2] AAPM, *Protocol for Heavy Charged-particle Therapy Beam Dosimetry* (American Institute of Physics, New York, 1986), AAPM report No. 16, published for the American Association of Physicists in Medicine.
[3] H. Bichsel and L. E. Porter, Phys. Rev. A25, 2499 (1982).
[4] B. L. Jhanwar, W. J. Meath, and J. C. F. MacDonald, Rad. Res. 96, 20 (1983).
[5] E. Shiles, T. Sasaki, M. Inokuti, and D. Y. Smith, Phys. Rev. B22, 1612 (1980).
[6] ICRU, *Stopping Powers of Electrons and Positrons* (International Commission on Radiation Units and Measurements, Bethesda, MD, 1984), ICRU report 37.
[7] C. Tschalär and H. Bichsel, Phys. Rev. 175, 476 (1968).
[8] H. Bichsel, Phys. Med. Biol. 27, 449 (1982).
[9] H. H. Andersen, J. F. Bak, H. Knudsen, and B. R. Nielsen, Phys. Rev. A16, 1929 (1977).
[10] R. Ishiwari, N. Shiomi-Tsuda, and N. Sakamoto, Nucl. Inst. Meth. B35, 118 (1988).
[11] C. J. Bakker and E. Segre, Phys. Rev. 84, 489 (1951).
[12] G. Nakano, K. R. MacKenzie, and H. Bichsel, Phys. Rev. 132, 291 (1963).
[13] J. A. Nordin and R. M. Henkelman, Phys. Med. Biol. 24, 781 (1979).
[14] ICRU, *Average Energy Required to Produce an Ion Pair* (International Commission on Radiation Units and Measurements, Bethesda, MD, 1979), ICRU report 31.

[15] H. Bichsel, in American Institute of Physics Handbook (McGraw-Hill, New York, 1972), Sect. 8d.
[16] R. Mather and E. Segrè, Phys. Rev. 84, 191 (1951).
[17] H. Bichsel and E. A. Uehling, Phys. Rev. 119, 1670 (1960).
[18] M. J. Berger and S. M. Seltzer, in *Studies in Penetration of Charged Particles in Matter* (National Academy of Sciences, Washington, D. C., 1964), Nat. Res. Council Publication 1133, pp. 69–98.
[19] C. Tschalär, Nucl. Inst. Meth. 61, 141 (1968).
[20] T. Hiraoka, K. Kawashima, and K. Hoshino, Br. J. Radiol. 55, 585 (1982).

Received May 10, 1989

研究論文

粒子線に対するガスのW値の評価

放射線医学総合研究所　物理研究部
平岡　武，川島　勝弘，星野　一雄，福村　明史

Estimation of w-values for particle beams in several gases

Takeshi Hiraoka, Katsuhiro Kawashima, Kazuo Hoshino and Akifumi Fukumura

(Received 26 Sep 1989)

Division of Physics, National Institute of Radiological Sciences, 9−1, anagawa−4−chome, Chiba-shi 260 Japan

Research Code No : 203.9
Key Words ; W-value, Particle beams, Ionization chamber, Gas ionization

The differential w-values were measured for proton, deuteron, ^{3}He ion, neutron and ^{60}Co gamma-ray beams. The measurements were made by eight ionization chambers with different shapes and sizes. The gases investigated were air, argon, nitrogen, carbon dioxide, methane and methane based tissue-quivalent gas, and the density of the gases at 0 ℃, 101.3 kpa is 1.293, 1.784, 1.250, 1.977 0.717 and 1.142 mg/cm^{3}, respectively. The tank gases were used of pure grade.

The differential w-values were determined from the Bragg-Gray cavity theory. For the 70 MeV proton beams, we estimated the w-value of 35.3, 27.0, 36.5, 34.3, 27.9 and 30.4 eV in the gases mentioned above, respectively. Our results agree with those recommended in ICRU report 31. Similar results were also obtained for the other particle beams. The use of these w-values for the evaluation of abosrbed dose with ionization chambers for proton beams gave good agreement with a tissue-equivalent calorimeter. The uncertainties of the w-values are estimatedto be 4.3%.

1. 緒　言

放射線の吸収線量を評価する場合、電離箱による方法が精度や便利さから最も一般的であり、現在ほとんどこの方法により絶対線量の評価が行われている。この方法には Bragg-Gray の空洞理論が適用され線量評価がなされるが、そのためには阻止能とW値の２つの物理パラメーターを知らなければならない。このうち阻止能は比較的精度よく算定できるが、W値は実験により求めなければならないため、全ての放射線に対して未だ不十分なデータしかない。空気以外のガスのW値について特にこのことが問題となる。放医研では速中性子線や陽子線の治療が行われており、近い将来重粒子線治療へ発展しようとしている。これらの放射線には組織等価物質プラスチック壁の電離箱と、組織等価ガスを組み合わせて線量評価するのが精度の点で一般的である。[1,2] そのためにはこのガスのW値が正確にわからなければならない。この研究では重粒子線に対するW値を評価することを目標に、放医研サイクロトロンから得られる陽子線、重陽子線、^{3}H粒子線、速中性子線に対する６種類のガスのW値を測定した。また比較のため ^{60}Co ガンマ線についても測定を行った。ここで求めたW値は微分型W値（以後W値と記す）である。

2. 研究方法

2. 1. W値の計算法

密度ρ_1のガス g_1 を満たした電離体積Vを有する電離箱の壁による吸収線量 Dm は、Bragg-Gray の空洞理論により次式で与えられる。

$$D_m = \frac{Q_1}{V\rho_1} W_1 \frac{(S/\rho)_m}{(S/\rho)_1} \qquad (1)$$

次に同じ電離箱に異なったガス g_2（密度 ρ_2）を満たして前と同じ条件で照射した場合の電離箱壁による吸収線量 Dm は次式で与えられる。

$$D_m = \frac{Q_2}{V\rho_2} W_2 \frac{(S/\rho)_m}{(S/\rho)_2} \qquad (2)$$

ここで両式のQとWは１と２によって示されたそれぞれのガスに対する電荷とW値である。$(S/\rho)_m$ は壁材の平均質量衝突阻止能（以下阻止能と略記）である。$(S/\rho)_1$ と $(S/\rho)_2$ はそれぞれガス g_1 と g_2 の阻止能である。（１）式と（２）式から次式が得られる。

$$\frac{W_1}{W_2} = \frac{Q_2}{Q_1} \frac{(S/\rho)_1}{(S/\rho)_2} \frac{\rho_1}{\rho_2} \qquad (3)$$

上式の阻止能比は比較的エネルギー依存性が小さく、また計算により正確に求められる。従って、W値の比が評価できることになる。

2. 2. 阻止能の算出

陽子以上の重い荷電粒子に対する阻止能の理論的取扱は Bethe の式より次式で与えられる。

$$S/\rho = \frac{0.30707}{\beta^2}\frac{Z}{A}\left\{\ln\left(\frac{2mc^2\beta^2}{1-\beta^2}\right) - \beta^2 - \ln I - \frac{C}{Z} - \delta\right\} \qquad (4)$$

ここでmc^2は電子の静止エネルギー。$\beta = v/c$で、cとvはそれぞれ光子と入射粒子の速度である。Z、A、Iはそれぞれ阻止物質の原子番号、原子量、平均励起エネルギーである。C／Zは内殻補正項、δは密度効果補正項である。このうち後者は入射粒子の静止エネルギー程度から影響が起きるので、ここでは零とした。C／Zには Andersen and Ziegler[3] の補正値を用いた。（4）式は正確には Bakas 補正項や Block 補正項が必要であるが、ここでは無視した。我々は以前行った測定からI値を評価した。図1はI／Zを原子番号の関数として、我々の測定値と他の評価値が示し

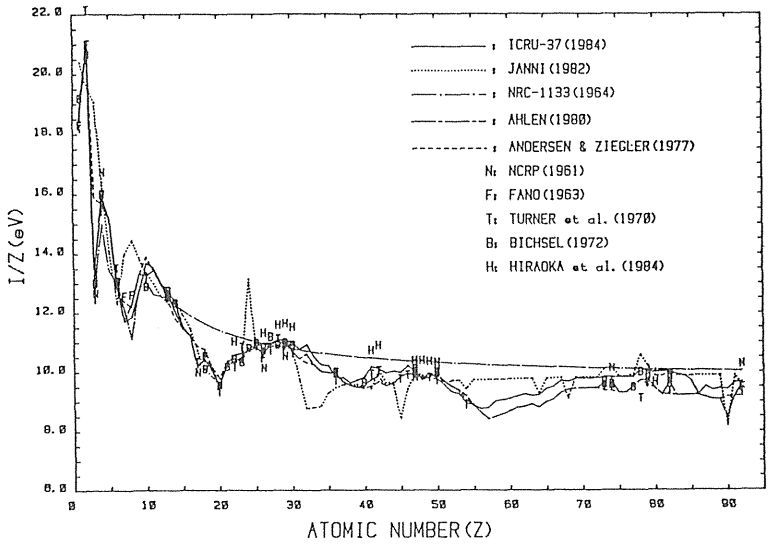

Fig. 1. I／Z as a function of atomic number

てある。これらのI値と（4）式により測定に用いた放射線に対するガスの阻止能を計算し表1に示した。また図2に陽子のエネルギーの関数として、窒素との阻止能比を示してある。表1の速中性子線に対しては5 MeV の陽子線に対する値を用いた。実際各電離箱に入射するエネルギーは公称エネルギーより低い値となるが、2図からもわかる様に、阻止能比のエネルギー依存性は小さいのでこの影響は無視できる。^{60}Co ガンマ線に対する値はICRリポート37の0.4 MeVの電子線に対する値を用いた。

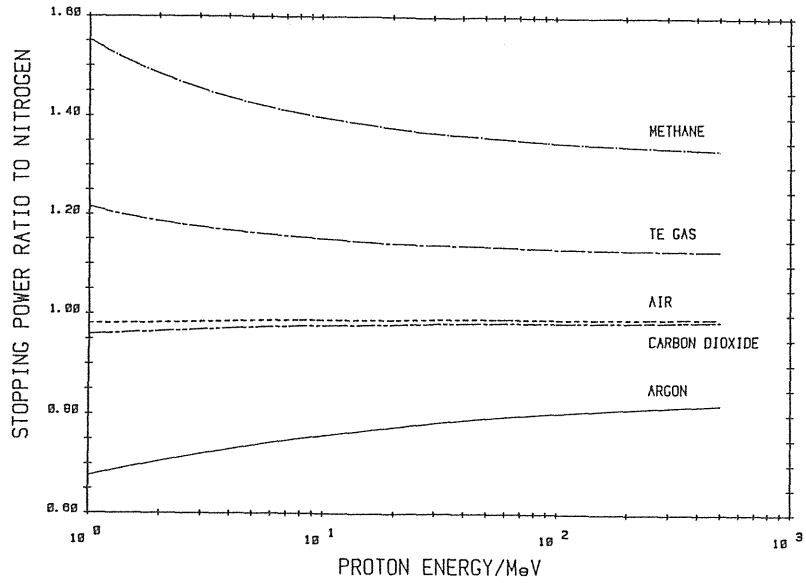

Fig. 2. Calculated stopping power ratio to nitrogen

Table 1. Estimated stopping power of the gases to be investigated

Gas	Cobalt-60 0.4MeV electron	Proton 70MeV proton	Deuteron 35MeV deuteron	Helium-3 95MeV ^{3}He	Neutron 5MeV proton
AIR	1.902	8.433	25.51	63.25	68.77
TEG	2.178	9.650	29.48	72.72	80.96
N_2	1.914	8.502	25.76	63.82	69.64
CO_2	1.906	8.370	25.26	62.71	67.84
AR	1.558	6.799	19.89	50.11	51.39
CH_4	2.576	11.51	35.55	87.21	99.28

2. 3. 放射線源

W値の測定に用いた放射線源は以下の通りである。

1) ^{60}Coガンマ線

線源電離箱間距離（SCD）＝80cm。 照射野（A）＝10×10 cm^2。

線量率（$\dot{D}$）＝0.5 Gy／min。

2) 70 MeV陽子線

照射位置から6 m上流に1mm厚のアルミニウム散乱フィルムを設置。 A＝4×4 cm^2。

$\dot{D}$＝15 Gy／min。

3) 35 MeV重陽子線

$A = 4 \times 4$ cm²。　$\dot{D} = 80$ Gy／min。

4) 99 MeV ^{3}He 粒子線

$A = 4 \times 4$ cm²。　$\dot{D} = 50$ Gy／min。

5) 速中性子線

30 MeV重陽子線を厚いベリリウムターゲットに衝突させて発生する速中性子線。

$A = 4 \times 4$ cm²。　SCD = 200 cm。　$\dot{D} = 0.5$ Gy／min。

Table 2. Ionization chambers used for the measurements of the differential w-value

Chamber	Shape	Volume (ml)	Wall mat.	Wall thick. (g/cm²)	Gap length (mm)	Schematic cross
150-TG	Sph.	0.922	A-150	0.142		
576-RTG	Sph.	1.06	A-150	0.570		
426-TTG	Cyl.	0.132	A-150	0.177	1.4	
401-ETG	P.P.	0.360	A-150	0.007	4	
T2	Cyl.	0.530	A-150	0.112	2.3	
PP-1	P.P.	0.603	Lucite	0.190	5	
1.3-TC	Cyl.	1.44	Teflon+ Carbon	0.336	3	
Fontenay	Cyl.	1.42	Aluminum	1.35	4	

2. 4. 電離箱

測定には平行平板形（P.P.）、円筒形（Gyl.）及び球形（Sph.）の電離箱8本を用いた。これは電離箱の形や大きさがW値の評価に影響を及ぼすかどうかを検討するためである。表2にそれら電離箱の型名、形状、電離体積、壁材質、壁厚、電極間隔及び断面図が示してある。陽子線に対しては全ての電離箱を、^{60}Co ガンマ線に対しては6種類を用いた。重陽子線と ^{3}He 粒子線には飛程の関係で平行平板形を、また速中性子線には反跳陽子の影響を大きくするため、A－150 及びルサイト壁の電離箱を測定に用いた。

2. 5. 照射及び測定条件

W値の測定に用いたガスは空気、アルゴン、窒素、二酸化炭素、メタン、組織等価であり、これらの0℃1気圧での密度はそれぞれ 1.293、1.784、1.250、1.977、0.717、1.142 mg／cm³ である。すべて高純度タンクガスで、約10 ml／min の流量率で測定した。電荷測定には振動容量電位計（Cary Model 401）にディジボルを接続して行った。

陽子線、重陽子線、^{3}He 粒子線に対しては、薄いアルミフォイルを電極とする電離箱をモニタとした。これには窒素ガスを40 ml／min の割で流し、－1000 V の印加電圧で作動させた。速中性子線に対しては、ベリリウムターゲット上の電流をモニタとした。

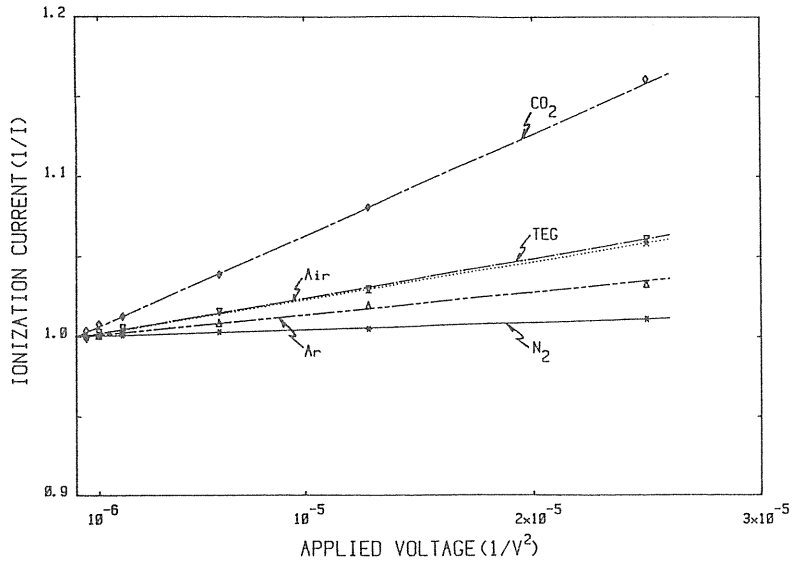

Fig. 3. Ionization current as a function of applied voltage

3. 結果及び討論

3. 1. イオン再結合損失

放医研サイクロトロンから得られる70MeV 陽子線の繰り返し周波数は 19 MHz である。従って、電離箱中でのイオンの移動度から考えると、イオン再結合損失に対してこの陽子線は連続放射線として扱うことができる。ここで測定した他の粒子線についても同様な結果を得た。平行板形電離箱に各測定ガスを満たし、重陽子線に対する飽和特性を測定し、イオン収集効率を求めた。近飽和領域での、印加電圧の２乗の逆数に対する電離電流の逆数の測定結果を図２に示す。図の縦軸は印加電圧が無限大の値を1.0に規格化してある。印加電圧が 200～1500 V の間で良い直線近似が得られた。これは一般再結合損失の理論を支持する結果であるが、初期再結合の詳細な影響については判断できない。同様な結果は他の粒子線についても得られた。

W値の測定時に於ける電離箱への印加電圧は形状、大きさ及び線量率によって異なるが、300～1000 V を加えた。これらは計算から、イオン再結合損失が 0.1％以下になるような電圧である。速中性子線は直接電離放射線でないため、イオン再結合損失も壁材質によって大きく異なるため、A－150 及びルサイト壁の電離箱を使用した。速中性子線に対するイオン再結合損失による誤差は最大0.2％と見積った。

Table 3. Polarity effects of the chambers for 70 MeV proton beams

Chamber	TEG	AIR	N_2	CO_2	CH_4	AR	Absolute Mean
426-TTG	-.19	-.07	-.12	-.14	-.35	-.30	.20±.11
401-ETG	.21	.15	.07	.10	.02	-.44	.17±.15
150-TG	.01	-.04	.11	.02	.12	-.28	.10±.10
PP-1	.16	.15	.26	.07	.26	.07	.16±.09
1.3-TC	.10	.07	.14	.13	.09	.04	.10±.04
Fontenay	-.02	.09	-.01	.00	-.08	.00	.03±.04
576-RTG	-.09	.00	.01	.00	.37	.23	.12±.15
T2	.06	-.07	-.01	.04	.08	-.09	.06±.03
Absolute Mean	.11±.08	.08±.05	.09±.09	.06±.06	.17±.14	.18±.15	

Table 4. Polarity effects of the chambers for ^{60}Co gamma rays

Chamber	TEG	AIR	N_2	CO_2	CH_4	AR	Absolute Mean
426-TTG	-.18	-.18	-.15	-.27	-.11	.00	.14±.09
401-ETG	.07	.01	.03	.00	.05	.14	.05±.05
150-TG	-.35	-.48	-.40	-.37	-.43	-.30	.39±.06
PP-1	-.63	-.67	.02	-.51	-.93	-.25	.50±.32
1.3-TC	-.25	.00	-.10	-.08	-.23	.00	.11±.11
Fontenay	-.06	-.10	-.11	-.11	-.07	.00	.08±.04
Absolute Mean	.26±.21	.24±.27	.14±.14	.22±.19	.30±.34	.12±.14	

3. 2. 極性効果

理想的な電離箱では、高圧電極への印加電圧の極性を変えても、収集される電荷量は同じになる。しかし、電離箱の構造や、放射線の線質によっては極性の違いによる収集電荷量に差を生ずる。正確な生成電荷量を得ることと、粒子線に対する種々の電離箱の極性効果を求めるための測定を行った。正及び負の印加電圧により得られる電荷をそれぞれ（＋）（－）とすると、極性効果（%）は次式により求めた。

$$\text{極性効果} = \frac{(+) - (-)}{(+) + (-)} \times 100 \qquad (5)$$

70MeV陽子線に対する前記電離箱の極性効果を表3に示す。W値の全ての測定は8回の平均値を取

った。各測定値の標準偏差は0.02 − 0.14 %以内で、（5）式で表現した場合はこの半分に相当する。従って、FontenayとT 2はノイズレベル以内と考えられるが、他の電離箱についてはガスによっては極性効果がはっきり表れている。速中性子線を除く粒子線に対しては、電離箱は極めて早く安定した。この原因は明らかでないが、直接電離放射線と間接電離放射線の違いによるものとも考えている。重陽子線及び ^{3}He 粒子線でも同様の結果であった。^{60}Co ガンマ線に対する値を表4に示す。401−ETG電離箱は壁厚が 7.0 mg／cm² とうすいため、付属のA−150プラスチックのビルドアップ板を装着して測定を行った。^{60}Co ガンマ線と中性子線は間接電離放射線であることから、両者は似た結果が得られた。但し、荷電粒子線にくらべると極性効果は大きかった。ガスでは一般にアルゴンとメタンの極性効果が大きい値を示した。

光子に対する極性効果は、一般にコンプトン散乱により放出または流入する電子によって説明されている。粒子線に対する極性効果を正確に説明することは、これらの結果からは困難である。電離箱の形、大きさ、ガス、壁材質、絶縁体と言った電離箱に原因する因子と、入射粒子のエネルギーやその種類、また放出される2次電子の影響と言った因子が複合して現れるものと考えられる。

Table 5. Ionization charge measured in several ionization chambers filld with the gases relative to air for 70 MeV proton beams

Chamber	TEG	AIR	N_2	CO_2	CH_4	AR
426-TTG	1.177	1.000	0.950	1.562	0.958	1.449
401-ETG	1.172	1.000	0.949	1.571	0.958	1.462
150-TG	1.176	1.000	0.942	1.562	0.963	1.470
PP-1	1.178	1.000	0.939	1.571	0.946	1.453
1.3-TC	1.167	1.000	0.948	1.536	0.962	(1.420)
Fontenay	1.180	1.000	0.944	1.571	0.960	1.455
576-RTG	1.176	1.000	0.942	1.550	0.960	1.462
T2	1.169	1.000	0.939	1.564	0.954	1.447
Mean	1.174±.005	1.000	0.944±.004	1.561±.012	0.958±.005	1.457±.009

3. 3. W 値

表5には70 MeV陽子線に対して、電離箱に各ガスを満たしたときの電荷を示してある。ここでは空気の値を1に規格化してある。アルゴンガスを満たした1.3 − TCの値を除けば、各ガスの値はよく一致している。^{60}Co ガンマ線の場合も、この電離箱でのアルゴンガスと他のガスの平均値を比較してみると、やはり 2.1 %低い値を示している。従って、W値の計算にはこの値は除いてある。

図4及び表6に各放射線に対して求めたガスのW値を示してある。W値の絶対値は基準の値を設定して評価した。表の * 記号の値がそれを示す。速中性子線に対するアルゴンガスの値だけが異常に大

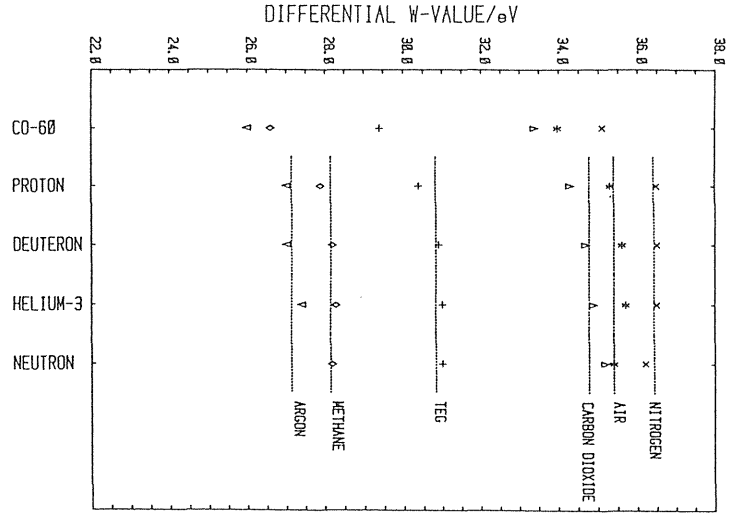

Fig. 4. Estimated differential w-values for the radiation qualities

大きい値である。速中性子線によって壁から放出される2次荷電粒子のスペクトル分布がわからないが、多くの高ＬＥＴ粒子を含んでおり、これらの影響や、またガスの純度や阻止能の評価精度等が複雑に影響し合っているものと考えられる。希ガスは昔から異常な電離現象を起こすガスとして知られており、その様な現れの一つかも知れない。この異常値を除けば、ここで用いた粒子線の範囲では、W値はほぼ一定と考えられる。図4の点線はこれら粒子線の平均値を示している。

粒子線に対する各種ガスのW値の算定精度を評価し表7に示す。全不確定度 4.3％に大きく影響するのは、基準のガスの評価精度である。しかしそのために、電荷測定は相対測定でよいことになり、これによる誤差を小さくすることができる。^{60}Coガンマ線に対しては 1.5％と評価した。

Table 5. Estimated differential w-values for the radiation qualities

Gas	Cobalt-60	Proton	Deuteron	Helium-3	Neutron
AIR	33.97*	35.3	35.6	35.7	35.4
TEG	29.4	30.4	30.9	31.0	31.0*
N_2	35.1	36.5*	36.5*	36.5*	36.2
CO_2	33.4	34.3	34.7	34.9	35.2
AR	26.0	27.0	27.0	27.4	30.3
CH_4	26.6	27.9	28.2	28.3	28.2

Table 7. Estimated uncertainty of the w-values

Source of error	Percentage
Reference w-value	4. 0
Charge measurement	0. 5
Stopping power	1. 5
Gas density	0. 1
Ion recombination	0. 2
Beam stability	0. 3
Total uncertainty	4. 3

4. 結　論

陽子線、重陽子線、^{3}He 粒子線及び速中性子線に対する空気、組織等価、窒素、二酸化炭素、アルゴン、メタンガスのW値を求めた。これら粒子線に対する各ガスの平均のW値はそれぞれ、35.5、30.8、36.4、34.8、27.1、28.2 eV であった。これらの値は ICRU リポート31の値ともよく一致している。我々が以前行った陽子線線量の国際相互比較での電離箱とカロリメータは良い一致が得られた。ここで求めた粒子線に対するW値の全不確定度は 4.3％と評価した。

米国の重粒子線治療用線量のプロトコール（AAPMリポート16）[4] に於て、陽子線に対する空気のW値は 34.3 eV が勧告されている。しかしここでの測定結果でも全不確定度の範囲内ではあるが、約3％小さい値である。このことは早川ら[5]によりやはり指摘されている。

線量測定用ガスとしては、希ガスであるアルゴンは微量の不純物の影響か、不安定な場合が多く、窒素、組織等価、空気を用いることが有効と思われる。

文　献

1) 平岡　武、川島勝弘、星野一雄、松沢秀夫 ： 放医研サイクロトロン速中性子線の線量測定、日本医放会誌、37、369-376、1977

2) 平岡　武 ： 高エネルギー陽子線の吸収線量の算定とその線量分布に関する研究、日本医放会誌、42、30-54、1982

3) Andersen, H. H. and Zidgler, J.F. : Hydrogen stopping powers and ranges in all elements, in Volume 3 of the Stopping and Ranges of Ions in Matter, 1977 Pergamon Press, New York

4) AAPM Report No. 16 : Protocol for Heavy Charged-Particle Therapy Beam Dosimetry, American Association of Physicists in Medicine, 1986, New York

5) Hayakawa, y. and Schechtman H. : Comments on the value of the average energy expended per ion pair formed in air for a proton beam recommended by the American Association of Physicists in Medicine, Med. Phys., 15, 778, 1988

研究論文

Small Scale Proton Dosimetry Intercomparison between Japan and USA

Takeshi Hiraoka, Katsuhiro Kawashima, Kazuo Hoshino, Kiyomitsu Kawachi, Tatsuaki Kanai, Akira Ito[1]*, Lynn. J. Verhey[2], Joseph.C. McDonald[3]** and I-Chang Ma[3]

Division of Physics, National Institute of Radiological Sciences, 9-1, Anagawa-4 chome, Chiba-shi 260, Japan

1 *Cyclotron Unit, The Institute of Medical Science, The University of Tokyo, 4-6-1 Shirokanedai, Minato-ku, Tokyo 108, Japan*

2 *Department of Radiation Medicine, Massachusetts General Hospital, Boston, Massachusetts 02114, USA*

3 *Radiation Biophysics Laboratory, Memorial Sloan-Kettering Institute, 1275 York Avenue, New York, New York 10021, U.S.A.*

* *Present Address, Department of Physics, Cancer Institute, 1-37-1 Kamiikebukuro, Toshima-ku, Tokyo 170, Japan*

** *Present Address, Health Physics Department, Battle Northwest Laboratory, Richland, Washington 99352, USA*

(Received 19 Sep 1989)

Research Code No : 203.9

Key Words : Dosimetry intercomparison, Proton beam, Absorbed dose, Bragg curve, Proton therapy

1. Introduction

High energy proton beams have been regarded as one of the more attractive particles for use in radiotheapy since in 1946 Wilson(1) suggested the application of the high energy proton beams for radiological purposes. In the National Institute of Radiological Sciences(NIRS), clinical trials of proton beams started in October 1979, using the spot scanning system in order to obtain the irradiation of large fields with homogeneous dose distributions. Measurements of absorbed dose in the proton beams were made by the use of ionization chambers and of a Faraday cup. The agreement of dose estimated by both methods is within the total uncertainties(2).

A proton dosimetry intercomparison between Japan and the United States was done in April 21-25, 1980 at NIRS under the US-Japan Cooperative Cancer Research Program. Physicists from the Institute of Medical Science of University of Tokyo (IMS), Massachusetts General

Hospital(MGH) and Memorial Sloan－Kettering Institute(MSKI) were participated in the dosimetry intercomparisons. During this time, radiobiological intercomparisons were also performed. For both intercomparisons, reasonable agreement were obtained.

2. Beam characteristics

The NIRS isochronous cyclotron can produce proton beems of a nominal energy of 70 MeV at the treatment site. A proton spot scanning system has been used in order to obtain the desired field sizes and shapes. In the system, maximum field of 20 x 20cm can be available to radiotherapy. Beam control systems and precise dose distributions have been described in anothr paper(3, 4, 5).

Figure 1 shows central axis depth dose curves in water. The solid line gives unmodulated beam and dotted line gives modulated beam with a fan shaped range modulator for making a spread out Bragg peak(SOBP) of 25 mm width. From the measurement of depth dose distribution in water for unmodulated beams, depth of the Bragg-peak, mean range, peak width(FWHM), and peak to plateau dose ratio are 37.81±0.13mm, 38.50±0.11mm, 3.31±0.09mm, and 5.834±0.051, respectively. The proton beam energy estimated from the mean range is 68.2±0.2 MeV using the tables of Janni(6).

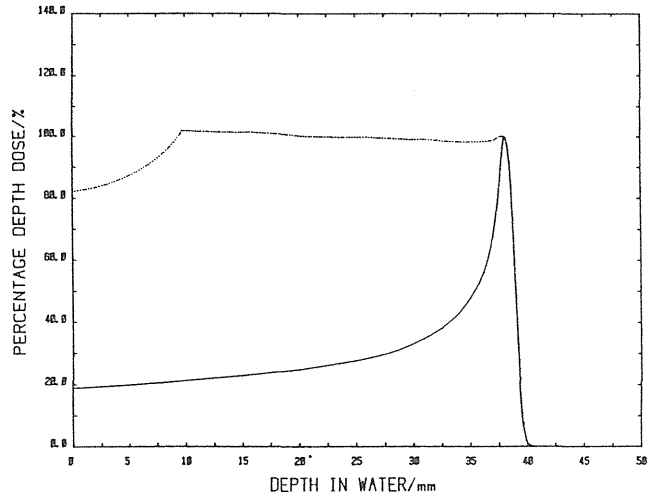

Fig.1. Depth dose distributions in water for unmodulated (solid line) and spread out Bragg peak (dotted line).

Dose intercomparisons were made at the entrance position of unmodulated beams and at the depth of 15 mm in Lucite for the spread out Bragg peak which is equivalent to 17.3 mm in water.

3. Materials

All the participants used ionization chambers as detectors except for MSKI which used a tissue equivalent calorimeter and an ionization chamber. Table 1 shows the detectors used and their specifications provided by each participant. The shape of the chambers

INSTITUTION	NIRS			MGH	IMS	MSKI	
DOSIMETER	PP-1	401-ETG	IC-18	IC-18	PPTE	IC-18	TE-Cal.
Shape	PP	PP	Cyl.	Cyl.	PP	Cyl.	
Volume(ml)	.603	.348	.153	.1	.66	.1	
Cavity Gas	TEG, Air, N2, CO2		TEG	TEG, Air	TEG	TEG	
Wall Mat.	Lucite	A-150	A-150	A-150	A-150	A-150	
Wall Thick. (g/cm2)	.155	.007	.177	.177	.11	.177	
Gap Length (mm)	5	4	1.4	1.4	5	1.4	
Appl. Volt. (V)	-500	-500	-500	+300	-300	+250	

Table 1. Detectors used for the intercomparison.

was either parallel plate(PP) or cylindrical(Cyl.). Methane-based tissue-equivalent gas(TEG) (7) and air were used as the chanmber gas for the dose comparesons.

4. Dose estimation with ionization chamber at NIRS

The techniques of absorbed dose determination employed by each participant are in the literature(8, 9). The Bragg-Gray cavity theory can be used to determine the sbsorbed dose in the medium. The absorbed dose in tissue for proton beams is given by

$$D_t = \frac{Q \times Wp/e \times (Sp)\text{wall/gas} \times K}{M \times (Sp)\text{wall/tissue}}$$

where D_t is tissue absorbed dose in Gy, Q is charge collected in coulomb, Wp is the average energy required to produce an ion pair in joule, e is the charge of the electron in coulomb, (Sp) wall/gas is the average stopping power ratio of the chamber wall relative to the chamber gas for protons, (Sp) wall/tissue is also the same ratio of the chamber wall relative to tissue for their particles, K is the correction factor including ion recombination loss, ambient temperature and pressure, etc., and M is the mass of gas in kg. The mass of gas in a chamber is determined by irradiation of the chamber in a photon field(Co-60). The intensity of the field can be measured using ionization chambers whose calibration is traceable to the national standardizing laboratory. The mass of the gas is given by

$$M = \frac{2.58 \times 10^{-2} \times Qg \times Wg/e \times (Sg)\text{wall/gas} \times K}{0.957 \times X \times Aeq \times (\mu en/\rho)\text{wall/tissus}}$$

where Qg is the charge collected in coulomb, X is exposure in C/kg. Aeq is the wall corrdction factor, $(\mu en/\rho)$wall/tissue is the mass energy absorption coefficient ratio of the chamber wall relative to tissue. Other factors with the subscript, g, denotes the value applicable to the calibration in gamma-ray field.

5. Irradiation conditions

One of the most important problems in dosimetry intercomparisons is the stability of the monitor chamber. Figure 2 shows a plot of the constancy of the thin walled transmission monitor chamber used during the intercomparison which was checked with a parallel plate chamber with a 0.118 g/cm^3 thick Lucite wall which was designed and constructed at NIRS. Ionization gas of the monitor chamber was nitrogen, with flow rate of 40 ml/min. It seems that the stability of the monitor is sufficiently good as a proton beam monitor. Figure 3 shows the results of changes in room temperature and atomospheric pressure at the same time corresponding to Figure 2. It can be seen that the variation of the correction factor for changes of mass of the gas in the chamber was less than 1% during the intercomparison. Figure 4 also shows the changes in temperature and pressure on April 21, 1980, when the most of the physical intercomparisons were performed. The data were taken at regular intervals of one minute. The spikes in the temperature record were due to the fact that someone worked near the thermistor sensor in the treatment room at that time.

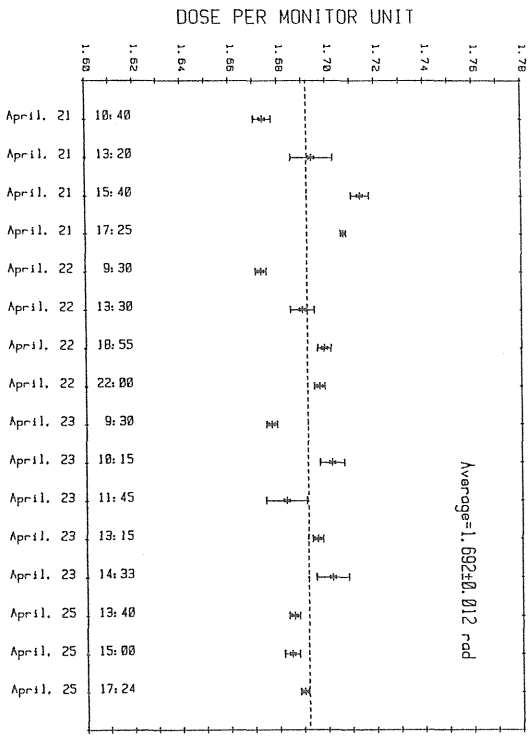

Fig.2. Plot of the constancy of the thin walled transmission monitor chamber during the intercomparison.

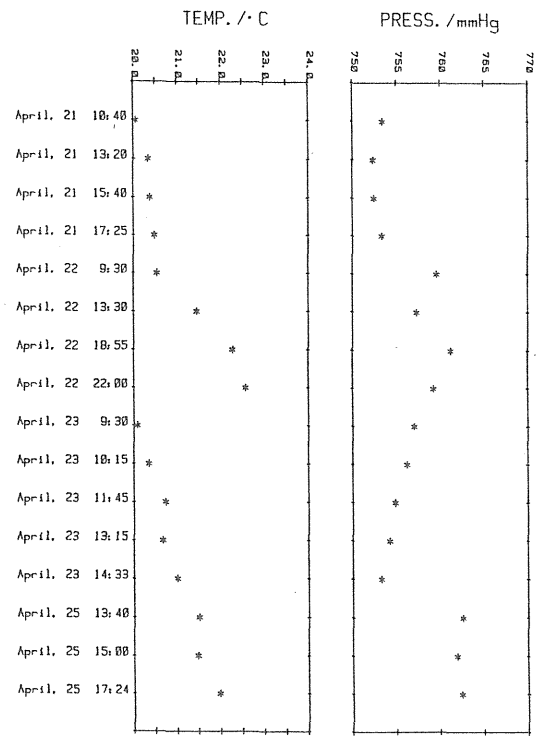

Fig.3. Room temperature and atomospheric pressure in the irradiation room during the inttercomparison.

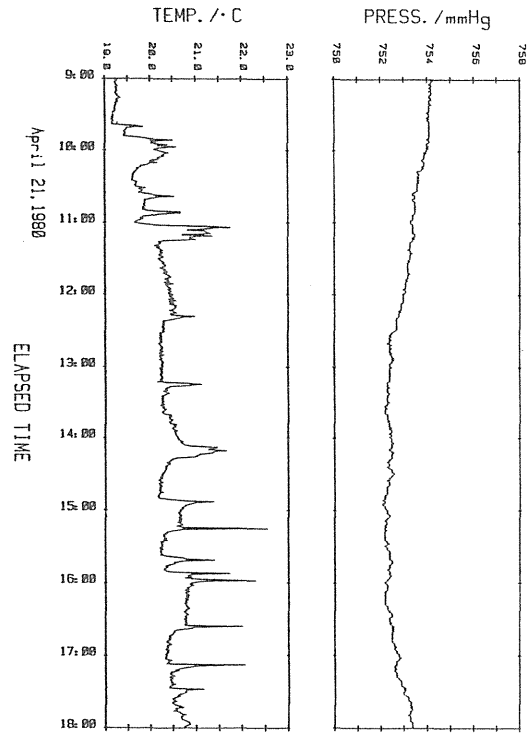

Fig.4. Changes in temperature and pressure on April 21.

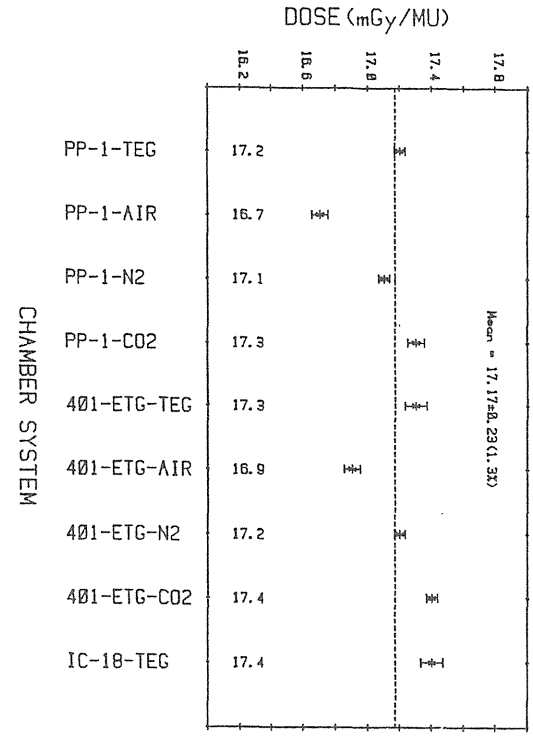

Fig.5. Results of tissue absorbed dose for NIRS chambers.

6. Results and discussion

NIRS used three different chamber systems and four ionization gases for the comparison. Figure 5 shows the results of the comparison of tissue absorbed dose per monitor unit at the entrance plateau for unmodulated beam. The agreement is quite acceptable but the values for air seem to be a bit low. Figure 6 shows the results of dose intercomparison at the entrance plateau for two different dose rates. The low dose rate is around 5 Gy/min and the high dose rate is ten times higher. No significant difference in measured dose appeared for both dose rates. The values for air estimated by MGH seemed to be small compared to the results of NIRS. Figure 7 shows the results at SOBP for two kinds of dose rates that are about 1.5 times larger than the entrance dose rates. The agreement is quite good for high dose rates. The value of the tissue equivalent calorimeter-(TE-CAL.*) is close to the mean value of all.

The main physical constants emploed for dose estimations with ionization chambers, based on Bragg-Gray cavity theory, are stopping power ratios and W-values. The NIRS has used values from Andersen-Ziegler(10) for stopping power ratio. On the other hand, other participants used the data of Janni(6). Fortunately, the error introduced by this difference is very small, because stopping power must be used as a ratio and the ratio varies slowly with energy. The NIRS used W-values from ICRU report 31(11), but MGH used other values. The difference is 2.6% both for air and TE gas. Using more accurate and reliable values for physical constants in all institutions can be considered important factors for maintain consistency in absorbed dose intercomparisons.

Figure 8 shows the photon beam equivalent response for the proton beams of

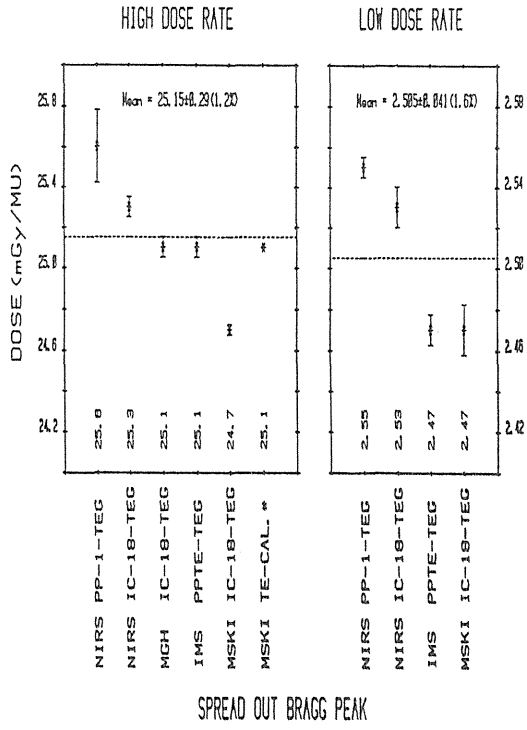

Fig.6 Results of dose intercomparison at the entramce plateau for two different dose rates.

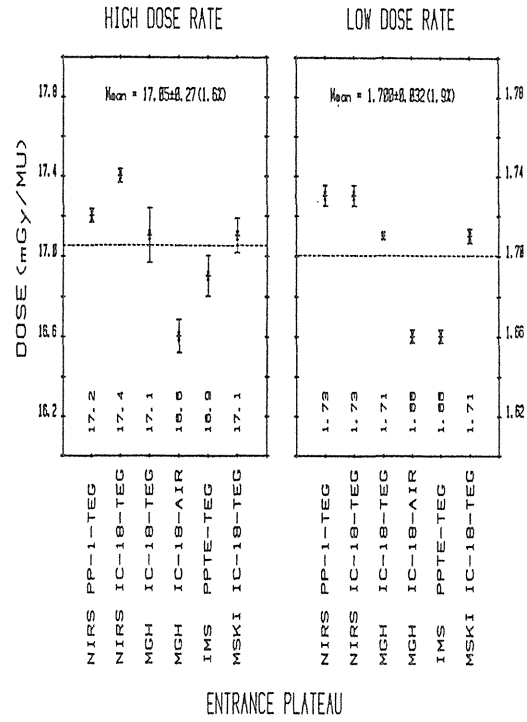

Fig.7. Results at the SOBP.

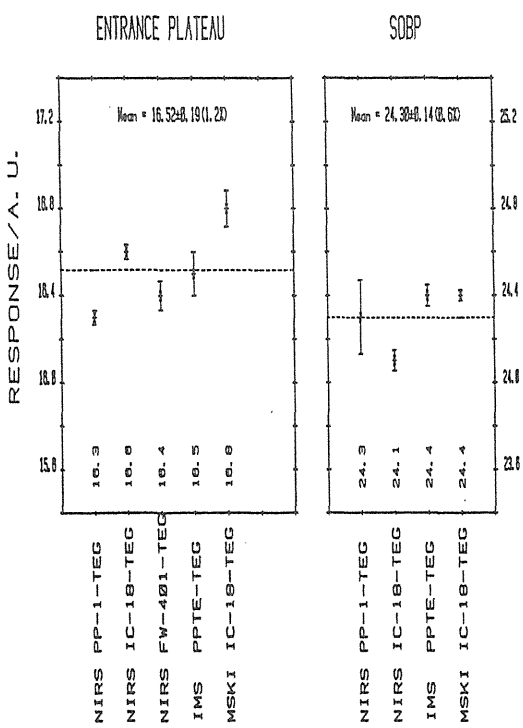

Fig.8. Photon beam equivalent response for the proton beams

the chambers filled with TE gas which were calibrated with the Co-60 gamma-rays at NIRS. The agreement is improved in comparison with Figures 6 and 7 indicating another possible source of uncertainty in the various home institution calibrations. If a single source is used for calibration, the agreement will be improved.

In conclusion, it has been shown that ionization chambers used by different individuals with different operating conditions and different gas can agree well with each other and with a TE calorimeter in these proton beams, when consistent calibrations and physical canstants are used.

References

1) Wilson, R.R. : Radiological use of fast protons, Radiology, 47 : 489−491, 1946.

2) Hiraoka, T. : Studies of abosrbed dose determinations and spatial dose distributions for high energy proton beams, Nippon Acta Radiolo., 42 : 30−54, 1982.

3) Kanai, T., Kawachi, K., Kumamoto, Y., Ogawa, H., Yamada, T., Matsuzawa, H. and Inada, T. : Spot scanning system for proton radiotherapy, Med. Phys., 7 : 365−369, 1980.

4) Hiraoka, T., Kawashima, K., Hoshino, K., Kawachi, K., Kanai, T. and Nakamura, Y.K. : Dose distrigutions of 70 MeV proton scanning beams for radiotherapy, Proc. 7th ICCR, 377−381, Kawasaki, Sep. 22−26, 1980.

5) Hiraoka, T., Kawashima, K., Hoshino, K., Kawachi, K., Kanai, T. and Matsuzawa, H. : Dose distributions for proton spot scanning beams : Effect by range modulstors, Nippon Acta Radiolo., 10 : 1214−1223, 1983.

6) Janni J.F. : Calculations of energy loss, range, pathlength, straggling, and the probability of inelastic nuclear collisions for 0.1−to 1000−MeV protons, AFWL−TR−65−150, 1966.

7) Rossi, H.H. and Failla, G. : Tissue equivalent ionization chambers, Nucleonics, 14 : 32−37, 1956.

8) Verhey, L.J., Koehler, A.M., McDonald, J.C., Goitein, M., Ma, I−Chang, Shneider, R.J. and Wagner, M. : The determination of absorbed dose in a proton beam for purposes of charged−particle radiation therapy, Radiat. Res., 79 : 34−54, 1979.

9) Ito, A., Ohmura, H., Hasegawa, T., Takenaka, E. and Sakamoto, K. : Absolute dosimetry of 52 MeV proton beam with ionization chambers, unpublished.

10) Andersen, H.H. and Ziegler, J.F. : Hydrogen stopping powers and ranges in all elements, The Stopping and Ranges of Ions in Matter, Pergamon Press, 1977.

11) ICRU Report 31 : Average energy required to produce an ion pair, International Commission on Radiation Units and Measurements, Washington, D.C., 1979.

JAERI - M
89-026

NEANDC(J)-133"U"
INDC(JPN)-120/L

PROCEEDINGS OF THE 1988 SEMINAR ON NUCLEAR DATA

March 1989

(Ed.) Tsuneo NAKAGAWA and Atsushi ZUKERAN*

日 本 原 子 力 研 究 所
Japan Atomic Energy Research Institute

3.15 Kerma factors for neutrons with energies above 20 MeV

K. Kitao

National Institute of Radiological Scienses

9-1, Anagawa-4-Chome, Chiba-Shi 260, Japan

Abstract

A short review is presented concerning the calculation of kerma factors for neutrons with energies above 20 MeV. Using the program ALICE, the light particle spectra from neutron-induced reaction and kerma factors for C, N, O and tissue have been calculated. The spectra are also compared with experimental results by Romero et al. at 27.4, 39.7 and 60.7 MeV neutron energy.

1. Introduction

Recent X-ray therapeutic apparatuses with energies tens of MV have provided the percent depth dose of 50% at 21 cm deep for a 10 cm x 10 cm field. For to achieve the level of depth dose in fast neutron teletherapy, the neutron beam have to be produced from the (p,n) reaction on beryllium with bombardment of protons with energy more than 70 MeV. Figure 1 shows values of the percent depth dose have been measured at some high energy accelerator em-ployed fast neutron therapy. The energy distribution of Be-p neutrons is varied with thickness of the beryllium target, backing materials and filter materials. In any case, calculations of neutron kerma factors for materials of biomedical importance have to extend for neutrons up to 100 MeV.

Neutron kerma factor for a given material is equal to the initial kintic energies of all the charged particles liberated by neutrons in a volume element of material. Then, kerma per unit fluence K(E), for monoenergetic neutrons with energy E, is defined by

$$K(E) = \Sigma_J \Sigma_I \langle E_{JI}(E) \rangle \sigma_J(E), \qquad (1)$$

where $\langle E_{JI}(E) \rangle$ is average energy transferred to the kinetic energy of Ith charged particle in Jth reaction, $\sigma_J(E)$ is the Jth reaction cross section at

particle energy E.

Cross section $\sigma_J(E) = \int d\sigma$ and $\langle E_{JI}(E)\rangle = (\int E_I d\sigma)_J / \int d\sigma$, then kerma factor is given by,

$$K(E) = \Sigma_J \Sigma_I \int E_I \, d\sigma_J,$$
$$= \Sigma_J \Sigma_I \int E_I (d\sigma/dE)_{JI} dE, \quad (2)$$

where $(d\sigma/dE)_{JI}$ is the spectrum of emitted Ith light charged particles from Jth reaction, and this is equal to the angle-integrated differential cross-section. Romero et al./1/ had made the measurements of neutron-induced charged particle (protons, deuterons, tritons, helium-3 and alpha particles) cross sections on tissue elements at 27.4, 39.7 and 60.7 MeV.

In this work, we assume C with a composition of 100% 12C, N with 100% 14N and O with 100% 16O, and compare charged particle emission spectra for C, N and O calculated by ALICE code/2/ with experimental spectra by Romero et al./1/ And, we have calculate kerma factors for C, N, O and ICRU muscle tissue, using the calculated spectra and the recoil kerma from that cited by Romero et al./1/

2. Status on kerma calculations

As it is shown in the table 1, since 1977 kerma factors for neutrons with energies above 20 MeV have been calculated for light elements by several groups (Alsmiller and Barish/3/, Wells/4/, Behrooz/5,6/, Caswell and Coyne/7/, Dimbylow/8,9/, Brenner/10/) based on calculated neutron cross sections or evaluation of limited experimental data. Therefore, there are significant discrepancies in the results.

Brenner/10/ had pointed out that all the nuclear models used in calculation of the neutron cross sections are quite adequate for the heavier elements in tissue but not suitable for low-mass nuclei. Experiments have predict that assumption of statistical evaporation as a means of de-excitation is reasonable for heavy and medium mass nuclei, but not for carbon. And assumption of an analytic form for the density of nuclear levels, as used in the pre-equilibrium model, cannot be justified for low-massnuclei,too.

3. Code ALICE and experimental spectra

We have used the code ALICE(ALICE/LIVERMORE 82)/2/, to calculate the

particle spectra emitted from the neutron induced reaction. Nobody hitherto have used this code for kerma calculation. For multiple particle emission, the ALICE code performs equilibrium (compound nucleus) decay calculations using the Weisskopf-Ewing evaporation model. Precompound decay is treated by the hybrid model. Emitted particle may be either neutron; n and p; n, p and α; n, p, α and d.

Spectra calculated by ALICE code for p, α and d from C at 27.7 MeV neutron energy, and form N at 39.7 MeV, have been compared with those measured by Romero et al./1/ And the spectra from O at 60.7 MeV compared with those of Dimbylow/9/. These results are shown in Figure 2 to 5. The calculated and experimental spectra are in agreement at 27.4 MeV.(Fig.2) However, deuteron spectra show disagreement all over the energy of emitted particles from N at 39.7 MeV, and from O at 60.7 MeV. At higher d-energies, ~15 MeV or more at 39.7 MeV and ~20 MeV or more at 60.7 MeV the calculated spectra are higher than experiment. At lower energy region, the calculated d spectra, as well as p, are lower than experiment. The trend can see in alpha spectra from O at 60.7 MeV.

In table 2, comparison between the calculated kerma values for light particles and the experimental values by Romero et al./1/ is presented. The calculated carbon kerma factors, included the recoil kerma factor cited by Romero et al./1/, are shown in table 3 together with those calculated by other authors. Using kerma factor calculated for C, N and O, kerma values for ICRU muscle tissue(with a composition of 10.1% H, 11.1% C, 2.6% N and 76.2% O by weight) have been derived at 27.4, 39.7 and 60.7 MeV neutron energy. Where the hydrogen kerma factors have used those of Bassel and Herling/11/. Figure 6 illustrates these results and compares with the values of other authors.

4. Conclusion

It is important to improve the reliability of the kerma calculation there are measurements of double differential cross sections for emitted charged particles from tissue and dosimeter elements bombarded by neutrons. Some discrepancies between the calculated kerma by the ALICE and the experimental values suggest to be need for a search for suitable parameter in application of the ALICE code.

References

1. Romero,J.L.,Brady,F.P. and Subramanian,T.S.: Proc. Int. Conf., Santa Fe, 1985, p.687.
2. Blann,M.and Bisplinghoff,J.: Lawrence Livermore National Laboratory Report UCLD-19614 (1982) unpublished.
3. Alsmiller,R.G. and J.Barish,J.: Health Phys. 33, 98 (1977).
4. Wells,A.H.: Rad. Res. 80, 1 (1979).
5. Behrooz,M.A.,Gillespie,E.J. and Watt,D.E.: Phys. Med. Biol. 26, 507 1981).
6. Behrooz,M.A. and Watt,D.E.: Radiat. Prot. Dosim. 1, 291 (1982).
7. R.S.Caswell et al.: Radiat. Res. 83, 217 (1980).
8. Dimbylow,P.J.: Phys. Med. Biol. 25, 637 (1980).
9. Dimbylow,P.J.: ibid. 27, 989 (1982).
10. Brenner,D.J.: ibid. 29, 437 (1983).
11. Bassel,R.H. and Herling, G.H.: Radiat. Res. 69, 210 (1977).

Table 1 A summary of kerma factor calculations.

Author	neutron energy	model or method
Alsmiller(1977)	<70 MeV	Intranuclear cascade model
Wells(1979)	<80	Intranuclear cascade + evaporation model
Caswell(1980)	20-30	Optical model
Dimbylow(1980)	<50	Continuous evaporation model
Behrooz(1981,82)	<60	---
Dimbylow(1982)	<50	NOPTIC(optical model) + GNASH + DWUCK
Brenner(1983)	<80	Intranuclear cascade model + optical model
Present work(1988)	<60	ALICE

Table 2 Comparison between the experimental values* and calculated kerma values by ALICE for emitted light particles. (in 10^{-15} Gy m^2)

	En = 27.4 MeV		39.7 MeV		60.7 MeV	
element	exp.	cal.	exp.	cal.	exp.	cal.
C	3.2(1)	2.73	3.6(1)	3.95	5.3(2)	5.77
N	2.3(2)	2.91	3.7(1)	4.09	5.8(6)	6.29
O	2.0(1)	2.22	2.9(1)	3.28	4.8(5)	5.13

* from ref./1/.

Table 3 Carbon kerma factor (in 10^{-15} Gy m^2)

Author	Neutron energy (MeV) 27.4	39.7	60.7
Werlls/4/	3.86	4.12	4.75
Dimbylow/8/	4.64	5.48	
Behrooz/5/	3.08	3.65	6.8
Behrooz/6/	3.25	3.82	6.4
Dimbylow/9/	3.7	4.1	5.4
Brenner/10/	3.72	3.87	4.71
Romero et al./1/	3.9(1)*	4.4(1)*	6.2(2)*
Present work	3.46+	4.74+	6.45+

* 4.0(1) means 4.0 ± 0.1.

+ value included the elasic and non-elastic recoil kerma from ref./1/.

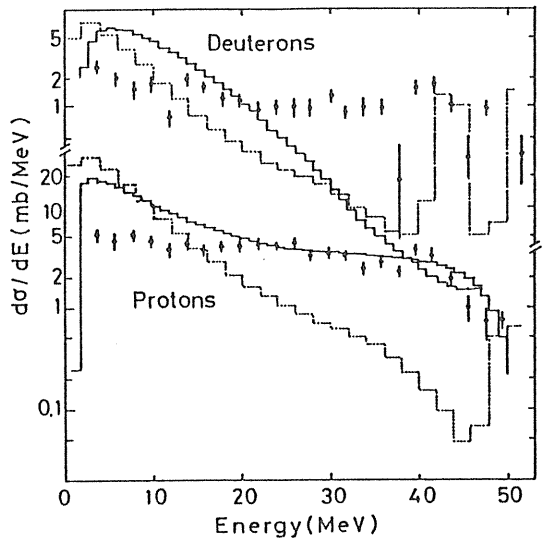

Fig. 5 A comparison between calculated and experimental proton and deuteron spectra produced by 60.7 MeV neutrons incident on O. ——, ALICE (present work); ..., GNASH + DWUCK (Dimbylow/9/); ●, experiment (from Dimbylow/9/)

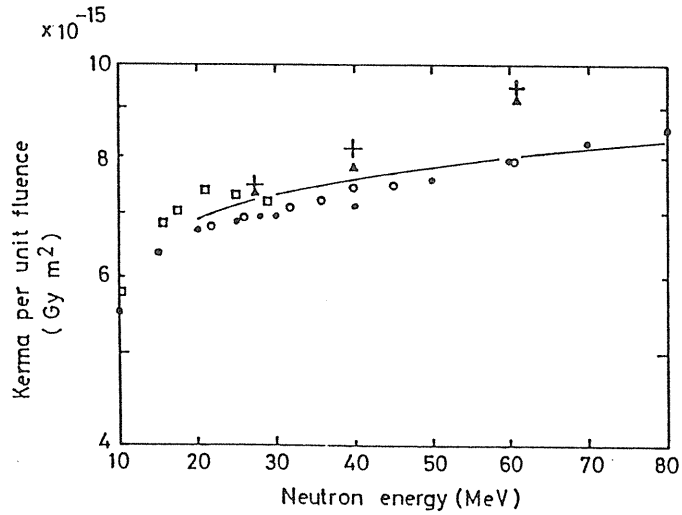

Fig. 6 Kerma per unit fluence for ICRU muscle tissue (see text, for its composition). +, Present work; △, ref./1/; ●, ref./9/; o, ref./4/; □, ref./7/ and ——, ref./10/.

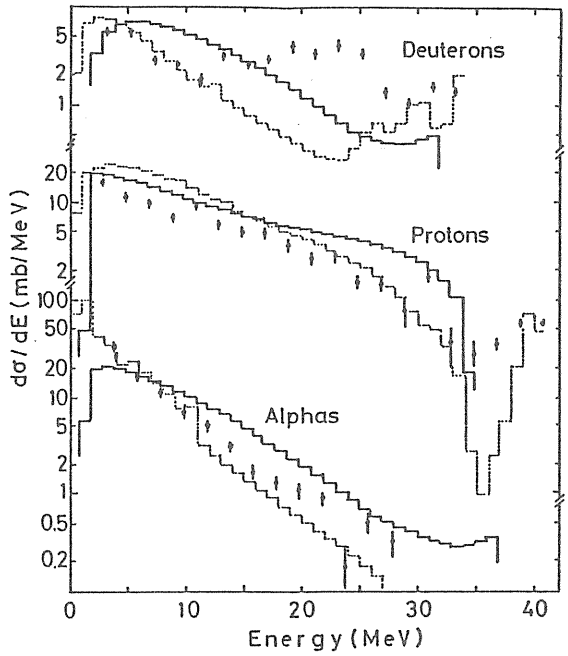

Fig. 3 A comparison between calculated and experimental charged particle spectra produced by 39.7 MeV neutrons incident on N. ——, ALICE (present work); ..., GNASH + DWUCK (Dimbylow/9/); ●, experiment (Romero et al./1/)

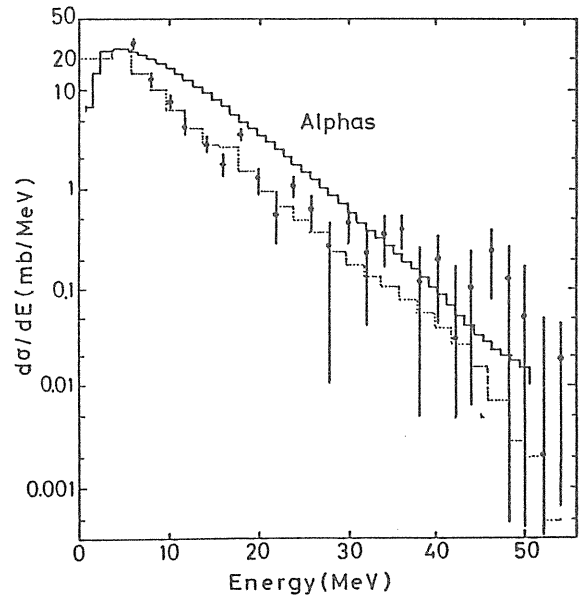

Fig. 4 A comparison between calculated and experimental alpha particle spectra produced by 60.7 MeV neutrons incident on O. ——, ALICE (present work); ..., GNASH + DWUCK (Dimbylow/9/); ●, experiment (from Dimbylow/9/)

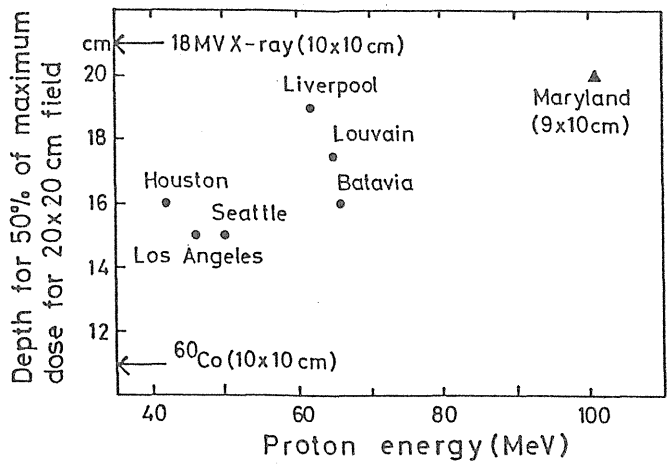

Fig. 1 Measured depth for 50 % maximum dose obtained by neutrons from thick beryllium target bombarding with protons.

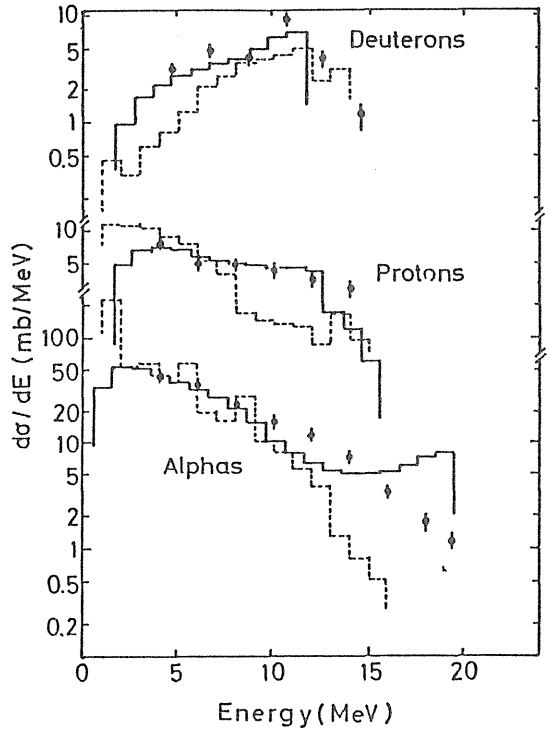

Fig. 2 A comparison between calculated and experimental charged particle spectra produced by 27.4 MeV neutrons incident on C. ——, ALICE (present work); ..., GNASH + DWUCK (Dimbylow/9/); ●, experiment (Romero et al./1/)

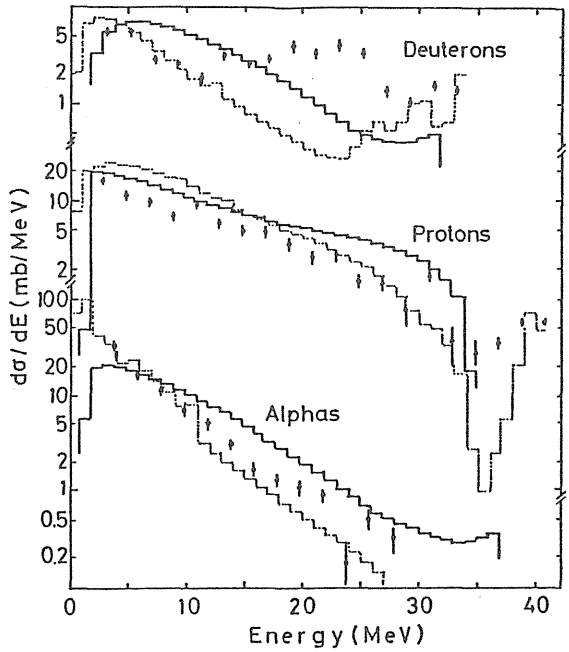

Fig. 3 A comparison between calculated and experimental charged particle spectra produced by 39.7 MeV neutrons incident on N. ——, ALICE (present work); ..., GNASH + DWUCK (Dimbylow/9/); ●, experiment (Romero et al./1/)

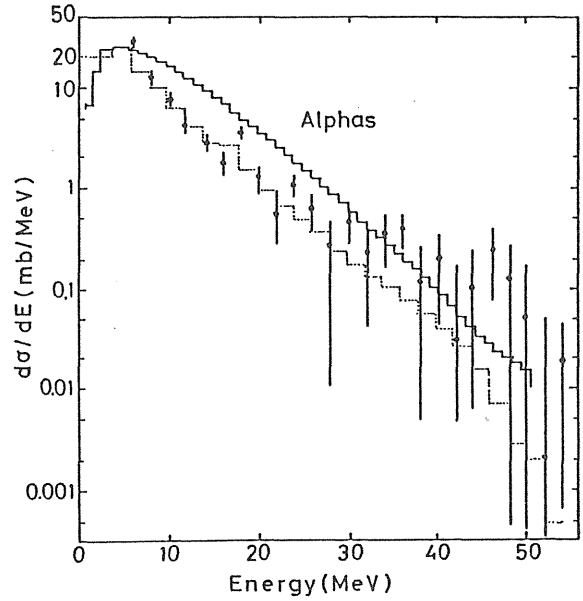

Fig. 4 A comparison between calculated and experimental alpha particle spectra produced by 60.7 MeV neutrons incident on O. ——, ALICE (present work); ..., GNASH + DWUCK (Dimbylow/9/); ●, experiment (from Dimbylow/9/)

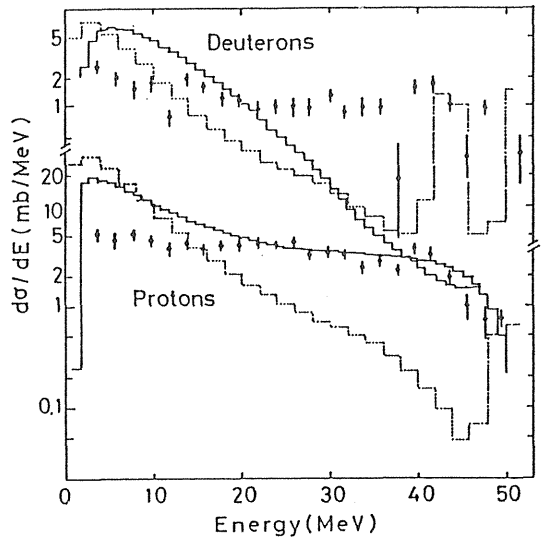

Fig. 5 A comparison between calculated and experimental proton and deuteron spectra produced by 60.7 MeV neutrons incident on O. ——, ALICE (present work); ..., GNASH + DWUCK (Dimbylow/9/); ●, experiment (from Dimbylow/9/)

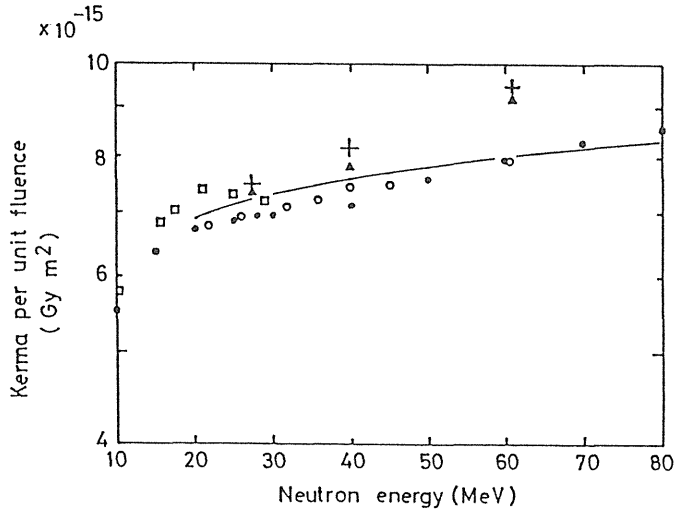

Fig. 6 Kerma per unit fluence for ICRU muscle tissue (see text, for its composition). +, Present work; △, ref./1/; ●, ref./9/; o, ref./4/; □, ref./7/ and ——, ref./10/.

Radiat. Phys. Chem. Vol. 34, No. 5, pp. 801–807, 1989
Int. J. Radiat. Appl. Instrum., Part C
Printed in Great Britain.

0146-5724/89 $3.00 + 0.00

A SPUR DIFFUSION MODEL APPLIED TO ESTIMATE YIELDS OF SPECIES IN WATER IRRADIATED BY MONOENERGETIC PHOTONS OF 50 eV–2 MeV

HIROSHI YAMAGUCHI
Division of Physics, National Institute of Radiological Sciences, 9-1, Anagawa 4-chome, Chiba 260, Japan

(*Received* 8 *August* 1988; *in revised form* 9 *December* 1988)

Abstract—A prescribed diffusion model has been developed to give G-values of water species produced by electrons taking into account the track structure of electrons. The model can explain experimental results of the Fricke dosimeter for various β emitter radionuclides. The present paper applies the model to the estimations of G-values of water species produced by monoenergetic photons. With the primary electron energy spectrum along a photon trajectory, which is here calculated by a Monte Carlo method, we can estimate G-values of the species on the basis of the G-values for electrons. The results for photons predict slightly different G-values for the Fricke dosimeter from those recommended by ICRU. Parameter sensitivity is discussed around the set of optimum values for the parameters of the model. In a discussion on the expression of the electron track structure a conclusion is reached that when we use electron energy degradation spectra in the way of the present model, the spur size distribution is of little importance.

1. INTRODUCTION

Yields of species (ions and free radicals) produced in water from ionizing radiation, as a function of time after an irradiation, is essential for the study of reaction mechanisms of radiation actions on living systems. These rely on theoretical estimations, since there are some difficulties in experimental methods to measure the yields of the species at a very early stage, for instance, from the time of 10^{-12} sec to 10^{-4} sec. In a previous work (Yamaguchi, 1987) we have developed a prescribed diffusion model to solve equations for diffusion-controlled reactions among the species produced in water by electrons taking into acount the electron track structure. Based on the Schwarz's model (1969) we define the interspur distance for every differential path segment of electron paths including the primary electron track and those of successive δ-rays. The concept of the interspur distance may improve the Schwarz's model, by allowing us to solve the reaction kinetics at a more microscopic level. The solutions of the equations for the electron path segments, grouped by their energies, give the differential G-values of the species. The integral G-values of the species are calculated through summation of the differential G-values weighted by the electron energy degradation spectrum for the primary electron. The spectrum contains information of the electron track structure. It has been shown that the calculated G-values for the Fricke dosimeter with this model agree well with the experimental values for a wide range of energies of electrons such as ^{3}H β-rays ($E_{av} = 5.7$ keV) and ^{90}Y β-rays ($E_{av} = 0.9314$ MeV) (Yamaguchi, 1987).

This paper applies the model further to estimate the yields of species in water irradiated by monoenergetic photons. The primary energy spectrum of electrons set in motion by a photon must be known to calculate the yields of the species by the photon. That is, the yields are calculated by weighting the integral G-values for the electrons with the primary electron energy spectrum. The previous calculations giving the integral G-values of electrons are revised in two points. Firstly we consider the time dependence of the reaction rate constants in the process of diffusion (Schwarz, 1969). Secondly we obtain the initial numbers of the species, e^-_{aq} and OH, from the experimental results by picosecond pulse radiolysis (Jonah and Miller, 1974; Jonah *et al.*, 1976).

The present calculation provides an estimation of the G-values of the Fricke dosimeter irradiated by the photons of energies from 50 eV to 2 MeV. In order to study the uncertainty of the results, we discuss the sensitivity of the parameters of the model around their optimum values. And we discuss the effect of the spur size distribution on the present model.

2. A PRESCRIBED DIFFUSION MODEL

It is assumed that at a time about 10^{-11} sec after the passage of the electron the radiolysis of water is described by:

$$H_2O \rightsquigarrow e^-_{aq}, H, H_3O^+, OH, H_2. \quad (1)$$

The subsequent reactions of these species are listed in Table 1 (Schwarz, 1969). These reactions mainly take place in a spur along electron traces. The species however may react with those in neighbouring spurs, when they are close enough to react according to the track structure at the beginning or in the course of the diffusion process.

Table 1. Reactions and rate constants

Reactions	$k \times 10^{-10}$ ($M^{-1} s^{-1}$)
(1) $e_{aq}^- + e_{aq}^- + 2H_2O \rightarrow H_2 + 2OH^-$	0.55
(2) $e_{aq}^- + H + H_2O \rightarrow H_2 + OH^-$	2.5
(3) $e_{aq}^- + H^+ \rightarrow H$	1.7
(4) $e_{aq}^- + OH \rightarrow OH^-$	2.5
(5) $e_{aq}^- + H_2O_2 \rightarrow OH^- + OH$	1.3
(6) $H + H \rightarrow H_2$	1.0
(7) $H + OH \rightarrow H_2O$	2
(8) $H + H_2O_2 \rightarrow H_2O + OH$	0.01
(9) $H^+ + OH^- \rightarrow H_2O$	10
(10) $OH + OH \rightarrow H_2O_2$	0.6

The initial electron track structure is described by the energy degradation spectrum $y(Q, E)$, the path length of the electron of degraded energy Q from the primary electron energy of E. In this paper the term "path" is used to denote an electron trace of the primary electron and of any δ rays, and the term "track" denotes only that of the primary electron.

The diffusion controlled reaction kinetics is described by a set of simultaneous differential equations in Table 2. Equations (T1) and (T4)–(T8) were given by Schwarz (1969) and Burn and Curtis (1972). The present model brings about equations (T9)–(T12), which are the results from the assumption that the Gaussian distribution holds for species other than e_{aq}^- in equation (T2) and a nonGaussian distribution for species e_{aq}^- in equation (T3). And we newly interpret the quantity Z_1 in equations (T9)–(T12) as interspur distance for an electron path segment, not the average interspur distance over all electron paths.

Table 2. Equations for a prescribed diffusion model

Equations for concentration C_i of species i

$$dC_i/dt = D_i \nabla^2 C_i - \sum_j k_{ij} C_i C_j + \sum_{j,k \neq i} k_{jk} C_j C_k - k_s C_i C_s, \quad \text{(T1)}$$

D_i = the diffusion constant of species i;

k_{ij} = the reaction rate constant between species i and species j;

$k_s C_i C_s$ = the rate of the reaction between species i and solute of C_s.

Distributions of species in a spur

$$C_i(r, z) = N_i \{1/(\pi b_i^2)^{3/2}\} \exp[-\{r^2 + (z - z_i)^2\}/b_i^2], \quad \text{for } i \neq e_{aq}^-, \quad \text{(T2)}$$

$$C_i(r, z) = N_i\{2/(\pi^2 b_i^3)\}(r/b_i) \exp[-\{r^2 + (z - z_i)^2\}/b_i^2], \quad \text{for } i = e_{aq}^-, \quad \text{(T3)}$$

b_i = the width parameter;

z_i = the position of the spur along the path;

N_i = the number of species in the spur.

Equations for N_i and b_i

$$dN_i/dt = -\sum_j k_{ij} N_i N_j f_{ij} + \sum_{j,k \neq i} k_{jk} N_j N_k f_{jk} - k_s C_s N_i, \quad \text{(T4)}$$

$$db_i^2/dt = 4D_i - \sum_j \beta_i(i, j) + \sum_{j,k \neq i} \beta_i(j, k) + \beta_i(j, s), \quad \text{(T5)}$$

$$\beta_i(i, j) = -b_i^2 k_{ij} N_i f_{ij} b_i^2/(b_i^2 + b_j^2), \quad \text{(T6)}$$

$$\beta_i(j, k) = b_i^2 k_{jk} (N_j N_k / N_i) f_{ij} [b_j^2 b_k^2/\{b_i^2 (b_j^2 + b_k^2)\} - 1], \quad \text{(T7)}$$

$$\beta_i(j, s) = -(b_i^2/N_i) k_{sj} N_j (1 - b_j^2/b_i^2), \quad \text{(T8)}$$

$$f_{ii} = g_{ii}/\pi, \quad \text{for } i = e_{aq}^-, \quad \text{(T9)}$$

$$f_{ij} = g_{ij}\{b_j^2/(b_i^2 + b_j^2)\}^{(1/2)}/4, \quad \text{for } i = e_{aq}^-, \ j = \text{the other}, \quad \text{(T10)}$$

$$g_{ij} = [1 + \{2\pi (b_i^2 + b_j^2)\}^{(1/2)}/Z_1]/\{\pi (b_i^2 + b_j^2)\}^{(3/2)}, \quad \text{(T11)}$$

$$f_{jk} = [1 + \{\pi (b_j^2 + b_k^2)\}^{(1/2)}/Z_1]/\{\pi (b_j^2 + b_k^2)\}^{(3/2)}, \quad \text{for } i, k \neq e_{aq}^-, \quad \text{(T12)}$$

where

Z_1 = the interspur distance for a electron path, and

$$k_{ij} = k_{diff}[1 + (k_{diff}/\{(4\pi)^{3/2}(D_i + D_j)^{3/2} t^{1/2}\})] \quad \text{(T13)}$$

where

k_{diff} = the long-time diffusion-controlled rate constant.

The interspur distance is defined:

$$Z_1 = Es/L_{1,c}; \quad (2)$$

where Es is the energy required to produce a spur, which is assumed to be constant for all electron paths, and $L_{1,c}$ is the restricted energy loss as defined by:

$$L_{1,c} = \int_0^c N_1(Q, u)(u + B)\, du + B_e \sigma_e(Q); \quad (3)$$

where $N_1(Q, u)du$ is the number of the first generation electrons with energy between u and $u + du$ generated per micrometer of electron path of energy Q, B is the ionization potential of the outermost orbital ($B = 12.6$ eV, Pagnamenta and Marshall, 1986), c is the cutoff energy, B_e is the mean excitation energy transfer, and $\sigma_e(Q)$ is the number of excitations of water molecules per micrometer of electron path of energy Q (Paretzke and Berger, 1978). We assume $B_e = 13$ eV, since the value of B_e is about 13 eV in the energy range of 10^2–10^5 eV (Paretzke and Berger, 1978).

The quantities Es and c are adjustable parameters which should be determined such that the calculations of Fricke G-values are in good agreement with the experiments.

3. G-VALUES BY MONOENERGETIC PHOTONS

The differential G-value $G_i'(Q)$ for species i, i-th radical and molecular products per 100 eV by the electron path segment of an electron of energy Q, is calculated from the solutions N_i of equation (T4) at a particular time:

$$G_i'(Q) = N_i/Es \times 100. \quad (4)$$

The integral G-value $G_i(E)$ for species i, the average yield of the i-th species per 100 eV over all electron paths from electrons of initial energy E is:

$$G_i(E) = \frac{\int_0^E G_i'(Q) y(E, Q) L(Q)\, dQ}{\int_0^E y(E, Q) L(Q)\, dQ}; \quad (5)$$

where $L(Q)$ is the LET, the linear energy transfer and $y(E, Q)$ is the energy degradation spectrum, which is calculated by the method of Pagnamenta and Marshall (1986).

For the photon which has a primary electron energy spectrum $P(E)$ the G-value G_i for species i is

given by:

$$G_i = \frac{\int_0^\infty P(E)G_i(E)\,dE}{\int_0^\infty P(E)\,dE}. \quad (6)$$

We calculate the G-value of the Fricke dosimeter under the aerobic condition by using the equation,

$$G(Fe^{3+}) = 3G(e_{aq}^-) + 3G(H) + G(OH) + 2G(H_2O_2). \quad (7)$$

4. RESULTS

Conditions of calculation

We assign numbers to each species as $e_{aq}^- = 1$, $H = 2$, $H^+ = 3$, $OH = 4$, $OH^- = 5$, $H_2O_2 = 6$ and $H_2 = 7$ to solve the equations in the Table 2. We ignore the term $k_sC_sN_i$ since we consider no solute in water. The reaction constants in Table 1 correspond to k_{diff} in equation (T13) and the diffusion constants are listed in Table 3, all of which are the same values as Schwarz's (1969). The values of the initial radii for species in Table 3 are the same values as Burn's (Burns *et al.*, 1984). The differential equations in the Table 2 are numerically solved from $t = 10^{-12}$ to 3×10^{-7} s (Yamaguchi, 1987). To determine the values of the variables Es and c we compared calculated G-values with experimental values of the Fricke dosimeter (Fregene, 1967) for four β rays and ^{60}Coγ rays.

Initial numbers of species

The experimental bases for the initial number of species in a spur is scarce. Jonah *et al.* (1976) measured the yields of the hydrated electron and OH radical using electron pulse radiolysis of electron energy of 20–22 MeV, and gave the yield of the hydrated electron as 4.6 ± 0.2 molecules/100 eV at the time of 100 ps and that of the OH radical as 5.9 ± 0.2 molecules/100 eV at 200 ps. The width of the sample cell containing water was 2 cm for picosecond pulse radiolysis. An electron energy of 20 MeV decreases to about 14.5 MeV on average after a passage through the water of 2 cm long, the range of which is 9.18 g/cm^2 in water (ICRU, 1970a). This energy change corresponds to three energy intervals from 12.7 to 21.7 MeV in our grouping of the electron energies (see later E_i for $i = 79$ and $i = 82$), in each of which we calculate the yield and define it as the differential G-value for the interval. Thus we may regard the above experimental G-values by picosecond pulse radiolysis as differential G-values for these three energy intervals, since we know that the yields are almost the same in these energy intervals. From extrapolation of these data down to the time of 10 ps we determined $N^0_{e_{aq}^-} = N^0_{H^+} = 4.78 \times Es/100$ and $N^0_{OH} = 6.86 \times Es/100$. We set $N^0_{OH} = N^0_{H_2O_2} = 0$ since these species are absent at the beginning. The values of N^0_H and $N^0_{H_2}$ are assumed to be the same as those of Schwarz, since the present values $G^0_{e_{aq}^-} = 4.78$ coincides with the Schwarz's value for the hydrated electron.

Table 3. Diffusion constants, initial radii and numbers of species

Species	$D \times 10^5$ (cm^2 s^{-1})	r^0 (A)	G^0 (100 eV^{-1})
1. e_{aq}^-	4.5	24.58	4.78
2. H	7	11.45	0.62
3. H^+	9	11.45	4.78
4. OH	2.8	11.45	6.86
5. OH^-	5	11.45	0
6. H_2O_2	2.2	11.45	0
7. H_2	8	11.45	0.15

Table 4. Calculated $G(Fe^{3+})$ values in comparison with the experimental

Radiation	Calculation	Experiment
β rays		
1. ^{3}H	12.91	12.9 ± 0.2
2. ^{35}S	14.76	14.3 ± 0.4
3. ^{90}Y	15.67	15.4 ± 0.4
4. ^{32}P	15.62	15.3 ± 0.5
γ rays		
^{60}Co	15.51	15.5 ± 0.3

Determination of values of Es and c

At first we set values of Es and c to obtain the differential G-value of the species in equation (4), and to calculate the integral G-value of the species using the energy degradation spectrum $y(E, Q)$ in equation (5). Then we calculate the G-value of the species for five radiations using their primary electron energy spectra and compare with experimental values. After repeating this process, we found the best values as $Es = 50$ eV and $c = 58.4$ eV. Table 4 shows the calculated G-values of Fricke dosimeters for the radiations. The differential G-value of the hydrated electron at the time of 100 ps was 4.63 ($G_{exp.} = 4.6$) and that of OH at the time of 200 ps was 5.85 ($G_{exp.} = 5.9$) from the present calculation. The calculated differential yields of these species are compared with the experiments as a function of time as shown in Fig. 1.

Primary electron energy spectrum of a monoenergetic photon

Monte Carlo calculations were made to create a photon trajectory in water and to obtain primary electron energy spectra. We used the photon cross sections for water from photon energy of 0.1 keV to 20 MeV by Hubbel (1977). We set the terminal energy of a photon trajectory at 50 eV. The photon cross sections from 100 to 50 eV are estimated by an extrapolation from those of 100 and 150 eV. For the Compton scattering processes we used the simulation program developed by Snyder *et al.* (1973). We assumed that when a photoelectric interaction between a photon and a water molecule takes place, 95% of them are on the electrons of K-orbits of oxygen and the other are on those of L-orbits of the

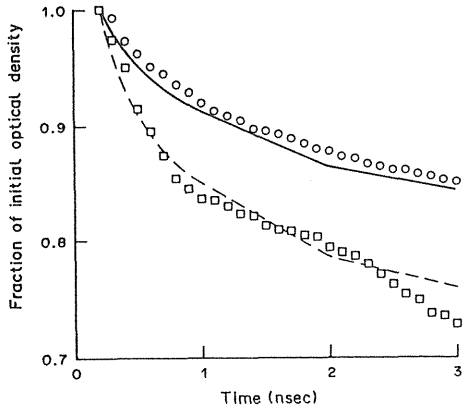

Fig. 1. Comparison of the calculations with experiments for the decay of e^-_{aq} (○) and OH (□) as measured using picosecond pulse radiolysis (Jonah *et al.*, 1976). The solid and dashed curves show the results from the present model for e^-_{aq} and OH respectively.

same atom (Hubbell, 1969) and that a $h\nu - 532$ eV K-photoelectron, a 518 eV Auger electron and a $h\nu - 23.7$ eV L-photoelectron are emitted respectively. We considered the irradiation under conditions of the charged particle equilibrium, thus all the kinetic energy of electrons at every interaction is registered in a array according to its energy. The arrays are divided by energy intervals of $\Delta E_i = E_{i+1} - E_i$ ($E_i = 14.6\zeta^i, \zeta = 2^{(1/4)}$, $i = 1, \ldots, 78$, from 14.6 eV to 10.83 MeV), which are the same energy intervals as the electron energy degradation spectrum $y(E, Q)$. The primary electron spectrum $P(E)$ for a monoenergetic photon was estimated after 40,000 samplings of photon interactions (Fig. 2). The G-values of species by the photons are calculated by equation (6) and given in Table 5. The G-values of Fricke dosimeter calculated by equation (7) are shown in Fig. 3 with the experimental values cited in ICRU report (1970b).

5. DISCUSSION

Parametric sensitivity analysis

The calculated G-values for Fricke dosimeter shown in Table 4 agree well with the experimental values. This agreement is due to the proper choice for the variables Es and c. Table 6 gives the summary of

Table 5. G-values of species in water produced by photons

E(keV)	$G(e^-_{aq})$	G(H)	$G(H^+)$	G(OH)	$G(OH^-)$	$G(H_2O_2)$	$G(H_2)$	$G(Fe^{3+})$
0.05	2.356	0.605	3.10	2.652	0.747	1.181	0.425	14.16
0.06	2.212	0.597	2.94	2.500	0.726	1.201	0.446	13.57
0.08	1.983	0.578	2.67	2.264	0.686	1.230	0.479	12.70
0.10	1.775	0.555	2.42	2.055	0.643	1.251	0.512	11.77
0.15	1.533	0.526	2.12	1.816	0.590	1.272	0.549	10.68
0.2	1.451	0.518	2.03	1.732	0.574	1.282	0.562	10.28
0.3	1.426	0.519	2.00	1.704	0.571	1.287	0.565	10.13
0.4	1.447	0.525	2.03	1.721	0.579	1.288	0.561	10.19
0.5	1.501	0.534	2.09	1.771	0.594	1.285	0.552	10.39
0.6	1.486	0.533	2.08	1.755	0.592	1.288	0.544	10.35
0.8	1.419	0.524	2.00	1.691	0.576	1.293	0.565	10.06
1.0	1.460	0.531	2.05	1.729	0.586	1.290	0.558	10.21
1.5	1.620	0.548	2.24	1.889	0.620	1.274	0.533	10.83
2.0	1.740	0.558	2.38	2.012	0.641	1.260	0.515	11.30
3.0	1.934	0.570	2.60	2.217	0.669	1.233	0.488	12.07
4.0	2.051	0.575	2.73	2.344	0.680	1.214	0.471	12.54
5.0	2.163	0.579	2.85	2.468	0.688	1.194	0.456	12.98
6.0	2.218	0.580	2.91	2.529	0.691	1.185	0.449	13.19
8.0	2.271	0.581	2.97	2.589	0.693	1.175	0.442	13.39
10.0	2.367	0.583	3.06	2.698	0.696	1.157	0.429	13.77
15.0	2.447	0.584	3.14	2.790	0.695	1.141	0.419	14.08
20.0	2.510	0.584	3.20	2.863	0.693	1.128	0.411	14.33
30.0	2.540	0.583	3.23	2.899	0.690	1.121	0.407	14.45
40.0	2.541	0.583	3.23	2.900	0.689	1.121	0.407	14.45
50.0	2.528	0.583	3.22	2.885	0.689	1.123	0.409	14.40
60.0	2.518	0.583	3.21	2.873	0.690	1.126	0.410	14.36
80.0	2.513	0.584	3.20	2.867	0.691	1.127	0.411	14.34
100.0	2.550	0.584	3.24	2.909	0.691	1.120	0.406	14.49
150.0	2.584	0.584	3.27	2.949	0.690	1.113	0.401	14.62
200.0	2.601	0.584	3.29	2.968	0.690	1.109	0.399	14.69
300.0	2.646	0.584	3.33	3.022	0.687	1.100	0.394	14.86
400.0	2.681	0.584	3.37	3.062	0.686	1.092	0.389	15.00
500.0	2.707	0.584	3.39	3.093	0.685	1.087	0.386	15.10
600.0	2.728	0.585	3.41	3.117	0.684	1.083	0.383	15.18
800.0	2.763	0.585	3.45	3.157	0.683	1.076	0.379	15.31
1000.0	2.790	0.585	3.47	3.188	0.683	1.070	0.375	15.42
1500.0	2.834	0.586	3.52	3.239	0.682	1.062	0.369	15.59
2000.0	2.862	0.587	3.54	3.271	0.683	1.056	0.366	15.70

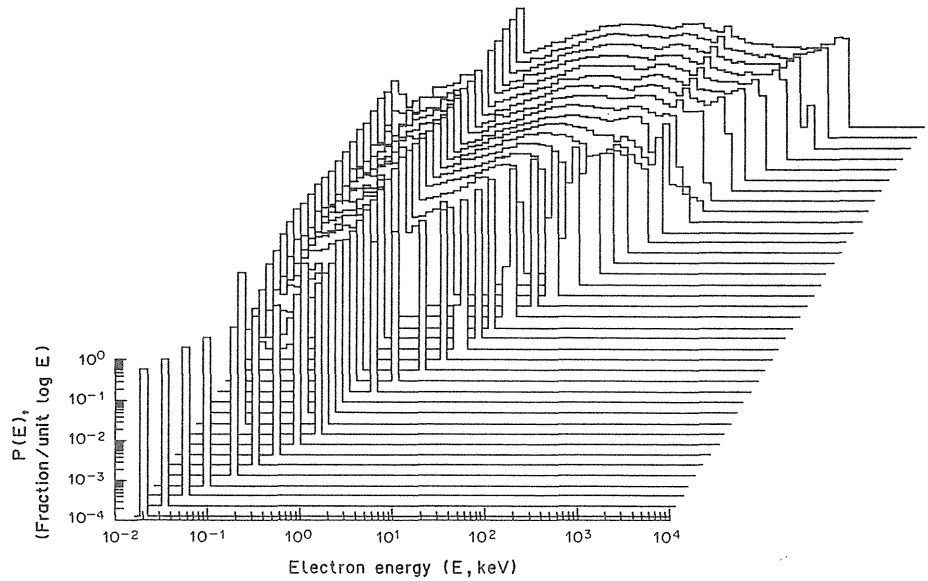

Fig. 2. The primary electron energy spectrum of monoenergetic photons. $P(E)$ is the fraction of electrons which are accumulated in the energy interval $\Delta E_i = E_{i+1} - E_i$ where $E_i = 14.6\,\zeta^i$eV ($i = 1, 2, \ldots, 78$) and $\zeta = 2^{(1/4)}$, after 40,000 interactions between water molecules and photons (Monte Carlo calculations). The horizontal lines represent all of the photon energies listed in Table 5.

the parametric sensitivity analysis around these optimum values $Es = 50$ eV and $c = 58.4$ eV with the G-values of Fricke dosimeter for ^{3}H β rays and ^{60}Co γ rays. The term $(Es\ \&\ N_i^0) \times 0.9$ in the Table 6 means the condition of a calculation that the value of $Es = 45$ eV ($= 50 \times 0.9$) and all values of N_i^0 in Table 3 are multiplied by 0.9 without changing the value of the other parameters. The value of Es is not independent of the values of N_i^0 provided that the energy to produce one ion pair is constant. The term $(Es\ \&\ N_i^0) \times 1.1$ means the calculation when Es and N_i^0 are increased by 10% of the optimum values. For the analysis on c the values of c were chosen according to the energy points which define the energy intervals for the electron energy degradation spectrum, again without changing the other parameters.

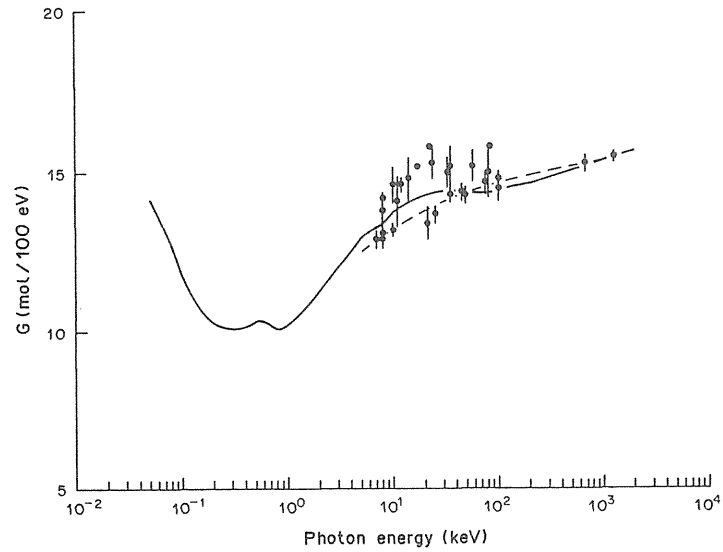

Fig. 3. The integral G-value $G(E)$ (solid line) of the Fricke dosimeter as a function of initial photon energy calculated by the present model. The dashed line shows the recommended values by ICRU report (1970b). The closed points show all experimental results which are cited in the same ICRU report.

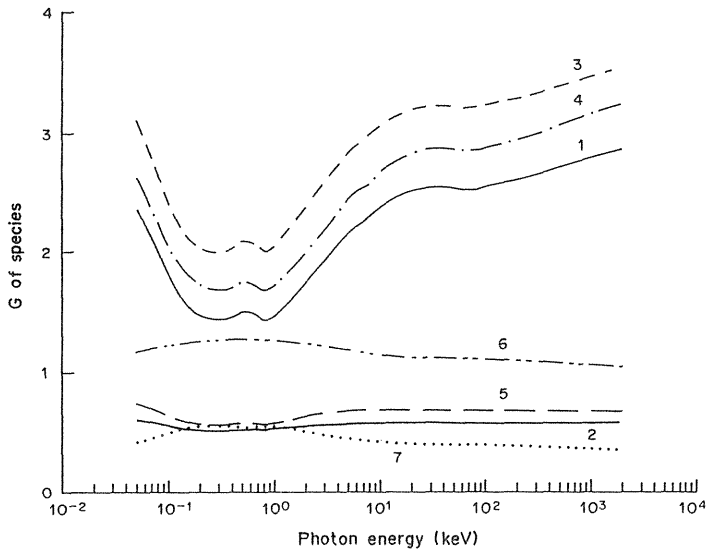

Fig. 4. The integral G-values of various species in water irradiated by photons, which are given in Table 5. Numbers indicate that $1 = e_{aq}^-$, $2 = H$, $3 = H^+$, $4 = OH$, $5 = OH^-$, $6 = H_2O_2$ and $7 = H_2$.

These results imply that a range of 45–55 eV as the value of Es in accordance with the change of N_i^0 values results in the agreement in the G-values of Fricke dosimeter within their experimental errors. For the value of c the range of 49.1–69.4 eV is possible with the same criterion as Es. In previous work (Yamaguchi, 1987) we obtained $c = 50$ eV, in which the time dependence of the reaction constants was ignored. The inclusion of the time dependence may change the value of c from 50 eV to the present 58.4 eV. Table 6 gives further the sensitivity analysis on the other parameters of k_i, D_i, and r_i^0. It is seen that the present values, in particular, of k_i and D_i, are critical to the present results. These values should be ascertained with less than 10% uncertainty.

Table 6. Sensitivity of the parameters around the optimum G-values of the Fricke dosimeter

	^{3}H β-rays (%)[a]	^{60}C γ-rays (%)[a]
Experiments	12.9 ± 0.2 (1.55)[b]	15.5 ± 0.3 (1.94)[b]
Optimum values	12.907	15.514
(Es & N_i^0) × 0.9	13.056 (1.15)	15.795 (1.81)
(Es & N_i^0) × 1.1	12.709 (−1.54)	15.225 (−1.87)
c × 0.71 (=41.3 eV)	13.288 (2.95)	15.644 (0.93)
c × 0.84 (=49.1 eV)	12.879 (−0.17)	15.506 (0.04)
c × 1.19 (=69.4 eV)	12.750 (−1.17)	15.463 (−0.24)
c × 1.41 (=82.6 eV)	12.612 (−2.24)	15.419 (−0.52)
k_i × 0.9	13.380 (3.67)	15.948 (2.80)
k_i × 1.1	12.422 (−3.75)	15.088 (−2.75)
D_i × 0.9	12.483 (−3.29)	15.112 (−2.59)
D_i × 1.1	13.290 (2.97)	15.859 (2.22)
r_i^0 × 0.9	12.628 (−2.16)	15.162 (−2.27)
r_i^0 × 1.1	13.157 (1.94)	15.813 (1.93)

[a]{(Calculation − Optimum)/Optimum} × 100.
[b]The experimental errors.

G-values of the species by photons

Agreement of the differential G-values of OH radicals between calculations and experiments becomes poorer after the time of 2.5 ns (Fig. 1). We may ascribe this disagreement to a large experimental uncertainty in the OH radical decay and kinetics (Trumbore *et al.*, 1978). Under the circumstances the reasonable result in the calculations for the G-value of Fricke dosimeter (Fig. 3) may have been obtained by a favorable compensation among the G-values of species which do not have enough experimental validation. Thus, the G-values of species in Table 5 (Fig. 4) should be experimentally checked.

In spite of this limitation, we believe that the present prediction (Table 5) for the G-value of the Fricke dosimeter for monoenergetic photons may well be practically useful. Two sets of experimental data for the Fricke dosimeter at high energies shown in the Fig. 3 are those for ^{137}Cs and ^{60}Co γ rays. The calculated curve seems to reproduce the trend of all the experimental values which are tabulated in Table 2.1 in ICRU report (1970b). The calculated values are larger by 3.2% for 5 keV and smaller by 2% for 100 keV than the values recommended by the ICRU.

Spur size distribution

A spur size distribution for the 1 MeV electron is calculated by Mozumder *et al.* (1966a, b) and has been used in the calculations of the prescribed diffusion model which assumes the average spur distance over all electron paths (Mozumder *et al.*, 1966a, b; Schwartz, 1969). We study the effect of this distribution in the present model. We consider spurs in which less than 6 ion pairs exist according to the definition of spur (Mozumder *et al.*, 1966a, b), and assume that

Table 7. Calculations including the spur size distribution

No. ion pairs	Fraction		Normalized fraction	
2	0.4784		0.5202	
4	0.3455		0.3757	
6	0.0957		0.1060	
Average no. OH $\langle N_i \rangle$	Pair	Fraction P_i	$\langle Es \rangle$ (eV)[a]	c (eV)
2	22	0.1699	29.15	34.7
3	24, 42	0.3681	43.73	49.1
4	26, 44, 62	0.3159	58.32	58.4
5	46, 64	0.1250	72.89	82.6
6	66	0.0212	87.46	98.2
G-values of Fricke dosimeter		^{3}H β-rays	^{60}Co γ-rays	
Experiments		12.9 ± 0.2	15.5 ± 0.3	
Calculations		13.14	15.52	

[a] $\langle Es \rangle = \langle N_i \rangle \times (100/6.86)$.

this distribution (upper rows in Table 7) is for that of the OH radical and holds for the other electron energies. Possible pairs among different sizes in neighbours are listed in middle rows of Table 7. For simplicity we solved equations for an average size $\langle N_i \rangle$ for these pairs, otherwise more complicated equations are needed for pairs of different sizes. The fractions for the average sizes were calculated by the normalized fractions of the original spur sizes. The value of $\langle Es \rangle$ is estimated by $\langle Es \rangle = \langle N_i \rangle \times 100/6.86$ for each average spur size, since the distribution of the size has been regarded as the number of OH radicals and the initial G-value of OH is assumed to be 6.86. The cutoff energy c was determined in the energy grouping, such that the value of c was the first energy point lager than each $\langle Es \rangle$. The initial numbers G_i^s and radii r_i^s of the species for each average spur size were estimated by (Schwarz, 1969) $G_i^s = G_i^0 \times \{\langle N_i \rangle / (6.86 \times 50/100)\} \times \langle Es \rangle / 100$ and $r_i^s = r_i^0 \times \{\langle N_i \rangle / (6.86 \times 50/100)\}^{1/3}$, where G_i^0 and r_i^0 are the values in Table 3. For each spur of average size we duplicated the calculations to get the differential G-values, the integral G-values and a composit integral G-values for the species by using the fractions P_i, then we obtained the G-values of Fricke dosimeter for ^{3}H β rays and ^{60}Co γ rays. Table 7 shows that the similar results as in Table 4 are obtained. This may imply that the use of the electron energy degradation spectrum fades out the effect of the spur size distribution and that the single size spur model with the electron energy degradation spectrum and the concept of the interspur distance of the electron path may satisfactorily explain the track structure of electrons in water.

Acknowledgements—The author wishes to thank for provision of the photon cross sections Dr K. Kitao, for the G-values of the Fricke dosimeter Dr K. Hoshino from NIRS, and for useful comments on this paper Dr A. J. Waker from the University of Leeds.

REFERENCES

Burns W. G. and Curtis A. R. (1972) *J. Phys. Chem.* **76**, 3008.
Burns W. G., Sims H. E. and Goodall J. A. B. (1984) *Radiat. Phys. Chem.* **23**, 143.
Fregene A. O. (1967) *Radiat. Res.* **31**, 256.
Hubbell J. H. (1969) *NSRDS-NBS 29*, 27.
Hubbell J. H. (1977) *Radiat. Res.* **70**, 58.
ICRU (1970a) Report No. 16. Linear energy transfer.
ICRU (1970b) Report No. 17. Radiation dosimetry: X rays generated at a potential of 5–150 kV.
Jonah C. D. and Miller J. R. (1974) *J. Phys. Chem.* **81**, 1974.
Jonah C. D., Matheson M. S., Miller J. R. and Hart E. J. (1976) *J. Phys. Chem.* **80**, 1267.
Mozumder A. and Magee J. L. (1966a) *Radiat. Res.* **28**, 203, 215.
Mozumder A. and Magee J. L. (1966b) *J. Chem. Phys.* **45**, 3332.
Pagnamenta A. and Marshall J. H. (1986) *Radiat. Res.* **106**, 1.
Paretzke H. G. and Berger M. J. (1978) *Proc. VIth Symp. Microdosim*, p. 749.
Schwarz H. A. (1969) *J. Phys. Chem.* **73**, 1928.
Snyder W. S., Ford M. R. and Warner G. G. (1973) *ORNL-4979*, 1.
Trumbore C. N., Short D. R., Fanning J. E. and Olsen J. H. (1978) *J. Phys. Chem.* **82**, 2762.
Yamaguchi H. (1987) *Radiat. Phys. Chem.* **30**, 279.

[Reprinted from *Scientific Papers of the Institute of Physical and Chemical Research*, 83, 17～18 (1989)]

Cellular Basis of Heavy Ion Particle Therapy: Cell Inactivation and LET

By

Hiroshi OHARA, Tatsuaki KANAI, Hiromi ITSUKAICHI, and Kumiko FUKUTSU

RIKAGAKU KENKYUSHO
(The Institute of Physical and Chemical Research)

Wako-shi, Saitama
351-01, JAPAN

(Received January 10, 1989)

Cellular Basis of Heavy Ion Particle Therapy: Cell Inactivation and LET

Hiroshi OHARA,* Tatsuaki KANAI,** Hiromi ITSUKAICHI,* and Kumiko FUKUTSU*

* *Section of High LET Radiation and Biomedical Studies, Division of Radiation Hazard*

** *Division of Accelerator Research, National Institute of Radiological Science, Anagawa, Chiba 260*

Ion beams of helium-4 of 18.5 MeV/amu and carbon helium-3 of 12 MeV/amu obtained from NIRS (National Institute of Radiological Sciences) cyclotron were degraded through aluminum absorbers of various thicknesses to obtain different quantities of LET (linear energy transfer). Dose-average LET was varied from 14.5 to 75 keV/μm for helium-4 and helium-3 beams and from 220 to 430 keV/μm for carbon beams. Chinese hamster V-79 cells attached to dishes were exposed to those monoenergetic single and mixed beams for a comparison with response survivals of cells for a given LET value. The present study aimed to elucidate a correlation between the cell killing effect and dose average LET as well as a difference between single and mixed irradiations. This study is useful for designing ridge filters and degraders for heavy ion therapy.

I. INTRODUCTION

The differences in biological effects due to radiation quality have been studied for many years. A general agreement is that the biological effects increase with an increase in LET up to 150 keV/μm and that the shape of the cell survival curve for mammalian cells is modified to show a remarkable reduction in the shoulder as LET increases.[1,4] LET is one of the most important quantities to describe the quality of radiation.

We are very much concerned with the biological effect of the mixed irradiation scheme if it is the same of the effect of single radiation for the same value of dose average LET. By superposing monoenergetic beams we have defined a dose-average LET desired for single and mixed irradiations. The results are discussed in terms of the microdosimetric concept.

II. MATERIALS AND METHODS

A subline of cultured mammalian cells of Chinese hamster V-79 cells were used for the present study and maintained with Eagle's MEM medium with 15% of fetal calf serum under the atmosphere of 95% air and 5% CO_2 mixture. A monolayer of cells attached to a dish (35 mmϕ) were irradiated in air without medium. All of ion beams of helium-4 (18.5 MeV/μm), of carbon and helium-3 (12 MeV/μm) were obtained from the cyclotron of NIRS. Cells were irradiated with these ion beams in a cell assembly at the final course of a beamline. Sample change was remotely controlled in irradiation. After irradiation, cells

were transplanted into assay dishes for checking cell survivals by colony formation. The absorbed dose for cellular materials was monitored by using a transmission ionization chamber. In order to determine the absorbed dose, the flux density was measured with a Farady cup. The stopping power was calculated by using Steward and Wallace's program.[5] The absorbed dose was also estimated from the Bragg-Gray cavity theory by using a parallel plate ionization chamber. The results of the two different dosimetries were in accord with each other within 1%. An LET spectrum was measured by using a proportional counter. The Bragg curve for dose-average LET was measured for the experiment everytime to compare the results with the theoretical ones. The fraction of dose for a mixed irradiation with a known LET was determined from the following equation

$$L_{mix} = L_{low} \cdot D_{low}/D + L_{high} \cdot D_{high} \quad (1)$$

where L_{low} and L_{high} stand for dose-average LET of mono-peaked radiation; D_{low} and D_{high} stand for the irradiation dose of single radiations with low and high LET and D stands for the total irradiation dose.

III. RESULTS

We investigated the dose survival responses of Chinese hamster V-79 cells vs. single and mixed LET spectra of monoenergetic α-particles of 14.5, 25, 35, 45, 60, and 75 keV/μm and carbon ions of 230–420 keV/μm. These curves were obtained by fitting the data to a linear-quadratic model.[2] These results indicate that cell killing ability increases as dose-average LET increases. Concomitantly, the shape of the survival curve was modified to be straight and steep, and its shoulder was reduced. When compared with that of single irradiation, the effects of mixed irradiations showed a close proximity to the beams in the range of dose-average LET of 14.5–75 keV/μm. The experiments, using carbon ions, showed a similar response to an exponential type of cell inactivation but no linear correlation between dose average LET and cell killing.

IV. DISCUSSION

We have considered the cell killing effect of mixed irradiation according to Zaider & Rossi's equation,[6] and analogized the survival parameter, α, to dose-average calculation [see MATERIALS AND METHODS; Eq. 1]. Thus, it was possible to obtain a linear relation between α and dose average LET in the range of LET less than 75 keV/μm. Similarly, the survival curve parameter, λ, in Goodhead's model[3] was also sohwn to be linear against an increase in dose average LET. These parameters are thought to be in close relation to such physical quantities as dose average LET. That such parameters showed the same variation with LET will provide a view in favor of the concept that the radiation induced lethal lesion can be caused by the one hit action in the track segment and that the number of induced lesions is proportional to the energy loss in the track segment.

References

1) E. A. BLAKELY, C. A. TOBIAS, T. C. H. YANG, K. C. SMITH, and J. T. LYMANN: *Radiat. Res.*, **80**, 122 (1979).
2) A. M. KELLER and H. H. ROSSI: *Radiat. Res.*, **75**, 471 (1978).
3) D. T. GOODHEAD: *Radiat. Res.*, **104**, S58 (1985).
4) F. Q. H. NGO, E. A. BLAKELY, and C. A. TOBIAS: *LBL-Report* 11220, 103 (1980).
5) P. STEWARD and R. WALLACE: UCRL-17314, Univ. California, 1966.
6) M. ZAIDER and H. H. ROSSI: *Radiat. Res.*, **83**, 732 (1980).

Chromosome Aberration Frequencies Produced by a 70-MeV Proton Beam

SHO MATSUBARA,* HIROSHI OHARA,† TAKESHI HIRAOKA,† SACHIKO KOIKE,† KOICHI ANDO,† HIROSHI YAMAGUCHI,† YUJI KUWABARA,* MASAO HOSHINA,* AND SOJI SUZUKI*

**Department of Radiology, Tokyo Medical and Dental University, School of Medicine, Tokyo, and †National Institute of Radiological Science, Chiba, Japan*

Reprinted from RADIATION RESEARCH, Volume 123, No. 2, August 1990

RADIATION RESEARCH 123, 182–191 (1990)

Chromosome Aberration Frequencies Produced by a 70-MeV Proton Beam

SHO MATSUBARA,* HIROSHI OHARA,† TAKESHI HIRAOKA,† SACHIKO KOIKE,† KOICHI ANDO,† HIROSHI YAMAGUCHI,† YUJI KUWABARA,* MASAO HOSHINA,* AND SOJI SUZUKI*

*Department of Radiology, Tokyo Medical and Dental University, School of Medicine, Tokyo, and †National Institute of Radiological Science, Chiba, Japan

MATSUBARA, S., OHARA, H., HIRAOKA, T., KOIKE, S., ANDO, K., YAMAGUCHI, H., KUWABARA, Y., HOSHINA, M., AND SUZUKI, S. Chromosome Aberration Frequencies Produced by a 70-MeV Proton Beam. *Radiat. Res.* 123, 182–191 (1990).

The effectiveness of a 70-MeV proton beam in the induction of chromosome aberrations was studied. We employed peripheral lymphocytes and analyzed the frequencies of dicentrics and rings after irradiation at doses ranging from 0.1 to 8.0 Gy at various depths within a Lucite phantom. The frequency of chromosome aberrations after irradiation with an unmodulated proton beam at 5 mm showed a dose–response relationship similar to that of ^{60}Co γ rays. However, irradiation at greater depths with the spread-out Bragg peak induced higher aberration frequencies at doses lower than those with γ rays. Furthermore, the distribution curve of chromosome aberration frequencies as a function of depth was found to be slightly different from the physically measured depth–dose curve. With the spread-out Bragg peak the biological effects were more marked at greater depths, resulting in a distribution of relative biological effectiveness values. The results obtained from chromosome aberration analysis may not be related directly to those for the relationship between dose and cell killing. Slight differences in values for relative biological effectiveness due to the change of dose and site of proton beam irradiation may not be important for practical proton beam therapy, but may be important in the prevention of late radiation injuries.

INTRODUCTION

It is widely believed that the greatest advantage of a high-energy proton beam in radiotherapy is its precise and selective spatial dose distribution, although its relative biological effectiveness (RBE) has been considered to differ little from that of a photon beam. The radiation dose delivered by a proton beam has a sharp maximal point, called the Bragg peak, due to particle deceleration, and shows a low level of lateral scatter. For radiotherapy (*1–7*), by varying the energy and the number of protons accelerated, the Bragg peak can be shaped to deliver homogeneous doses of radiation to irregularly outlined three-dimensional volumes. Values found in a number of studies undertaken to investigate the RBE of protons, mostly by assessing the cell-killing effect, have ranged from about 0.8 to 2.0 (*8–15*). A survey of RBE values reported for high-energy protons indicates that RBE is a function of the biological end point as well as beam parameters (*9–12*). Chromosome analysis using peripheral lymphocytes is now accepted as a sensitive and reliable indicator of biological effect (*6, 8, 16–22*). No effect of spreading the Bragg peak of the proton beam was detected using cell killing as the end point. In this study, we have employed analysis of chromosome aberrations to detect differences in the effects of the different segments of a 70-MeV proton beam.

MATERIALS AND METHODS

Dose Distribution and Dosimetry

A cyclotron unit at the National Institute of Radiological Science, Chiba, was used in this study. A parallel plate ionization chamber with a guard plate was employed to determine the absorbed dose and dose distribution. This chamber (FWT Model EIC-1) was made of A150 plastic and was small in size and filled with methane-based tissue-equivalent gas (TE). Based on the calibration of ^{60}Co γ rays, the active collecting volume of the chamber was determined to be 0.348 ml. The proton beam with a maximum initial energy of 70 MeV from the unit demonstrated a sharp Bragg peak at 31.8 mm in the Lucite phantom (Fig. 1). In Fig. 2, the relative dose as a function of depth for a Bragg peak, spread out and flattened by a range modulator, is shown. The physical measurement of dose distribution in the spread-out peak was made at 0.5-mm increments in depth in the Lucite phantom located behind a range modulator which consisted of a rotating wheel with blades of various thickness. Mean dose-averaged values for linear energy transfer (LET) of the modulated beam were calculated using Janni's stopping-power table (*24*). The marked increase in LET values observed with increase in depth, even after beam modulation (Fig. 3), is considered due to the significant dependence of stopping power on proton energy. The sharp change in the curve, calculated as a function of depth (Fig. 3), corresponds to the build-up point on the depth–dose curve in Fig. 2.

0033-7587/90 $3.00

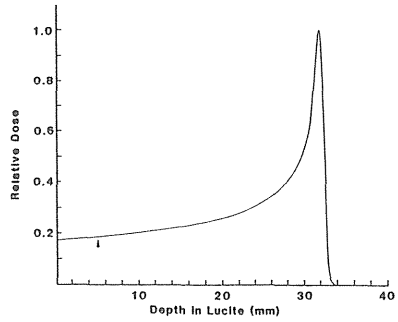

FIG. 1. Depth–dose distribution of a 70-MeV proton beam in an unmodulated form within a Lucite phantom. The arrowhead indicates the position at which the blood sample was irradiated to obtain a dose–response relationship for chromosome aberrations.

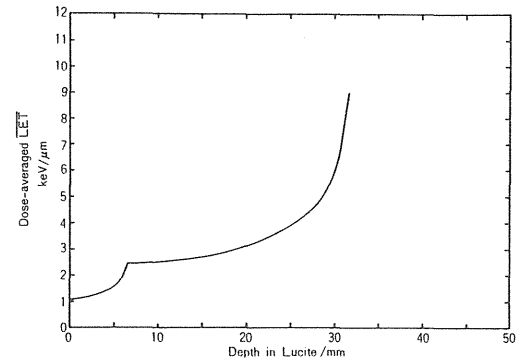

FIG. 3. Mean dose-averaged LET values of the 70-MeV modulated proton beam were calculated using Janni's stopping-power table (*24*). LET values of the modulated beam are clearly demonstrated to increase with increasing depth.

Exposure to Proton Beam

Venous blood was drawn from healthy 20-year-old donors who had no history of exposure to ionizing radiation, except for routine chest X-ray examinations. The heparinized blood was irradiated in small plastic tubes (outer diameter 5.3 mm; inner diameter 4.0 mm; No. 1693, Shibata) set in a special stand of a Lucite phantom. Employing modulated as well as unmodulated beams, we irradiated 0.3-ml blood samples in a central portion of a 4 × 4-cm broad-beam irradiation portal at a distance of 6.0 m from the 1-mm aluminum scattering foil. The plastic tube was 2 cm long, and the dose distribution was quite uniform, varying not more than 1.0%. The dose rates we used were 2.0 and 6.0 Gy per minute.

Dose–response relationships at various depths. Irradiation was performed to obtain the dose–effect relationship of chromosome aberration frequencies in blood samples in small plastic tubes placed in a Lucite phantom at depths of 5, 15, and 25 mm. The depths at which the blood was irradiated were obtained by using the Lucite absorbers, as illustrated in Fig. 4. The irradiation at the 5-mm position (a) was performed using only the unmodulated beam, but the modulated beam was used at 15 mm (b) and 25 mm (c). The radiation doses we employed were 0.1, 0.2, 0.5, 1.0, 2.0, 3.0, 4.0, 6.0, and 8.0 Gy at a dose rate of 2.0 Gy per minute. The dose–effect relationship thus obtained was then compared with that observed after irradiation with 0.1, 0.2, 0.3, 0.5, 1.0, 2.0, 3.0, 4.0, 6.0, and 8.0 Gy of ^{60}Co γ rays at a dose rate of 0.8 Gy per minute.

Depth–dose distribution within the phantom. The whole blood in small plastic tubes was exposed to fixed proton beam doses, i.e., radiation doses of 1.0 and 2.5 Gy were used in the first experiment and doses of 4.0 and 6.0 Gy in the second, to determine the change in RBE values derived from chromosome aberration frequencies induced in samples at various depths within the phantom. The dose rate was 6.0 Gy per minute. The depths as arranged by the placement of absorbers were 10, 17, 22, 26, 29, 31, and 32 mm. Irradiation was at room temperature, and blood culture was started within 2 h of the completion of irradiation.

Lymphocyte Culture, Slide Preparation, and Chromosome Analysis

After irradiation, the blood was cultured in 5 ml RPMI-1640 culture medium with 1 ml fetal bovine serum after the addition of 0.2 ml phytohe-

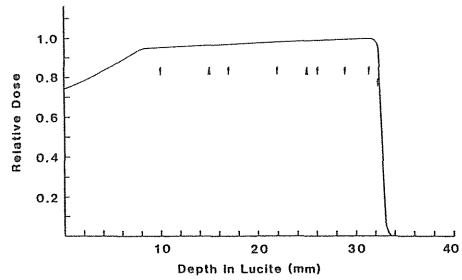

FIG. 2. Depth–dose distribution of a 70-MeV proton beam in a modulated form within a Lucite phantom. The spread-out Bragg peak is illustrated. The arrowheads indicate the positions at which blood samples were irradiated to obtain dose–response relationships of chromosome aberrations. Arrows indicate the positions at which blood samples were irradiated to obtain RBE values based on chromosome analysis.

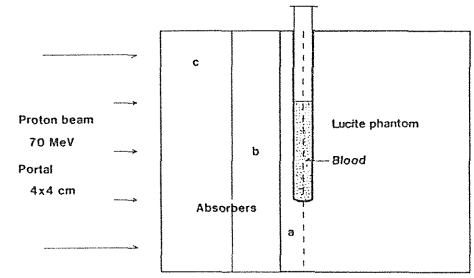

FIG. 4. Plastic tubes of 4-mm inside diameter containing the blood samples were placed in a Lucite phantom and irradiated with a 70-MeV proton beam through a lateral 4 × 4-cm portal. The depths at which the blood samples were irradiated were arranged using absorbers b and c, and the dose–response relationship was obtained. To investigate the depth–dose relationship, various other kinds of absorbers were used.

TABLE I
Distributions of Dicentrics and Rings among the Cells Irradiated with 70-MeV Proton Beams at Depth of 5 mm

Radiation dose (Gy)	Number of cells scored	Number of dicentrics and rings	Number of cells with indicated number of dicentrics and rings								Mean (dicentrics and rings per cell) ± SE	σ^2/Y	U
			0	1	2	3	4	5	6	7			
0.1	600	4	596	4							0.007 ± 0.003	0.99	−0.10
		(2)[a]	(598)	(2)							(0.003 ± 0.002)	(1.00)	(−0.04)
0.2	400	4	396	4							0.01 ± 0.005	0.99	−1.23
		(0)	(400)	(0)							(0)	—	—
0.5	300	12	288	12							0.04 ± 0.01	0.96	−0.47
		(2)	(298)	(2)							(0.007 ± 0.005)	(1.00)	(−0.06)
1.0	300	18	282	18							0.06 ± 0.01	0.94	−0.72
		(4)	(296)	(4)							(0.013 ± 0.007)	(0.99)	(−0.14)
2.0	100	36	70	25	4	1					0.36 ± 0.06	1.04	0.29
		(7)	(93)	(7)	(0)	(0)					(0.07 ± 0.03)	(0.94)	(−0.46)
3.0	100	60	55	32	11	2					0.60 ± 0.08	0.98	−0.14
		(10)	(90)	(10)	(0)	(0)					(0.10 ± 0.03)	(0.91)	(−0.68)
4.0	100	96	38	35	21	5	1				0.96 ± 0.09	0.92	−0.5
		(18)	(84)	(14)	(2)	(0)	(0)				(0.18 ± 0.04)	(1.05)	(0.37)
6.0	100	206	9	29	34	13	8	4	3		2.06 ± 0.14	0.95	0.36
		(32)	(70)	(28)	(2)	(0)	(0)	(0)	(0)		(0.32 ± 0.05)	(0.81)	(−1.30)
8.0	50	162	0	4	15	12	7	8	4		3.24 ± 0.21	0.65	−1.73
		(27)	(28)	(18)	(3)	(1)	(0)	(0)	(0)		(0.54 ± 0.10)	(0.92)	(−0.41)

[a] Centric and acentric rings in parentheses.

magglutinin (PHA, M-type). The cultures were incubated at 37°C for 48 h and Colcemid (demecolcine) was added at a final concentration of 0.5 μg/ml at 24 h after the start of incubation. The harvested lymphocytes were treated with a hypotonic solution of 0.075 *M* KCl and stained with Giemsa solution after fixation. To confirm whether we could exclude the presence of second-division cells in the present lymphocyte culture method, another culture technique with fluorescence plus Giemsa staining was also employed using 4.0- and 6.0-Gy-irradiated and nonirradiated control blood (*16*). For these 48 h of culture, 5-bromodeoxyuridine (BrdU) and Colcemid were added at the start of incubation and 24 h before har-

TABLE II
Distributions of Dicentrics and Rings among the Cells Irradiated with 70-MeV Proton Beams at Depth of 15 mm

Radiation dose (Gy)	Number of cells scored	Number of dicentrics and rings	Number of cells with indicated number of dicentrics and rings								Mean (dicentrics and rings per cell) ± SE	σ^2/Y	U
			0	1	2	3	4	5	6	7			
0.1	450	6	444	6							0.013 ± 0.005	0.99	−0.18
		(1)[a]	(449)	(1)							(0.002 ± 0.002)	(1.00)	(0)
0.2	400	12	388	12							0.03 ± 0.01	0.97	−0.41
		(5)	(395)	(5)							(0.013 ± 0.006)	(0.99)	(−0.16)
0.5	300	17	283	17							0.06 ± 0.01	0.95	−0.67
		(3)	(297)	(3)							(0.010 ± 0.006)	(0.99)	(−0.10)
1.0	200	27	173	24	3						0.15 ± 0.03	1.06	0.56
		(8)	(192)	(8)	(0)						(0.040 ± 0.014)	(0.96)	(−0.38)
2.0	100	46	64	27	8	1					0.46 ± 0.07	1.03	0.22
		(5)	(95)	(5)	(0)	(0)					(0.050 ± 0.022)	(0.96)	(−0.32)
3.0	100	68	50	35	13	1	1				0.68 ± 0.08	0.98	−0.14
		(12)	(88)	(12)	(0)	(0)	(0)				(0.12 ± 0.03)	(0.89)	(−0.82)
4.0	100	104	36	34	20	10					1.04 ± 0.10	0.93	−0.50
		(15)	(85)	(13)	(2)	(0)					(0.17 ± 0.04)	(1.08)	(0.59)
6.0	100	199	7	31	34	16	9	2	1		1.99 ± 0.12	0.73	−1.85
		(22)	(78)	(16)	(6)	(0)	(0)	(0)	(0)		(0.28 ± 0.06)	(1.16)	(1.16)
8.0	—												

[a] Centric and acentric rings in parentheses.

TABLE III
Distributions of Dicentrics and Rings among the Cells Irradiated with 70-MeV Proton Beams at Depth of 25 mm

Radiation dose (Gy)	Number of cells scored	Number of dicentrics and rings	Number of cells with indicated number of dicentrics and rings								Mean (dicentrics and rings per cell) ± SE	σ^2/Y	U
			0	1	2	3	4	5	6	7 8 9			
0.1	550	9	541	9							0.016 ± 0.005	0.99	−0.26
		(2)[a]	(548)	(2)							(0.004 ± 0.003)	(1.00)	(−0.04)
0.2	400	14	387	12	1						0.035 ± 0.006	1.11	1.62
		(6)	(394)	(6)	(0)						(0.015 ± 0.006)	(0.99)	(−0.19)
0.5	200	17	185	13	2						0.09 ± 0.02	1.16	1.60
		(5)	(195)	(5)	(0)						(0.025 ± 0.011)	(0.98)	(−0.22)
1.0	200	32	169	30	1						0.16 ± 0.03	0.91	−0.97
		(7)	(193)	(7)	(0)						(0.035 ± 0.013)	(0.97)	(−0.33)
2.0	100	46	62	31	6	1					0.46 ± 0.07	0.94	−0.43
		(9)	(91)	(9)	(0)	(0)					(0.09 ± 0.03)	(0.92)	(−0.60)
3.0	100	80	48	31	14	7					0.80 ± 0.09	1.09	0.64
		(14)	(86)	(14)	(0)	(0)					(0.14 ± 0.04)	(0.87)	(−0.96)
4.0	100	113	31	37	22	8	2				1.13 ± 0.10	0.91	−0.64
		(19)	(81)	(19)	(0)	(0)	(0)				(0.19 ± 0.04)	(0.82)	(−1.31)
6.0	100	197	8	28	34	22	6	1	1		1.97 ± 0.11	0.67	−2.35
		(20)	(82)	(16)	(2)	(0)	(0)	(0)	(0)		(0.20 ± 0.05)	(1.01)	(0.07)
8.0	100	353	0	7	27	26	16	10	6	3 2 3	3.53 ± 0.19	0.98	−0.14
		(61)	(60)	(23)	(14)	(2)	(1)	(0)	(0)	(0) (0) (0)	(0.61 ± 0.09)	(1.26)	(3.08)

[a] Centric and acentric rings in parentheses.

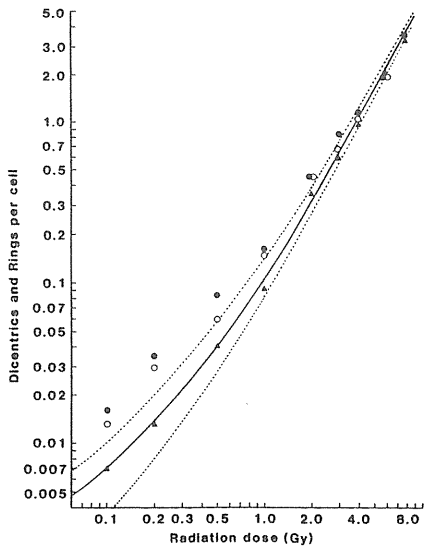

FIG. 5. Dose–response relationships of chromosome aberration frequencies obtained at three depths. Solid triangles: irradiated at 5 mm with the unmodulated beam, indicated by the arrowhead in Fig. 1. Open circles: irradiated at 15 mm with the modulated beam, indicated by one of the arrowheads in Fig. 2. Closed circles: irradiated at 25 mm with the modulated beam, indicated by another arrowhead in Fig. 2. A solid line indicates the dose–response relationship due to ^{60}Co γ irradiation with 95% confidence limits (shown as dotted lines).

vest, respectively. The metaphase slides were processed with hypotonic solution and fixed, treated with Hoechst-33258 solution, exposed to ultraviolet light, and finally stained with Giemsa solution. Metaphases beyond first division were identified by the harlequin-stained figures on chromosome slide preparations. The slides were coded before being scored.

In the present chromosome analysis, only dicentrics and centric and acentric rings were analyzed, because they could be scored easily and accurately and are commonly recognized as a biological dosimeter. The number of cells examined ranged from 100 to 600, a larger number of cells being examined for the lower dose ranges. However, for depths of 5 and 15 mm, only 50 and 25 cells, respectively, could be scored for the 8.0-Gy dose point; the results for 15 mm are not reported. For analysis of the dose–effect relationship, the data were fitted by least-squares regression analysis to a linear-quadratic model.

RESULTS

We determined the effectiveness of both the unmodulated beam and the spread-out Bragg peak for the induction of chromosome aberrations in samples of blood irradiated in the beams as shown in Figs. 1 and 2.

No second mitotic figures were observed among the metaphases of 4.0- and 6.0-Gy-irradiated lymphocytes or in the nonirradiated controls on the preparation slides obtained by the fluorescence plus Giemsa technique, although no further detailed data are given in this paper. Therefore, we evaluated cells processed by the conventional method with the addition of Colcemid at 24 h after the start of incubation. For the control frequency of chromosome aberrations in unirradiated donor, 1050 metaphases were scored and two dicentrics were observed (0.0019 ± 0.0013). The dose–

TABLE IV
Distributions of Dicentrics and Rings among the Cells Irradiated with ^{60}Co γ Rays

Radiation dose (Gy)	Number of cells scored	Number of dicentrics and rings	Number of cells with indicated number of dicentrics and rings								Mean (dicentrics and rings per cell) ± SE	σ^2/Y	U
			0	1	2	3	4	5	6	7			
0.1	550	4	546	4							0.007 ± 0.004	0.99	−0.10
		(0)[a]	(550)	(0)							(0)	—	—
0.2	500	7	493	7							0.014 ± 0.005	0.99	−0.21
		(0)	(500)	(0)							(0)	—	—
0.3	400	9	392	7	1						0.02 ± 0.01	1.20	3.04
		(2)	(398)	(2)	(0)						(0.005 ± 0.004)	(1.00)	(−0.05)
0.5	300	12	288	12							0.04 ± 0.01	0.96	−0.47
		(2)	(298)	(2)							(0.007 ± 0.005)	(1.00)	(−0.06)
1.0	200	20	182	16	2						0.10 ± 0.02	1.11	1.08
		(3)	(197)	(3)	(0)						(0.02 ± 0.01)	(0.99)	(−0.12)
2.0	100	34	73	20	7						0.34 ± 0.06	1.08	0.58
		(4)	(96)	(4)	(0)						(0.04 ± 0.02)	(0.97)	(−0.25)
3.0	100	62	52	37	8	3					0.62 ± 0.08	0.94	−0.43
		(9)	(91)	(9)	(0)	(0)					(0.09 ± 0.03)	(0.92)	(−0.60)
4.0	100	105	32	41	17	10					1.05 ± 0.09	0.85	−1.00
		(14)	(86)	(10)	(2)	(0)					(0.14 ± 0.04)	(1.16)	(1.18)
6.0	100	229	7	24	27	23	13	6			2.29 ± 0.13	0.76	−1.71
		(47)	(53)	(30)	(4)	(3)	(0)	(0)			(0.47 ± 0.07)	(1.09)	(0.65)
8.0	100	360	0	11	10	27	28	12	8	4	3.60 ± 0.15	0.65	−2.49
		(63)	(37)	(25)	(13)	(4)	(0)	(0)	(0)	(0)	(0.63 ± 0.09)	(1.18)	(1.22)

[a] Centric and acentric rings in parentheses.

response relationship for the aberrations induced by the 70-MeV proton beam showed a trend somewhat similar to the relationship for ^{60}Co γ rays. However, there appeared to be some differences in efficiency of aberration induction among the lymphocytes irradiated at depths of 5, 15, and 25 mm (Tables I, II, and III) (Fig. 5). These aberration frequencies were expressed in equations based on a linear-quadratic model shown as $Y = \alpha D + \beta D^2$, where Y and D indicate the yield of dicentrics plus rings and the dose in grays, respectively. α and β are the coefficients giving a best fit to the data points. The dose–effect relationships can thus be expressed as follows at each depth.

5 mm: $Y = (8.72 \pm 2.65) \times 10^{-2} \times D + (4.03 \pm 0.40) \times 10^{-2} \times D^2$

15 mm: $Y = (1.43 \pm 0.30) \times 10^{-1} \times D + (2.65 \pm 0.50) \times 10^{-2} \times D^2$

25 mm: $Y = (1.78 \pm 0.43) \times 10^{-1} \times D + (3.08 \pm 0.35) \times 10^{-2} \times D^2$

TABLE V
RBE Values of 70-MeV Proton Beams at Different Depths of Irradiation

Proton dose (Gy)	Depth of irradiation		
	5 mm	15 mm	25 mm
0.1	1.0 ± 0.7[a]	1.8 ± 1.2	2.3 ± 1.2
0.2	0.9 ± 0.5	2.1 ± 1.0	2.5 ± 1.2
0.5	1.0 ± 0.4	1.5 ± 0.5	2.1 ± 0.8
1.0	0.9 ± 0.3	1.5 ± 0.3	1.6 ± 0.5
2.0	1.1 ± 0.3	1.3 ± 0.3	1.4 ± 0.3
3.0	1.0 ± 0.2	1.1 ± 0.2	1.4 ± 0.2
4.0	0.9 ± 0.1	1.0 ± 0.1	1.1 ± 0.2
6.0	0.9 ± 0.1	0.9 ± 0.1	0.9 ± 0.1
8.0	0.9 ± 0.1		1.0 ± 0.1

[a] Mean ± SE.

The dose–response relationship of frequency of chromosome aberrations induced by ^{60}Co γ rays (Table IV) is given by the following equation:

$$Y = (6.11 \pm 0.49) \times 10^{-2} \times D + (5.03 \pm 0.14) \times 10^{-2} \times D^2.$$

Compared to the aberration frequencies due to ^{60}Co γ-ray exposure, no remarkable difference was elicited in the frequencies obtained by irradiation with the unmodulated proton beam at the site of 5-mm depth in all dose ranges.

TABLE VI
Distributions of Dicentrics and Rings among the Cells Irradiated with 70-MeV Proton Beams at Different Depths (1.0 Gy)

Depth (mm)	Number of cells scored	Number of dicentrics and rings	Number of cells with indicated number of dicentrics and rings								Mean (dicentrics and rings per cell) ± SE	σ^2/Y	U
			0	1	2	3	4	5	6	7			
10	150	16	135	14	1						0.11 ± 0.03	1.03	0.22
		(2)[a]	(148)	(2)	(0)						(0.01 ± 0.01)	(0.99)	(−0.08)
17	200	23	177	23							0.12 ± 0.02	0.89	−1.13
		(1)	(199)	(1)							(0.01 ± 0.01)	(1.00)	—
22	300	37	264	35	1						0.12 ± 0.02	0.93	−0.82
		(5)	(295)	(5)	(0)						(0.02 ± 0.01)	(0.99)	(−0.18)
26	300	35	267	31	2						0.12 ± 0.02	1.01	0.10
		(9)	(291)	(9)	(0)						(0.11 ± 0.01)	(0.97)	(−0.35)
29	350	47	304	45	1						0.13 ± 0.02	0.91	−1.19
		(13)	(337)	(13)	(0)						(0.04 ± 0.01)	(0.97)	(−0.47)
31	250	45	208	40	1	1					0.18 ± 0.03	1.00	0.02
		(8)	(242)	(8)	(0)	(0)					(0.03 ± 0.01)	(0.97)	(−0.31)
32	250	46	210	34	6						0.18 ± 0.03	1.08	0.87
		(13)	(237)	(13)	(0)						(0.05 ± 0.01)	(0.95)	(−0.56)

[a] Centric and acentric rings in parentheses.

However, the modulated beam at 15 and 25 mm was more effective than the γ rays in the low-dose range. This was more marked at 25 mm.

The RBE values of the proton beam were obtained by comparing the chromosome aberration yields observed at 5 mm, 15 mm, and 25 mm with the yields induced by ^{60}Co γ irradiation. The results suggested RBE values of about 2 in the lower dose range at 15 and 25 mm and around unity at higher dose levels (Table V). However, at 5 mm no increase in RBE value was observed (Table V, Fig. 5).

The chromosome aberration frequencies induced by irradiation with the modulated beam at various depths in the Lucite phantom revealed a specific relationship between depth at which blood is irradiated and frequency of aberrations. The frequency of aberrations after exposure to 1.0 Gy starting at the 10-mm depth gradually increased and reached a maximum at 32 mm (Table VI). Thus the ratio of aberration frequencies for the 32-mm point relative to the 10-mm point was 1.6 (Fig. 6). The depth–dose distribution obtained by irradiation at 2.5 Gy also showed the same

TABLE VII
Distributions of Dicentrics and Rings among the Cells Irradiated with 70-MeV Proton Beams at Different Depths (2.5 Gy)

Depth (mm)	Number of cells scored	Number of dicentrics and rings	Number of cells with indicated number of dicentrics and rings								Mean (dicentrics and rings per cell) ± SE	σ^2/Y	U
			0	1	2	3	4	5	6	7			
10	200	52	156	35	7	1					0.26 ± 0.04	1.12	1.16
		(9)[a]	(191)	(9)	(0)	(0)					(0.045 ± 0.015)	(0.96)	(−0.43)
17	—	—											
		(−)											
22	200	68	149	37	11	3					0.34 ± 0.04	1.26	2.56
		(11)	(189)	(11)	(0)	(0)					(0.06 ± 0.02)	(0.95)	(−0.53)
26	200	85	129	58	12	1					0.43 ± 0.05	0.93	−0.66
		(14)	(186)	(14)	(0)	(0)					(0.07 ± 0.02)	(0.94)	(−0.68)
29	100	48	63	29	6	1	1				0.48 ± 0.07	1.16	1.15
		(10)	(90)	(10)	(0)	(0)	(0)				(0.10 ± 0.03)	(0.91)	(−0.67)
31	100	51	67	19	10	4					0.51 ± 0.07	1.37	2.61
		(13)	(87)	(13)	(0)	(0)					(0.13 ± 0.03)	(0.88)	(−0.89)
32	100	64	99	40	9	2					0.43 ± 0.05	1.05	0.36
		(10)	(140)	(10)	(0)	(0)					(0.07 ± 0.02)	(0.94)	(0.55)

[a] Centric and acentric rings in parentheses.

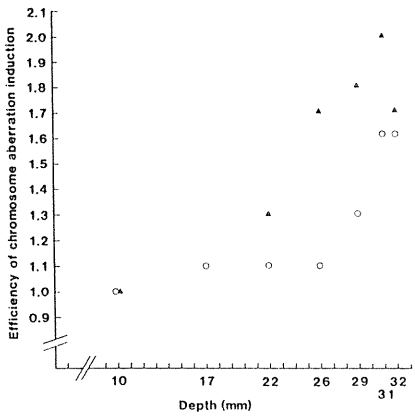

FIG. 6. Depth–dose distribution of the 70-MeV modulated proton beam estimated from chromosome aberration frequencies. The units on the ordinate are ratios of aberration frequencies along various depths. Open circles: 1.0 Gy; solid triangles: 2.5 Gy.

tendency seen for 1.0-Gy irradiation, although the aberration yield at 32 mm was slightly lower than the yields at 29 and 31 mm (Table VII). The maximum aberration frequency obtained at a depth of 31 mm was two times higher than that at 10 mm (Fig. 6). Another series of comparisons of the frequency of aberrations for 4.0 and 6.0 Gy at various depths (Table VIII and IX) resulted in almost the same distribution pattern described above, and the ratios of maximum aberration frequency at a depth of 29 mm relative to frequencies at 10 mm were 1.6 and 1.6, respectively (Fig. 7).

The spread-out peak of the 70-MeV proton beam in the present study revealed an almost flat contour in the physically measured dose distribution, not unlike that reported by other authors. However, the present results using chromosome aberration analysis as a measure of biological effectiveness suggest that relative dose is not constant over the spread-out Bragg peak but changes with depth between 10 mm and the deepest site of the spread-out peak. This result suggested the possibility of a more marked biological effect in deeper areas even within the spread-out peak.

DISCUSSION

Using chromosome aberrations as a biological end point of radiation damage, we investigated the dose–effect relationship for a 70-MeV proton beam and its depth–dose distribution. We also investigated the dose–effect relationship in the dose range down to 0.1 Gy, because the effect of proton irradiation on the induction of chromosome aberrations in such a low-dose range, which may exist in the peripheral and/or surrounding normal areas of radiotherapy portals, has not been studied extensively (*25*). The observed aberration frequencies for cells irradiated at 15 and 25 mm were found to be a little higher per unit dose than those caused by doses of less than 2.0 Gy of ^{60}Co γ rays. However, no enhanced values were observed at higher doses such as 4.0, 6.0, and 8.0 Gy. The dose–response relationships of chromosome aberration frequencies due to the proton beam irradiation have been reported by many authors, and the frequencies have been found to be largely dependent on proton energy (*8, 13, 16, 26, 27*). Radiation effects were

TABLE VIII

Distributions of Dicentrics and Rings among the Cells Irradiated with 70-MeV Proton Beams at Different Depths (4.0 Gy)

Depth (mm)	Number of cells scored	Number of dicentrics and rings	Number of cells with indicated number of dicentrics and rings								Mean (dicentrics and rings per cell) ± SE	σ^2/Y	U
			0	1	2	3	4	5	6	7			
10	100	83	42	40	12	5	1				0.83 ± 0.09	0.98	−0.18
		(14)[a]	(86)	(14)	(0)	(0)	(0)				(0.14 ± 0.03)	(0.87)	(−0.96)
17	100	102	33	41	18	7	1				1.02 ± 0.09	0.87	−0.91
		(13)	(87)	(13)	(0)	(0)	(0)				(0.13 ± 0.03)	(0.88)	(−0.89)
22	100	109	34	36	20	7	3				1.09 ± 0.11	1.00	0.02
		(18)	(83)	(16)	(1)	(0)	(0)				(0.18 ± 0.04)	(0.94)	(0.44)
26	100	123	25	38	26	11					1.23 ± 0.10	0.74	−1.86
		(23)	(78)	(21)	(1)	(0)					(0.23 ± 0.04)	(0.87)	(−0.95)
29	100	129	28	36	19	13	4				1.29 ± 0.11	0.99	−0.06
		(22)	(79)	(20)	(1)	(0)	(0)				(0.22 ± 0.04)	(0.88)	(−0.87)
31	100	49	69	20	7	2	1	1			0.49 ± 0.09	1.71	5.05
		(9)	(92)	(7)	(1)	(0)	(0)	(0)			(0.09 ± 0.03)	(1.14)	(1.06)
32	100	23	83	11	6						0.23 ± 0.05	1.31	2.19
		(7)	(93)	(7)	(0)						(0.07 ± 0.03)	(0.94)	(−0.46)

[a] Centric and acentric rings in parentheses.

TABLE IX
Distributions of Dicentrics and Rings among the Cells Irradiated with 70-MeV Proton Beams at Different Depths (6.0 Gy)

Depth (mm)	Number of cells scored	Number of dicentrics and rings	Number of cells with indicated number of dicentrics and rings								Mean (dicentrics and rings per cell) ± SE	σ^2/Y	U
			0	1	2	3	4	5	6	7			
10	100	176	9	35	36	12	7	1			1.76 ± 0.11	0.66	−0.17
		(29)[a]	(74)	(23)	(3)	(0)	(0)	(0)			(0.29 ± 0.05)	(0.93)	(−0.51)
17	100	185	12	28	34	17	7	2			1.85 ± 0.12	0.75	−0.13
		(21)	(81)	(17)	(2)	(0)	(0)	(0)			(0.21 ± 0.05)	(0.99)	(−0.07)
22	100	203	12	27	29	18	8	4	2		2.03 ± 0.14	0.96	−2.21
		(38)	(65)	(32)	(3)	(0)	(0)	(0)	(0)		(0.38 ± 0.05)	(0.79)	(−1.51)
26	100	218	4	32	30	16	13	4	1		2.18 ± 0.13	0.76	−1.67
		(35)	(68)	(29)	(3)	(0)	(0)	(0)	(0)		(0.35 ± 0.05)	(0.83)	(−1.23)
29	100	284	3	16	31	18	15	11	5	(1)	2.84 ± 0.16	0.85	−1.05
		(51)	(60)	(31)	(7)	(2)	(0)	(0)	(0)	(0)	(0.51 ± 0.07)	(1.01)	(0.07)
31	100	54	71	16	7	3	1	1	1		0.54 ± 0.11	2.22	8.69
		(12)	(90)	(8)	(2)	(0)	(0)	(0)	(0)		(0.12 ± 0.04)	(1.23)	(1.63)
32	100	19	85	11	4						0.19 ± 0.05	1.24	1.76
		(6)	(94)	(6)	(0)						(0.06 ± 0.02)	(0.95)	(−0.39)

[a] Centric and acentric rings in parentheses.

found to be influenced by the sites at which the cells were irradiated, as reported previously (*9–11*). Elevated chromosome aberration frequencies were found to be induced when the blood was irradiated at deeper sites within the beam spread out by a range modulator. Thus the RBE values obtained at 25 mm were suggested to be around 2 in a lower-dose range such as 0.1 to 0.5 Gy. Elevation of chromosome aberration frequencies was found to be less remarkable, and an RBE value of about 2 was estimated only at the doses of 0.1 and 0.2 Gy, when the blood was irradiated at 15 mm. The unmodulated proton beam irradiation at a depth of 5 mm in the Lucite phantom did not induce an elevation in chromosome aberration frequencies even in the low-dose range compared to the aberrations induced by ^{60}Co γ rays, resulting in RBE values of around unity over the dose range 0.1 to 8.0 Gy. Values for the RBE of a proton beam ranging from 0.8 to 2.0 have been reported (*8–15*). In the present study, however, the dose and depth at which the blood was irradiated were found to have a considerable influence upon the RBE values of the proton beam.

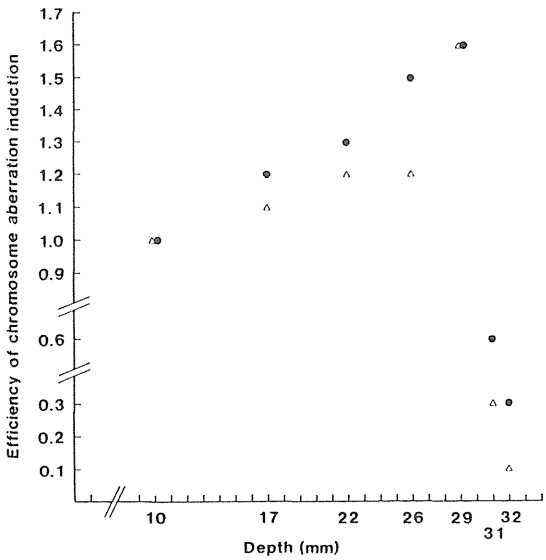

FIG. 7. Depth–dose distribution of the 70-MeV modulated proton beam estimated from chromosome aberration frequencies. The units on the ordinate are ratios of aberration frequencies along various depths. Solid circles: 4.0 Gy; open triangles: 6.0 Gy.

The measured RBE values as a function of depth based upon chromosome aberration frequencies revealed an appreciable slope even within the spread-out peak of the 70-MeV proton beam, i.e., the irradiation at deeper sites within the spread-out peak resulted in higher aberration frequencies per unit dose. The chromosome aberration frequencies observed at the deeper sites of the spread-out peak were 1.5 to 2.0 times higher than those seen at shallower sites within the same broadened peak. These results could be explained by the increase in LET with depth in the spread-out peak, which was calculated using Janni's atomic data and nuclear data table, as illustrated in Fig. 3. Furthermore, comparing the change in LET reflected in Fig. 3 and the change in the aberration frequencies in Figs. 6 and 7,

LET appears to have more influence on the induction of chromosome aberrations at lower doses than at higher doses.

In this study of proton beam dose distribution, we performed two experiments and observed slight discrepancies between them as illustrated in Figs. 6 and 7. This difference may be explained by the diameter of the small plastic tubes in which the blood was irradiated, which might have been a little too large for evaluation of the sharp reduction in the relative dose in the spread-out peak of the 70-MeV proton beam. It is possible that at this point in the beam, half of the blood within the tube did not receive a uniform dose, even though the remaining half was fully exposed to the proton beam. This possibility may be verified by the presence of more dispersed distribution of aberrations as shown in Tables VII to IX.

The value of RBE is not constant, but varies depending upon the biological end point and the dose. Differences between the RBE values obtained here and those reported by other investigators (*8–15*) can be explained as follows: (1) The chromosome aberration assay system that we employed in this study is much more sensitive than any other biological parameters. (2) The RBE values investigated in this study were for doses down to 0.1 Gy.

In radiotherapy, it is essential to restrict the radiation dose only to the target area of the tumor and to eliminate unnecessary irradiation to the surrounding normal tissue. For this requirement, the proton beam appears to give the ideal depth–dose distribution among the various types of external beam therapy. In fact, superior clinical results have been reported employing proton beam therapy for the control of selected malignant diseases in more than 5000 patients (*5*). Therefore, with respect to treatment with a high-energy proton beam, the increase in RBE values at low doses and also the possibility of a nonflat distribution of RBE values within the spread-out peak area may indicate factors to be considered for the prevention of late effects due to genetically injured but surviving cells.

RECEIVED: June 28, 1989; ACCEPTED: March 26, 1990

REFERENCES

1. J. O. ARCHAMBEAU, G. W. BENNETT, G. S. LEVINE, R. COWEN, and A. AKANUMA, Proton radiation therapy. *Radiology* **110**, 445–457 (1974).
2. I. V. CHUVILO, L. L. GOLDIN, S. V. KHOROSHKOV, S. E. BLOKHIN, V. M. BREYEV, I. A. VORONTSOV, V. V. ERMOLAYEV, Y. L. KLEINBOCK, M. I. LOMAKIN, M. F. LOMANOV, V. Y. MEDVED', N. A. MILIOKHIN, V. M. NARINSKY, L. M. PAVLONSKY, G. G. SHIMCHUCK, A. I. RUDERMAN, G. D. MONZUL, E. L. SHUVALOV, V. N. KISELIOVA, E. I. MAROVA, L. E. KIRPATOVSKAYA, E. I. MINAKOVA, V. A. KRYMSKY, A. F. BROVKINA, G. D. ZARUBEY, I. M. RESHETNIKOVA, and A. V. KAPLINA, ITEP synchrotron proton beam in radiotherapy. *Int. J. Radiat. Oncol. Biol. Phys.* **10**, 185–195 (1984).
3. A. M. KOEHLER and W. M. PRESTON, Protons in radiation therapy. *Radiology* **104**, 191–195 (1972).
4. J. E. MUNZENRIDER, M. AUSTIN-SEYMOUR, P. J. BLITZER, R. GENTRY, M. GOITEIN, E. S. GRAGOUDAS, K. JOHNSON, A. M. KOEHLER, P. MCNULTY, G. MOULTON, E. OSBORNE, J. M. SEDDON, H. D. SUIT, M. URIE, L. J. VERHEY, and M. WAGNER, Proton therapy at Harvard. *Strahlentherapie* **161**, 756–763 (1985).
5. J. M. SLATER, D. W. MILLER, and J. O. ARCHAMBEAU, Development of a hospital-based proton beam treatment center. *Int. J. Radiat. Oncol. Biol. Phys.* **14**, 761–775 (1988).
6. H. SUIT, M. GOITEN, J. MUNZENRIDER, L. VERHEY, P. BLITZER, E. GRAGOUDAS, A. M. KOEHLER, M. URIE, R. GENTRY, W. SHIPLEY, M. URANO, J. DUTTENHAVER, and M. WAGNER, Evaluation of the clinical applicability of proton beams in definitive fractionated radiation therapy. *Int. J. Radiat. Oncol. Biol. Phys.* **8**, 2199–2205 (1982).
7. H. TSUNEMOTO, S. MORITA, T. ISHIKAWA, S. FURUKAWA, K. KAWACHI, T. KANAI, and H. OHARA, Proton therapy in Japan. *Radiat. Res.* **104**, S235–S243 (1985).
8. D. BETTEGA, S. DUBINI, A. M. F. CONTI, T. PELUCCHI, and L. T. LOMBARDI, Chromosome aberrations induced by protons up to 31 MeV in cultured human cells. *Radiat. Environ. Biophys.* **19**, 91–100 (1981).
9. E. J. HALL, A. M. KELLERER, H. H. ROSSI, and Y. P. LAM, The relative biological effectiveness of 160 MeV protons, II. *Int. J. Radiat. Oncol. Biol. Phys.* **4**, 1009–1013 (1978).
10. P. J. KLIAUGA, R. D. COLVETT, Y. P. LAM, and H. H. ROSSI, The relative biological effectiveness of 160 MeV protons. I. Microdosimetry. *Int. J. Radiat. Oncol. Biol. Phys.* **4**, 1001–1008 (1978).
11. M. R. RAJU, H. I. AMOLS, E. BAIN, S. G. CARPENTER, R. A. COX, and J. B. ROBERTSON, A heavy particle comparative study. Part III: OER and RBE. *Br. J. Radiol.* **51**, 712–719 (1978).
12. J. B. ROBERTSON, J. R. WILLIAMS, R. A. SCHMIDT, J. B. LITTLE, D. F. FLYNN, and H. D. SUIT, Radiobiological studies of a high-energy modulated proton beam utilizing cultured mammalian cells. *Cancer* **35**, 1664–1677 (1975).
13. S. L. TODOROV, Y. G. GRIGOR'EV, N. I. RIZHOV, B. A. IVANOV, T. S. MALYUTINA, and M. S. MILEVA, Dose–response relationship for chromosome aberrations induced by X-rays or 50 MeV protons in human peripheral lymphocytes. *Mutat. Res.* **15**, 215–220 (1972).
14. M. URANO, M. GOITEN, L. VERHEY, O. MENDIONDO, H. D. SUIT, and A. KOEHLER, Relative biological effectiveness of a high energy modulated proton beam using a spontaneous murine tumor *in vivo*. *Int. J. Radiat. Oncol. Biol. Phys.* **6**, 1187–1193 (1980).
15. M. URANO, L. VERHEY, M. GOITEIN, J. E. TEPPER, H. D. SUIT, O. MENDIONDO, E. S. GRAGOUDAS, and A. KOEHLER, Relative biological effectiveness of modulated proton beams in various murine tissues. *Int. J. Radiat. Oncol. Biol. Phys.* **10**, 509–514 (1984).
16. M. BAUCHINGER, Cytogenetic effects in human lymphocytes as a dosimetry system. In *Biological Dosimetry* (W. G. Eisert and M. L. Mendelsohn, Eds.), pp. 15–24. Springer-Verlag, Berlin, 1984.
17. A. A. EDWARDS, D. C. LLOYD, and J. S. PROSSER, The induction of chromosome aberrations in human lymphocytes by accelerated charged particles. *Radiat. Protect. Dosim.* **13**, 205–209 (1985).
18. D. C. LLOYD and A. A. EDWARDS, Chromosome aberrations in human lymphocytes: Effect of radiation quality, dose and dose rate. In *Radiation-Induced Chromosome Damage in Man* (T. Ishihara and M. S. Sasaki, Eds.), pp. 23–49. Alan R. Liss, New York, 1983.
19. D. C. LLOYD, An overview of radiation dosimetry by conventional

cytogenetic methods. In *Biological Dosimetry* (W. G. Eisert and M. L. Mendelsohn, Eds.), pp. 3–14. Springer-Verlag, Berlin, 1984.

20. S. MATSUBARA, Y. KUWABARA, J. HORIUCHI, S. SUZUKI, M. HOSHINA, and T. KATO, A comparative study of dose distribution of a high-energy electron beam and chromosome aberration frequencies. *Br. J. Radiol.* **59**, 1001–1005 (1986).
21. S. MATSUBARA, Y. KUWABARA, J. HORIUCHI, S. SUZUKI, and A. ITO, Dose distribution of neutron beam and chromosome analysis. *Int. J. Radiat. Oncol. Biol. Phys.* **14**, 503–509 (1988).
22. M. S. SASAKI, Radiation-induced chromosome aberrations in lymphocytes: possible biological dosimeter in man. In *Biological Aspects of Radiation Protection* (T. Sugahara and O. Hug, Eds.), pp. 81–91. Igaku-Shoin, Tokyo, 1971.
23. T. HIRAOKA, Studies of absorbed dose determinations and spatial dose distributions for high energy proton beams. *Nippon Acta Radiol.* **42**, 30–54 (1982).
24. J. F. JANNI, Proton range-energy tables, 1 keV–10 keV. *At. Data Nuclear Data Tables* **27**, 147–529 (1982).
25. M. M. URIE, J. M. SISTERSON, A. M. KOEHLER, M. GOITEIN, and J. ZOESMAN, Proton beam penumbra: Effects of separation between patient and beam modifying devices. *Med. Phys.* **13**, 734–741 (1986).
26. A. A. EDWARDS, D. C. LLOYD, J. S. PROSSER, P. FINNON, and J. E. MOQUET, Chromosome aberrations induced in human lymphocytes by 8.7 MeV protons and 23.5 MeV helium-3 ions. *Int. J. Radiat. Biol.* **50**, 137–145 (1986).
27. T. TAKATSUJI, H. TAKEKOSHI, and M. S. SASAKI, Induction of chromosome aberrations by 4.9 MeV protons in human lymphocytes. *Int. J. Radiat. Biol.* **44**, 553–562 (1983).

RAPID COMMUNICATION Jpn. J. Cancer Res. 81, 112–114, February 1990

Etoposide Protects Mice from Radiation-induced Bone Marrow Death

Sigeru Yamada,[1,2] Koichi Ando,[1] Sachiko Koike[1] and Kaichi Isono[2]

[1]*Division of Clinical Research, National Institute of Radiological Sciences, 9-1 Anagawa 4-chome, Chiba 260 and* [2]*Second Department of Surgery, School of Medicine, Chiba University, 8-1 Inohana 1-chome, Chiba 280*

Etoposide is known to inhibit the activity of topoisomerase II, and to possess radiosensitizing effects. In this paper we show that pretreatment of mice with etoposide one day before whole-body irradiation had a protective effect against radiation-induced bone marrow death. The LD50/30 of mice given radiation alone was 8.26 Gy while that of mice given etoposide one day before whole-body irradiation was 10.35 Gy. The number of endogenous colony-forming units surviving in whole body-irradiated mice was significantly increased by pretreatment with etoposide.

Key words: Etoposide — Radioprotection — Bone marrow toxicity

The dose-limiting factor of etoposide, which is being used increasingly in the treatment of malignancy, is myelosuppression, such as leukocytopenia and thrombocytopenia. Combination of fractionated WBI and high-dose etoposide with bone marrow transplantation has also been used for advanced hematologic malignancies.[1-3] However, there are no published data describing the effects on bone marrow toxicity of the combined modality, even though both radiation and etoposide cause hematological suppression. In this communication, we report that pretreatment of mice with etoposide protected animals from radiation-induced bone marrow death.

The animals were 8- to 12-week-old C3H/HeMsNrsf-ICR female mice. They were produced and maintained in our SPF (specific pathogen-free) facilities at the National Institute of Radiological Sciences. Etoposide (Nihon Kayaku Ltd., Tokyo) was diluted with Ringer's solution immediately before ip injection, and 30 μg/g of etoposide in a volume equal to 0.01 ml/g body weight was used throughout these experiments. This amount of etoposide was approximately one-half of LD50 and caused no apparent toxicity in our experimental animals.

For WBI, mice were put in lucite holders without anesthesia, and received single doses of γ-rays from a ^{137}Cs unit with a dose rate of 0.96 Gy/min. Eight mice were used for each point and the observation period was 30 days. In the endogenous spleen colony assay,[4] the spleen was removed and fixed in Bouin's solution 9 days after irradiation. The number of spleen colonies on the surface of the spleen was macroscopically counted.

The time course of the combined modality was investigated by employing various time intervals between WBI and etoposide treatments (Fig. 1). The radiation dose used here was 7.7 Gy, which killed all mice by day 30. When etoposide was administered one day after WBI or later, no change in survival rate was observed. In contrast, administration of etoposide prior to WBI protected the mice from radiation-induced bone marrow death: eight out of eight mice (100%) survived when etoposide was administered one day before WBI. Less effective protection was observed when the time interval between etoposide and WBI was prolonged up to 9 days.

Figure 2 shows radiation dose-mortality relationships (LD50/30) after the combination modality in which mice received etoposide one day before various doses of WBI. The LD50/30 of mice given radiation alone was 8.26 Gy (7.98–8.53 Gy, 95% confidence) while that of mice given etoposide one day before WBI was 10.35 Gy (10.01–10.68 Gy). The dose modification factor (DMF) was 10.35/8.26, i.e., 1.24.

The effects of the combination modality on the hematopoietic system were investigated by endogenous spleen colony-forming assay. Etoposide was administered one day before WBI. As shown in Fig. 3, etoposide pretreatment resulted in an upward shift of the radiation dose-response curve, with a minimal change in D_0 (radiation dose required to reduce the colony number by 1/e); D_0 was 0.98 (0.81–1.16) Gy for radiation alone and 0.82 (0.67–0.99) Gy for etoposide-pretreated mice.

The present experiments have clearly demonstrated that a larger number of endogenous colony-forming units survived in mice that received etoposide one day before radiation than in mice that received radiation alone.

Etoposide interacts with topoisomerase II, an enzyme that catalyzes alterations in the topology of DNA through an ATP-dependent strand-passing reaction. This enzyme produces an enzyme-bridged DNA strand break

Abbreviations: WBI, whole-body irradiation; CFU-S, colony-forming units in spleen.

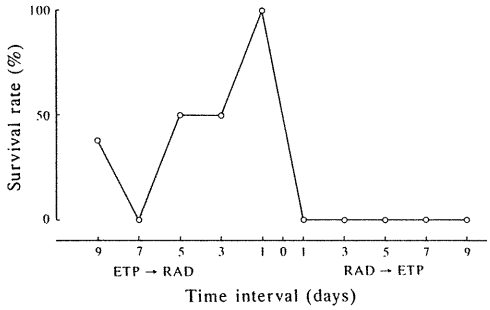

Fig. 1. Effect of timing in the combination modality of WBI and etoposide. Mice received an ip administration of 30 μg/g etoposide either before or after 7.7 Gy WBI. Eight mice were used at each point, and survival rates were determined at 30 days after irradiation. No mice survived after WBI without etoposide.

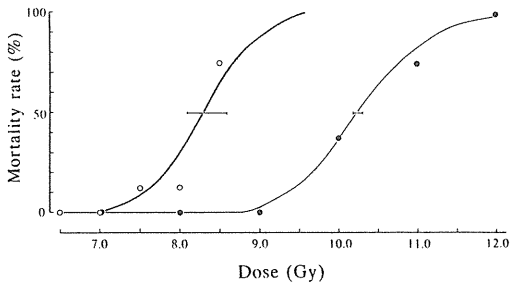

Fig. 2. Radiation dose-mortality relationship. Mice received an ip administration of 30 μg/g etoposide one day before various doses of WBI. Eight mice were used at each point, and mortality rates were determined at 30 days after irradiation. LD50/30 values were calculated by probit analysis. Open and closed circles represent the radiation alone control group and the etoposide plus radiation group, respectively.

which has been termed "the cleavable complex."[5-7] Etoposide stabilizes the cleavable complex and results in both increased DNA strand breaks and inhibition of rejoining.[5-8] Topoisomerase II seems to play a positive role in rejoining of radiation-induced double-strand breaks, and etoposide may suppress repair of DNA damage caused by radiation.[9] Cell cycle distribution is also modified by etoposide.[10, 11] Low and high concentrations of etoposide arrest cells at G_2 and S phase, respectively. These activities of etoposide, except S phase arrest, imply that cells exposed to etoposide could be sensitized to radiation. The combination of radiation and etoposide showed a significant enhancement of *in vitro* cell killing as compared with radiation alone.[12] Etoposide seems to inhibit repair of potentially lethal radiation damage. Clinical studies suggest that etoposide may be the agent responsible for enhanced radiation response in patients with small cell lung cancer.[13, 14]

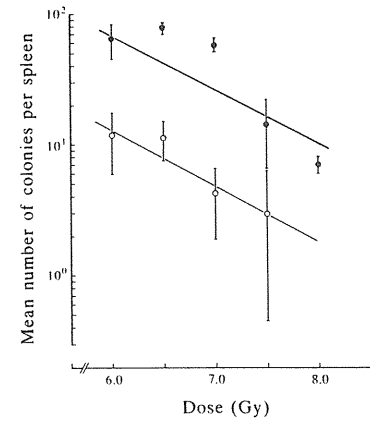

Fig. 3. Survival curve of endogenous CFU-S. Mice received either WBI alone (○) or 30 μg/g etoposide one day before WBI (●). Symbols and bars are mean and 95% confidence limits, respectively.

This is the first report to describe the radioprotective activity of etoposide. Some other cytotoxic agents including cytosine arabinoside, methotrexate, chlorambucil and cyclophosphamide are known to reduce radiation toxicity when administered to mice prior to WBI.[15] These agents do not change the radiosensitivity of the hematopoietic stem cells, but accelerate regeneration of the cells surviving radiation damage.

The finding that endogenous CFU-S formation was increased by administration of etoposide implies the following possibilities for the underlying mechanism of the protection: 1) etoposide increases CFU-S, 2) regeneration of CFU-S is accelerated by etoposide, and 3) the cell cycle of CFU-S is modified by etoposide to a more resistant distribution. We are now investigating these possibilities.

(Received November 18, 1989/Accepted December 25, 1989)

REFERENCES

1) Blume, K. G., Forman, S. J., O'Donnel, M. R., Nademance, A. P., Snyder, D. S., Schmidt, G. M., Fahey, J. L., Metter, G. E., Hill, L. R., Findley, D. O. and Sniecinski, I. J. Total body irradiation and high dose etoposide. *Blood*, **69**, 1015–1020 (1987).
2) Schmitz, N., Gassmann, W., Rister, W., Johannson, W., Suttorp, W., Brix, M., Holuthuis, J. J. M., Heit, W., Hertenstein, B., Schaub, J. and Loffler, H. Fractionated total body irradiation and high-dose VP-16-213 followed by allogenic bone marrow transplantation in advanced leukemias. *Blood*, **72**, 1567–1573 (1988).
3) Gassmann, W., Uharek, L., Wottage, H-U., Schmitz, N., Loffler, H. and Mueller-Ruchholtz, W. Comparison of cyclophosphamide, cytarabine and etoposide as immunosuppressive agents before allogeneic bone marrow transplantation. *Blood*, **72**, 1574–1579 (1988).
4) Till, J. E. and McCulloch, E. A. Direct measurement of radiation sensitivity of normal mouse bone marrow cells. *Radiat. Res.*, **14**, 213–222 (1961).
5) Chen, G. L., Yang, L., Rowe, T. C., Halligan, B. D., Tewey, K. M. and Liu, L. F. Nonintercalative antitumor drug reaction of mammalian DNA topoisomerase 2. *J. Biol. Chem.*, **259**, 13560–13566 (1984).
6) Liu, L. F., Rowe, T. C., Yang, L., Tewey, K. M. and Chen, G. L. Cleavage of DNA by mammalian DNA topoisomerase 2. *J. Biol. Chem.*, **258**, 15365–15370 (1983).
7) Rowe, T. C., Tway, K. M. and Lin, L. F. Identification of the breakage-reunion subunit of T4 DNA topoisomerase. *J. Biol. Chem.*, **259**, 9177–9181 (1984).
8) Tewey, K. M., Chen, G. L., Nelson, E. M. and Liu, L. F. Intercalative antitumor drugs interfere with the break-reunion reaction of mammalian DNA topoisomerase 2. *J. Biol. Chem.*, **259**, 9182–9187 (1984).
9) Evans, H. H., Ricanati, M., Horng, M. and Mencl, J. Relationship between topoisomerase 2 and radiosensitivity in mouse L5178Y lymphoma strains. *Mutat. Res.*, **217**, 53–63 (1989).
10) Krishan, A., Paika, K. and Frei, E. Cytofluorometric studies on the action of podophyllotoxin and epipodophyllotoxins. *J. Cell Biol.*, **66**, 521–530 (1975).
11) Miyamoto, H., Ito, M., Araya, Y., Takaoka, K., Isobe, H., Dosaka, H., Inoue, S., Kawakami, Y. and Mizuno, S. Etoposide effect on cell cycle kinetics of a human lung cancer cell line. *Jpn. J. Cancer Chemother.*, **11**, 1237–1243 (1984).
12) Kubota, N., Ikegami, T., Watai, K., Kakehi, M. and Matsui, K. Effect of combined treatment of HeLa S3 cells with radiation and etoposide on cell survival. *Nippon Acta Radiol.*, **48**, 80–86 (1988).
13) McCrecken, J. D., Janaki, L. N., Taylor, S. B., Shanker, P. G., Weiss, G. B., Gordon, W., Vance, J. R. and Crowley, J. Concurrent chemotherapy and radiotherapy for limited small-cell carcinoma of the lung. *Semin. Oncol.*, **13**, 31–36 (1986).
14) Perry, M. C., Eaton, W. L., Propert, K. J., Ware, J. H., Zimmer, B., Chahinian, A. P., Skarin, A., Carey, R. W., Kreisman, H., Faulkner, C., Comis, R. and Green, M. R. Chemotherapy with or without radiation therapy in limited small-cell carcinoma of the lung. *N. Engl. J. Med.*, **316**, 912–918 (1987).
15) Millar, J. L., Blackett, N. M. and Husspith, B. M. Enhanced post-irradiation recovery of haemopoietic system in animals pretreated with a variety of cytotoxic agents. *Cell Tissue Kinet.*, **11**, 543–553 (1978).

Int. J. Radiation Oncology Biol. Phys., Vol. 17, pp. 125–130
Printed in the U.S.A.

0360-3017/89 $3.00 + .00

● *Original Contribution*

EFFECT OF COMBINATION THERAPY OF RADIATION AND LOCAL ADMINISTRATION OF OK-432 ON A MURINE FIBROSARCOMA

MINORU MUKAI, M.D., PH.D.,* KOICHI ANDO, D.D.S., PH.D., D.M.SC.,†
SACHIKO KOIKE, M.S.† AND KOICHI NAGAO, M.D., PH.D.

National Institute of Radiological Sciences, 9-1, Anagawa 4-chome, Chiba-shi, Japan 260 and
Department of Pathology [K.N.], Teikyou University, Ichihara-shi, Chiba, 290 Japan

The effects of a combination therapy of radiation and local administration of OK-432, which is one of BRMs (biological response modifiers), were studied using a radioresistant murine fibrosarcoma with weak immunogenicity. Fifty percent tumor control doses were 83.5 (79.6–87.4) Gy in animals given radiation alone and 64.3 (57.9–71.0) Gy in animals given OK-432 immediately after radiation, indicating that this biological response modifier can enhance the radiation dose effectiveness by a factor of 83.5/64.3, that is, 1.30. Histological observations of treated tumors showed that the combination therapy induced a marked infiltration with lymphocytes and prominent degeneration and necrosis of the tumor cells. Examination of subsets of the infiltrating lymphocytes using the monoclonal antibodies showed that Lyt-2 positive lymphocytes were more abundant in the group given the combination therapy than in the radiation alone group on day 5 ($p > 0.05$). Two days later, Lyt-1, Lyt-2, and L3T4 positive lymphocytes increased in the group given the combination therapy, whereas these lymphocytes disappeared in the group given radiation alone.

OK-432, Radiation, Combination therapy, Biological response modifier, Lymphocytes subsets, NFSa.

INTRODUCTION

OK-432 is a streptcoccal preparation (5, 12) produced in Japan, and has host-mediated as well as direct antitumor action (14). The intradermal administration of OK-432 is already in clinical trials as a postoperative adjuvant therapy in Japan. We have devised a new preoperative combination therapy which involves the local administration of OK-432 and chemotherapy against gastric cancer (10) and have observed the disappearance of palpable primary tumors in several patients within as short as 2 weeks after therapy. This new combination therapy of OK-432 with radiation was also used in several cases of esophageal cancer, achieving complete regression of the tumor mass with preoperative irradiation at a relatively low dose of 30 Gy in two cases (9).

As there are not many reports on the antitumor potential of the combination therapy with radiotherapy and local administration of OK-432, we investigated and report here on basic mechanisms underlying the combination therapy using a weakly immunogenic tumor.

METHODS AND MATERIALS

Animal-tumor system

C3H/HeMsNrsf mice were housed in SPF (specific pathogen free) facilities and used in experiments at an age of 8–12 weeks. The tumor used here was the NFSa fibrosarcoma which spontaneously originated in a C3H mouse and is weak immunogenic (11). Sixteen generations of NFSa stored frozen in liquid nitrogen were implanted into mice subcutaneously. Tumor cell suspensions were prepared from tumors of approximately 2 cm diameter, which were surgically removed and cut into pieces with scissors. These pieces were stirred for 20 minutes in Dulbecco's solution, containing 0.2% trypsin, and filtered through a No. 200 stainless mesh to purify a single cell suspension. Cell viability was confirmed by phase contrast microscopy and usually exceeded 95%. Approximately 10^6 cells were injected into the right hind leg of syngeneic mice (1).

OK-432* is a heat and penicillin-treated lyophilized powder of Su-strain of Streptcoccus Pyogenes A3 (12). A

Summary of this paper was presented at the 34th Annual Scientific Meeting of Radiation Research Society which was held in Las Vegas, Nevada, April 12–17, 1986.

* Hospital Division.
† Division of Clinical Research.
Reprint requests to: Dr. Minoru Mukai.

Accepted for publication 18 January 1989.

* Chugai Pharmaceutical Co., Tokyo, Japan.

unit of 1 KE includes 0.1 mg of this dried bacteria, and is not adjusted by any standard activity. OK-432 was dissolved in physiological saline and the suspension was administered to mice intratumorally with a microsyringe in volumes ranging from 40 to 80 μl. For simultaneous administration with tumor cells, 20 μl of OK-432 was mixed with an equal volume of tumor cell suspension. The control mice received an equal volume of physiological saline.

Irradiation

Gamma rays were obtained from a ^{137}Cs unit at a dose rate of 1.9 Gy/min at 21 cm and 0.7 Gy/min at 35 cm FSD, respectively. Animals were anesthetized with 0.05 mg/g Nembutal prior to radiation. All mice were treated with a single dose of radiation to leg tumors.

Assay methods

Tumor Growth Delay: Three diameters of each tumor, a, b, and c were measured at least twice a week with calipers. Tumor volumes were calculated using the elipsoid equation, $V = \pi \times a \times b \times c/6$. Significant difference was evaluated by Student's t-test and χ^2-test.

TCD_{50} (the radiation dose by which 50% of irradiated tumors could be cured) Assay: Leg tumors were irradiated at 7 mm in diameter with ^{137}Cs gamma rays and tumor control was determined at 120 days after irradiation. Each dose point consisted of 16 mice, and a total of 90 mice were used for each assay. The results were processed by probit analysis to calculate the 50% tumor control dose together with the 95% confidence limit.

Lymphocytes subsets: Tumors were surgically removed from mice. A single cell suspension was obtained by pressing the tumors through stainless mesh and washing out with RPMI-1640 (supplemented with 5% fetal calf serum). Mononucleated cells in the Ficoll-Paque† solution were separated by differential centrifugation and washed two times with phosphate-buffered saline containing 10% bovine serum albumin. The mean number of collected mononucleated cells were 1.35×10^6 which contained 43 ± 19% (mean and S.D.) of lymphocytes. The viability of these cells, which was determined by the trypan-blue dye exclusion method, was 53 ± 19% (mean and S.D.). An appropriate number of lymphocytes, ranging from 2,000 to 10,000, were transferred into each Fisher tube. These cells were reacted with FITC-conjugated monoclonal antibodies‡ such as anti-Lyt-1 (Pan T cells), anti-Lyt-2 (Killer/Suppressor T cells), and anti-L3T4 (Helper/Inducer T cells) for 45 minutes under 0°C. After the reaction, fluorescence intensity emitted from antibody-bound lymphocytes was measured by FACS440. For each sample, nonspecific fluorescence was measured and subtracted from the total fluorescence to give a specific value.

Effect of local administration of OK-432 on tumor growth

The mixture of OK-432 with 1×10^6 NFSa cells was implanted subcutaneously into the right hind legs of mice and the days required for these tumors to reach 1000 cu · mm, that is, tumor growth time, were studied. At a dose of 0.5 KE or higher, OK-432 significantly inhibited the tumor growth; tumor growth time for control group was 11.5 ± 0.6 days, whereas those for 0.5 KE and 1.0 KE groups were 15.0 ± 1.4 ($p < 0.01$) and 18.0 ± 2.0 ($p < 0.001$) days, respectively. With 2 KE of OK-432, tumor take was noted in only one (12.5%) of eight mice, the remaining seven mice developed no tumor in the subsequent 6 months of follow-up.

The inhibitory effect of local administration of OK-432 on the established tumors was studied (Fig. 1). First, OK-432 was intratumorally administered when leg tumors reached 7 mm in diameter. Tumor growth was slightly inhibited by 4 and 8 KE of OK-432, whereas no growth inhibition was achieved by 2 KE. Second, the tumor growth inhibitory effects of OK-432 at doses of 2, 4, and 8 KE combined with 55 Gy irradiation were studied using tumor growth delay assay. OK-432 was intratumorally injected shortly after irradiation. No complete regressions were noted in animals receiving radiation alone, whereas 2/8, 5/8, and 6/8 tumors disappeared in animals given 2 KE, 4 KE, and 8 KE of OK-432, respectively. All the

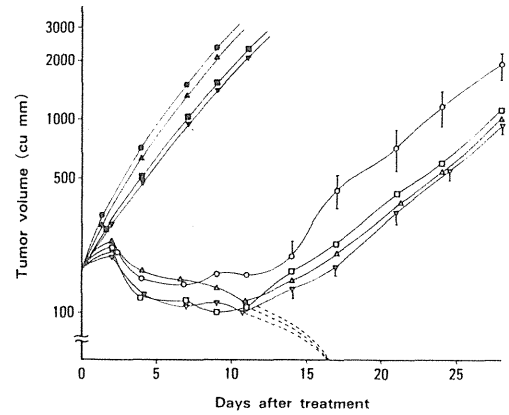

Fig. 1. Effect on tumor growth of local OK-432 administration. An intratumoral injection of 0KE (○, ●), 2 KE (△, ▲), 4 KE (□, ■), or 8 KE (▽, ▼) of OK-432 was made to 7 mm leg tumors which received either 55 Gy gamma rays (open symbols) or no irradiation (closed symbols) shortly before OK-432 injection. In the combination therapy, two out of eight tumors in the 2 KE group, five out of eight in the 4 KE group and six out of eight in the 8 KE group regressed by day 20 (dotted lines). Symbols and bars indicate means and 95% confidence limits.

† Pharmacia, Uppsala, Sweden.

‡ Beckton-Dickinson, Mountainview, CA.

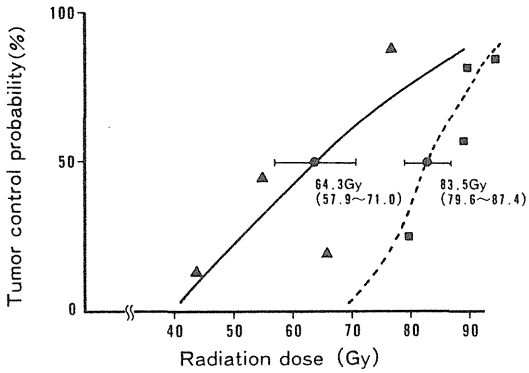

Fig. 2. Effect of local OK-432 administration on tumor control radiation dose. TCD_{50} values were obtained by probit analysis in the group given radiation alone (■) and the group given radiation plus 4 KE of OK-432 (▲).

combination therapies enhanced growth delay of tumors that did not completely regress after the treatments. Tumor cure rate, which was defined if mice were free of tumors for 4 months after treatment, was significantly different ($p < 0.05$) between the 4 KE group (four out of eight tumors) and the radiation alone group (zero out of eight tumors), whereas no significant differences were observed between the other groups treated with OK-432. Third, optimal Time for OK-432 Administration was examined. Leg tumors were locally irradiated with 40 Gy of gamma rays, and at various times between 2 days prior to and 7 days after irradiation, they received OK-432 administration. Tumor volume 20 days after irradiation was compared between control and experimental groups. A significant tumor growth inhibition was noted in the group given OK-432 immediately following irradiation; that is, 1702 ± 268 cu. mm for the radiation alone group and 1114 ± 243 cu. mm for the radiation plus OK-432 group. Administering OK-432 immediately before irradiation also achieved a significant inhibition of tumor growth. However, the tumor growth inhibitory effect of OK-432 was not detected when the time interval between OK-432 administration and irradiation was set for 1 day or over.

Tumor control doses (TCD_{50})

Based on the analysis of TCD_{50} curves, the 50% tumor control radiation dose in the group given 4 KE of OK-432 immediately following the irradiation was compared with that in the group given irradiation alone (Fig. 2). TCD_{50} in the group treated with irradiation alone was 83.5 (79.6–87.4) Gy and the group given the combination therapy with OK-432 was 64.3 (57.9–71.0) Gy. Thus, OK-432 administration immediately after irradiation appears to reduce radiation dose by a factor of 83.5/64.3, that is, 1.30.

Histological finding

Effects of the combination therapy were compared with that of radiotherapy alone by histological examination. A leg tumor that received 45 Gy of gamma rays and 2 KE of OK-432 was sectioned and processed by standard histological procedures. Figure 3 (left) shows the histology

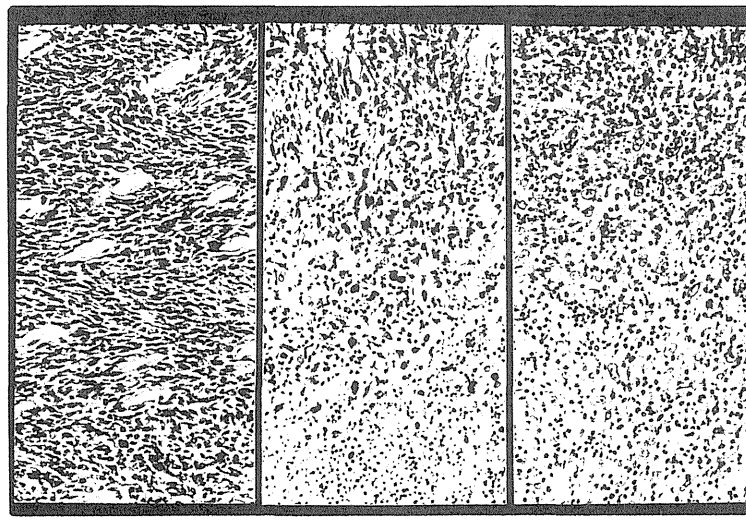

Fig. 3. Histology of NFSa tumor. The left column shows the histology of undifferentiated fibrosarcoma in the untreated control animal. The center column shows the histology of the tumor 6 days after radiotherapy with 45 Gy. The right column shows the histology of the tumor 6 days after the combination therapy with 45 Gy radiation and 2 KE of OK-432 (100×, H.E.).

of the undifferentiated fibrosarcoma in an untreated control animal. Six days after treatment with radiation alone, occasional necrotic changes have developed (Fig. 3, center). However, the histology of the peritumoral region was characterized by active proliferation of tumor cells, decreasing degeneration of tumor cells, and a slight infiltration of lymphocytes. In the group given the combined treatment, necrotic tumor cells were also observed on day 6 (Fig. 3, right). In this tumor, necrotic and degenerative changes were also seen for tumor cells in the peritumoral region. Furthermore, there was a marked infiltration of lymphocytes both in the inside and in the peripheral region of the tumor.

Subsets of lymphocytes

Lymphocytes infiltrating into tumor tissue were analyzed after the combination therapy of 40 Gy irradiation with or without 4 KE of OK-432. Tumors were resected and served for the analysis on day 5 and 7 of these treatments. As the cell yield of lymphocytes was too low to evaluate for the no treatment and OK-432 alone groups, data for these groups were not presented here.

First, percent Lyt-1 positive lymphocytes were compared between the radiation alone and combined treatments (Fig. 4). Each point represents an individual mouse. There was no significant difference between the two groups on day 5. Lymphocytes in the group given the combination therapy significantly ($p < 0.05$) increased on day 7, compared with day 5. We could not evaluate the data in the radiation alone group on day 7 because of low cell yield.

Second, percent Lyt-2 positive lymphocytes were studied (Fig. 5). There was a significant difference ($p < 0.05$) between the groups given radiation alone and combination therapy on day 5. These lymphocytes increased ($p < 0.1$) in percentage on day 7 in the group given combination therapy. Here again, the number of lymphocytes were too small to evaluate for the radiation alone group.

Third, percent L3T4 positive lymphocytes were studied (Fig. 6). There was no significant difference between the radiation alone group and the group given combination therapy on day 5. This type of lymphocyte increased ($p < 0.05$) on day 7 in the group given combination therapy. We could not, however, evaluate the data of the group given radiation alone on day 7.

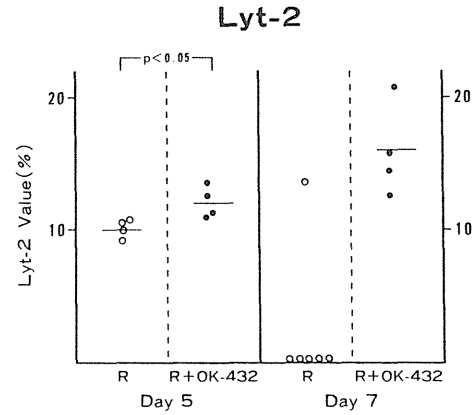

Fig. 5. Lyt-2 positive lymphocytes on day 5 and on day 7 were compared between the group given radiation alone (O) and the combination therapy of 40 Gy of radiation and 4 KE of OK-432 (●).

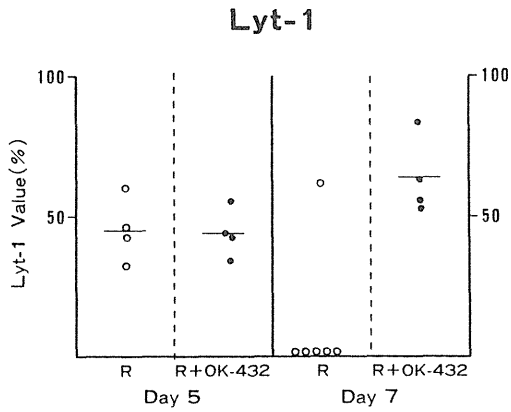

Fig. 4. Lyt-1 positive lymphocytes on day 5 and on day 7 were compared between the group given radiation alone (O) and the combination therapy of 40 Gy of radiation and 4 KE of OK-432 (●). Each point shows an individual tumor.

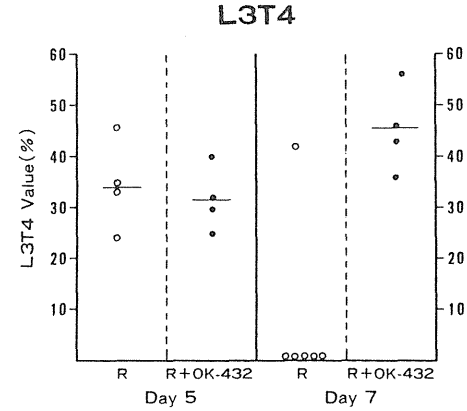

Fig. 6. L3T4 positive lymphocytes on day 5 and on day 7 were compared between the group given radiation alone (O) and the combination therapy of 40 Gy of radiation and 4 KE of OK-432 (●).

DISCUSSION

There are many reports on antitumor activities of BRMs. Milas *et al.* (6, 7) show that systemic administration of C. parvum exerts antitumor activities against immunogenic murine fibrosarcomas. The effect of the combination therapy of radiation and systemic administration of OK-432 is reported (8) on MM46 which has strong immunogenicity. In our experiment, however, systemic administration of OK-432 did not show any antitumor effect on the weakly immunogenic NFSa tumor (data not shown).

There are no reports on the effect of the combination therapy of radiation and topical administration of BRMs including OK-432. In the present study, topical administration of OK-432 showed antitumor activity when combined with radiotherapy. The radiation dose required for equal tumor response was about 20 Gy less in animals treated with OK-432 compared with animals treated with radiation alone (Fig. 2). The NFSa tumor cells have a D_0 (radiation dose to kill tumor cells by a factor of 1/e) of 4 Gy (1), and consequently, the additional cell killing exerted by OK-432 would be $(1/e)^{20/4}$, i.e. 7×10^{-3}. It follows that approximately 150 cells (i.e., 1/0.007) should have been killed by OK-432.

OK-432 is known to activate the immune system including killer T cells (2), natural killer (NK) cells (13), lymphokine activated killer (LAK) cells (3) in rodents, and neutrophils in humans (4). Histological findings in the present report demonstrated prominently infiltrated lymphocytes into the NFSa tumor tissue 6 days after the combination therapy. Sixty percent of these lymphocytes were Lyt-1 positive T cells (Fig. 4). Lyt-2 positive lymphocytes were more abundant ($p < 0.05$) in the group given the combination therapy than in the radiation alone group on day 5. Lyt-1, Lyt-2, and L3T4 positive lymphocytes in the groups given the combination therapy marginally increased from day 5 to day 7, whereas these lymphocytes disappeared in the group given radiation alone. These data are consistent with the results of histological examination. As Lyt-2 positive cells were only one lymphocytes that showed a significant increase by the additional treatment of OK-432, we are looking on the induction of killer/suppressor T cells as mechanisms underlying the effect of the combination therapy. This does not exclude the possibility that any immunocytes other than Lyt-2 positive lymphocytes engage in the antitumor effect of the combination therapy. The time interval between radiation and the administration of OK-432 was critical for the combination therapy, and simultaneous administration of OK-432 with irradiation was the most effective treatment. When the two treatments were separated by 1 day or longer, the antitumor activity of OK-432 was diminished. It is possible, at least in theory, that OK-432 inhibits the repair of radiation damage which is usually completed within several hours (11). The fact that less growth inhibition was achieved for the preirradiation treatment than the simultaneous one suggests that direct cytotoxicity of OK-432 (14) may not be responsible for the effect of combination therapy. A possible explanation for the cause of the ineffective outcome that was observed at the preirradiation treatment is that radiation might damage a variety of effector cells which had been attracted to the injection site of OK-432.

Clinical application of OK-432 has already been attempted on malignant ascites and it has been found that tumor cells were surrounded and probably destroyed by neutrophils in ascites sample (4). This means that separated tumor cells are easily damaged by contact with OK-432. Some tumor cells are feasible to be killed by OK-432 alone (14). Other tumor cells might be partially damaged by OK-432 and recognized as foreign by neutrophils. As the response of the established and solid tumors to OK-432 alone in the present experiments was marginal, we suggest that OK-432 should be used in combination with radiotherapy. In this combination therapy, we propose that radiation plays an important role as "the attacker" on malignant tumor cells and OK-432 acts as "the sweeper" inducer which attracts many effector cells to local site and sweeps the damaged tumor cells by radiation.

REFERENCES

1. Ando, K.; Koike, S.; Fukuda, N.; Kanehira, C. Independent effect of a mixed-beam regimen of fast neutron and gamma rays on a murine fibrosarcoma. Radiat. Res. 98:96–106; 1984.
2. Hojo, H.; Hashimoto, Y. Cytotoxic cell induced in tumor bearing rats by a streptcoccal preparation OK-432. Gann 72:692–699; 1981.
3. Ishida, N.; Saito, M.; Manjo, M. Induction of LAK cells in peritoneal cavity of mice after IP injection of OK-432 and antitumor effect of these LAK cells. Jpn. J. Cancer Chemother. 11(12), Part 2:2681–2690; 1984.
4. Katano, M.; Torisu, M. New approach to management of malignant ascites with a streptcoccal preparation OK-432. II. Inflammatory cell-mediated tumor cell destruction. Surgery 93:365–373; 1983.
5. Koshimura, S.; Shimizu, R.; Fujimura, A.; Okamoto, H. Experimental anticancer studies. XXI. Effect of penicillin treatment of hemolytic streptcoccus on its anticancer activity. Gann 55:233–236; 1964.
6. Milas, L.; Gutterman, U. J.; Basic, I.; Hunter, N.; Mavlight, M. G.; Hersh, M. E.; Withers, H. R. Immunoprophylaxys and immunotherapy for murine fibrosarcoma with C. Granulosum and C. parvum. Int. J. Cancer 14:493–503; 1974.
7. Milas, L.; Hunter, N.; Basic, I.; Withers, H. R. Complete regression of an established murine fibrosarcoma induced by systemic application of Corynebacterium granulosum. Cancer Res. 34:2470–2475; 1974.
8. Mukae, S.; Norimura, T.; Tsuchiya, T. Effect of immunomodifier on radiation-induced antitumor immunity following local irradiation to tumor.—1. OK-432—Nippon acta radiologica 47:838–844; 1987.
9. Mukai, M.; Ryu, T.; Kikuchi, T.; Ariga, T.; Nagashima, T.; Koh, Z.; Yamazaki, Y.; Odaka, M.; Satoh, H.; Nagao, K.

Preoperative combination therapy involving local administration of a nonspecific immunoactivated preparation (OK-432) and chemotherapeutic preparations for patients with stomach cancer. Jpn. J. Cancer Chemother. 12(4):880–886; 1985.

10. Mukai, M.; Yamazaki, Y.; Amano, H.; Hiura, T.; Oda, S.; Namiki, S.; Nakajima, K.; Nagao, K. Preoperative immunochemotherapy for gastric cancer combined with perifocal administration of OK-432. Jpn. J. Cancer Chemother. 11(5): 1071–1077; 1984.
11. Murray, D. W.; Jenkins, T.; Meyn, R. E. The efficiency of DNA strand-break repair in two fibrosarcoma tumors and in normal tissue of mice irradiated in vivo with X rays. Rad. Res. 100:171–181; 1984.
12. Okamoto, H.; Shoin, S.; Koshimura, S.; Shimizu, R. Studies on the anticancer and streptolysin S-forming abilities of hemolytic streptococci. Jpn. J. Microbiol. 11:323–326; 1973.
13. Oshima, K.; Kano, S.; Takaku, F.; Okamura, K. Argumentation of mouse natural killer cell activity by a streptcoccal preparation, OK-432. J. Natl. Cancer Inst. 65:1265–1269; 1980.
14. Sakurai, Y.; Tsukagoshi, S.; Satoh, H.; Akiba, T.; Suzuki, S.; Takagaki, Y. Tumor inhibitory effect of a streptcoccal preparation (NSC-B 116209). Cancer Chemother. Rep. 56: 9–17; 1972.

[Reprinted from *Scientific Papers of the Institute of Physical and Chemical Research*, 83, 40-41 (1989)]

Radioprotection from Fast Neutron Irradiation by WR151327

By

Koichi ANDO, Hiroshi OHARA, Satoru MATSUSHITA, Sachiko KOIKE, Shigeo FURUKAWA, and David J. GRDINA

RIKAGAKU KENKYUSHO
(The Institute of Physical and Chemical Research)

Wako-shi, Saitama
351-01, JAPAN

(Received January 10, 1989)

Radioprotection from Fast Neutron Irradiation by WR151327

Koichi ANDO,* Hiroshi OHARA,* Satoru MATSUSHITA,*
Sachiko KOIKE,* Shigeo FURUKAWA,* and David J. GRDINA**

* *National Institute of Radiological Sciences, Chiba 260*

** *Argonne National Laboratory, Argonne, Illinois, U.S.A.*

I. INTRODUCTION

Recent investigations into protection against high-LET radiation have centered around thiophosphoroates. Administration of WR-2721 before neutron irradiation has resulted in dose modification factors (DMFs) of 1.3 through 1.4.[1] Furthermore, WR-151327 shows DMF of 2.2 after fission neutron irradiation, a figure being much larger than that after γ-ray irradiation in the same $LD_{50/6}$ assay.[2] However, such a large DMF is not reported for WR-151327 after other fission neutron[3] nor accelerator fast neutron irradiations.[2] We investigated the *in vivo* protective effectiveness of WR-151327 against cyclotron fast neutron irradiation. We also report DMFs of WR-151326, an active form of WR-151327, using *in vitro* V79 cells.

II. MATERIALS AND METHODS

The radioprotector WR-151327 [$CH_3NH(CH_2)_3NH(CH_2)_3SPO_3H_2 3H_2O$] was dissolved in 0.85% NaCl solution and 400 mg/kg was intraperitoneally administered to mice 30 min before irradiation. C3H female mice at the age between 10–14 weeks old were used. Animals were kept on a 7 a.m. (light) to a 7 p.m. (dark) cycle and provided acid water. For *in vitro* experiments, WR-151326 was used. WR-151326 was dissolved in physiological saline and added to culture medium 30 min before irradiation at a concentration of 4 mM. V79 chinese hamster cells were kept in F10 medium supplemented with 15% fetal calf serum, and their exponentially growing cells served for experiments. Neutron sources used for these experiments were a cyclotron (30 MeV d-Be, Ed = 13 MeV, 60–70 cGy/min) and a Van de Graaff accelerator (Ed = 2.8 MeV, 10 cGy/min). For low-LET irradiation, a ^{137}Cs γ-ray unit (21 cm FSD, 190 cGy/min) and an X-ray machine (200 kVp, 20 mA, 61.5 cm FSD, 60 cGy/min) were used.

III. RESULTS

The radioprotective efficiency of WR-151326 on cell kill was assessed by *in vitro* colony formation. When radiation doses resulting in a 10% surviving fraction were chosen, DMFs were 2.2 after X-rays and 1.5 after fast neutrons irradiations.

For an *in vivo* study, WR-151327 was used. First, radioprotection against gastrointestinal damage was investigated using $LD_{50/7}$ as an endpoint. DMFs were 1.5 after ^{137}Cs γ ray

TABLE I. *DMFs by WR151327 (WR151326*)*

	V79*	Gut early reaction	Skin early reaction	Skin late reaction	Leg late reaction
X/γ ray	2.2	1.5	1.6–1.7	1.7–1.8	1.2–2.0
Fast neutron	1.5	1.2	1.3–1.5	1.3–1.5	1.1–1.4

irradiation and 1.2 after cyclotron fast-neutron irradiation. Second, skin and supporting tissue damage was assessed after local irradiation to leg. Skin shrinkage caused by irradiation was quantified by measuring the distance between two spots which had been tattooed to skin prior to irradiation. When 50% skin shrinkage doses were compared between control and experimental groups at 20 and 40% skin shrinkage levels, DMFs were 1.6–1.7 after γ-ray irradiation (day 50) and 1.3–1.5 after cyclotron fast-neutron irradiation (day 60). When late effect was concerned, DMFs were 1.7–1.8 after γ rays (days 260–270) and 1.3–1.5 (day 260) after cyclotron fast-neutron irradiations. A late effect was also investigated for a supportive tissue by measuring the leg length. The difference in length between irradiated and unirradiated legs in a single mouse was calculated. Fifty percent leg contracture dose was obtained by probit analysis. When leg contracture of 3 mm through 6 mm was concerned, DMFs were 1.2–2.0 after γ-ray (days 260–270) and 1.1–1.4 after cyclotron fast-neutron irradiations (day 260).

Histological examination indicated that irradiated skin developed marked hyperplasia. The thicknesses of epidermis and of dermis were measured on histological sections taken from mice that received WR-151327 and fast-neutron irradiation 11 months in advance. The dose dependence of hyperplasia was observed for both dermis and epidermis. Significant correlation was observed between the skin shrinkage and the epidermis hyperplasia.

References

1) J. S. Rasey, N. J. Nelson, P. Mahler, K. Anderson, K. A. Krohn, and T. Menard: *Radiat. Res.*, **97**, 598 (1984).
2) C. P. Sigdestad, D. J. Grdina, A. M. Connor, and W. R. Hanson: *Radiat. Res.*, **106**, 224 (1986).
3) L. K. Steel, A. J. Jacobs, L. I. Giambarresi, and W. E. Jackson III: *Radiat. Res.*, **109**, 469 (1987).

Reprinted from the Archives of Pathology and Laboratory Medicine
May 1989, Volume 113

Prognostic Significance of Langerhans' Cell Infiltration in Radiation Therapy for Squamous Cell Carcinoma of the Uterine Cervix

Takashi Nakano, MD; Kuniyuki Oka, MD; Tatsuo Arai, MD;
Shinroku Morita, MD; Hiroshi Tsunemoto, MD

• **Prognostic significance of Langerhans' cell (LC) infiltration in cancer nests was studied in 391 patients with squamous cell carcinomas of the uterine cervix. They were treated with radiation therapy alone. Langerhans' cells were identified by immunohistochemical staining for S100 protein. Langerhans' cells were present mainly in the intercellular spaces of tumor cells. The LC infiltration rates were higher in stage II (31.0%) or stage III (26.9%) than in stage I (17.5%) or stage IV (7.8%). The patients with LC infiltration showed a significantly better five-year survival rate than those without LC infiltration (68% and 56.1%, respectively). This significant difference was observed especially in stage III and it was suggestive in stage IV diseases. These results suggest that LCs in cancer nests may play a significant role in the immunologic defense against cancer in advanced stage of cervical cancer.**

(*Arch Pathol Lab Med* 1989; 113:507-511)

Langerhans' cells (LCs) are dendritic mononuclear cells characterized by an inclusion of Birbeck's granules and expressions of human leukocyte antigen (HLA)-DR, OKT6, and S100 proteins.[1-3] Langerhans' cells are derived from the bone marrow and are present in the normal uterine cervix as well as in the skin, lymph nodes, and other tissues.[4] During the past decade, in vitro studies have demonstrated that they played a critical role as effective antigen-presenting cells in the induction of many types of T-lymphocyte responses.[5-8] Recent histopathologic studies showed LC infiltration in cancer nests of several cancers.[9-15] These investigations suggested that LC infiltration in cancer nests had a significant immunologic relationship with the tumor cells. Some of these studies also demonstrated a better survival rate for the patients with the LC infiltration than those without it.[12-14]

These LC infiltrations have already been described in uterine disease in relation to the host immune response by a few investigators.[16-18] However, prognostic significance of the LC infiltration for cervical carcinoma has not yet been studied. This study determines the prognostic significance of the LC infiltration in patients with invasive carcinoma of the uterine cervix. In addition, the relationships between the LC infiltration and the clinical stage, age, and histologic subtype are also evaluated and described.

Accepted for publication Sept 14, 1988.
From the Hospital Division, National Institute of Radiological Sciences, Chiba, Japan.
Reprint requests to Hospital Division, National Institute of Radiological Sciences, 4-9-1 Anagawa, Chiba 260, Japan (Dr Nakano).

PATIENTS AND METHODS

Three hundred ninety-one patients with squamous cell carcinoma of the uterine cervix who were treated with radiation alone, from 1975 to 1980, at the National Institute of Radiological Sciences hospital (Chiba, Japan) were studied. The clinical staging and histologic classification were based on the criteria of the International Federation of Gynecology and Obstetrics (London)[19] and the World Health Organization (Geneva) classification,[20] respectively. Radiation therapy protocol is shown in Table 1. All patients were treated with high-dose rate intracavitary irradiation and external irradiation. Devices of intracavitary irradiation were TAO-type applicators commonly used in Japan. External irradiation was performed with anteroposterior and posteroanterior parallel opposed ports with or without a central shielding according to the protocol. The total dose at Point A from the intracavitary sources varied from 15 to 30 Gy. The pelvic lymph nodes were exposed with 45 to 55 Gy from the external ports. The weights of dose were altered according to the stages and tumor volumes. All patients were followed-up for more than six years.

Histologic Study

Three hundred ninety-one biopsy specimens were obtained from the tumors of the uterine cervix, which were immediately fixed with 10% formaldehyde solution and embedded in Paraplast. The sections, 4 μm in thickness, were stained with hematoxylin-eosin and the immunoperoxidase staining was performed according to Taylor's method.[21] Endogenous peroxidase of the sections was blocked with methanol containing 1% hydrogen peroxide, then the sections were treated with trypsin.[22] They were incubated with the anti-cow S100 protein (1:100, Dako, Copenhagen) for one hour at room temperature. Subsequently, they were treated with peroxidase-antiperoxidase complex (1:100, Dako) and they were developed by diaminobenzidine (3-3′-diaminobenzidine tetrahydrochloride, Dojin Chemicals, Tokyo) reaction. They were histologically examined and classified into three groups according to the grade of the LC infiltration as follows: grade (++), more than ten S100-positive cells infiltrating under magnification field (X100) in cancer nests of the tumors (Fig 1); grade (+), less than ten S100-positive cells infiltration (Fig 2); grade (−), no infiltration of the S100-positive cells (Fig 3).

Six paraffin-embedded specimens of the patients with S100 protein-positive cell infiltration were stained for HLA-DR antigens. Anti HLA-DR antibody (BioGenex Laboratory, Dublin, Calif)[23] and LN-3 antibody (specific for HLA-DR, Techniclone International, Santa Ana, Calif)[24] were used for the immunohistochemical staining. The specimens were incubated with the former antibody for two hours at 37°C and with the latter for one hour at room temperature, respectively. Subsequently, they were treated by avidin-biotin-peroxidase complex method and developed by diaminobenzidine reaction.

Prognostic Study

The infiltration rates of LCs in cancer nests were evaluated according to the clinical stages and histologic subtypes. The absolute five-year survival rates in 391 patients examined histologically were obtained according to the clinical stages, histologic subtypes, and degrees of the LC infiltration.

All results for the incidence of LC infiltration and five-year survival rates were statistically analyzed with χ^2 test and Peto's log-rank test.[25]

RESULTS

The distribution of the patients and five-year absolute survival rates by clinical stages and histologic subtypes are shown in Table 2. The differences in these five-year survival rates

*Table 1.—Treatment Policies of Combined Radiotherapy With External and Intracavitary Irradiation for Cervical Carcinoma**

Stages	Tumor Diameter, cm	External Irradiation			Intracavitary Irradiation Point A dose, Gy/Fractions
		WP, Gy	CS, Gy	Total Gy	
I	...	...	45	45	29/5
II	<5 cm	...	50	50	29/5
	>5 cm	20	30	50	23/4
III	<5 cm	20-30	30-20	50	23/4
	>5 cm	30-40	25-15	50-55	15/3-20/4
IV	...	40-50	−15	50-60	15/3-20/4

*WP indicates whole pelvic field; CS, central shielding field. External irradiation is performed five fractions weekly, giving fraction doses of 1.8 Gy for whole pelvic irradiation and 2.0 Gy for central shielding pelvic field.

Fig 1.—Langerhans' cells in carcinoma of uterine cervix, showing marked infiltration and grade (++) (×180). Peroxidase-antiperoxidase immunostained with anti-S100 protein antibody.

Fig 2.—Langerhans' cells in carcinoma of uterine cervix, showing slight infiltration and grade (+) (×180). Peroxidase-antiperoxidase immunostained with anti-S100 protein antibody.

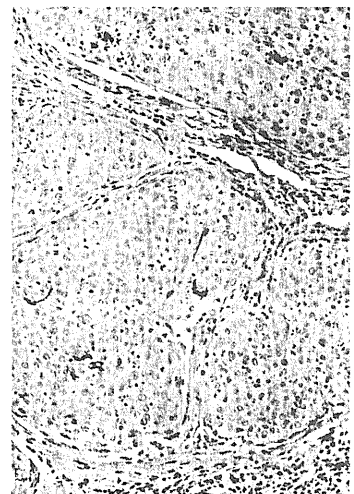

Fig 3.—No detectable Langerhans' cells in cancer of uterine cervix, showing grade (−) (×180). Peroxidase-antiperoxidase immunostained with anti-S100 protein antibody.

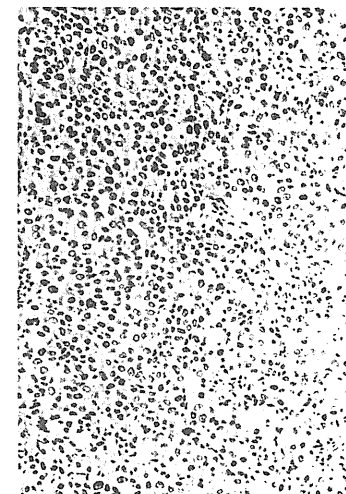

among three subtypes were not statistically significant.

Histologic Findings

The S100-positive cells were observed mainly in the intercellular space of the tumor (Figs 1 and 2). These cells were characterized by dendritic cells possessing cytoplasmic processes among the tumor cells (Fig 4). In addition, they expressed HLA-DR (Fig 5, left) and LN-3 antigens (Fig 5, right) as well as macrophages, neutrophils, and lymphocytes. Hence, they were characterized by the S100-positive and HLA-DR-positive cells, indicating that they are LCs.

Relationship of LC Infiltration and Ages, Clinical Stages, and Histologic Subtypes

The incidences of LC infiltration in the cancer nests are shown in Table 3. Ninety-five (24%) of 391 patients demonstrated the LC infiltration, showing grades (++) and (+) infiltrations.

The mean ages of the patients with grades (++), (+), and (−) were 62.1, 60.9, and 60.9 years, respectively. There were no significant differences among the three groups.

The incidence of the LC infiltration is shown according to the clinical stages in Table 4. The LC incidence in the stage IV patients was 8% and significantly lower ($P < .05$) than the incidence of stages II and III patients. The rate in stage II patients was also slightly higher than that of stage I patients, although the difference was not statistically significant ($P = .1$).

The incidence of the LC infiltration were analyzed according to the histologic subtypes (Table 5). These incidences were not significantly different among these three histologic subtypes.

Relationship of the LC Infiltration and Prognosis

Absolute five-year survival rates are shown according to the degree of the LC infiltration in Table 3. A five-year survival rate of the grade (+) patients was significantly better than that of the grade (−) patients ($P < .05$). In addition, five-year survival rate of 94 patients with grade (++) or grade (+) infiltration was 67.4%, which was significantly better than that of the grade (−) patients ($P < .025$). However, no significant difference in the survival rate was observed between the grade (++) and grade (+) patients (Table 3). Accordingly, five-year survival rates were analyzed by combining grade (+) and grade (++) as a positive LC infiltration group. Table 6 shows the absolute five-year survival rates according to

Table 2.—Distribution of Patients and Five-Year Absolute Survivals According to Clinical Stages and Histologic Subtypes

	Patients		Five-Year Survivals,
	No.	%	%
Clinical stages			
I	40	10.2	90
II	84	21.5	73.8
III	216	55.2	58.2
IV	51	13.0	17.6
Histologic subtypes			
Keratinizing	62	15.9	61.3
Large-cell nonkeratinizing	288	73.7	57.2
Small-cell nonkeratinizing	41	10.5	63.4

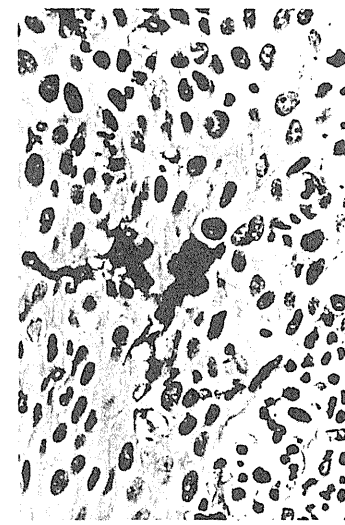

Fig 4.—Langerhans' cells in carcinoma of uterine cervix, showing dendritic cytoplasmic processes among cancer cells (×710). Peroxidase-antiperoxidase immunostained with anti-S100 protein antibody.

Fig 5.—Left, Dendritic cell stained with anti-human leukocyte antigen-DR antibody, indicating Langerhans' cells (×680). Right, Dendritic cells stained with anti-LN-3 antibody, indicating Langerhans' cells (×680).

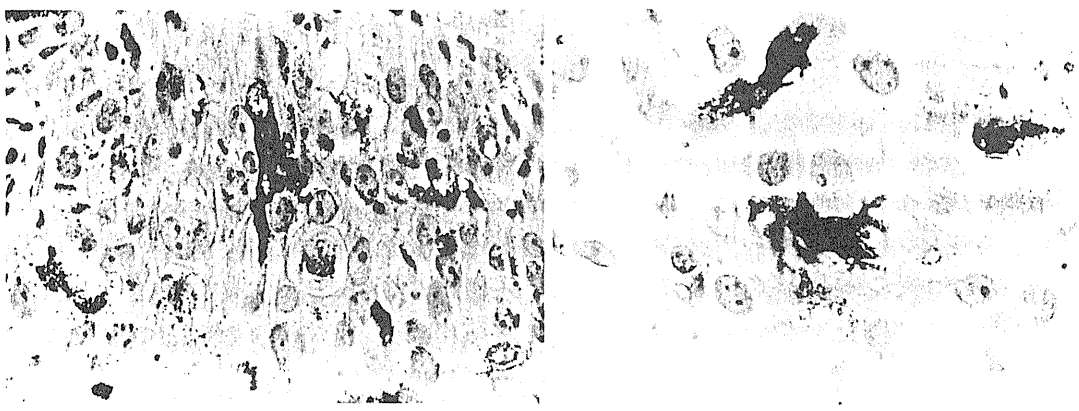

Table 3.—Distribution of Patients and Absolute Five-Year Survivals According to Grade of Langerhans' Cell (LC) Infiltration

Grade of LC Infiltration	Patients		Five-Year Survivals,
	No.	%	%
(++)	51	13.0	62.7
(+)	44	11.3	72.7*
(+ or ++)	95	24.3	67.4†
(−)	296	75.7	55.6
Total	391	100	58.7

*$P < .05$; $\chi^2 = 4.45$ against survival of grade (−) group.

†$P < .025$; $\chi^2 = 5.08$ against survival of grade (−) group.

Table 4.—Correlation Between Langerhans' Cell (LC) Infiltration and Clinical Stages

Grade of LC Infiltration	No. (%) of Patients				
	Stage I	Stage II	Stage III	Stage IV	Total
(++)	3	12	34	2	51
(+)	4	14	24	2	44
(++ or +)	7 (18)*	26 (31)	58 (27)	4 (8)†	95 (24)
(−)	33	58	158	47	296
Total	40	84	216	51	391

*The percentage of stage I patients with LC infiltration was slightly lower than that in stage II patients ($P = .1$).

†The percentage of stage IV patients with LC infiltration (grade [++] or [+]) was significantly lower than those of patients in all, stage II and stage III disease, $P < .05$.

Table 5.—Correlation Between Langerhans' Cell (LC) Infiltration and Histologic Subtype in Patients With Cervical Cancer

Grade of LC Infiltration	Histologic Subtypes							
	Keratinizing		Large Cell		Small Cell		Total	
	No.	%	No.	%	No.	%	No.	%
(++)	11	17.7	35	12.2	5	12.2	51	13.0
(+)	7	11.3	30	10.4	7	17.1	44	11.3
(−)	44	71.0	223	77.4	29	70.7	296	75.7

Table 6.—Absolute Five-Year Survivals According to the Grades of Langerhans' Cell (LC) Infiltration and Clinical Stages

LC Infiltration	Five-Year Survival Rates (%) In Stages*			
	I	II	III	IV
With infiltration	86 (6/7)	65 (17/26)	69 (40/58)†	50 (2/4)‡
Without infiltration	91 (30/33)	78 (45/58)	54 (86/158)	13 (6/47)
Total	90 (36/40)	74 (62/84)	58 (126/216)	16 (8/51)

*Numbers in parentheses indicate the number of patients dead of disease out of the total number of patients.

†Five-year survival rate of patients with LC infiltration was significantly higher than those without LC infiltration in stage III disease; $P < .05$.

‡$P < .05$ by χ^2 test against five-year survival rate of patients without LC infiltration in stage IV disease.

the clinical stages. No significant difference was found in the survival rate for the stages I and II between the patients with and without LC infiltrations. However, a statistically significant difference was observed between the stage III patients with and without the LC infiltrations ($P < .05$). There was also a significant difference between the two groups for stage IV by χ^2 test ($P < .05$), although it was not statistically significant by Peto's log-rank test because of a small number of the LC-positive patients. These two LC-positive patients are surviving more than nine years following radiotherapy, with no evidence of disease.

COMMENT

The LC infiltration in human cervical intraepithelial neoplasia has been described by a few investigators.[17,18] However, little is known of the quantitative assessment and prognostic significance of the LC infiltration. The purpose of this article was to analyze the relationship between the LC infiltration and the prognosis of the patients with carcinoma of the uterine cervix. This study seems to be of value because a substantial number of the patients who were treated with radiation therapy alone according to the same protocol were analyzed and, furthermore, all of them were followed-up for more than six years.

In our study, many LCs were found mainly in the intercellular space in cancer nests of the cervical carcinoma, whereas a few LCs were observed in the connective tissue surrounding cancer nests. These histologic findings were similar to those observed in the nasopharyngeal carcinomas showing squamous cell type microscopically.[12] However, the frequent infiltration of LCs was reported both in the cancer nests and in the surrounding connective tissue in the gastric cancer.[13] Hence, our findings and these reports suggested that the pattern of LC distribution in cancer lesion was different among the various cancers or between squamous cell carcinoma and adenocarcinoma.

Only 24% of the patients with cervical carcinoma showed a positive LC infiltration in this study, whereas the incidence in the squamous cell carcinomas of the lung and carcinomas of the nasopharynx were reported to be 57% (8/14) and 67% (6/9), respectively.[10,12] Accordingly, the incidence of the LC infiltration in squamous cell carcinoma of the cervix was lower than those in other sites. The ages and histologic subtypes had no influence on the incidence as in other reports.[12,13] Therefore, stimulation for the LC infiltration by cervical cancer may be lower than those by the other carcinomas, though the reason of the lower incidence is unclear.

This study showed significantly better prognosis in the patients with LC infiltration than those without it. This positive correlation to prognosis was observed especially in stage III and it was suggestive in stage IV patients, but not in stages I and II patients. Similarly, the positive correlation was reported in 38 patients with stage III gastric carcinomas.[13] However, in the 40 patients with stage I adenocarcinomas of the lung, the positive correla-

tion was also reported.[11] Therefore, the positive correlation is observed in different clinical stages according to various cancers. The reason for the absence of the prognostic difference in stages I and II disease in our study may be partially due to the good prognosis of these stages in our hospital (Table 2). That is, the superior local control ability of radiation therapy may hide the prognostic significance of LC infiltration in the early stages.

The increase in the LC infiltration in cervical neoplasia has suggested a specific immune response against the neoantigens.[17] Hence, the high incidence of the LC infiltration in stages II and III disease of this study may be related to a specific immune response against the cervical cancer. In contrast, the significantly low LC infiltration rate (8%) in stage IV cervical cancer in this study may suggest immunosuppression in the advanced stages as reported on various tumors.[26,27] Moreover, the evidence that two patients of four LC-positive patients in stage IV are surviving more than nine years may suggest that LC infiltration represent a positive immune response against cancer even in the advanced stage, though a further substantial study is needed for confirmation.

The patients with marked LC infiltration were described to have a better survival than those with slight LC infiltration in a small number of 14 nasopharyngeal carcinomas.[12] However, our study consisting of substantial patients showed no significant difference in prognosis between the grades (++) and (+). Our results may suggest that the positive LC infiltration is a preferable prognostic factor in advanced cervical cancer, regardless of the degree of LC infiltration.

Regarding the radiation sensitivity of LC, it has been reported that doses of 7.5 Gy had no effect on LC membrane markers on the guinea pig[28] and that LC alloantigen-presenting capacity had not totally disappeared after a single irradiation of 36 Gy.[29,30] This study showed that LC may play an important role with immunosuppressive irradiation of a large field encompassing all pelvic lymph nodes. Hence, it is suggested that LC is radioresistant[31] and LCs may be effective for the immune reaction even during the conventional radiotherapy.

This study indicated that the LC infiltration influenced the prognosis of the patients in advanced stages, especially in stage III, of carcinoma of the uterine cervix. This LC infiltration suggested a significant role of the host-defense mechanism against tumors.

We thank Muneyasu Urano, MD, Department of Radiation Medicine, Massachusetts General Hospital, Boston, for his assistance in the preparation of this manuscript; Hiroshi Ohtsu, MD, for his appropriate advice; Ryuzo Ohuchi and Tomoko Suzuki for their excellent technical assistance; and Mizuho Sakurai for her secretarial assistance.

References

1. Marcelus CJM, Blanken R, Nanninga J, et al: Defined in situ enumeration of T6 and HLA-DR expressing epidermal Langerhans cells: Morphologic and methodologic aspects. *J Invest Dermatol* 1986;87:698-702.

2. Murphy GF, Bhan AK, Sato S, et al: Characterization of Langerhans cells by the use of monoclonal antibodies. *Lab Invest* 1981;45:465-468.

3. Cocchia D, Michetti F, Donato R: Immunochemical localization of S-100 antigen in normal human skin. *Nature* 1981;294:85-87.

4. Stingl G, Tamaki K, Kats SI: Origin and function of epidermal Langerhans cells. *Immunol Rev* 1980;53:149-174.

5. Stephen IK, Kevin DC, Iijima M, et al: The role of Langerhans cell in antigen presentation. *J Invest Dermatol* 1985;85:96s-98s.

6. Nussenzweig MC, Steinman RM, Gutchinov B, et al: Dendritic cells and accessory cells for the development of antitrinitrophenyl cytotoxic T lymphocytes. *J Exp Med* 1980;152:1070-1084.

7. Klinkert WEFF, Labadie JH, Bowers WE: Accessory and stimulating properties of dendritic cells and macrophages isolated from various rat tissues. *J Exp Med* 1982;156:1-19.

8. Faure M, Frappaz A, Schmitt D, et al: Role of HLA-DR-bearing Langerhans cells and epidermal indeterminate cells in the in vitro generation of alloreactive cytotoxic T cells in man. *Cell Immunol* 1984;83:271-279.

9. Nakajima T, Watanabe S, Sato Y, et al: Immunohistochemical demonstration of S-100 protein in malignant melanoma and pigmented nevus, and its diagnostic application. *Cancer* 1982;50:912-918.

10. Watanabe S, Sato Y, Kodama T, et al: Immunohistochemical study with monoclonal antibodies on immune response in human lung cancer. *Cancer Res* 1983;43:5883-5889.

11. Furukawa T, Watanabe S, Kodama T, et al: T-zone histiocytes in adenocarcinoma of the lung in relation to postoperative prognosis. *Cancer* 1985;56:2651-2656.

12. Nomori H, Watanabe S, Nakajima T, et al: Histiocytes in nasopharyngeal carcinoma in relation to prognosis. *Cancer* 1986;57:100-105.

13. Tsujitani S, Furukawa T, Tamada R, et al: Langerhans cells and prognosis in patients with gastric carcinoma. *Cancer* 1987;59:501-505.

14. Smolle J, Soyer HP, Ehall R, et al: Langerhans cell density in epithelial skin tumors correlates with epithelial differentiation but not with the peritumoral infiltrate. *J Invest Dermatol* 1986;87:477-479.

15. McArdle JP, Knight GM, Halliday HK, et al: Quantitative assessment of Langerhans cells in actinic keratosis, Bowen's disease, keratoacantoma, squamous cell carcinoma and basal cell carcinoma. *Pathology* 1986;18:212-216.

16. Morris HHB, Gatter KC, Stein H, et al: Langerhans cell in human cervical epithelium: An immunohistological study. *Br J Obstet Gynaecol* 1983;90:400-411.

17. Morris HHB, Gatter KC, Sykes G, et al: Langerhans cell in human cervical epithelium: Effects of wart virus infection and intraepithelial neoplasia. *Br J Obstet Gynaecol* 1983;90:412-420.

18. McArdle JP, Muller HK: Quantitative assessment of Langerhans' cells in human cervical intraepithelial neoplasia and wart virus infection. *Am J Obstet Gynecol* 1986;154:509-515.

19. Annual report on the results of treatment in carcinoma of the uterus, vagina and ovary. Radiumhemmet, Sweden, 1976, vol 16: *FIGO.*

20. Poulsen HE, Taylor CW, Sobin LH: *Histological Typing of Female Genital Tract Tumors.* Geneva, World Health Organization, 1975, No. 13.

21. Taylor CR: An immunohistological study of follicular lymphoma, reticulum cell sarcoma and Hodgkin's disease. *Eur J Cancer* 1976;12:61-75.

22. Isaacson P, Wright DH, Judd MA, et al: Primary gastro intestinal lymphomas: A classification of 66 cases. *Cancer* 1979;43:1805-1819.

23. Kohler G, Milstein C: Continuous cultures of fused cells secreting antibody of predefined specificity. *Nature* 1975;256:495.

24. Marder RJ, Variakojis D, Silver J, et al: Immunohistochemical analysis of human lymphomas with monoclonal antibodies to B cell and Ia antigens reactive in paraffin sections. *Lab Invest* 1985;52:497-504.

25. Peto R, Pike MC, Armitage P: Design and analysis of randomized clinical trials requiring prolonged observation of each patient. *Br J Cancer* 1977;35:1-39.

26. Fujisawa T, Waldman SR, Yonemoto R: Leukocyte adherence inhibition by soluble tumor antigens in breast cancer patients. *Cancer* 1977;39:506-513.

27. Concannon JP, Dalbow MH, Davis W, et al: Immunoprofile studies for patients with bronchogenic carcinoma-III: Multivariate analysis of immune tests in correlation with survival. *Int J Rad Oncol Biol Phys* 1978;4:255-261.

28. Belsito DV, Baer RL, Thorbecke GJ, et al: Effect of glucocorticosteroids and gamma radiation on epidermal Langerhans cells. *J Invest Dermatol* 1984;82:136-138.

29. Breathnach SM, Katz SI: Effect of x-irradiation on epidermal immune function: Decreased density and alloantigen-presenting capacity of Ia+ Langerhans cells and paired production of epidermal cell-derived thymocyte activating factor (ETAF). *J Invest Dermatol* 1985;85:553-558.

30. Groh V, Meyer JC, Panizzon R, et al: Soft x-irradiation influences the integrity of Langerhans cells: A histochemical and immunohistochemical study. *Dermatologica* 1984;168:53-60.

31. Gallily R, Feldman M: The role of macrophages in the induction of antibody in x-irradiated animals. *Immunology* 1967;12:197-206.

Printed and Published in the United States of America

J. Jpn. Soc. Ther. Radiol. Oncol. 1: 165-170, 1989

MODIFICATION OF TUMOR RADIOSENSITIVITY IN MICE BY N-METHYLFORMAMIDE

Mayumi IWAKAWA*1,2, Koichi ANDO*1, Sachiko KOIKE*1
and Hideyo TAKAHASHI*2

(*Received 23 March 1989, accepted 7 June 1989*)

Abstract N-methylformamide (NMF) is a known maturation agent, capable of inducing in vitro neuroblastoma differentiation. In this paper, the radiosensitizing effects of NMF on an in vitro murine neuroblastoma were investigated. A/J mice bearing i. m. C-1300 tumors were treated i. p. with NMF daily for 6 days. NMF administered at a dosage of 300 mg/kg significantly inhibited tumor growth. NMF treatment alone inhibited growth of a 300 cu. mm tumor for 12.5 days, comparable to the effects of 22.5 Gy gamma irradiation. When irradiation and NMF treatment were combined, the effect was more than additive, particularly at higher irradiation doses. These results suggest that NMF may be useful as an irradiation modifier for the clinical treatment of neuroblastoma.

Key words: N-methylformamide, Maturation agent, Neuroblastoma, Radiosensitizer

INTRODUCTION

Neuroblastoma is one of the most common solid tumors of infancy and childhood, accounting for 7% of all childhood cancers diagnosed each year and 15% of all cancer deaths among children worldwide[1]. Clinical observations indicate that neuroblastomas are relatively radiosensitive [1-4]. Local radiotherapy is frequently used for primary tumors, bone metastases, soft tissue masses, and the hepatic infiltration of neuroblastoma. Recent investigations have used total body irradiation and supralethal chemotherapy followed by bone marrow reconstitution. The development and use of radiation modifiers is expected to help prevent radiation damage to normal tissue and facilitate total cancer cure.

The polar solvent N-methylformamide (NMF)[5,6] is currently being evaluated as an anti-neoplastic agent by the National Cancer Institute (NCI) in the US[7]. The pharmacology and pharmokinetics of NMF have been investigated in mice and in humans[8-11]. Results from pre-clinical studies suggest that NMF has radiosensitizing, chemosensitizing and differentiating effects, depending on tumor type[5,6,12,13]. NMF is also known to act as a maturational agent, capable of inducing the differentiation of neuroblastomas in vitro[13]. Here, we investigate the radiosensitizing effects of NMF on the C-1300 neuroblastoma grown as a solitary tumor in isogeneic mice.

MATERIALS AND METHODS

Mice

Inbred female A/J mice, bred and maintained in our own specific pathogen-free mouse colony. Mice were 8-10 weeks old at the beginning of the experiments, and housed 5-6 to a cage during the experiments.

岩川 真由美, 安藤 興一, 小池 幸子, 高橋 英世
*1 Division of Clinical Research, National Institute of Radiological Sciences, 9-1, Anagawa 4-chome, Chiba-shi 260, Japan.
*2 Department of Pediatric Surgery, the Chiba University.

Tumor

Experiments were performed using C-1300 in vivo tumor cells[14], which can be readily transplanted to mice. The tumors were prepared by 0.1% trypsin-pancreatin digestion of non-necrotic tumor tissue, which ensures over 90% cell viability. 5×10^5 cells were transplanted i. m. to the right hind leg of mice.

Treatment

For local tumor irradiation, mice were anesthetized and immobilized using tape, with the leg tumor (size: 8.5–9.0 mm) situated in the middle of the irradiation field to insure homogenous dose distribution. Irradiation was performed using a single Cs-137 unit (FSD: 21 cm, 1.9 Gy/min).

NMF (Aldrich) was dissolved in phosphate-buffered saline and injected i. p. in a volume equal to 0.01 m*l*/g body weight. Based on the clinical trial schedule of NCI[13], 300 mg/kg of NMF was administered for 6 consecutive days beginning when the tumor measured 9.0–9.5 mm in diameter.

Tumor growth (TG) time assay

Three diameters of each tumor (a, b and c) were measured with a caliper three times a week after treatments. Tumor volume was calculated by the formula π abc/6.

Using software developed by S. Satoh in our lab[15], the time for each tumor to reach 5 times its initial tumor volume was determined by linear regression analysis. The time required for half the tumors to reach 5 times the initial tumor volume was calculated by probit analysis, and designated TG time.

RESULTS

Fig. 1 shows the effects of six daily injections of NMF (300 mg/kg i. p.) on the growth of C-1300 tumors. NMF treatment diminished C-1300 tumors and delayed growth by approximately 13 days. The outcome is comparable to subjecting this specific tumor to 22.5 Gy of gamma ray irradiation.

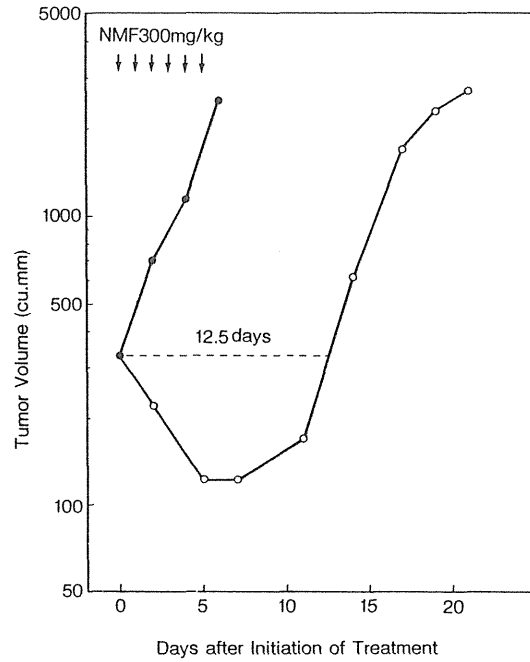

Fig. 1. Growth of C-1300 leg tumors in mice untreated (●) or treated with NMF (○).

To determine the radiosensitizing effects NMF, C-1300 leg tumors were irradiated with 5, 10, 15, 22.5 or 30 Gy on the fourth day of a six-day series of daily NMF injections (300 mg/kg). Tumors ranged in size from 9.0–9.5 mm at the beginning of NMF treatment, and shrunk down to 8.5 mm at the time of irradiation. NMF treatment enhanced irradiation-induced growth delay (Fig. 2). Irradiation doses of 10 Gy and 22.5 Gy increased TG time by 5.2 days and 12.8 days, respectively. Supplementary NMF injections significantly prolonged the duration of this tumor growth retardation; in the case of 30 Gy irradiation, tumor growth was inhibited for 40 days. As shown in Fig. 3, the result of combining NMF with irradiation produces more than an additive effect, especially at the higher irradiation doses.

NMF treatment diminished the size of primary tumors but could not control spontaneous metastasis. Mice treated with NMF and an irradiation dose of 22.5 Gy or over exhibited complete remission of the primary

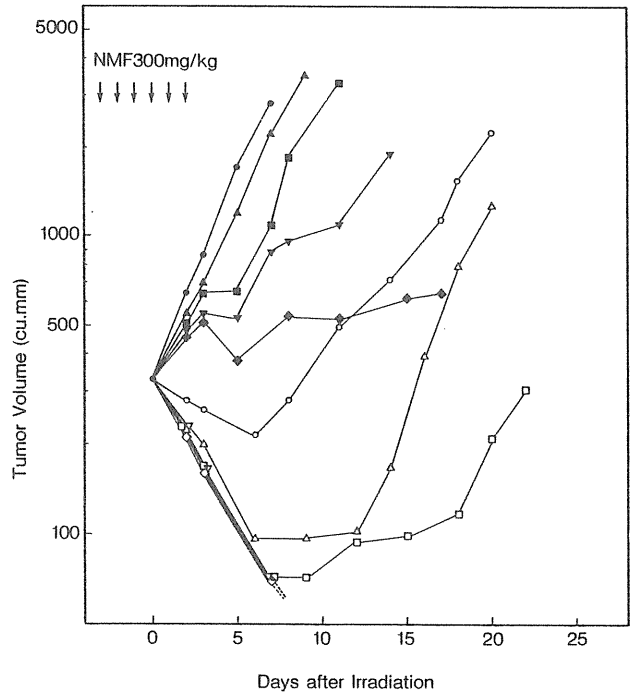

Fig. 2. Growth of C-1300 leg tumors in mice treated with 5 Gy (●), 10 Gy (▲), 15 Gy (■), 22.5 Gy (▼), 30 Gy (◆), 5 Gy plus NMF (○), 10 Gy plus NMF (△), 15 Gy plus NMF (□), 22.5 Gy plus NMF (▽), or 30 Gy plus NMF (◇). NMF (300 mg/kg) was given i.p. 3 times before and 3 times after irradiation when tumors had grown to 8.5 mm in diameter.

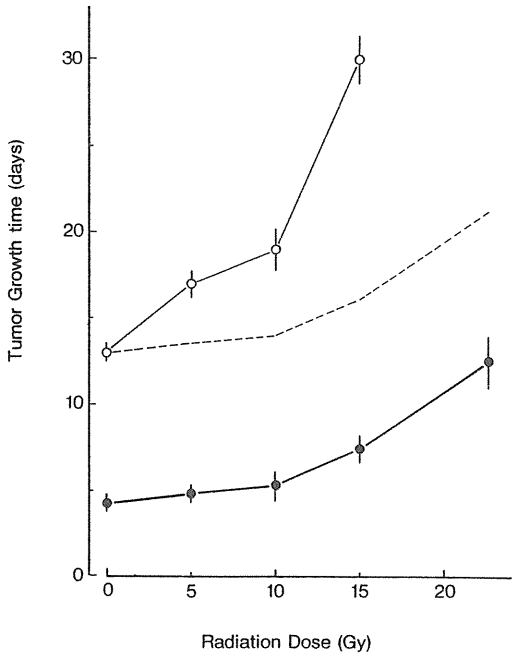

Fig. 3. Relationship between radiation dose and tumor growth (TG) time. Closed (●) and open (○) circles represent radiation alone and radiation plus NMF, respectively. Mean and 95% confidence intervals calculated from data shown in Fig. 2. Dotted line is a theoretical dose-response curve representing independent action for NMF and radiation.

tumor, but died from metastases. It was impossible to complete a TCD-50 assay using this C-1300 experimental model.

DISCUSSION

NMF is a planar, polar compound that has demonstrated both cytostatic/cytotoxic and differentiating activity in vitro[13,16]. The National Cancer Institute (NCI) decided to evaluate NMF as an anti-neoplastic agent based on preclinical screening data indicating that NMF has substantial antitumor activity against human colon, lung and mammary tumor xenografts implanted beneath the renal capsule in athymic mice[7]. Elsewhere, we reported the effect of NMF and ionizing radiation on an in vivo FSA murine tumor and its pulmonary metastasis[5]. We also determined the acute radioresponse of normal tissues in mice receiving systemic NMF administrations. NMF administered in a dosage of 300 mg/kg for 8 days had little direct effect on FSA tumor growth, but it enhanced the growth-inhibiting action of ionizing radiation with dose enhancement factors ranging from 1.5 to 1.7. NMF also enhanced the lethal effect of radiation against FSA micrometastases[5]. NMF combined with radiation therapy promoted the formation of endogenous spleen colonies but had no effect on the LD50/30, or on the survival rate of jejunal crypt cells and spermatogonia. These data indicate that NMF increased the radiosensitivity of the FSA tumor and its metastases without increasing the radioresponse of the normal tissues tested.

In this report, we have shown that NMF has a strong inhibitory effect on the growth of murine neuroblastomas. NMF completely inhibited the growth of 9-mm C-1300 murine tumors during treatment (Fig. 1). Previous studies have shown that NMF exhibits antitumor activity against small-sized tumors[12]. The current study shows that NMF can also have significant effect against large-sized C-1300 tumors. It is known that NMF inhibits tumor growth differently for different tumors[17]. The current study suggests that neuroblastoma may be a good candidate for treatment by NMF.

It is important to consider possible mechanisms by which NMF exerts its radiosensitizing effect. There are several views on NMF activity. First, NMF might effect the structure of chromatin, making it more sensitive to radiation. The effects of NMF on radiation-induced DNA damage and repair in vitro were investigated using the alkaline elution assay[18]. DNA-protein crosslinks (DPCs) increased linearly as a function of increasing gamma-ray dose. NMF increased the variety of gamma-ray-induced DNA lesions. This enhancement of radiation-induced DPCs suggests that NMF modifies the relationship between DNA and chromatin protein.

Second, Cordeiro and Savarese suggested that NMF-mediated radiosensitization in clone A cells might be due to the depletion of glutathione (GSH)[19]. However, Arundel did not observe glutathione depletion in either clone A or HCA-1 cells[21]. Further investigations should clarify the subject. Third, NMF may sensitize hypoxic cells. Leith found that daily injections of NMF could eliminate hypoxic cells from HCY-15 tumors[20]. This may explain the NMF-mediated radiosensitization of solid tumors. Arundel observed that NMF-induced cytotoxic effects occurred selectively on hypoxic cells[21]. The pleiotropic nature of NMF accounts for these three different views, and should be investigated further to better elucidate NMF's mechanism of action.

One might expect a TCD50 assay would more accurately reveal the modifying effect of NMF on radiation treatment. We attempted a TCD50 assay but could not complete it due to the death of mice during the experiment. Mice irradiated with doses of over 35 Gy died from liver metastases even when the primary tumor was cured. NMF-treated mice lived longer than mice treated with irradiation alone, but there was no significant difference in survival rate. Bennett observed

increased metastatic capacity in murine melanoma following the induction of differentiation[21]. Low or high levels of differentiation were generated by culturing at either low or high extracellular pH in the presence of melanocyte-stimulating hormone. Metastatic capacity was determined from colonizations of the lung following i.v. injection in mice. Takenaga reported the enhanced metastatic potential of cloned Lewis carcinoma cells (P-29) following treatment in vitro with dimethly sulfoxide (DMSO)[22]. The enhanced lung-colonizing ability of P-29 cells treated with DMSO, a polar solvent, is due to increased adhesiveness, resulting in arrest and retention in the lung of the host, and degradative enzyme activities. We reported, however, that NMF could reduce metastases which had already been established at the time of NMF administration[20]. It is not known whether NMF has a beneficial effect on the process of metastasis similar to its effect on primary tumor growth. We are currently attempting to determine the mechanism of radiosensitization and antimetastatic activity of NMF.

REFERENCES

1) D'Angio, G. J. and Evans, A. E.: Cyclic, low-dose total body irradiation for metastatic neuroblastoma. *Int. J. Radiat. Oncol. Biol. Phys.* **9**: 1961-1965, 1983.
2) Wheldon, T. E., O'Donoghue, J., Gregor, A. et al.: Radiobiological considerations in the treatment of neuroblastoma by total body irradiation. *Radiother. and Oncol.* **6**: 317-326, 1986.
3) Kun, L. E., Casper, J. T., Kline, R. W. and Piaskowski, V. D.: Fractionated total body irradiation for matastatic neuroblastoma. *Int. J. Radiat. Oncol. Biol. Phys.* **7**: 1599-1620, 1981.
4) Halperin, E. C. and Cox, E. B.: Radiation therapy in the management of neuroblastoma. The Duke University medical center experience 1976-1984. *Int. J. Radiat. Oncol. Biol. Phys.* **12**: 1829-1837, 1986.
5) Iwakawa, M., Milas, L., Hunter, N. and Tofilom, P. J.: Modification of tumor and normal tissue radioresponse in mice by N-methylformamide. *Int. J. Radiat. Oncol. Biol. Phys.* **13**: 55-60, 1987.
6) Arundel, C., Bock, S., Brock, W. A. and Tofilon, P. J.: Radiosensitization of primary human tumor cell cultures by N-methylformamide. *Int. J. Radiat. Oncol. Biol. Phys.* **13**: 753-757, 1987.
7) National Cancer Institute Clinical Brochure: N-methylformamide (NMF). Bethesda, MD., National Cancer Institute, NSC 3051, June, 1982.
8) Gescher, A., Gibson, N. W., Hickman, J. A. *et al.*: N-methylformamide: Antitumor activity and metabolism in mice. *Br. J. Cancer* **45**: 843-850, 1982.
9) Brindley, C., Gescher, A., Harpur, E. S. *et al.*: Studies of the pharmacology of N-methylformamide in mice. *Cancer Treat. Rep.* **66**: 1957-1965, 1982.
10) Threadgill, M. D., Axworthy, D. B., Baillie, T. A. *et al.*: Metabolism of N-methylformamide in mice: Primary kinetic deuterium isotope effect and identification of S-(N-methycarbamoyl) glutathione as a metabolite. *J. Pharmacol. Exp. Ther.* **242**: 312-319, 1987.
11) Rowinsky, E. K., Noe, D. A., Orr, D. W. *et al.*: Clinical pharmacology of oral and i.v. N-methylformamide: a pharmacologic basis for lack of clinical antineoplastic activity. *J. Natl. Cancer Inst.* **80**: 671-678, 1988.
12) Leith, J. T., Lee, E. S., Vayer, A. J. *et al.*: Enhancement of the response of human colon adenocarcinoma cells to X-irradiation and cis-platinum by N-methylformamide (NMF). *Int. J. Radiat. Oncol. Biol. Phys.* **11**: 1971-1976, 1985.
13) Clagett-Carr, K., Sarpsy, G., Plownan, J. *et al.*: N-methylformamide: Cytotoxic, Radiosensitizer, or Chemosensitizer. *J. Clin. Oncol.* **6**: 906-918, 1988.
14) Pons, G., O'Dea, R. F. and Mirkin, B. L.: Biological characterization of the C-1300 murine neuroblastoma: An in vivo neural crest tumor model. *Cancer Res.* **42**: 3719-3723, 1982.
15) Satoh, S., Koike, S. and Ando, K.: A standard software for tumor growth delay assay. National Institute for Radiological Sciences Annual Report ISSN 0439-5956 NIRS-27, p. 80, 1988.
16) Collins, S. J., Ruscetti, F. W., Gallagher, R. E., and Gallo, R. C.: Terminal differentiation of human promyelocytic leukemia cells induced by dimethyl sulfoxide and other polar solvents. *Proc. Natl. Acad. Sci. U. S. A.* **75**: 2458-2462, 1978.
17) Iwakawa, M., Tofilon, P. J., Hunter, N. *et al.*: Antitumor and antimetastatic activity of the differentiating agent N-methylformamide in murine tumor systems. *Clin. Expl. Metastasis* **5**: 289-300, 1987.

18) Arundel, C. M., Tofilon, P. J.: Enhancement of radiation-induced DNA-protein crosslinking by N-methylformamide. *Radiat. Res.* **110**: 294-304, 1987.
19) Cordeiro, R. F. Savarese T. M.: The role of glutathione depletion in the mechanism and action of N-methylformamide and N, N-dimethylformamide in a cultured human colon carcinoma cell line. *Cancer Res.* **46**: 1297-1305, 1986.
20) Leith, J. T.: Modification of the hypoxic fraction of a xenografted human colon tumor by differentiation-inducing agents. *J. Natl. Cancer Inst.* **80**: 444-447, 1988.
21) Bennett, D. C., Dexter, T. J., Ormerod, E. T. *et al.*: Increased experimental metastatic capacity of a murine melanoma following induction of differentiation. *Cancer Res.* **46**: 3239-3244, 1986.
22) Takenaga, K.: Enhanced metastatic potential of cloned low-matastatic Lewis lung carcinoma cells treated in vitro with dimethyl sulfoxide. *Cancer Res.* **44**: 1122-1127, 1984.

要旨：N-methylformamide（NMF）は，分化誘導剤の一つであり，既に in vitro において，神経芽腫の分化を促すことが報告されている．今回我々は，マウス神経芽腫に対する放射線療法における，NMF の放射線増感作用につき検討を加えた．A/J マウスの大腿部に移植した C-1300 腫瘍に NMF を 6 日間腹腔内投与した．この NMF 300 mg/kg 連続投与は，300 cu. mm 体積の腫瘍に対して増殖抑制作用を示し，12.5 日の growth delay をもたらした．この効果は，本腫瘍に対する 22.5 Gy の γ 線照射に匹敵する．NMF と放射線との併用効果は相加作用以上の結果となり，神経芽腫の集学的治療に於ける NMF の，放射線療法の増感剤としての臨床的有効性が示唆された．

Synthesis and evaluation of ^{11}C-PK 11195 for *in vivo* study of peripheral-type benzodiazepine receptors using position emission tomography

Kenji HASHIMOTO, Osamu INOUE, Kazutoshi SUZUKI,
Toshiro YAMASAKI and Masaharu KOJIMA

Reprint from Annals of Nuclear Medicine Vol. 3 No. 2
July 1989

Annals of Nuclear Medicine Vol. 3, No. 2, 63-71, 1989

Synthesis and evaluation of ^{11}C-PK 11195 for *in vivo* study of peripheral-type benzodiazepine receptors using position emission tomography

Kenji HASHIMOTO,* Osamu INOUE,** Kazutoshi SUZUKI,**
Toshiro YAMASAKI** and Masaharu KOJIMA***

**Department of Radiopharmaceutical Chemistry, Faculty of Pharmacy & Pharmaceutical Sciences, University of Fukuyama*
***Division of Clinical Research, National Institute of Radiological Sciences*
****Department of Radiopharmaceutical Chemistry, Faculty of Pharmaceutical Sciences, University of Kyushu*

The biodistribution of ^{3}H-PK 11195, an antagonist of the peripheral-type benzodiazepine receptors, was studied in mice. High accumulations of radioactivity in the heart, lung, spleen, kidney and adrenal were observed after intravenous injection of tracer amounts of ^{3}H-PK 11195 into the mice. The radioactivity in the heart, lung, spleen, kidney and adrenal was significantly decreased by the coadministration of carrier PK 11195, which indicated that PK 11195 specifically binds to the receptors. No radioactive metabolites were observed in the heart, lung and brain 20 min after intravenous administration of ^{3}H-PK 11195. The accumulation of ^{3}H-PK 11195 in the lung was not affected by pretreatment with either α-methyl benzylamine or imipramine, suggesting that ^{3}H-PK 11195 specifically binds to the receptors. The ratios of radioactivity of the kidney, adrenal and spleen to blood increased as a function of time, whereas that of the lung and heart rapidly reached to a steady state. ^{11}C-PK 11195 was synthesized by the N-methylation of desmethyl precursor yielding more than 100 mCi with high specific activity (more than 1.4 Ci/μmol). The labeling and purification procedure was completed within 23 min after the end of bombardment (EOB). The ^{11}C-PK 11195 solution for injection seems to have a high potential for the *in vivo* study of the peripheral-type benzodiazepine receptors in the living human by means of positron emission tomography (PET).

Key words: PK 11195, Peripheral-type benzodiazepine receptor, Positron emission tomography, *In Vivo* binding, Carbon-11

INTRODUCTION

In vivo studies of the central-type benzodiazepine receptors in the living human brain using positron emission tomography (PET) have recently been reported.[1-5] Benzodiazepine receptors are classified as central-type or peripheral-type on the basis of on their relative affinities for clonazepam and Ro 5-4864[7-chloro-1,3-dihydro-1-methyl-5-(p-chlorophenyl)-2H-1, 4-benzodiazepin-2-one].[6] The results of a thermodynamic analysis indicated that PK 11195 [1-(2-chlorophenyl)-N-methyl-N-(1-methylpropyl)-3-isoquinoline carboxamide] might be an antagonist and Ro 5-4864 an agonist at the peripheral-type benzodiazepine receptors.[7] ^{3}H-Ro 5-4864 and ^{3}H-PK 11195 have been used to identify, characterize and localize the peripheral-type benzodiazepine receptors in the peripheral organs as well as in the central nervous system.[7-12] In the brain, high densities of

Received February 22, 1988; revision accepted September 29, 1988.

For reprints contact: Kenji Hashimoto, Department of Radiopharmaceutical Chemistry, Faculty of Pharmacy & Pharmaceutical Sciences, University of Fukuyama, 985 Higashimura-cho, Fukuyama 729-02, Japan

peripheral-type benzodiazepine receptors have been observed in the choroid plexus, ependyma and olfactory bulb.[11,13-15] Recently, high accumulations of ^{3}H-PK 11195 in the transplanted glioma in the rat were reported.[16] In the periphery, high concentrations of the peripheral-type benzodiazepine receptors have been reported in several organs including the kidney, nasal epithelium, lung, heart and endocrine organs such as the adrenal, testis and pituitary gland.[17-20] Although the precise physiological function of the peripheral-type benzodiazepine receptors is still unclear, several laboratories have reported interaction between these receptors and calcium channels in the heart[21-23] or anion transport system in the kidney.[24] And changes in the density (Bmax) of the peripheral-type benzodiazepine receptors in the kidney following pretreatment with diuretic furosemide have recently been reported.[24]

In a previous paper, we reported that ^{3}H-PK 11195 had a high potential as a radiotracer for the *in vivo* study of the peripheral-type benzodiazepine receptors.[25] In the present paper, we studied in more detail the biodistribution and *in vivo* stability of ^{3}H-PK 11195 in mice. In order to determine whether a high accumulation of ^{3}H-PK 11195 in the lung was due to the specific binding with receptors or to linked to the active transport system for basic amines, the effects of basic amines on the lung uptake of ^{3}H-PK 11195 were also examined. Finally, a high specific activity ^{11}C-PK 11195 solution for injection was prepared for the *in vivo* study of the peripheral-type benzodiazepine receptors in man with PET.

MATERIALS AND METHODS

1. Materials

^{3}H-PK 11195 (87 and 90 Ci/mmol) was obtained from New England Nuclear, Boston, MA, USA. PK 11195 and desmethyl PK 11195 were donated by Dr. G. Le Fur (Pharmuka Laboratories, Gennevillers, France). Paraquat (Sigma, St Louis, MO, USA), 6-hydroxydopamine hydrobromide (Sigma) and furosemide (WACO Pure Chemical Industries Ltd.,) were used. Other chemicals were purchased commercially.

2. Distribution of radioactivity in mice after intravenous administration of ^{3}H-PK 11195

In this study, male ddy mice (30–35 g) were used. Two-tenths mL of ^{3}H-PK 11195 solution (1 μCi) was intravenously injected into the mice, which were then killed by decapitation at 1, 5, 10 and 20 min after injection of the tracer. The blood, heart, lung, liver, spleen, kidney, adrenal and brain were removed and weighed, each sample being incinerated with a sample oxidizer (Aloka, ACS-113) and the percentage of injected dose per gram tissue (% dose/g) in each sample was determined with a liquid scintillation counter (Aloka, LSC-1000).

In the carrier-added experiment, two-tenths mL of ^{3}H-PK 11195 (1 μCi, 5 mg/kg) was intravenously injected into the mice, and the radioactivity in the tissues was determined as described above. The solution for injection of ^{3}H-PK 11195 (5 mg/kg) was a 10% emulsion with Nikkol HCO 40 (emulsifier, Nikko Chemicals, Tokyo).

3. In vivo competitive inhibition of specific binding by carrier PK 11195

Two-tenths mL of ^{3}H-PK 11195 solution (0.1, 10, 30, 100, 300 and 1000 μg/kg, ca. 1 μCi) was intravenously injected into the male ddy mice (30–35 g), which were then killed by decapitation at 5 min after injection. The radioactivity in the blood, heart, lung and brain was determined as described above. Various doses of ^{3}H-PK 11195 solution were prepared by diluting 10% emulsion with Nikkol.

4. In vivo stability of ^{3}H-PK 11195 in the mice

About 12 μCi of ^{3}H-PK 11195 was intravenously injected into the male ddy mouse. Twenty min after injection of the tracer, the mouse was killed by decapitation, and the heart, lung and brain were quickly removed. Each organ was homogenized with 1 mL of saline, and 100 μL of the homogenate was sampled as a standard for the determination of extraction efficiency. One mg of carrier PK 11195 and 400 μL of ethyl acetate were added to the 400 μL of the homogenate, then radioactive materials were extracted. Extraction efficiencies in the heart, lung and brain determined by comparison with the standard were more than 95, 95 and 90% respectively. Organic extractable materials were analyzed by thin-layer chromatography (TLC, silicagel; chloroform: methanol= 95: 5, Rf value=0.48, chloroform: diethyl ether: hexane=1: 1: 1, Rf value=0.16).

5. Effects of basic amines on the lung uptake of ^{3}H-PK 11195

α-Metyl benzylamine (1 and 10 mg/kg) and imipramine (25 mg/kg) were intraperitoneally injected into the male ddy mice. Two-tenths mL of ^{3}H-PK 11195 (1 μCi) was intravenously injected into the mice 10 min after pretreatment with these amines. The radioactivity in the blood, heart, lung and brain 5 min after injection of the tracer was determined as described above. α-Metyl benzylamine hydrochloride and imipramine hydrochloride solutions for injection were diluted with distilled water in a volume of 0.1 mL/10 g body weight.

6. Effect of various drugs on the biodistribution of ^{3}H-PK 11195 in the mice.

Two-tenths mL of ^{3}H-PK 11195 solution (1 μCi) was

intravenously injected into the male C3H mice 2 days after intraperitoneal administration of paraquat (30 mg/kg), which were than killed by decapitation 5 min after injection of the tracer. The blood, heart, lung, adrenal and brain were removed and the radioactivity in each sample was determined as described above.

Two-tenths mL ^{3}H-PK 11195 (1 μCi) was intravenously injected into the male C3H mice 1 week after the second injection of 6-hydroxydopamine (50 mg/kg/day×2, i.v.) or vehicle. The radioactivity in the blood, heart, lung, kidney, adrenal and brain 5 min after injection of the tracer was determined as described above.

Two-tenths mL of ^{3}H-PK 11195 (1 μCi) was intravenously injected into the male ddy mice 6 hr after the last injection of furosemide (50 mg/kg/day×5, i.p.) or vehicle (5% Tween-80 suspension in saline). The radioactivity in the blood, heart, lung, liver, spleen, kidney, adrenal and brain 5 min after injection of the tracer was determined as described above.

7. Preparation of ^{11}C PK 11195 solution for injection

^{11}C-Methyl iodide was prepared as described previously.[26] ^{11}C-PK 11195 was synthesized by the alkylation of the desmethyl precursor with ^{11}C-methyl iodide in dimethylformamide solution (DMF: DMSO: NaH=350: 150: 15, 500 μL) at room temperature for 1 min, and purified by preparative high performance liquid chromatography (HPLC) (Megapack SIL C18-column, 7.2×250 mm, JASCO, Tokyo, Japan) eluting with a solvent (acetonitrile: 0.01 M ammonium acetate: phosphoric acid=70.9: 29.1: 0.05) at a flow rate of 6 mL/min. The radioactive peak corresponding to PK 11195 was corrected in a sterile flask containing 150 μL of Tween-80, evaporated to dryness in a rotary evaporator and dissolved in 10 mL of saline with 80 μL of ethyl alcohol filtered through a 0.22 μm Milex filter. Radiochemical purity and specific activity of the ^{11}C-PK 11195 solution were determined by analytical HPLC (Finepack SIL, C18-column, acetonitrile: 0.01M ammonium acetate: phosphoric acid=195: 65: 0.125) at a flow rate of 3 mL/min.

RESULTS

As shown in Table 1, high accumulations of radioactivity in the heart, lung, spleen, kidney and adrenal after intravenous administration of ^{3}H-PK 11195 were observed. A moderate accumulation of radioactivity in the brain after injection of the tracer was also observed. The time courses of radioactivity in the heart, lung and brain rapidly decreased, whereas increases in radioactivity in the spleen, kidney and adrenal were observed. The half-lives of radioactivity in the heart and lung were almost the same as that of radioactivity in the blood, which indicated that the tracer kinetics rapidly reached a steady state after intravenous administration.

In the carrier-added experiment, the radioactivity in the heart, lung, spleen, kidney and adrenal were much less than in the carrier-free state, as shown in Table 2. The biodistributions of radioactivity in the blood, heart, lung and brain 5 min after intravenous administration of various doses of ^{3}H-PK 11195 are summarized in Fig. 1. The radioactivity in the heart and lung was significantly decreased in a dose dependent manner, whereas the radioactivity in the blood and brain was unchanged by the coadministration of carrier PK 11195.

Thin-layer chromatograms of radioactive materials in the heart, lung and brain 20 min after intravenous administration of ^{3}H-PK 11195 indicated that almost all of the radioactivity in the heart, lung and brain was due to unmetabolized PK 11195 (Fig. 2).

The effects of α-methyl benzylamine (1 and 10 mg/kg) and imipramine were examined in order to determine whether the high accumulation of ^{3}H-PK 11195 in the lung was due to the specific binding with the receptors or linked to the amine uptake system.

Table 1 Distribution of radioactivity in mice after intravenous administration of ^{3}H-PK 11195.

(% dose/g)

	Control			
	1 min	5 min	10 min	20 min
Blood	5.60±0.22	2.02±0.18	1.43±0.25	0.939±0.08
Heart	28.67±3.16	20.00±2.23	14.11±0.87	10.52±0.87
Lung	72.25±13.6	32.00±7.39	22.21±3.08	13.63±2.69
Liver	3.32±0.31	6.03±1.03	7.36±0.52	7.81±1.14
Spleen	5.23±1.61	10.79±2.11	10.77±0.42	10.91±1.50
Kidney	14.02±3.82	19.52±1.11	19.88±0.57	19.72±1.93
Adrenal	40.50±15.6	61.08±15.9	82.84±14.5	100.2±23.6
Brain	4.14±0.34	2.33±0.16	1.45±0.10	1.09±0.18

Three mice in each group; average±1 SD

Table 2 Distribution of radioactivity in mice after intravenous administration of carrier-added ^{3}H-PK 11195 (% dose/g)

	Carrier-added (5 mg/kg)			
	1 min	5 min	10 min	20 min
Blood	2.74±0.21	1.60±0.07	1.09±0.02	0.709±0.10
Heart	8.30±0.52	2.80±0.27	1.65±0.15	0.996±0.03
Lung	3.91±0.46	2.71±0.26	1.90±0.20	1.33±0.17
Liver	5.91±1.91	12.77±0.51	11.25±1.22	7.03±0.39
Spleen	2.23±0.30	1.89±0.16	1.33±0.14	0.991±0.05
Kidney	10.10±0.61	4.70±0.11	3.97±0.16	3.25±0.28
Adrenal	52.88±4.96	18.35±3.48	18.24±5.34	16.97±6.91
Brain	5.01±0.22	2.16±0.19	0.963±0.13	0.398±0.03

Three mice in each group; average±1 SD

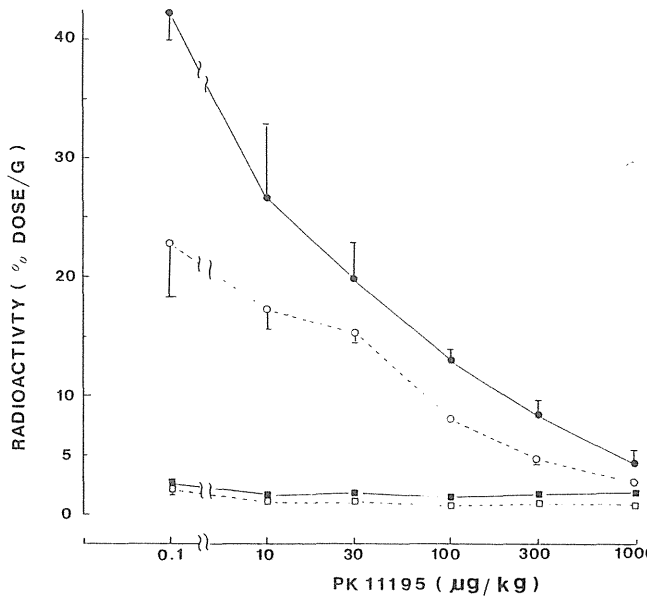

Fig. 1 *In vivo* competitive inhibition of specific binding by carrier PK 11195. The radioactivity in the heart (○···○), lung (●—●), brain (■—■) and blood (□···□) was expressed as percentage pet gram organs (% dose/g) as described in Materials and Methods. Values are presented as the average±1 SD for three mice of each point.

As shown in Table 3, the uptake of ^{3}H-PK 11195 in the lung as well as the other organs 5 min after injection of the tracer was not significantly changed by pretreatment with these basic amines. Further, we studied the effects of paraquat, which was used as an animal model of the lung damage,[27,28] neurotoxin 6-hydroxydopamine and diuretics furosemide on the biodistribution of ^{3}H-PK 11195 in the mice after injection of the tracer. No significant changes in the biodistribution of ^{3}H-PK 11195 were found following pretreatment with these drugs, as shown in Table 4.

^{11}C-PK 11195 was synthesized by the alkylation of N-desmethyl PK 11195 with ^{11}C-methyl iodide (Fig. 3) (29), and purified by radio-UV HPLC (Fig. 4) yielding more than 100 mCi of ^{11}C-PK 11195 solution. The labeling and purification procedure was completed within 23 min after the end of bombardment (EOB). The radiochromatogram of the ^{11}C-PK 11195 solution is shown in Fig. 5. Radiochemical purity was more than 99.9%, and specific activity of the ^{11}C-PK 11195 solution was determined to be more than 1.4 Ci/μmol by radio-HPLC.

DISCUSSION

The *in vivo* mapping of various receptors in the brain and heart in the intact human with PET has recently

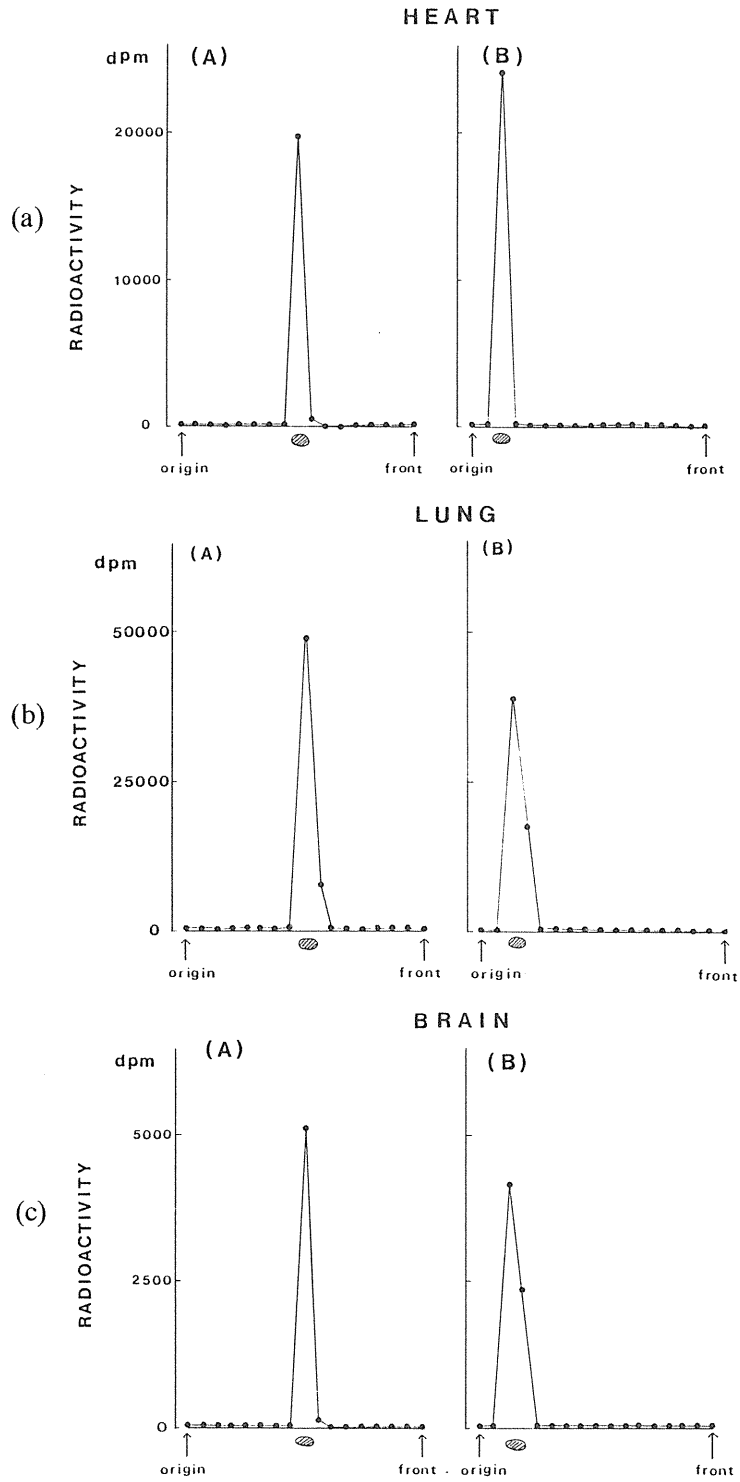

Fig. 2 Thin-layer chromatograms of radioactive materials in the heart, lung and brain removed 20 min after intravenous administration of ^{3}H-PK 11195 (12 μCi) into the mouse. ▨: Cold PK 11195 detected by u.v. lump. Solvent system; (A), chloroform: methanol=95: 5, Rf value=0.48 (B), chloroform: diethyl ether: hexane=1: 1: 1, Rf value=0.16

Table 3 Effects of basic amines on the distribution of radioactivity in mice at 5 min after intravenous administration of ^{3}H-PK 11195

(% dose/g)

	Blood	Heart	Lung	Brain
Control	1.35±0.21	16.58±1.92	34.47±8.39	1.91±0.33
α-Methyl Benzylamine (1 mg/kg)	1.66±0.45	17.55±2.28	37.52±2.23	2.02±0.34
α-Methyl Benzylamine (10 mg/kg)	1.67±0.03	15.59±1.39	29.46±5.89	1.86±0.17
Imipramine (25 mg/kg)	1.44±0.14	16.52±2.95	33.41±10.86	1.81±0.27

Three mice in each group; average±1 SD
α-Methyl benzalamine (1 and 10 mg/kg) and imipramine (25 mg/kg) were intraperitoneally injected into the mice 10 min before i.v. injection of the tracer.

Table 4 Effects of various drugs on the distribution of radioactivity in mice at 5 min after intravenous administration of ^{3}H-PK 11195

(% Dose/g)

	Control	Paraquat
Blood	2.95±0.23	3.03±0.61
Heart	24.1±2.68	26.0±4.04
Lung	43.5±7.10	51.0±10.2
Adrenal	107±38.5	90.7±12.3
Brain	3.07±0.09	3.85±0.52

Three mice in each group; average±1 SD

(% Dose/g)

	Control	6-OHDA
Blood	1.51±0.15	2.22±0.26
Heart	19.6±2.65	19.3±1.17
Lung	40.8±8.40	64.7±11.3
Kidney	16.8±3.63	13.0±2.44
Adrenal	63.5±12.7	64.7±11.3
Brain	2.67±0.29	2.88±0.05

Three mice in each group; average± 1 SD

(% Dose/g)

	Control	Furosemide
Blood	1.49±0.23	1.73±0.10
Heart	15.1±1.38	18.7±2.28
Lung	24.2±8.16	31.6±1.98
Liver	5.50±1.06	5.93±0.89
Spleen	8.73±2.00	8.47±1.38
Kidney	18.1±3.87	20.3±2.92
Adrenal	87.6±4.01	99.9±23.8
Brain	1.77±0.23	2.25±0.16

Three mice in each group; average±1 SD

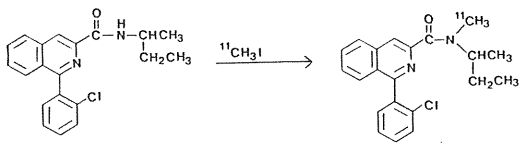

Fig. 3 Synthesis of ^{11}C-PK 11195

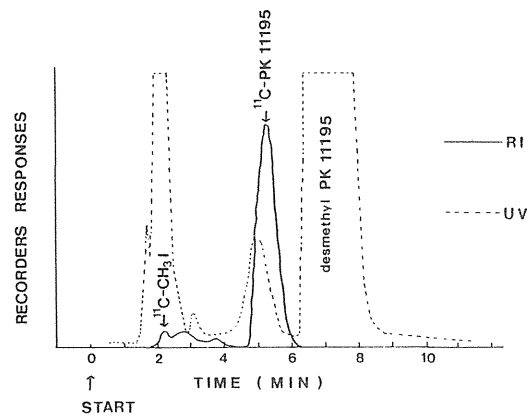

Fig. 4 Purification of ^{11}C-PK 11195 by HPLC

been performed. For this purpose, the selection of a suitable radioligand is very important in order to obtain high permeability to the cell membrane, high affinity with the receptor and high stability *in vivo*. ^{3}H-PK 11195 was found to be satisfied in the above critical conditions as follows: 1) High uptake of radioactivity in each organ was observed 1 min after intravenous administration of ^{3}H-PK 11195. 2) The radioactivity in the heart, lung, spleen, kidney and adrenal was found to be specifically bound with receptors in the carrier-added experiments. 3) TLC analysis showed ^{3}H-PK 11195 to be quite stable in the heart, lung and brain for at least 20 min after injection of the tracer.

Very high accumulations of radioactivity in the heart, lung, spleen, kidney and adrenal following intravenous administration of ^{3}H-PK 11195 were observed. More than 80% of the total radioactivity in the lung and heart was found to be due to the

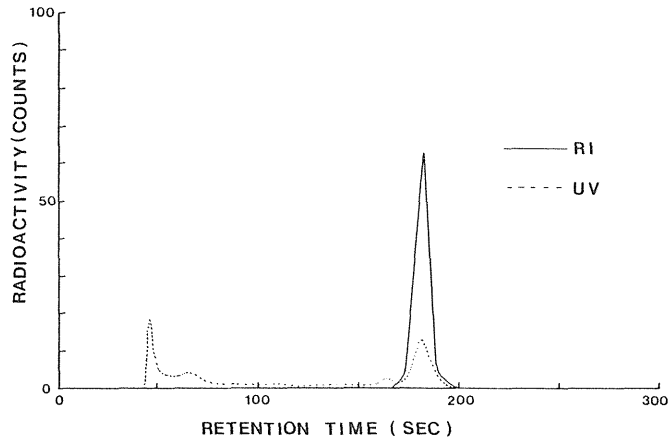

Fig. 5 HPLC of ^{11}C-PK 11195 solution for injection: conditions Finepack SIL (JASCO); solvent system, CH_3CN: 0.01 M CH_3COONH_4: H_3PO_4=195: 65: 0.125
Retention time of ^{11}C-PK 11195 (3 min), Flow rate 3 ml/min

specific binding with receptors. The time courses of radioactivity in the heart and lung after injection of the tracer were parallel to that in the blood, which suggested that the *in vivo* kinetics of ^{3}H-PK 11195 would reach the steady state soon after intravenous administration. These *in vivo* characteristics of ^{3}H-PK 11195 simplify the estimation of the binding potential (BP=Bmax/Kd) of the receptors. Since a considerable amount of peripheral-type benzodiazepine receptors exists in the platelets (30), a rapid estimating method for the determination of the free ligand concentration in the blood is required for the quantitative analysis of receptors.

From the previous data *in vitro*,[17] high densities of the peripheral-type benzodiazepine receptors have been observed in the heart, lung, kidney, adrenal and other organs, while the physiological functions of this receptor were not clearly understood. In order to examine the relationship between the peripheral-type benzodiazepine receptors and the catecholaminergic neurons, we studied the effect of neurotoxin 6-hydroxydopamine on the biodistribution of ^{3}H-PK 11195 in the mice. The present results indicated that the peripheral-type benzodiazepine receptors might not be regulated by the catecholaminergic neurons. Since it has been shown that the peripheral-type benzodiazepine receptors could be coupled to the calcium channel in the heart,[21,22] the *in vivo* study of the peripheral-type benzodiazepine receptors with ^{11}C-PK 11195 and PET would be of great value in the investigation of the living human heart.[31,32] In fact, Charbonneau et al. had already started a clinical study with ^{11}C-PK 11195 and PET.[33]

It has been recognized that the lung plays an important role in the regulation of a lot of circulating substances, including endogenous and exogenous

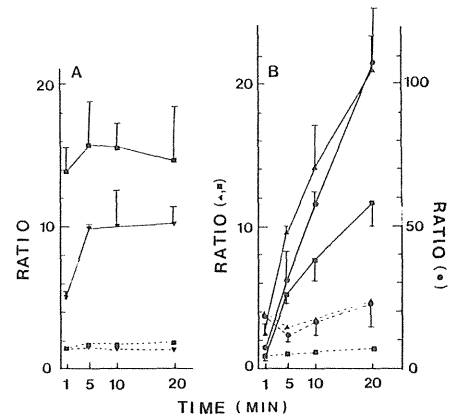

Fig. 6 Time courses of ratio of radioactivity in each organs to that in blood. (A) (▼—▼) and (■—■) are expressed as ratios of radioactivity in the heart and lung to the radioactivity in the blood in the carrier-free state. (▼---▼) and (■---■) are ratios in the carrier-added state. Three mice in each group; average±1 SD
(B) (■—■), (▲—▲) and (●—●) are ratios of radioactivity in the spleen, kidney and adrenal to the radioactivity in the blood in the carrier-free state. (■---■), (▲---▲) and (●---●) are ratios in the carrier-added state. Three mice in each group; average±1 SD

amines, and high accumulations of the basic amines in the lung have been widely reported.[34-38] We examined the effects of basic amines (α-methyl benzylamine and imipramine) on the lung uptake of ^{3}H-PK 11195 in order to determine whether the high accumulation of ^{3}H-PK 11195 in the lung was due to the specific binding with receptors or to the uptake system of basic amines. These results indicate that

the uptake of ^{3}H-PK 11195 in the lung might be due to the specific binding with receptors. It is also of interest to investigate the lung functions as receptor levels under various diseases with ^{11}C-PK 11195 and PET. However, the lung uptake of ^{3}H-PK 11195 in the paraquat pretreated mice, which was used as animal model of lung damage,[27,28] was unchanged when compared with that in the control mice. Further studies on the functional role of peripheral-type benzodiazepine receptors in the lung are necessary.

The distributions of radioactivity in the spleen, kidney and adrenal were increased over a period of 20 min after injection of the tracer. The time courses of the ratio of radioactivity in each organ to that in blood are shown in Fig. 6. The ratios in these organs were significantly decreased by treatment with carrier PK 11195. Since these ratios in the spleen, kidney and adrenal were increased over a period of 20 min after injection of the tracer, this radioligand would be suitable for the imaging of the spleen, kidney and adrenal. One possible reason for the difference between the binding kinetics of this radioligand *in vivo* in these three organs and other organs such as heart might be due to the different subclass of peripheral-type benzodiazepine receptors. It has recently been reported that the peripheral-type benzodiazepine receptors in the kidney was regulated by an anion transport system.[24] In the present study, the biodistribution of ^{3}H-PK 11195 in the kidney as well as other organs was not significantly changed by pretreatment with diuretic furosemide. Studies to further determine the relationship between the biodistribution of ^{3}H-PK 11195 in the kidney and anion transport system are necessary.

The distribution of radioactivity in the mouse brain 5 min after injection of ^{3}H-PK 11195 was not decreased by treatment with various doses of PK 11195. However, the radioactivity in the brain 10 and 20 min after injection of the tracer was slightly reduced by carrier PK 11195. Autoradiographic distribution of ^{3}H-PK 11195 5 min after intravenous injection was found in the ventricular structures, such as the choroid plexus and ependyma (data not shown). However, it was recently reported that marked species differences exist in the distribution and density of the peripheral-type benzodiazepine receptors in the brain.[39,40] It is necessary to remember this in connection with the *in vivo* study of the peripheral-type benzodiazepine receptors in the living human brain.

Furthermore, the ^{11}C-PK 11195 solution for injection was able to be obtained in high yield with high specific activity and high radiochemical purity.

In conclusion, ^{11}C-PK 11195 would be a suitable radioligand for the *in vivo* study of the peripheral-type benzodiazepine receptors in the living human with PET.

ACKNOWLEDGMENTS

This study was supported by special coordination funds for promoting science and technology in Japan. The authors thank Drs. Y. Kasida, Y. Tateno and T. Goromaru for their valuable advice, Mrs. K. Tamate and Mrs. F. Mikado for their technical assistance with the synthesis of ^{11}C-PK 11195, and Dr. G. Le Fur (Pharumuka Laboratories, Gennevillers, France) for supplying PK 11195 and desmethyl PK 11195.

REFERENCES

1. Samson Y, Hantraye P, Baron JC, et al: Kinetics and displacement of ^{11}C-Ro 15-1788, a benzodiazepine antagonist, studied in human brain *in vivo* by positron emission tomography. *Eur J Pharmacol* 110: 247–251, 1985
2. Persson A, Ehrin E, Eriksson L, et al: Imaging of ^{11}C-labelled Ro 15-1788 binding to benzodiazepine receptors in the human brain by positron emission tomography. *J Psychiat Res* 19: 609–622, 1985
3. Shinotoh H, Yamasaki T, Inoue O, et al: A study of benzodiazepine receptor in human brain using ^{11}C-Ro 15-1788 and positron emission tomography. *Kaku Igaku* 22: 1789–1797, 1985
4. Shinotoh H, Yamasaki T, Inoue O, et al: Visualization of specific binding sites of benzodiazepine in human brain. *J Nucl Med* 27: 1593–1599, 1986
5. Frost JJ, Wagner HN, Dannals RF, et al: Imaging of benzodiazepine receptors in man with ^{11}C-suriclone by positron emission tomography. *Eur J Pharmacol* 122: 381–383, 1986
6. Braestrup C, Squires RF: Specific benzodiazepine receptors in rat brain characterized by high-affinity ^{3}H-diazepam binding. *Proc Natl Acad Sci USA* 74: 3805–3809, 1977
7. Le Fur G, Vaucher N, Perrier ML, et al: Differentiation between two ligands for peripheral benzodiazepine binding sites, ^{3}H-Ro 5-4864 and ^{3}H-PK 11195, by thermodynamic studies. *Life Sci* 33: 449–457, 1983
8. Le Fur G, Perrier ML, Vaucher N, et al: Peripheral benzodiazepine binding sites: effect of PK 11195, 1-(2-chlorophenyl)-N-methyl-N-(1-methylpropyl)-3-isoquinoline carboxamide. I. *in vitro* studies. *Life Sci* 32: 1830–1847, 1983
9. Le Fur G, Guilloux F, Rufat P, et al: Peripheral benzodiazepine binding sites: effect of PK 11195, 1-(2-chlorophenyl)-N-methyl-N-(1-methylpropyl)-3-isoquinoline carboxamide. II. *in vivo* studies. *Life Sci* 32: 1849–1856, 1983
10. Benavides J, Guilloux F, Rufat P, et al: *In vivo* labelling in several rat tissues of "peripheral type" benzodiazepine binding sites. *Eur J Pharmacol* 99: 1–7, 1984
11. Richards JG, Schoch P, Mohler H, et al: Benzodiazepine receptors resolved. *Experientia* 42: 121–126, 1986
12. Dubroeucq MC, Benavides J, Doble A, et al: Stereoselective inhibition of the binding of ^{3}H-PK 11195 to peripheral-type benzodiazepine binding sites by a

quinolinepropanamide derivative. *Eur J Pharmacol* 128: 269–272, 1986
13. Benavides J, Quateronet D, Imbault F, et al: Labelling of "peripheral-type" benzodiazepine binding sites in the rat brain by using ^{3}H-PK 11195, an isoquinoline carboxamide derivative: kinetic studies and autoradiographic localization. *J Neurochem* 41: 1744–1750, 1983
14. Benavides J, Savaki HE, Malgouris C, et al: Autoradiographic localization of peripheral benzodiazepine binding sites in the cat brain with ^{3}H-PK 11195. *Brain Res Bull* 13: 69–77, 1984
15. Anholt RRH, Murphy KMM, Mack GE, et al: Peripheral-type benzodiazepine receptors in the central nervous system: localization to olfactory nervous. *J Neurosci* 4: 593–603, 1984
16. Starosta-Rubinstein S, Ciliax BJ, Penney JB, et al: Imaging of a glioma using peripheral benzodiazepine ligands. *Proc Natl Acad Sci USA* 84: 891–895, 1987
17. De Souza EB, Anholt RRH, Murphy KMM, et al: Peripheral-type benzodiazepine receptors in endocrine organs: autoradiographic localization in rat pituitary, adrenal and testis. *Endocrinology* 116: 567–573, 1985
18. Benavides J, Malgouris C, Imbault F, et al: Peripheral-type benzodiazepine binding sites in rat adrenals: binding studies with ^{3}H-PK 11195 and autoradiographic localization. *Arch Int Pharmacodyn* 226: 38–49, 1983
19. Anholt RRH, De Souza EB, Kuhar MJ, et al: Depletion of peripheral-type benzodiazepine receptors after hypophysectomy in rat adrenal gland and testis. *Eur J Pharmacol* 110: 41–46, 1985
20. Anholt RRH, Pedersen PL, De Souza EB, et al: The peripheral-type benzodiazepine receptors: localization to the mitochondrial outer membrane. *J Biol Chem* 261: 576–583, 1986
21. Mestre M, Carriot T, Belin C, et al: Electrophysiological and pharmacological evidence that peripheral type benzodiazepine receptors are coupled to calcium channels in the heart. *Life Sci* 36: 391–400, 1985
22. Mestre M, Carriot T, Neliat G, et al: PK 11195, an antagonist of peripheral type benzodiazepine receptors, modulates BAY K 8644 sensitive but not β- or H_2-receptor sensitive voltage operated calcium channels in the guinea pig heart. *Life Sci* 39: 329–339, 1986
23. Bolger GT, Weissman BA, Lueddens H, et al: Dihydropyridine calcium channel antagonist binding in non-mammalian vertebrates: characterization and relationship to "peripheral-type" binding sites for benzodiazepine. *Brain Res* 368: 351–356, 1986
24. Basile AS, Lueddens HWM, Skolnick P: Regulation of renal peripheral benzodiazepine receptors by anion transport inhibitors. *Life Sci* 42: 715–726, 1988
25. Inoue O, Yamasaki T, Hashimoto K, et al: Evaluation of ^{3}H-PK 11195 as a radioligand for the *in vivo* study of peripheral benzodiazepine receptor. *Kaku Igaku* 22: 1385–1389, 1985
26. Suzuki K, Inoue O, Hashimoto K, et al: Computer-controlled large scale production of high specific activity ^{11}C-Ro 15-1788 for PET studies of benzodiazepine receptors. *Int J Appl Radiat Isot* 36: 971–976, 1985
27. Divertie MB, Owen CA, Barham SS, et al: Accumulation of radionuclide-labelled platelets and fibrinogen in paraquat-damaged rat lungs. *Am Rev Respir Dis* 125: 574–578, 1982
28. Rose MS, Lock EA, Smith LL, et al: Paraquat accumulation: tissue and species specifity. *Biochem Pharmacol* 25: 419–423, 1976
29. Camsonne R, Crouzel C, Comar D, et al: Synthesis of N-(^{11}C)methyl, N-(methyl-1 propyl), (chloro-2 phenyl)-1-isoquinoline carboxamide-3 (PK 11195): a new ligand for peripheral benzodiazepine receptors. *J Label Compounds Radiopharm* 21: 985–991, 1984
30. Benavides J, Quarteronet D, Plouin PF, et al: Characterization of peripheral type benzodiazepine binding sites in human and rat platelets by using ^{3}H-PK 11195. Studies in hypertensive patients. *Biochem Pharmacol* 33: 2467–2472, 1984
31. Mestre M, Carriot R, Belin C, et al: Electrophysiological and pharmacological characterization of peripheral benzodiazepine receptors in a guinea pig heart preparation. *Life Sci* 35: 953–962, 1984
32. Mestre M, Bouetard G, Uzan A, et al: PK 11195, an antagonist of peripheral benzodiazepine receptors, reduces ventricular arrhythmias during myocardial ischemia and reperfusion in the dog. *Eur J Pharmacol* 112: 257–260, 1985
33. Charbonneau P, Syrota A, Crouzel C, et al: Peripheral-type benzodiazepine receptors in the living heart characterized by positron emission tomography. *Circulation* 73: 476–483, 1986
34. Anderson MW, Orton Tc, Pickett RD, et al: Accumulation of amines in the isolated perfused rabbit lung. *J Pharmacol Exp Ther* 189: 456–466, 1974
35. Iwasawa Y, Gillis CN: Pharmacological analysis of norepinephrine and 5-hydroxytryptamine removal from the pulmonary circulation: differentiation of uptake sites for each amine. *J Pharmacol Exp Ther* 188: 386–393, 1974
36. Fowler JS, Gallagher BM, Macgregor RR, et al: Carbon-11 labelled aliphatic amines in lung uptake and metabolism studies: potential for dynamic measurements *in vivo*. *J Pharmacol Exp Ther* 198: 133–145, 1976
37. Hashimoto K, Inoue O, Suzuki K, et al: Synthesis and evaluation of ^{11}C-cyanoimipramine. *Nucl Med Biol* 14: 587–592, 1987
38. Moretti JL, Holman BL, Delmon L, et al: Effect of antidepressant and narcoleptic drugs on N-isopropyl p-iodoamphetamine biodistribution in animals. *J Nucl Med* 28: 354–359, 1987
39. Cymerman U, Pazos A, Palacios JM: Evidence for species differences in "peripheral" benzodiazepine receptors: an autoradiographic study. *Neurosci Lett* 66: 153–158, 1986
40. Pazos A, Cymerman U, Probst A, et al: "Peripheral" benzodiazepine binding sites in human brain and kidney: autoradiographic studies. *Neurosci Lett* 66: 147–152, 1986

Measurement of Regional Myocardial Blood Flow in Hypertrophic Cardiomyopathy: Application of the First-Pass Flow Model Using [^{13}N]Ammonia and PET

KATSUYA YOSHIDA, MD, MASAHIRO ENDO, PhD, TOSHIHARU HIMI, MD, AKIHIKO KAGAYA, MD, YOSHIAKI MASUDA, MD, YOSHIAKI INAGAKI, MD, HIROSHI FUKUDA, MD, TAKESHI IINUMA, PhD, TOSHIRO YAMASAKI, MD, NOBUO FUKUDA, MD, and YUKIO TATENO, MD

Third Department of Internal Medicine, Chiba University School of Medicine (K.Y., T.H., A.K., Y.M., Y.I.), and Division of Clinical Research, National Institute of Radiological Sciences (M.E., H.F., T.I., T.Y., N.F., Y.T.), Chiba, Japan

ABSTRACT **Positron emission tomography (PET) has become an important tool in the study of regional myocardial blood flow. The purpose of the present study was to measure regional myocardial blood flow using dynamic [^{13}N]ammonia PET and the first-pass flow model. Thirteen patients with hypertrophic cardiomyopathy, and with a considerably thickened ventricular wall (25 mm or greater), were selected for the study in order to minimize errors due to spillover of radioactivity from blood to the myocardium and to the underestimation of myocardial activity caused by the partial volume effect. Arterial input function was determined by assigning a region of interest to the left atrial cavity on the PET images. Using left atrial and myocardial time-activity curves, regional myocardial blood flow was calculated using the first-pass flow model. Mean myocardial blood flow ranged from 47.8 to 76.5 ml/min per 100 g (63.0 ± 9.4). Regional myocardial blood flow in the septum was significantly lower than in the anterior and lateral walls of the left ventricle ($P < .01$). These results indicate the potential usefulness of dynamic PET in the measurement of regional myocardial blood flow in man.**

Key words: **Regional myocardial blood flow, hypertrophic cardiomyopathy, first-pass flow model, [^{13}N]ammonia, Positron emission tomography**

INTRODUCTION

Positron emission tomography (PET) offers the potential of noninvasive measurement of regional myocardial blood flow in man. Mullani and Gould developed the first-pass flow model for the measurement of regional blood flow [1] using first-pass tracer kinetics [2]. This model can be applied to the human heart using dynamic PET and [^{13}N]ammonia.

However, the capability of this procedure is limited because of the relative low sensitivity and spatial resolution of most existing PET devices. The former problem could be overcome through the use of a high sensitivity PET device (POSITOLOGICA-II) [3]. We previously performed serial 5.5 sec PET scans in man after an intravenous injection of [^{13}N]ammonia using this PET device and demonstrated a temporal relationship between arterial input function and myocardial tracer concentrations [4]. The relatively low resolution causes the partial volume effect and the bidirectional cross-contamination of recorded counts between myocardium and blood [5]. In the present study, we selected patients with hypertrophic cardiomyopathy in order to minimize these problems.

The purpose of the present study was the measurement of regional myocardial blood flow in patients with hypertrophic cardiomyopathy using dynamic [^{13}N]ammonia PET and the first-pass flow model.

MATERIALS AND METHODS

Patient selection

We selected 13 patients with a clinical and echocardiographic diagnosis of hypertrophic cardiomyopathy (Table 1). The study group was composed of nine males and four females, ranging in age from 26 to 66 years with a mean age of 46 years. Cardiac catheterization was performed in nine patients (nos. 2, 3, 5, 6, 7, 8, 10, 11, and 12). The

Received January 21, 1989; accepted March 26, 1989.

Address correspondence to Kaysuya Yoshida, MD, Third Department of Internal Medicine, Chiba University School of Medicine, 1-8-1 Inohana, Chiba-shi, Chiba 280, Japan.

TABLE 1 Patient data

Patient no.	Age (yr)/sex	BP	HR	mMBF	RMBF		
					Septum	Anterior	Lateral
1	51/M	126/80	60	49.5	44.9	50.7	50.0
2	56/M	138/84	60	51.7	49.0	56.9	52.5
3	62/M	160/80	68	65.2	59.2	62.3	73.4
4	40/M	138/92	66	47.8	48.4	46.0	49.9
5	36/M	122/70	72	73.6	71.6	76.9	79.0
6	43/F	130/84	54	64.6	63.7	64.6	63.3
7	66/M	108/70	52	70.9	68.0	69.5	75.5
8	32/M	102/54	64	69.9	42.9	73.7	80.1
9	35/F	104/60	62	58.2	42.8	61.0	70.6
10	45/M	120/82	64	56.1	51.6	61.7	64.4
11	45/M	136/78	66	68.8	66.0	69.8	73.1
12	26/F	96/56	50	65.9	50.1	66.7	72.2
13	64/F	164/90	68	76.5	68.0	73.4	80.6
Mean				63.0	55.9*	64.1**	68.0
± SD				9.4	10.5	9.1	11.1

BP = blood pressure (mm Hg); HR = heart rate (/min); MBF = myocardial blood flow (ml/min per 100 g); RMBF = regional myocardial blood flow; mMBF = mean myocardial blood flow.
*$P < .01$ compared to anterior and lateral flow values.
**$P < .05$ compared to lateral flow values.

interventricular pressure gradient was observed in two patients (nos. 6 and 7). Coronary angiograms were normal in all nine patients studied. The patterns of left ventricular hypertrophy were identified using two-dimensional echocardiography. In all patients, substantial portions of both the ventricular septum and the left ventricular free wall were considerably thickened. In patients 1, 2, 3, and 4, the hypertrophied segments of the septum and free wall were nearly equal in thickness. In the other patients, the predominant region of left ventricular hypertrophy was in the ventricular septum. All patients underwent contrast enhanced X-ray CT, as outlined below, to measure the thickness of the ventricular septum, the anterior wall, and the lateral wall of the left ventricles. Written informed consent was obtained from all patients.

Preparation of [^{13}N]ammonia

Nitrogen-13 was produced using the medical cyclotron of the National Institute of Radiological Sciences through the bombardment of pure water with proton beams by the $^{16}O(p,\alpha)^{13}N$ reaction. The product was reduced to ammonia and collected in physiological saline. The radiochemical purity of [^{13}N]ammonia was greater than 99.9% [6].

Positron emission tomography

Tomography was performed using a whole-body positron tomograph (POSITOLOGICA-II) [3]. This device permitted the serial acquisition of data in 5.5 sec intervals and provided five transaxial sections simultaneously. Midpoints of the sections were separated by 18 mm. Sensitivities for a 20 cm diameter phantom were 22.5 and 33.6 kcps/μCi/ml for in-plane and cross-plane, respectively. Tomographic images were collected and reconstructed in a 128 × 128 matrix. The spatial resolution for the reconstructed image was 13 mm FWHM at the center, and the in-plane and cross-plane slice thicknesses were 13 and 10 mm, respectively.

Initially, blank data for the correction of detector efficiency and transmission data for tissue attenuation correction were collected using the Ge-68/Ga-68 source built into the POSITOLOGICA-II. Subsequently, a bolus of 6–13 mCi of [^{13}N]ammonia contained in 2–5 ml of saline solution was injected intravenously from the antecubital vein with a 15–20 ml flush. An initial set of twenty 5.5 sec images were acquired, followed by a 30 sec image at the same level. Transmission scans contained 25–60 million counts for all five slices; emission images contained 0.3–1 million counts in the early 5.5 sec scan and 1.4–2.8 million counts in the late 30 sec scan for all five slices. The count losses at the high count rate were corrected with an object-independent method using a single count rate [7]. All reconstructions were performed without ECG gating. All images were corrected for physical decay of the tracer. The scale used for display and photography was normalized to the peak counts in each image.

Data analysis: calculation of regional myocardial blood flow

Regional myocardial [^{13}N] activity was determined at three different scan levels (left atrial, mid-ventricular, and low-ventricular level). At each tomographic level, one to seven square-shaped regions of interest (ROIs) were assigned. Each ROI was 1.0 cm^2 in area. The wall thickness corresponding to each location was measured by contrast enhanced X-ray CT imaging at approximately the same level. Each thickness ranged from 25 to 40 mm.

The underestimation of myocardial [^{13}N] activity due to the partial volume effect was less than 5%, that is, the calculated count recovery coefficient is about 0.95 for a wall thickness of 25 mm with an imaging resolution of 13 mm FWHM [8,9]. The overestimation due to the spillover of [^{13}N] activity from blood pools can be considered to be negligible on the late tomographic images, when the [^{13}N] activity has been cleared from blood pools.

On a scan 18 mm cephalad to the mid-ventricular level, the left atrium was visible. In order to obtain the arterial input function, a slice at this level was selected and an ROI was assigned to the center of the left atrial cavity. The left atrial size was measured using the X-ray CT image at approximately the same level. The maximum anteroposterior diameter of the left atrium ranged from 36 to 48 mm. The transverse diameter ranged from 62 to 80 mm. Accordingly, no attempt was made to correct for errors due to the partial volume effect or the spillover of [^{13}N] activity from the myocardium. From these ROIs, time-activity curves of the myocardium and the arterial blood were determined.

With these data, regional myocardial blood flow (RMBF) was calculated using the first-pass flow model. This model is based on a hypothesis: During the initial pass of a tracer through an organ, there exists a time before the tracer reaches the venous drainage, when all the tracer is within the organ of interest. Using this premise, RMBF can be calculated using the following equation:

$$\mathrm{RMBF} = \frac{\mathrm{Cm}\ (T)}{\int_0^T C_a(t)dt \cdot g} \cdot 100\ (\mathrm{ml/min\ per\ 100\ g})$$

where Cm(T) is the activity in the myocardium at time, T (PET number/min per pixel); Ca(t) is the activity in the arterial blood at time, t (PET number/min per pixel); t is the elapsed time since injection; T is the integral time of Ca(t); and g is the myocardial density (1.05 g/ml).

The above relationship is valid for all times until initial venous effluent of tracer occurs. After that time, the value of flow should decrease as the tracer begins to leave the region of interest. This hypothesis was tested by generating graphs of the calculated value of flow as a function of the integral time, T.

Also, the bolus arrives in coronary artery slightly later than the left atrium. In order to investigate the inaccuracy of the flow values calculated by the input function from the left atrium, flow vs. time curves were also generated for conditions in which the arterial activity curve was shifted later by 1 and 2 sec increments.

In order to validate the reproducibility of this technique for flow measurement, duplicate determinations were made in three patients (nos. 4, 12, and 13) and the percent difference between two repeated measurements was calculated. The second measurement was performed 50–60 min after the first injection of [^{13}N]ammonia with no movement of the patients after the first scan.

X-ray computed tomography (CT)

Contrast enhanced X-ray CT without ECG gating was performed with a GE CT/T 8800 as described previously [10]. Each patient was examined in a supine position during full expiration. First, conventional nonenhanced scans were done with 1 cm thick slices from the aortic arch to the diaphragm. Subsequently, three scans were obtained immediately after each bolus intravenous administration of 15–20 ml Renographin 76 (76% megulumine diatrizoate) at approximately the same levels as the PET slices: the left atrial, mid-ventricular, and low-ventricular levels. The left ventricular wall thickness and the left atrial size were measured using these images.

Statistical analysis

Flow values are expressed as mean ± 1 standard deviation (SD). Flow in the ventricular septum, the anterior wall, and the lateral wall of the left ventricle at the mid-ventricular level were compared using Friedmann's test, followed by a Wilcoxon signed-ranks test.

RESULTS

Initial passage of the tracer through the heart was obtained with serial 5.5 sec PET images. Examples of serial images are shown in Figure 1. Figure 2a shows the time-activity

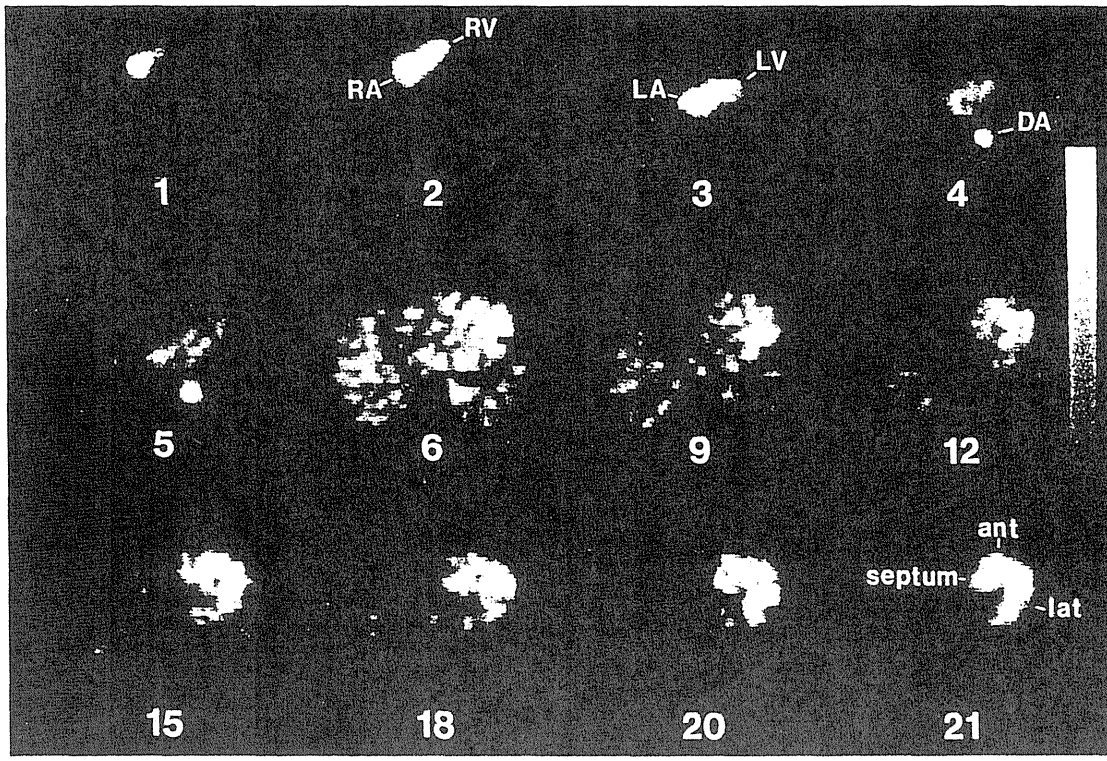

Fig. 1. Serial PET images at the mid-ventricular level in patient 7. The 5.5 sec sampling time permits visualization of the initial passage of the tracer through the heart. Nos. indicate the frame numbers. The last frame (no. 21) represents a 30 sec image. RA and LA = right and left atrium; RV and LV = right and left ventricle; DA = descending aorta; ant = anterior; lat = lateral wall of the left ventricle; septum = ventricular septum.

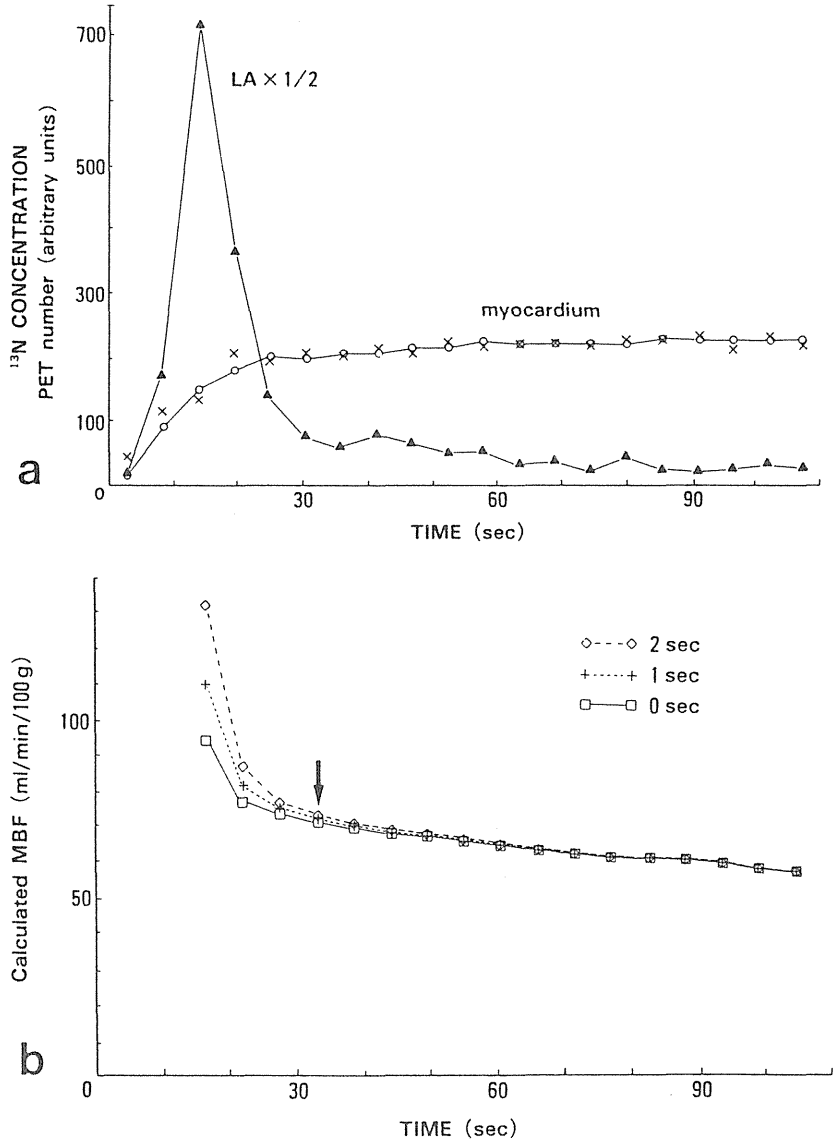

Fig. 2. **a:** Myocardial and left atrial time-activity curves in the same patient as in Figure 1. The myocardial data (cross marks) were obtained by summation of all myocardial ROIs and smoothed using a three-point smoothing algorithm. Circles indicate the myocardial smoothed data. **b:** Flow vs. time curves of a. The dashed and dotted lines indicate flow vs. time curves in which the arterial activity profiles were shifted to a later time (1 and 2 sec) than those of the left atrium. The final value of flow used in the clinical analysis was selected at the sixth frame (arrow) in this case.

curves of the myocardium from all myocardial ROIs and the arterial blood from a left atrial ROI in the same patient as in Figure 1. Arterial [^{13}N] activity reached its peak by the third frame. Next, an early, rapid clearance phase occurred, which was nearly complete at the sixth frame. Myocardial [^{13}N] activity rapidly increased up to this frame and cleared slowly from blood pools while myocardial [^{13}N] activity increased gradually. Figure 2b illustrates the time vs. flow curves from Figure 2a. The flow value before the fifth frame was extremely high due mainly to the spillover of activity from the left ventricular blood pool. After the sixth frame, the flow value decreased gradually as the tracer began to leave the myocardial region of interest. The final flow value used in the clinical analysis was selected at the sixth frame in this case. In the 13 cases in our study, the time point (T) in the clinical analysis varied from the sixth to the eighth frame.

The flow values for all 13 patients are listed in Table 1. Mean myocardial blood flow, obtained by averaging the flow

values in all ROIs, ranged from 47.8 to 73.6 ml/min per 100 g (63.0 ± 9.4). At the mid-ventricular level, the ROIs were the ventricular septum, the anterior wall, and the lateral wall of the left ventricle. The regional myocardial blood flow in the ventricular septum was significantly lower than in other regions at this level ($P < .01$).

In patients 8, 9, and 12, diminished [^{13}N] activity in the ventricular septum was clearly demonstrated in the PET images. Figure 3 shows the myocardial perfusion patterns from patient 8. In this case, subendocardial biopsies were obtained from the septal and anterior walls of the right ventricle (Fig. 4). Cell disorganization and interstitial fibrosis were predominant in the septal region, but could not be detected in the anterior region.

The results of the duplicate determinations obtained for 27 ROIs in three patients were in good agreement (percent differences 6.5 ± 7.4%, $r = .92$, $y = 0.96x + 3.4$) (Fig. 5).

DISCUSSION

Myocardial [^{13}N]ammonia concentrations

We selected patients with hypertrophic cardiomyopathy with wall thicknesses greater than twice the FWHM to minimize any possible errors due to partial volume and spillover effects [5]. In order to render this technique useful for a more general cardiology population, further studies are required to correct partial volume and spillover effects [11]. The PET images were recorded in an ungated mode to assemble all the available counts and to obtain the best data during tomography. ROIs were assigned in the center of the myocardium to minimize spillover of activity from adjacent regions. Thus, minor inhomogeneities of regional myocardial blood flow, especially subendocardial ischemia, cannot be distinguished using our technique.

Arterial input function

The arterial input function can be determined in cardiac PET studies from an ROI over the left ventricle, left atrium, and aorta. Weinberg et al. [12] have recently compared the measurements of left ventricular blood pool activity using PET with beta probe measurements of arterial blood withdrawn directly from the left ventricle using ^{82}Rb and [^{13}N]ammonia. Time-activity curve shapes obtained with these two measurements matched well, and the integral arterial input function were in good agreement. However, the arterial blood concentration of the left ventricle may be overestimated, especially in patients with hypertrophic cardiomyopathy, due to spillover of radioactivity from the myocardium. The previous work in our laboratory [13] has

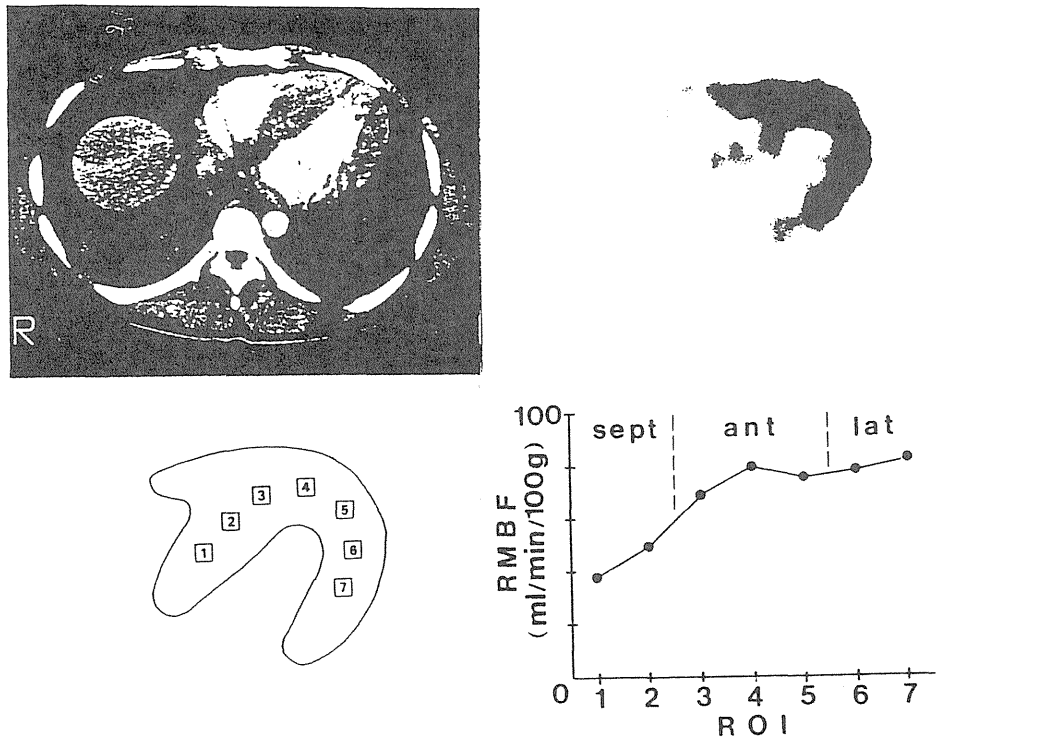

Fig. 3. Upper panel displays the comparison between X-ray CT image (left) and PET image (right) at approximately the same level in patient 8. Diminished accumulation of [^{13}N] activity in the septum is clearly demonstrated. Seven ROIs are assigned at this level (lower left panel). Regional myocardial blood flow was reduced in the septum (lower right panel).

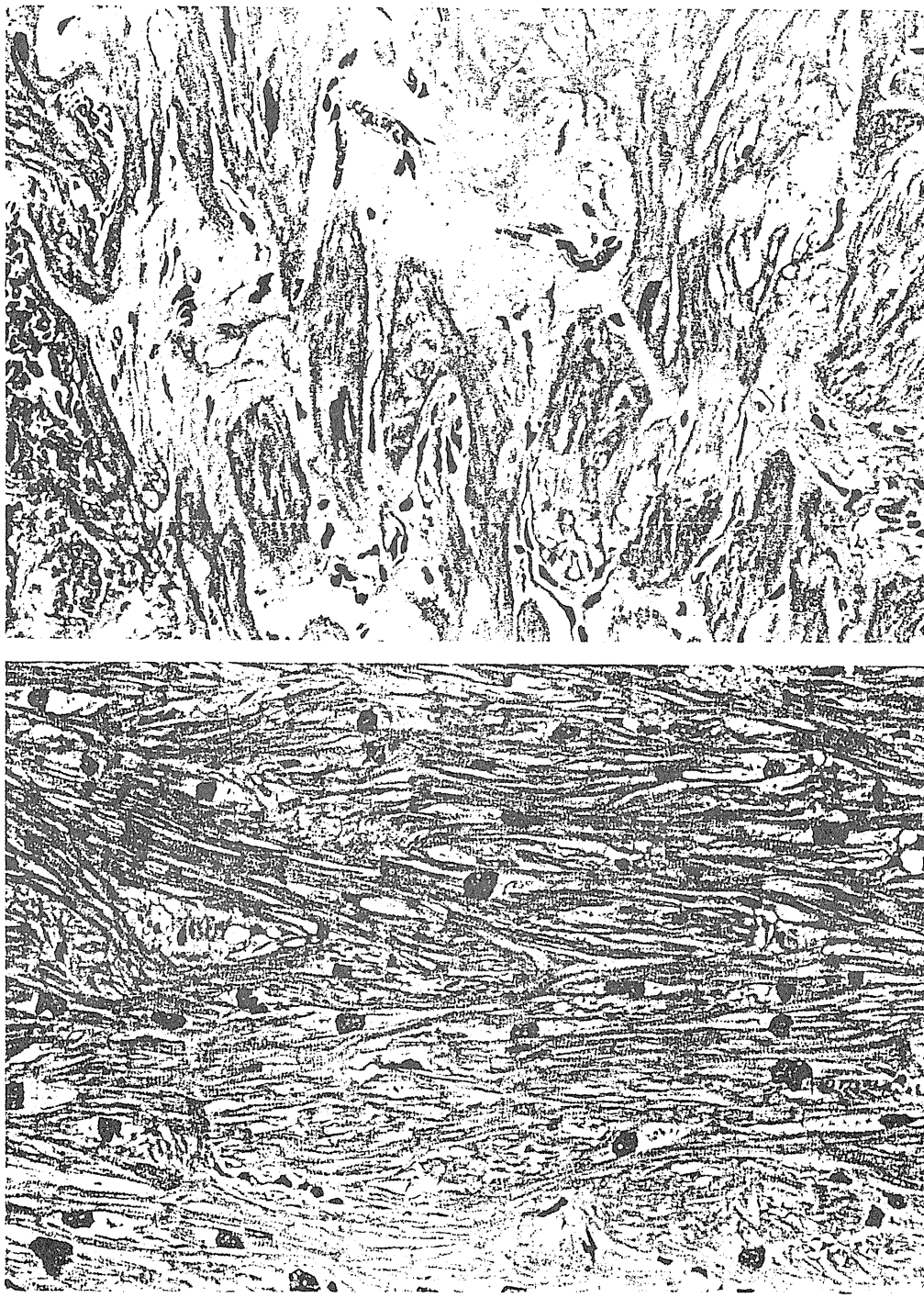

Fig. 4. Histologic sections of the septal (upper panel) and anterior (lower panel) walls of the right ventricle from patient 8. Cell disorganization and interstitial fibrosis are marked in the septal region. (Hematoxylin and eosin stain; original magnification ×400).

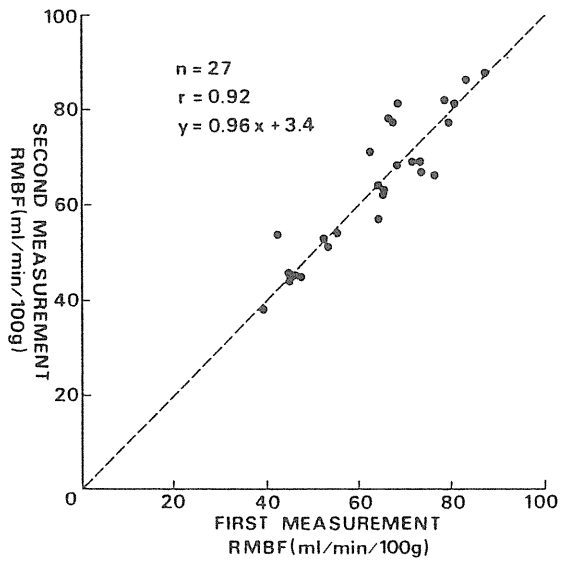

Fig. 5. Duplicate determinations of myocardial blood flow in three patients. The first and second values are plotted against each other. Dashed line indicates the line of identity.

shown that this limitation can be overcome by assigning an ROI over the left atrium.

Measurement of myocardial blood flow

The technique developed for measuring myocardial blood flow in this study was derived from previously described and validated first-pass tracer fractionation methods [1,2]. Mullani and Gould demonstrated the general model with a canine heart by using an intravenous bolus injection of rubidium-82 with beta probes and then compared this with the microsphere technique [1]. They have also shown that venous egress of the tracer from the region introduces errors of flow value underestimation [14]. Lear et al. [15] have recently applied this model to the measurement of renal transplant perfusion using Tc-99m DTPA. They demonstrated the extent of errors due to venous egress of the tracer from the region by calculating the flow vs. time curves. In the present study, the time point used for the actual flow measurement was also based on an analysis of the flow vs. time curves. Early in the time course, all of the tracer can be considered to be totally extracted from the region of interest. However, spillover effect introduced errors of flow value overestimation. At later times, the flow value decreased as the tracer began to leave the myocardial region of interest. Thus, the time point T, at which the first-pass arterial input appeared nearly complete, was chosen as a comparison between these effects. Finally, Mullani and Gould reported fast bolus injection of Rb-82 from the femoral vein in dog studies [1] and the arterial bolus was shorter in duration than in our data. Consequently, although [^{13}N]ammonia has higher extraction fraction than does Rb-82 on the myocardium [16,17], it is possible that small amount of tracer could have passed through the myocardium within the time point in our study.

The arterial input function was obtained by assigning an ROI over the left atrium in this study. However, the bolus arrives in the coronary artery slightly later than it does in the left atrium. The simulation in which the arterial activity curve was shifted later (Fig. 2b) demonstrated errors of flow values calculating by the left atrial input function that were greatest early in the time course and decreased with time to insignificance. Underestimation of flow value due to this effect was less than 5% at the time point in the clinical analysis.

The potential of [^{13}N]ammonia as an indicator of regional myocardial blood flow has been suggested by Schelbert et al. [16]. Shah et al. [18] demonstrated an excellent correspondence between PET measurements of myocardial blood flow using [^{13}N]ammonia and simultaneous in vitro microsphere measurements, with an almost linear relationship to flows of 44–200 ml/min per 100 g in canine studies. However, in experimental studies, changes in the metabolic state of the heart can affect the trapping mechanism of this tracer [19,20]. In addition, we studied only a narrow range of blood flow at rest. Therefore, further studies are required to address these limitations. Rosenspire et al. [21] have recently characterized the metabolic degradation of [^{13}N]ammonia in human blood. Within the first minute, the N-13-labeled metabolites in arterial blood may be assumed to be negligible.

Using the technique developed in this study, mean myocardial blood flow in 13 patients with hypertrophic cardiomyopathy was 63.0 ± 9.4 ml/min per 100 g. Selwyn et al. [22] measured regional myocardial blood flow in patients with myocardial infarction using PET with human albumin microspheres labeled with ^{11}C. The regional myocardial blood flow in areas remote from the infarct was 82.0 ± 32.0 ml/min/100 g. Iida et al. [23] have recently reported myocardial blood flow using $H_2{}^{15}O$ and dynamic PET. Normal mean myocardial blood flow was 95.0 ± 9.0 ml/min per 100 g. Myocardial blood flow per gram of tissue in patients with hypertrophic cardiomyopathy has been measured using the ^{133}Xe washout technique [24] and coronary sinus blood flow corrected for left ventricular mass [25,26]. Mean myocardial blood flow was significantly lower in patients with hypertrophic cardiomyopathy compared with normal subjects. Our data may also indicate a reduced mean myocardial blood flow in hypertrophic cardiomyopathy. However, the slightly lower values in our study could be related to the assumptions in our technique. Further studies are required to evaluate these points.

Regional myocardial blood flow in hypertrophic cardiomyopathy

Regional abnormalities of myocardial blood flow in hypertrophic cardiomyopathy have been suggested by thallium perfusion studies, which demonstrated reversible and irreversible perfusion defects in the septum [27,28]. Grover-McKay et al. [29] have recently reported the relative decrease in myocardial blood flow in the septum compared with the lateral wall using [^{13}N]ammonia and PET. These find-

ings may express regional ischemia or fibrosis. In our study, regional myocardial perfusion in the septum was significantly lower than in other regions. In patient 8, the histological findings support these data. In addition, Nagata et al. [30] have recently reported thallium perfusion and cardiac enzyme abnormalities in patients with familial hypertrophic cardiomyopathy who show dilatation or diminished contraction of the left ventricle. In our study, patients 8 and 9 showed dilatation of the left ventricle.

Finally, our approach was limited to patients with widespread hypertrophy involving the ventricular septum as well as portions of the free wall. This pattern was classified as type III according to the criteria of Maron et al. [31]. Further studies are required to investigate the perfusion abnormalities in other types of hypertrophic cardiomyopathy.

CONCLUSIONS

We measured regional myocardial blood flow in 13 patients with hypertrophic cardiomyopathy using dynamic [^{13}N]ammonia PET and the first-pass flow model. Mean myocardial blood was 63.0 ± 9.4 ml/min per 100 g. Regional myocardial blood flow in the septum was significantly lower than in the anterior and lateral walls of the left ventricle. These results indicate the potential usefulness of dynamic PET in the measurement of regional myocardial blood flow in man.

ACKNOWLEDGMENTS

This research was a part of the research project "Medical applications of the particle accerelator" at the National Institute of Radiological Sciences. We thank K. Lance Gould, M.D., and Nizar A. Mullani, B.S., University of Texas Medical School at Houston, for their thoughtful review of the manuscript. We also thank Nobuhiro Morooka, M.D., and Shigeru Watanabe, M.D., Chiba University School of Medicine, for performing the contrast enhanced X-ray CT studies, and Kazutoshi Suzuki, Ph.D. and Kazuhiko Tamate, the PET research staff at the National Institute of Radiological Sciences, for producing the [^{13}N]ammonia. We also thank Kazuhiko Kudo, M.D., and Shun Ozawa, M.D., Funabashi Medical Center, for performing the cardiac catheterization in patient 8. This work was supported in part by a Grant from the Ministry of Education of Japan (570404).

REFERENCES

1. Mullani NA, Gould KL: First-pass measurements of regional blood flow with external detectors. J Nucl Med 24:577–581, 1983.
2. Sapirstein LA: Fractionation of the cardiac output of rats with isotopic potassium. Circ Res 4:689–892, 1956.
3. Tanaka E, Nohara N, Tomitani T, Yamamoto M, Murayama H, Iinuma T, Tateno Y, Ishimatsu K, Takami K, Hayashi T: A whole body positron tomography, POSITOLOGICA-II—Design and performance evaluation. In Raynoud C (ed): "Proceedings of the Third World Congress on Nuclear Medicine and Biology, August–September 1982," Vol 1. Paris: Pergamon Press, pp 535–538, 1982.
4. Yoshida K, Himi T, Shukuya M, Masuda Y, Inagaki Y, Endo M, Fukuda N, Yamasaki T, Iinuma T, Tateno Y: Fast dynamic study in cardiac positron CT using ^{13}N-ammonia in man. Eur J Nucl Med 12:226–230, 1986.
5. Henze E, Huang SC, Ratib O, Hoffman E, Phelps ME, Schelbert HR: Measurements of regional tissue and blood-pool radiotracer concentrations from serial images of the heart. J Nucl Med 24:987–996, 1983.
6. Suzuki K, Tamate K: Automatic production of $^{13}NH_3$ and L-[^{13}N]glutamate ready for intravenous injection. Int J Appl Rad Isot 35:771–777, 1984.
7. Endo M, Nohara N, Iinuma TA, Shinoto H, Tanaka E, Yoshida K, Himi T, Kagaya A, Ogushi A, Inoue S: Count rate characteristics and count loss correction of positologica II: A whole body positron emission tomograph. Radioisotopes 36:221–226, 1987.
8. Budinger TF: Instrumentation trends in nuclear medicine. Semin Nucl Med 7:285–297, 1977.
9. Hoffman EJ, Huang SC, Phelps ME: Quantification in positron emission tomographs: I. Effects of object size. J Comput Assist Tomogr 3:299–308, 1979.
10. Masuda Y, Yoshida H, Morooka N, Watanabe S, Inagaki Y: The usefulness of X-ray computed tomography for the diagnosis of myocardial infarction. Circulation 70:217–225, 1984.
11. Endo M, Yoshida K, Iinuma T, Tateno Y, Masuda Y: Correction of activity cross-contamination between myocardium and cardiac cavity in quantitative PET using factor analysis (Abstr.) J Nucl Med 29:866, 1988.
12. Weinberg IN, Huang SC, Hoffman EJ, Araujo L, Nienaber C, Grover-McKay M, Dahlbom M, Schelbert H: Validation of PET-acquired input functions for cardiac studies. J Nucl Med 29:241–247, 1988.
13. Yoshida K, Endo M, Fukuda H, Himi T, Kagaya A, Masuda Y, Inagaki Y, Iinuma T, Yamasaki T, Fukuda N, Tateno Y: Measurement of arterial activity concentrations in cardiac PET studies. (Abstr.). J Nucl Med 29:866, 1988.
14. Mullani NA, Gould KL: First-pass measurement of regional blood flow with external detectors (Letters to the editor, Reply). J Nucl Med 25:831–836, 1984.
15. Lear JL, Raff U, Jain R, Horgan JG: Quantitative measurement of renal perfusion following transplant surgery. J Nucl Med 29:1656–1661, 1988.
16. Schelbert HR, Phelps ME, Huang SC, MacDonald NS, Hanse H, Selin C, Kuhl DE: N-13 ammonia as an indicator of myocardial blood flow. Circulation 63:1259–1272, 1981.
17. Ziegler WH, Goresky CA: Kinetics of rubidium uptake in the working dog heart. Circ Res 29:208–220, 1971.
18. Shah A, Scelbert HR, Schweiger M, Henze E, Hansen H, Sellin C, Huang SC: Measurement of regional myocardial blood flow with N-13 ammonia and positron-emission tomography in intact dogs. J Am Coll Cardiol 5:92–100, 1985.
19. Bergmann SR, Hack S, Tewson T, Welch MJ, Sobel BE: The dependence of accumulation of $^{13}NH_3$ by myocardium on metabolic factors and its implications for quantitative assessment of perfusion. Circulation 61:34–43, 1980.
20. Rauch B, Helus F, Grunze M, Braumwell E, Mall G, Hasselbach W, Kubler W: Kinetics of ^{13}N-ammonia uptake in myocardial single cells indicating potential limitations in its applicability as a marker of myocardial blood flow. Circulation 71:387–393, 1985.
21. Rosenspire KC, Schwaiger M, Mangner TJ, Hutchins GD, Shaw LE, Sutorik A, Kuhl DE: Metabolic fate of N-13 ammonia in human blood: Implications for quantification of myocardial blood flow (Abstr.). J Nucl Med 29:783, 1988.
22. Selwyn AP, Shea MJ, Foale R, Deanfield JE, Wilson R, deLandsheere CM, Turton DL, Brady F, Pike VW, Brookes DI: Regional myocardial and organ blood flow after myocardial infarction: Application of the microsphere principle in man. Circulation 73:433–443, 1986.
23. Iida H, Kanno I, Takahashi A, Miura S, Murakami M, Takahashi K, Ono Y, Shishido F, Inugami A, Tomura N, Higano S, Fujita H, Sasaki H, Nakamichi H, Mizusawa S, Kondo Y, Uemura K: Measurement of absolute myocardial blood flow with $H_2{}^{15}O$ and dynamic positron-emission tomography. Strategy for quantification in relation to the partial-volume effect. Circulation 78:104–115, 1988.
24. Weiss MB, Ellis K, Sciacca RR, Johnson LL, Schmidt DH, Cannon PJ: Myocardial blood flow in congestive and hypertrophic cardiomyopathy. Relationship to peak stress and mean velocity of circumferential fiber shortening. Circulation 54:484–494, 1976.
25. Pasternac A, Noble J, Streulens Y, Elie R, Henschke C, Bourassa MG: Pathophysiology of chest pain in patients with cardiomyopathies and normal coronary arteries. Circulation 65:778–789, 1982.
26. Shimamatsu M, Toshima H: Impaired coronary vasodilatory capacity after dipyridamole administration in hypertrophic cardiomyopathy. Jpn Heart J 28:387–401, 1987.
27. Pitcher D, Wainwright R, Maisey M, Curry P, Sowton E: Assessment of chest pain in hypertrophic cardiomyopathy using exercise thallium-201 myocardial scintigraphy. Br Heart J 44:650–656, 1980.
28. Hanrath P, Mathey D, Montz R, Thiel U, Vorgringer H, Kuper W, Schneider C, Bleifeld W: Myocardial thallium imaging in hypertrophic obstructive cardiomyopathy. Eur Heart J 2:177–185, 1981.
29. Grover-McKay M, Schwaiger M, Krivokapich J, Perloff JK, Phelps ME, Schelbert HR: Regional myocardial blood flow and metabolism at rest in mildly symptomatic patients with hypertrophic cardiomyopathy. J Am Coll Cardiol 13:317–324, 1989.
30. Nagata S, Park Y, Minamikawa T, Yutani C, Kamiya T, Nishimura T, Kozuka T, Sakakibara H, Nimura Y: Thallium perfusion and cardiac enzyme abnormalities in patients with familial hypertrophic cardiomyopathy. Am Heart J 109:1317–1322, 1985.
31. Maron BJ, Gottdiener JS, Epstein SE: Patterns and significance of distribution of left ventricular hypertrophy in hypertrophic cardiomyopathy. A wide angle, two dimensional echocardiographic study of 125 patients. Am J Cardiol 48:418–428, 1981.

Psychopharmacology (1989) 99:202–207

Psychopharmacology

Detection of benzodiazepine receptor occupancy in the human brain by positron emission tomography

Hitoshi Shinotoh [1,2], Masaomi Iyo [1], Tatsuo Yamada [2], Osamu Inoue [1], Kazutoshi Suzuki [1], Takashi Itoh [1], Hiroshi Fukuda [1], Toshiro Yamasaki [1], Yukio Tateno [1], and Keizo Hirayama [2]

[1] Division of Clinical Research, National Institute of Radiological Sciences, 4-9, Anagawa 1-chome, Chiba-shi, Chiba 260, Japan
[2] Department of Neurology, Chiba University School of Medicine, 1-8-1, Inohana-cho, Chiba-shi, Chiba 280, Japan

Abstract. Benzodiazepine receptor occupancy in the brain following oral administration of clonazepam (CZP) with a dose of 30 μg/kg in six healthy young men and a further dose of 50 μg/kg in one of the subjects was estimated by carbon-11 labeled Ro15-1788 and positron emission tomography (PET). The effects of CZP on the latency of auditory event-related potentials (P300) were also studied. Overall brain ^{11}C uptake was depressed and the % inhibition of ^{11}C uptake in the gray matter of the brain at 30 min after [^{11}C]Ro15-1788 injection was 15.3–23.5% (mean, $n=6$) following 30 μg/kg CZP when compared with that in the control experiment without any previous treatment. The ^{11}C uptake in the cerebral cortex in the subject who received both doses decreased in a dose-related manner after 30 μg/kg and 50 μg/kg CZP. The P300 latency was prolonged significantly by 30 μg/kg CZP [31.6 ± 16.3 ms (mean ± SD, $n=6$), $P<0.05$]. The P300 latency in the same subject was prolonged in a dose-related manner by 30 μg/kg and 50 μg/kg CZP. The technique using [^{11}C]Ro15-1788 and PET permits comparison of the pharmacological effects with the percentage of receptor sites which benzodiazepines occupy in the human brain. P300 also seems to be useful to investigate the pharmacological effects of benzodiazepines.

Key words: Benzodiazepine – Receptor – Positron emission tomography – Event-related potential – Ro15-1788

To date, pharmacokinetics has been mainly concerned with monitoring drug levels in the blood. However, plasma pharmacokinetics alone may not be sufficient to predict the duration and level of the clinical effects of benzodiazepines (Bellantuono et al. 1980; Ansseau et al. 1984). Rather, the clinical effects of benzodiazepines appear to be mediated via binding to specific central nervous system receptors and only the measurement of the amount of receptors occupied by a given benzodiazepine and the duration of that binding may be reliably correlated with the level and the duration of the clinical effects (review in Möhler and Richards 1983).

The feasibility of studying benzodiazepine receptors in living baboons using [^{11}C]Ro15-1788 and positron emission tomography (PET) has already been well documented (Hantraye et al. 1984, 1987a, b; Chavoix et al. 1988). Carbon-11 labeled Ro15-1788 has been also successfully used for imaging benzodiazepine receptors in the human brain with PET (Samson et al. 1985; Persson et al. 1985; Shinotoh et al. 1986; Pappata et al. 1988). Carbon-11 radioactivity in the human brain reaches a peak within 12 min following IV injection of [^{11}C]Ro15-1788 and shows a high ratio of specific to non-specific binding thereafter. Therefore, [^{11}C]Ro15-1788 should be a suitable ligand for detecting the change of benzodiazepine receptor binding and monitoring the level of benzodiazepine receptor occupancy by benzodiazepines in the human brain.

The present study was undertaken to determine if the level of benzodiazepine receptor occupancy in the human brain after therapeutic doses of oral clonazepam (CZP) can be detected by [^{11}C]Ro15-1788 and PET.

Benzodiazepines impairs the cognitive, learning, and memory performance of human subjects (Loke et al. 1985; Roy-Byrne et al. 1987). The event-related potentials have been shown to be intimately related to cognition and P300 latency can generally be regarded as reflecting stimulus evaluation time (Kutas et al. 1977; Ritter et al. 1979; McCarthy et al. 1981; Callaway 1983). The effects of CZP on P300 would seem to be worth investigating along with the PET study.

Materials and methods

Subjects. Five healthy young male students served as subjects on two occasions, another student on three occasions in this study. They were aged from 21 to 25 years, their height was 175.1 ± 7.0 cm (mean ± SD, $n=6$) and their body weight was 64.8 ± 8.2 kg (mean ± SD, $n=6$). All subjects had not taken any drug at least 1 month prior to the study. Informed written consent was obtained from each of the subjects.

Reproducibility of PET measurements was assessed on two male subjects, aged 49 and 69 years. Reproducibility of P300 measurements was assessed on six subjects (four males and two females, aged 22–35 years).

Experimental procedure. Five subjects were studied on 2 separate days from 1 to 2 weeks apart, another on 3 separate days. They had a light breakfast before 8 a.m. on the

Offprint requests to: H. Shinotoh

day of the study. The PET study was performed at around noon at the National Institute of Radiological Sciences without any previous drug treatment on the first occasion. Then the subjects were transferred to Chiba University and auditory event-related potentials (P300) were measured at around 15:00 hours. On the second occasion, CZP (30 μg/kg, 104 nmol/kg) was administered orally about 1.5 h prior to the PET study. Then the PET study and P300 measurement were performed at about the same time as on the first occasion. One of the subjects (subject 1) took part in a third experiment, in which he received 50 μg/kg (173 nmol/kg) CZP orally 1.5 h before IV injection of [^{11}C]Ro15-1788 and the PET study and P300 measurement were performed at about the same time as on the first occasion.

CZP plasma level. Blood samples were drawn at 0.5, 1, 1.5, 2 (just after PET study), and 5 h after oral CZP administration for the serial measurement of CZP plasma level in three of the subjects. Blood samples were drawn once just after the PET study in the other subjects. The plasma samples were frozen and stored at −20° C until analysis. CZP plasma levels were determined using gas chromatographic techniques (Beharrell et al. 1972).

PET. Carbon-11 labeled Ro15-1788 was produced by methylation of nor-Ro15-1788 with [^{11}C]methyl iodide (Suzuki et al. 1985). Radiochemical purity was >99% and the specific activity of [^{11}C]Ro15-1788 at the end of preparation was from 400 to 2500 Ci/mmol.

The three-ring PET system was used to follow radioactivity in five sections covering an axial distance of 72 mm of the brain (Takami et al. 1983). The spatial resolution of the reconstructed images is about 10 mm full width at half maximum, and the slice thickness is 13 mm for direct slices and 10 mm for cross slices.

The head was positioned with the aid of a vertical laser line so that the lowest slice corresponded to 10 mm above the subject's canthomeatal line. On the second and third occasion, the subject's head was carefully positioned as on the first occasion, so that the same level of the head was scanned on all three occasions. After the head was in place, a transmission scan was performed with a ring phantom containing germanium-68 for attenuation correction. Two venous cannulae were inserted in a right and a left antecubital vein for isotope injection and blood aspiration.

Specific activity of [^{11}C]Ro15-1788 at the time of injection was 66–1550, 426±430 Ci/mmol (mean±SD, $n=13$). A dose of 5.5±1.7 mCi, 7.8±6.3 μg, 415±374 pmol/kg (mean±SD, $n=13$) of [^{11}C]Ro15-1788 was injected in each subject. Serial dynamic scans (each scan took 1 min) were performed for 30 min without interval starting just at the time of injection. Timed venous blood samples were collected sequentially during emission scan. Venous blood (1 ml) was counted in a sodium-iodide scintillation counter to obtain the total radioactivity in each sample. Then 2 ml methylene chloride was added to 1 ml of the blood and mixed well. The radioactivity in the extracted fraction of the blood with methylene chloride was counted. With this technique, the recovery of unchanged [^{11}C]Ro15-1788 as an internal standard to blood was more than 98%. The thin layer chromatography analysis showed no radioactivity other than that of the unchanged [^{11}C]Ro15-1788 in the extracted fraction of the blood 20 min after injection. Thus the extracted fraction of blood with methylene chloride contained almost all the unchanged [^{11}C]Ro15-1788.

The radioactivity measured by PET and the blood radioactivity measured by a well counter were adjusted to allow for physical decay at the time of injection. The reconstructed PET images were displayed on a 128×128 pixel matrix. Regions of interest were in the left frontal cortex, the left temporal cortex, the left occipital cortex, the left basal ganglia, the left thalamus and the cerebellum. Calibration of the tomograph to obtain the actual regional isotope concentration in the brain from the reconstructed image was performed by imaging a homogenous phantom filled with a known concentration of germanium-68. The radioactivity in the brain and the blood was expressed as normalized activity, defined as:

$$\frac{\text{tissue radioactivity/cm}^3}{\text{injected radioactivity/g body weight}}$$

Benzodiazepine receptor occupancy. Benzodiazepine receptor occupancy was estimated by obtaining the % inhibition of ^{11}C uptake at 30 min after injection of [^{11}C]Ro15-1788 in each of the brain regions in the presence of CZP when compaired with that in the control experiment. The validity of this method is based on the fact that [^{11}C]Ro15-1788 reaches near-equibrium within 20 min following injection and the ratio of specific binding to non-specific binding at 30 min after injection is high enough to ignore the non-specific binding and regard total binding as specific binding (Shinotoh et al. 1986).

P300. Event-related potentials were elicited by presenting a series of binaural 990 and 1980 Hz tones at 65 db SPL with 5 ms rise/fall and a 50 ms plateau time. Changes in the target frequency were employed to produce an easy discrimination task. The tones were presented in a random

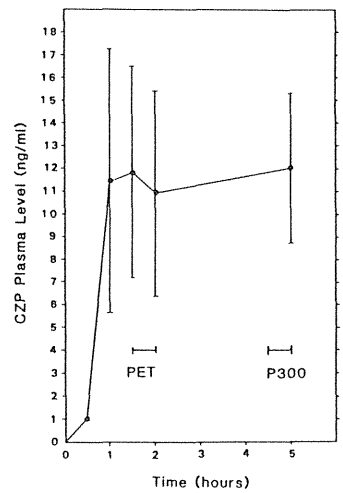

Fig. 1. Time course of the plasma level of clonazepam when the subjects received 30 μg/kg clonazepam at time 0 (mean±SD, $n=3$)

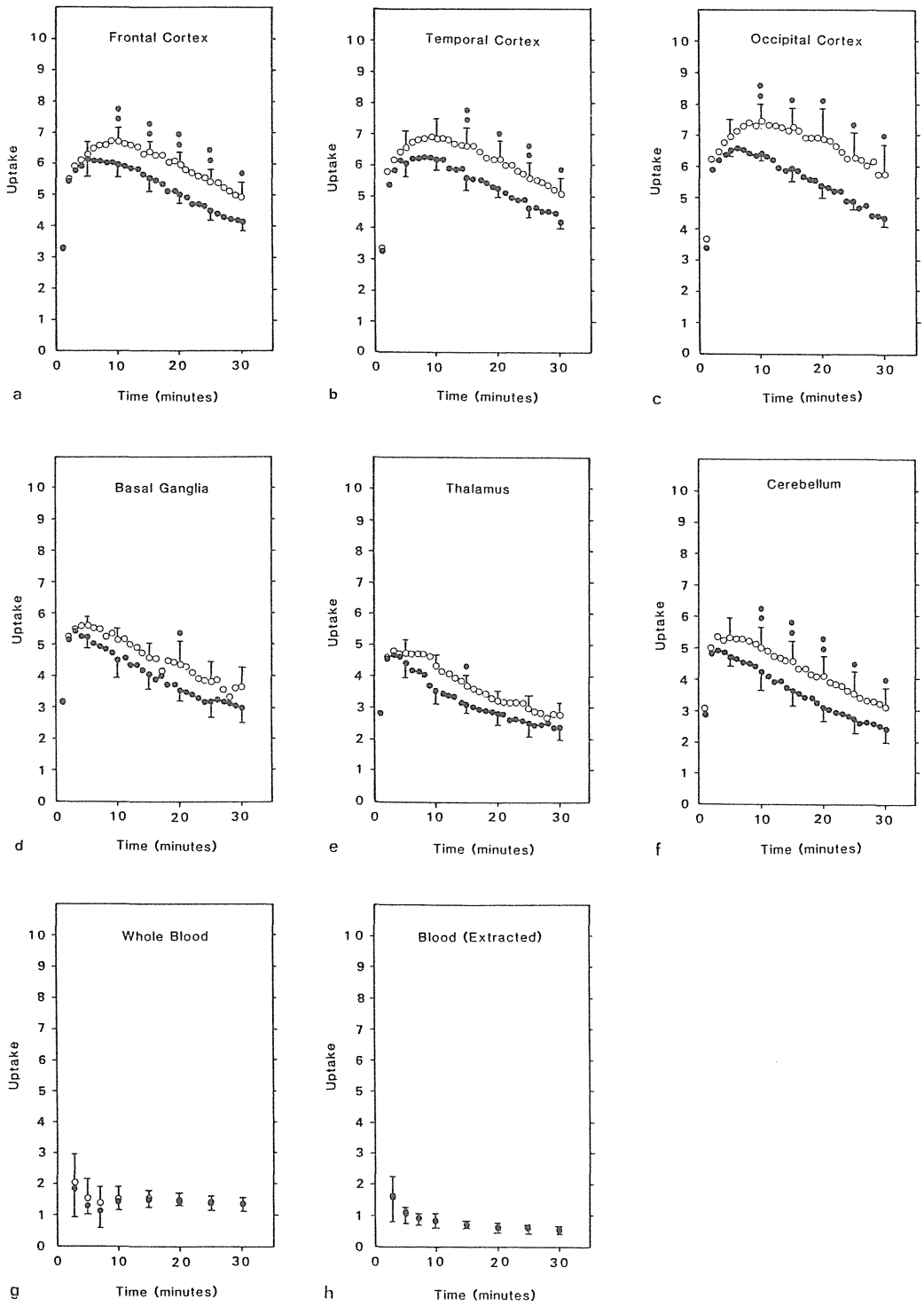

Fig. 2a–h. Time courses of ^{11}C uptake **a** in the frontal cortex, **b** in the temporal cortex, **c** in the occipital cortex, **d** in the basal ganglia, **e** in the thalamus, **f** in the cerebellum, **g** in whole blood, **h** in the extracted fraction of the blood. ^{11}C uptake is expressed in the unit, which is described in the text. *Open circle* (o) represents ^{11}C uptake in the control experiment without any previous treatment and *closed circle* (●) represents ^{11}C uptake in the experiment with 30 μg/kg CZP. * $P<0.05$, ** $P<0.01$ (paired t-test)

sequence from 1 to 1.5 s with the high (target) tone occuring 15% of the time and the low (non-target) tone 85% of the time. Subjects were instructed to count the number of the target tone mentally and then given a brief practice session to insure that they could discriminate the tones.

Electroencephalographic activity was recorded with a time constant of 1.5 s, at the Fz, Cz, Pz, Oz electrode site of the 10–20 system with plate electrodes affixed with electrode paste and tape, referred to linked earlobes with a forehead ground. Wave forms were averaged on line by an averager which also controlled the artifact rejection (Neuropack 8, Nihon Kohden). The EEG was digitized for 875 ms with a 125 ms prestimulus baseline. Trials on which the EEG exceeded +87.5 μV were automatically rejected. P300 represents the average of 30 responses for the target tones. The latency of the components of the event-related potentials were measured on CRT with a screen cursor. The positive component with a peak latency of 250–500 msec at Pz was labeled P300 and the amplitude from the prestimulus baseline to the peak of P300 was calculated.

Data analysis. Effects of CZP on the P300 latency, the P300 amplitude and the ^{11}C uptake in each of the brain regions were analysed using Student's paired *t*-test.

Results

Clinical effects of CZP

All the subjects fell asleep for 0.5–1 h before and during the PET study. They were drowsy and they felt unsteady on walking for 4–5 h after receiving CZP.

CZP plasma level

The CZP plasma level just after PET study with 30 μg/kg CZP was 5.8–15.6, 8.8±3.7 ng/ml (mean±SD, $n=6$) and 21.8 ng/ml with 50 μg/kg CZP in subject 1. Serial measurement of CZP plasma levels showed that they reached a plateau level within 1.5 h after oral administration and was fairly constant until the end of the experiment (Fig. 1).

Kinetics of [^{11}C]Ro15-1788

In the control experiment without CZP treatment, carbon-11 radioactivity in the brain reached a peak within 12 min and the highest uptake was observed in the occipital cortex, followed by that in the frontal and the temporal cortex. A moderate uptake was observed in the cerebellum, the basal ganglia, and the thalamus (Fig. 2*a–f*). The uptake in brain stem and white matter was lowest (data not shown). This distribution corresponded well with the known distribution of benzodiazepine receptors in the brain (Richards and Möhler 1984).

The radioactivity in the whole blood showed a slight, and transient increase 10–16 min following injection and remained at a constant level thereafter (Fig. 2*g*). The radioactivity in the extracted fraction of the blood (unchanged [^{11}C]Ro15-1788) decreased gradually until the end of the experiment (Fig. 2*h*).

When the subject received CZP, a similar distribution of carbon-11 radioactivity was observed to that in the control experiment. However, carbon-11 radioactivity in the brain reached a peak earlier (within 9 min following injection) than that in the control experiment and the overall ^{11}C uptake was lower than that in the control experiment (Fig. 2*a–f*). The kinetics of ^{11}C radioactivity in the blood was almost the same as those in the control experiment (Fig. 2*g*, *h*).

The % inhibition of ^{11}C uptake in each of the brain regions at 30 min after injection were 15.3–23.5% by 30 μg/kg CZP (Table 1). The ^{11}C uptake in the cerebral cortex at 30 min after injection decreased in a dose-related manner by CZP in subject 1 (Fig. 3).

Reproducibility of measurements (brain uptake of [^{11}C]Ro15-1788 at 30 min after injection) without any previous drug treatment at intervals on the order of several months was assessed on two normal volunteers. The result demonstrated a variation of less than 7% in the cerebral cortex, 11% in the cerebellum, 15% in the basal ganglia and 22% in the thalamus (Table 2).

P300

The P300 latency in the control experiment was 359±14 ms (mean±SD, $n=6$) and after administration of 30 μg/kg CZP was 393±32 ms (mean±SD, $n=6$). The latency of P300 prolonged 37±23 ms in the presence of 30 μg/kg CZP (mean±SD, $n=6$) (Fig. 4) and the difference was signifi-

Table 1. Per cent inhibition of ^{11}C uptake at 30 min

	30 μg/kg CZP mean±SD, $n=6$	50 μg/kg CZP $n=1$
Frontal cortex	15.3±9.0	30.1
Temporal cortex	17.6±7.8	30.1
Occipital cortex	23.5±10.2	30.1
Basal ganglia	22.9±10.7	6.8
Thalamus	16.4±14.7	26.8
Cerebellum	21.5±14.5	27.3

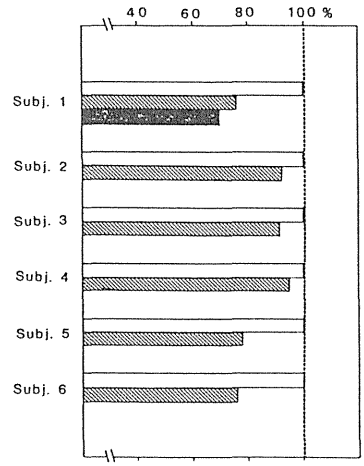

Fig. 3. The % inhibition of ^{11}C uptake in the frontal cortex in each of the six subjects. □ Control; ▨ CZP 30 μg/kg; ■ CZP 50 μg/kg

Table 2. Comparison of repeat PET measurements (^{11}C uptake at 30 min after injection) without treatment

	49/M			69/M		
	1st	2nd	% change	1st	2nd	% change
Frontal cortex	5.89	5.99	1.5	6.51	6.23	−4.21
Temporal cortex	5.45	5.86	7.6	6.68	6.23	−6.66
Occipital cortex	5.85	5.93	1.2	7.22	7.27	0.66
Basal ganglia	3.83	4.42	15.5	4.10	4.15	1.27
Thalamus	3.15	3.04	− 3.5	3.40	4.15	22.20
Cerebellum	3.69	3.26	−11.6	4.10	4.04	−1.48

^{11}C uptake is expressed in the unit described in the text

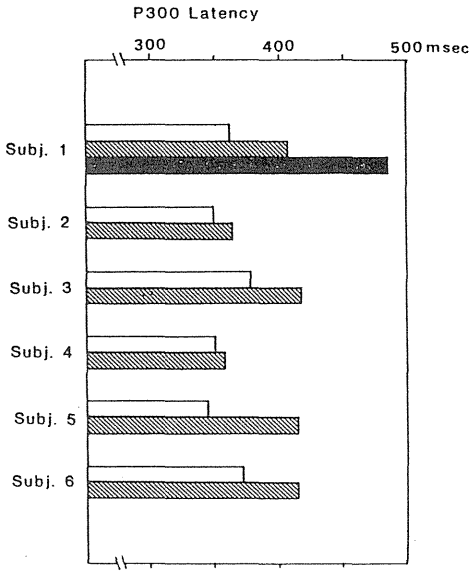

Fig. 4. The P300 latency in each of the six subjects. □ Control; ▨ CZP 30 μg/kg; ■ CZP 50 μg/kg

Table 3. Comparison of repeat P300 measurements without treatment

Age/Sex	Latency (ms)			Amplitude (μV)		
	1st	2nd	Change	1st	2nd	Change
22/M	384	380	−4	12.4	4.1	−8.3
25/F	352	354	2	7.6	11.3	3.7
26/M	378	378	0	21.2	14.4	−6.8
27/M	368	378	10	14.1	11.6	−2.5
30/F	350	364	14	20.3	15.8	−4.5
35/M	344	346	2	8.4	7	−1.4

cant (paired t-test, $P<0.05$). The P300 amplitude in the control experiment was 21.9 ± 6.0 μV (mean ± SD, $n=6$) and after administration of 30 μg/kg CZP was 19.5 ± 7.9 μV (mean ± SD, $n=6$). The difference was not significant (paired t-test, $P>0.05$).

Reproducibility of P300 measurements at 1 week interval was assessed on six normal volunteers and the result demonstrated a variation of less than 14 ms (4%) in the latency. The amplitude of P300 in the two studies were rather variable [up to 8.3 μV (66%)] (Table 3).

Discussion

The present paper reports on the feasibility of detecting the level of benzodiazepine receptor occupancy by therapeutic doses of benzodiazepine with PET.

All subjects fell asleep for 0.5–1 h and suffered from ataxia by oral CZP (30 and 50 μg/kg). The CZP plasma level in each subject reached a therapeutic level, which has been reported to be 3.0–34.6 ng/ml for the treatment of epilepsy (Naito et al. 1987), by a single oral administration of CZP (30 and 50 μg/kg) and was fairly constant during the whole experiment. The half-life of CZP plasma levels after oral administration has been reported to be 20–40 h (Naestoff et al. 1973).

The specific activity of [^{11}C]Ro15-1788 at injection in this study was very high and only tracer doses of [^{11}C]Ro15-1788 were injected in each of the subjects, which produced brain concentrations far below those necessary for saturation of benzodiazepine receptors in the brain. Since benzodiazepine receptor concentration in the human frontal cortex has been reported to be 125 fmol/mg tissue (Whitehouse et al. 1985), less than 5% of benzodiazepine receptors were believed to be occupied by [^{11}C]Ro15-1788 in the frontal cortex in this study. Thus the amount of [^{11}C]Ro15-1788 bound to the specific binding sites should be directly proportional to the number of receptor "free" at that moment, i.e., not occupied by CZP.

The kinetics of [^{11}C]Ro15-1788 in the control experiment were the same as those reported previously (Persson et al. 1985; Samson et al. 1985; Shinotoh et al. 1986). When the subjects took CZP orally, the brain radioactivity reached a peak earlier and the clearance of ^{11}C became faster than that in the control experiment. The ^{11}C uptake at 30 min after injection decreased significantly in the cerebral and the cerebellar cortex by 30 and 50 μg/kg CZP when compared with that in the control experiment. The change in ^{11}C kinetics following CZP was similar to those in the partial saturation experiments after co-injection of unlabeled Ro15-1788 (Pappata et al. 1988) and the result indicates that specific binding sites were partially saturated by orally administered CZP, and injected [^{11}C]Ro15-1788 competes for a limited number of binding sites in the brain.

Another possible explanation for the apparent decrease of ^{11}C uptake in the brain by CZP is that CZP alters non-specific uptake of [^{11}C]Ro15-1788 into the brain, by changing the regional cerebral blood flow and/or blood-brain permeability of the radioligand. However, Miller et al. (1987) reported that the brain concentrations of Ro15-1788 were similar in animals treated with saturating doses of lorazepam when compaired with vehicle treated controls. Thus, unlabeled benzodiazepines do not appear to alter non-specific uptake of [^{11}C]Ro15-1788 into the brain.

Our experiment revealed the effective doses of CZP (30 μg/kg) produced only 15.3–23.5% inhibition of [^{11}C]Ro15-1788 binding, indicating that only a small proportion of receptors need to be occupied in vivo in the human brain to produce pharmacological effects, such as sleep and ataxia.

We investigated the effects of CZP on P300 and found that CZP produced a significant prolongation of P300 la-

tency. Although, to the best of our knowledge, there have been no reports concerning the effects of benzodiazepines on P300, there have been several reports, which have explored the effects of drugs on P300 (Callaway 1983; Strauss et al. 1984; Naylor et al. 1985; Herning et al. 1985; Blackwood et al. 1986; Teo and Ferguson 1986). Callaway (1983) reported that scopolamine slowed P300 latency, and in a reasonably dose-dependent fashion. Teo and Ferguson (1986) reported that digestion of ethanol prolonged P300 latency in a dose-dependent manner and the P300 amplitude was reduced by ethanol but not in a dose-dependent manner. It appears that P300 is useful for the subjective measurement of pharmacological effects of drugs.

This technique using [^{11}C]Ro15-1788 and PET permits comparison of the pharmacological effects of benzodiazepines with the percentage of receptor sites which they occupy in the human brain. P300 also seems to be useful to investigate the pharmacological effects of benzodiazepines. These techniques open up a new field of clinical pharmacology. Future studies should elucidate the level and duration of benzodiazepine receptor occupancy in the human brain and its relationship to the pharmacological effects of various benzodiazepines.

Acknowledgements. The authors wish to thank Japan Roches Company for providing us Ro15-1788 and Nor-Ro15-1788. The authors also thank Tamate K for technical assistance for producing [^{11}C]Ro15-1788 and Yoshida K, Himi S and Nishio M for technical assistance in the PET study.

References

Ansseau M, Doumont A, Frenckell RV, Collard J (1984) Duration of benzodiazepine clinical activity: lack of direct relationship with plasma half-life. Psychopharmacology 84:293–298

Beharrell GP, Hailey DM, McLaurin MK (1972) Determination of nitrazepam (Magadon) in plasma by electron capture gas-liquid chromatography. J Choromatogr 70:45–52

Bellantuono C, Reggi V, Tognoni G, Garattini S (1980) Benzodiazepines: clinical pharmacology and therapeutic use. Drugs 19:195–219

Blackwood DHR, Christie JE (1986) The effects of physostigmine on memory and auditory P300 in Alzheimer-type dementia. Biol Psychiatry 21:557–560

Callaway E (1984) Human information-processing: some effects of methylphenidate, age and scopolamine. Biol Psychiatry 19:649–662

Chavoix C, Hantraye P, Brouillet E, Guibert B, Fukuda H, Sayette VDL, Fournier D, Naquet R, Maziere M (1988) Status epilepticus induced by pentylenetetrazole modulates in vivo [^{11}C]Ro15-1788 binding to benzodiazepine receptors. Effects of ligands acting at the supramolecular receptor complex. Eur J Pharmacol 146:207–214

Hantraye P, Kaijima M, Prenant C, Guibert B, Sastre J, Crouzel M, Naquet R, Comar D, Maziere M (1984) Central type benzodiazepine binding sites: a positron emission tomography study in the baboon's brain. Neurosci Lett 48:115–120

Hantraye P, Brouillet E, Guibert B, Chavoix C, Fukuda H, Prenant C, Crouzel M, Naquet R, Maziere M (1987a) Pentylenetetrazol-induced seizure is not mediated by benzodiazepine receptors in vivo. Neuropharmacol 26:1509–1512

Hantraye P, Chavoix C, Guibert B, Fukuda H, Brouillet E, Dodd RH, Prenant C, Crouzel M, Naquet R, Maziere M (1987b) Benzodiazepine receptors studied in living primates by positron emission tomography: inverse agonist interactions. Eur J Pharmacol 138:239–247

Herning RI, Jones RT, Hooker WD, Tulunay FC (1985) Information processing components of the auditory event related potential are reduced by cocaine. Psychopharmacology 87:178–185

Kutas M, McCarthy G, Donchin E (1977) Augmenting mental chronometry: the P300 as a measure of stimulus evaluation time. Science 197:792–795

Loke WH, Hinrichs JV, Ghoneim MM (1985) Caffeine and diazepam: separate and combined effects on mood, memory, and psychomotor performance. Psychopharmacology 87:344–350

MacCarthy G, Donchin E (1980) A metric for thought: a comparison of P300 latency and reaction time. Science 211:77–80

Miller LG, Greenblatt DJ, Paul SM, Shader RI (1987) Benzodiazepine receptor occupancy in vivo: correlation with brain concentrations and pharmacodynamic actions. J Pharmacol Exp Ther 240:516–522

Möhler H, Richards JG (1983) Benzodiazepine receptors in the central nervous system. In: Costa E (ed) The benzodiazepines: from molecular biology to clinical practice. Raven Press, New York, pp 93–116

Naestoft J, Lund M, Larsen NE, Hvidberg EF (1973) Assay and pharmacokinetics of clonazepam in humans. Acta Neurol Scand [Suppl 49] 53:103–108

Naito H, Wachi M, Nishida M (1987) Clinical effects and plasma concentrations of long-term clonazepam monotherapy in previously untreated epileptics. Acta Neurol Scand 76:58–63

Naylor H, Halliday R, Callaway E (1985) The effect of methylphenidate on information processing. Psychopharmacology 86:90–95

Pappata S, Samson Y, Chavoix C, Prenant C, Maziere M, Baron JC (1988) Regional specific binding of [^{11}C]Ro15-1788 to central type benzodiazepine receptors in human brain: quantitative evaluation by PET. J Cereb Blood Flow Metab 8:304–313

Persson A, Ehrin E, Eriksson L, Farde L, Hedstrom CG, Litton JE, Mindus P, Sedvall G (1985) Imaging of [^{11}C]-labelled Ro15-1788 binding to benzodiazepine receptors in the human brain by positron emission tomography. J Psychiatr Res 19:609–622

Richards JG, Möhler H (1984) Benzodiazepine receptors. Neuropharmacology 23:233–242

Ritter W, Simson R, Vaughan HG, Friedman D (1979) A brain event related to the making of a sensory discrimination. Science 203:1358–1361

Roy-Byrne PP, Uhde TW, Holcomb H, Thompson K, King AK, Weingartner H (1987) Effects of diazepam on cognitive process in normal subjects. Psychopharmacology 91:30–33

Samson Y, Hantraye P, Baron J-C, Soussaline F, Comar D, Maziere M (1985) Kinetics and displacement of [^{11}C]Ro15-1788, a benzodiazepine antagonist, studied in human brain in vivo by positron tomography. Eur J Pharmacol 110:247–251

Shinotoh H, Yamasaki T, Inoue O, Itoh T, Suzuki K, Hashimoto K, Tateno Y, Ikehira H (1986) Visualization of specific binding sites of benzodiazepine in human brain. J Nucl Med 27:1593–1599

Strauss J, Lewis JL, Klorman R, Peloquin L-J, Perlmutter RA, Salzman LF (1984) Effects of methylphenidate on young adults' performance and event-related potentials in a vigilance and a paired-associates learning test. Psychophysiol 21:609–621

Suzuki K, Inoue O, Hashimoto K, Yamasaki T, Kuchiki M, Tamate K (1985) Computer-controlled large scale production of high specific activity [^{11}C]Ro15-1788 for PET studies of benzodiazepine receptors. Int J Appl Radiat Isot 36:971–976

Takami K, Ueda K, Okajima K, Tanaka E, Nohara N, Tomitani T, Murayama H, Shishido F, Ishimatsu K, Ohgushi S, Inoue Y, Takakusa Y, Hayashi T, Nakase S (1983) Performance study of whole-body, multislice positron computed tomograph -Positologica II-. IEEE Trans Nucl Sci NS-30:734–738

Teo RKC, Ferguson DA (1986) The acute effects of ethanol on auditory event-related potentials. Psychopharmacology 90:179–184

Whitehouse PJ, Trifiletti RR, Jones BE, Folstein S, Price DL, Snyder SH, Kuhar MJ (1985) Neurotransmitter receptor alterations in Huntington's disease: autoradiographic and homogenate studies with special reference to benzodiazepine receptor complexes. Ann Neurol 18:202–210

Received May 23, 1988 / Final version April 25, 1989

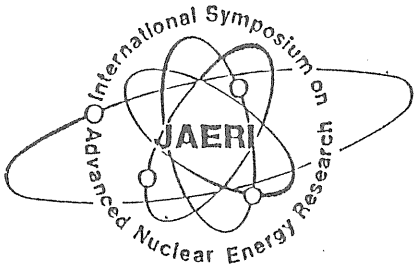

PROCEEDINGS

The 2nd International Symposium on ADVANCED NUCLEAR ENERGY RESEARCH — Evolution by Accelerators —

January 24-26, 1990
at
Mito Plaza Hotel
Mito, Ibaraki, Japan

Organized and Sponsored
by
Japan Atomic Energy Research Institute
in Collaboration with
The Atomic Energy Society of Japan and
The Physical Society of Japan

PRODUCTION OF RADIOPHARMACEUTICALS WITH HIGH SPECIFIC ACTIVITY

Suzuki K. and Inoue O.
National Institute of Radiological Sciences
9-1, 4-Chome, Anagawa, Chiba-Shi, 260, Japan
0472-51-2111

Introduction

In bio-medical research, various kinds of radioisotopes and their labeled compounds have been applied and used. Among them, ^{3}H and ^{14}C-labeled compounds have revealed biochemical processes such as transport, metabolism and binding because of their availability of labeling of various biochemical molecules. Another important point which should be considered in radio-tracer technique is the specific activity of labeled compounds. For example, investigation of binding characteristics of receptors have been able to be performed by development of ^{3}H-labeled ligands with high specific activity. As shown in Fig 1, several bioactive molecules, which seem to act at very low concentrations less than 10^{-12} M have been discovered. For example, stimulation of luteinizing hormone releasing hormone(LHRH) by leukotrien C_4 was reported to be observed at concentrations ranging from 10^{-12} to 10^{-18} M (Kyriaki,1986). With regard to dose response curve of leukotrien C_4, a bell-shaped curve was found, which indicated non-linear drug-recepter interaction. In order to investigate mechanism for such bioactive molecules with target cells or recepters, development of new labeling technique with very high specific activity is needed. For this purpose, labeled compounds with short-lived isotopes have high potency.

By the recent advance in positron emission tomography(PET), the external measurement of biochemical processes in living animal and human have been able to be done. Indeed, this new in vivo measurement method have of great value, however it also require to dissolve various problems in biochemistry in vivo. For example, it has been reported that there are significant differences of ligand-recepter binding between tissue-homogenate, tissue slice and intact animal. As shown in Fig 2, cooperativity of ^{3}H-morphine binding with receptors was only seen when tissue slice was used instead of tissue homogenate (Davis, 1977). As the cooperativity of proteins seems to have important roles for physiological

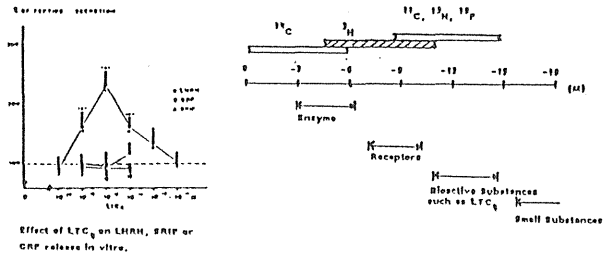

Fig.1 Radioisotopes in biochemistry and concentration range

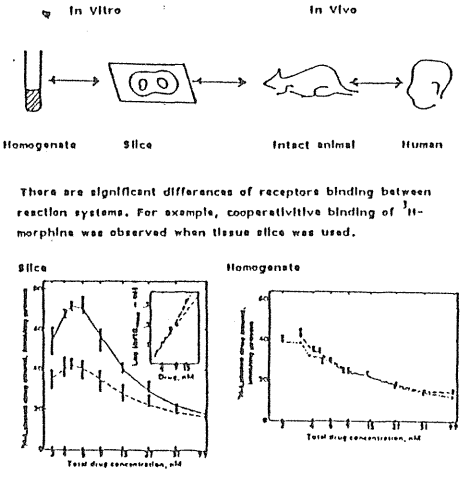

Fig.2 Applications of radiotracers with high specific activity(Davis,1977)

function, more detailed studies using various kinds of labeled ligands with high specific radioactivity are needed. Positron-emitter-labeled ligands with high specific activity will be of high potency for these future research, since it can be applied both in vitro and in vivo.

PRACTICALLY ATTAINABLE SPECIFIC ACTIVITY

Short-lived positron emitters such as ^{11}C, ^{13}N, ^{15}O and ^{18}F are very important in the field of nuclear medicine and biochemistry, since they can be produced easily with a commercially available compact cyclotron and give the labelled compounds which play important roles in biochemical processes. Since theoretical specific activities of these nuclides are extremely high, compared to those of ^{3}H and ^{14}C, as shown in Tab.1, the requirements for higher specific activity may be satisfied. However, practically attainable specific activities are much lower than the theoretical ones due to isotopic dilution in the course of target preparation, irradiation, labelling procedure, etc. A number of ^{11}C-labelled radiopharmaceuticals and useful precursors, such as $[^{11}C]CH_3I$(Iwata 1979, Crouzel 1987), $[1-^{11}C]RCH_2I$(R=alkyl group, Langstrom, 1986), $[2-^{11}C](CH_3)_2CO$ (Berger, 1980) and $[^{11}C]HCHO$ (Berger, 1979) have been synthesized from $[^{11}C]CO_2$. Non-radioactive CO_2 is liable to be contaminated in a target gas, a production system and reagents used for labelling, and causes isotopic dilution of $^{11}CO_2$ to lead to a decrease of specific activity of ^{11}C-labelled precursors and radiopharmaceuticals. $[^{11}C]HCN$ (Christman, 1975) may be an alternative precursor to attain higher specific activity since it is synthesized from $[^{11}C]CH_4$ which is produced directly in a target box (target gas: N_2 containing ~5% H_2), and not from $[^{11}C]CO_2$. High specific activity of $[^{18}F]F_2$, as shown in Tab.1 was achieved after the development of a small volume target box (~0.2 ml $[^{18}O]H_2O$), designed to stand high beam current irradiation and to meet the requirement for further organic synthesis. Current specific activities of $[^{13}N]N_2$ and $[^{15}O]O_2$ are not high enough. At present, the efforts to achieve high specific activity for these nuclides seem not to be enough, compared to the efforts for $[^{11}C]C$ and $[^{18}F]F_2$. This may be due to too short half-lives of the nuclides.

PRODUCTION OF ^{11}C-labelled compounds with HIGH SPECIFIC ACTIVITY

$[^{11}C]CH_3I$ is the most widely used precursor for ^{11}C-labelling since it can be easily and rapidly synthesized from $[^{11}C]CO_2$ and it can react with pharmacologically active and interesting compounds by N-, S-, ^{11}O-methylation reactions. At NIRS, many ^{11}C-labelled compounds such as Ro15-1788, N-methylspiperone, SCH23390, cyanoimipramine, phenethylamine, benzylamine and PK11195 have been produced at high radiochemical purity, high radiochemical yield and high specific activity by the reactions with $[^{11}C]CH_3I$ and used clinically with PET for the in vivo studies of receptor and enzyme in brain. A production method of $[^{11}C]$Ro15-1788 is presented bellow, as an example for the productions of radiotracers with high specific activity, labelled with positron emitters.

$[^{11}C]$Ro15-1788 was synthesized and purified automatically with a specially designed equipment(Suzuki, 1985). Fig.3 shows the set up of the equipment. More than 99.999% pure nitrogen gas loaded into a target box (front diameter 20 mm, rear diameter 30 mm, length 150 mm) at a pressure of 1.4 MPa was irradiated at 10-15 uA for 20-50 minutes by 18 MeV protons(14.2 MeV on target) from the NIRS AVF cyclotron. ^{11}C activity generated by the $^{14}N(p,alpha)^{11}C$ reaction was converted to $[^{11}C]CO_2$ by passage through the CuO column (at 800 C) and then introduced into the cooled reaction vessel RV1 (<-5 C) with 0.7 mL THF solution of $LiAlH_4$ (LAH), prepared carefully under innert atmosphare with air-tight distillation apparatus, at a flow rate of 200 mL/min. After trapping $[^{11}C]CO_2$, THF in RV1 was evaporated by heating under nitrogen gas flow, then, 0.2 mL of water was added after cooling RV1. Generated $[^{11}C]CH_3OH$ was distilled into RV2 (130 C) with 1 mL HI(refluxing) under a flow of nitrogen (70 mL/min), where $[^{11}C]CH_3I$ was synthesized by reaction with HI. Then, $^{11}CH_3I$ was collected in RV3 at about -10 C after purification with Ascarite and phosphorus pentoxide. $[^{11}C]CH_3I$ was allowed to react with 1 mg

Tab.1 Theoretical and practically attainable specific activity

Nuclide	Half Life	Theoretical Value GBq/umol	Practical Value GBq/umol	Author
^{3}H	12.33 y	1.1	—	
^{14}C	5730 y	0.0023	—	
^{11}C	20.4 m	340000	120 (Ro15-1788 - $^{*}CH_3I$)	Suzuki (1985)
			11000 ($^{*}CH_4$)	Berger (1983)
			185 (Alprazolam - $CH_3{}^{*}COOHgBr$)	Banks (1986)
			130 (Prazosin - $^{*}CH_3I$)	Dikeic (1986)
			140 ($H^{*}CH$)@	Fowler (1982)
^{13}N	10.0 m	700000	7 (GABA - $^{*}NH_3$)@	Lambrecht(1986)
^{15}O	122 s	3400000	—	
^{18}F	109.7 m	63000	5200 ($^{*}F^{-}$)	Bergman (1988)
			1900 ($^{*}F^{-}$)	Kilbourn (1986)
			>300 (spiperone - $^{*}F^{-}$)	Hamacher (1986)

@: at the end of bombardment

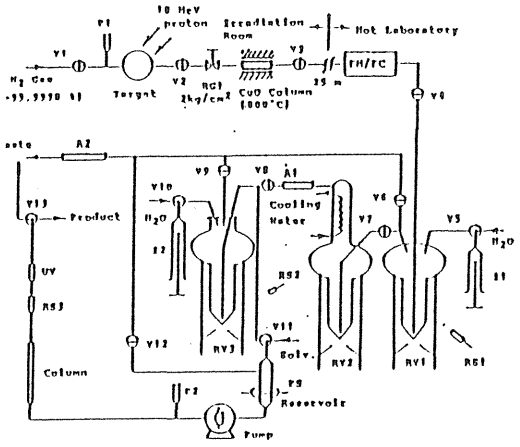

Fig.3 Schematic diagram of the apparatus for the automatic production of ^{11}C-Ro15-1788

V1-V13: Electric valves, RV1-RV3: reaction vessels connected to elevator-direct attachments with cooling, heating and temperature measuring devices (-15 C - 200 C), PI and PT: pressure transducers, PCV: pressure regulator, FM/FC: flow sensor/controller, I1 and I2: syringe for water injection, RS1-RS3: radioactivity sensors, PS: photosensor, UV: detector for u.v. absorption, AL1: absorber (Askalite/P_2O_5), AL2: absorber (Molecular Sieve 5A)

nor-Ro 15-1788 in 0.5 mL DMF containing ca. 1 mg NaH at about 50 C for 1 minute in RV3. The reaction mixture was transferred from RV3 into the reservoir and separated on a Megapak SiI C_{18} column (7.2 x 250 mm, JASCO, Tokyo, Japan) eluting with acetonitrile : 6 mM-H_3PO_4 (35 : 65) at a flow rate of 5 mL/min. The fraction containing [^{11}C]Ro15-1788 (ca.10 mL) was collected in a sterilized flask and evaporated to dryness manually with a rotary evaporator under reduced pressure on a water bath, dissolved in 10 mL sterile isotonic saline solution and filtered through a 0.22 um Millex filter.

The chemical and radiochemical purities of the products were determined using a Finepak SIL C_{18}T column (4.6 x 250 mm, JASCO, Japan) eluting with acetonitrile : 6 mM-H_3PO_4 (60 : 40) at a flow rate of 4 mL/min. The amounts of nor-Ro 15-1788 and Ro 15-1788 were determined by comparison with the corresponding standards. The tests for the presence of pyrogen and bacteria in the product were carried out with Pyrogent (Mallinckrodt Inc, U.S.A.) and Bactec Model RJ01 (Johnston Laboratory, Inc. U.S.A.)

Tab.2 summarizes the results of typical three successive productions of [^{11}C]Ro15-1788, aiming at high specific activity. Each product was sufficient to carry out three clinical studies (0.2 - 0.4 GBq of [^{11}C]Ro15-1788 with specific activity higher than 1.9 GBq/umol was required for one clinical study.) since the yield (10 +/- 2.0 GBq/batch) and the specific activity (110 +/- 20 GBq/umol) of [^{11}C]Ro15-1788 were very high.

The following precautions were taken to prepare [^{11}C]Ro15-1788 with high specific activity, that is, preventing the system from CO_2 contamination by using pure nitrogen gas as a target material, decreasing the volume of the system by using a conical target (inner volume; 75 mL) and fine tubing (i.d. 0.5 mm), drying radioactivity flow line by heating reaction vessels and the CuO column under a pure nitrogen gas flow, sealing the target box with metal instead of rubber 'O' ring, preparing and handling the THF solution of LAH carefully under innert atmosphere and shortening the time required for radiosynthesis and quality control of [^{11}C]Ro15-1788.

Tab.2 Results in the synthesis of ^{11}C-Ro15-1788 for clinical use.

	Run 1	Run 2	Run 3	Average
Yield (mCi)	330	299	191	276+/-76
Radiochemical yield (%)	55.1	55.6	41.8	50.8+/-7.8
Radiochemical purity (%)	99.2	99.1	99.6	99.3+/-0.3
Specific activity (Ci/umol)	3.2	3.2	2.3	2.9+/-0.5
Carrier Ro 15-1788 (umol)	0.107	0.094	0.082	0.094+/-0.013
Ro 15-5520 (umol)	0.033	0.016	0.117	0.055+/-0.054
Pyrogen and bacteria	free	free	free	free
Synthesis time (min.)	23.4	26.6	25.3	25.1+/-1.6

'Irradiation; 18.2 MeV proton, 16-20 uA, 32-40 min.
'Target gas; pure nitrogen (>99.9998 %), 14 kg/cm^2, 15 cm length.
'Yield and specific activity are the value for an I.v. injectable C11-Ro 15-1788.

PROBLEMS CAUSED BY HIGH SPECIFIC ACTIVITY

In the preparation and storage of radiopharmaceuticals with high specific activity, several problems, such as radiolytic decomposition, reactions with trace impurities in solvent and adsorption on the surface of reaction vessels or storage bottles may occure. Complete elimination of substrates from products is also important since they have frequently the similar biochemical effects as products and the amount of substrate used for radio-synthesis is much larger compared to that of product. We observed several ^{11}C-labelled compounds in the DMF solution which was used to trap [^{11}C]CH_3I (specific activity : 74 - 260 GBq/umol) and left at room temperature for a few minutes. This phenomenon was not observed when the specific activity of [^{11}C]CH_3I was much lower and carefully purified DMF was used as solvent. MacGregor et al (1987) reported on the radiolytic self-decomposition of [^{18}F]-N-methylspiperone([^{18}F]NMS) with high specific activity. They synthesized 19 - 37 MBq/ml of [^{18}F]NMS saline solutions with specific activity of 150 -300 GBq/umol and observed the decrease of radiochemical purity of 10 - 25 % by radiolysis during the first hour. They showed that the rate of decomposition of [^{18}F]NMS was proportional to the specific activity of the tracer. We also observed the phenomenon of radiolytic decomposition in the preparation of an ^{11}C.v. injectable 3-N-[^{11}C]methylspiperone([^{11}C]NMS) solution with high specific activity and high radiochemical purity for the measurement of dopamine-D2 recepter in brain with PET (Suzuki, 1990). The radiochemical purity of products varied widely (99 - 90 % at EOS) from batch to batch. Impurities were observed even immediately after

the end of synthesis (including dispensation procedure) and radiochemical purity decreased gradually with time. Radiolytic decomposition of [^{11}C]NMS is described below as a typical example of problem accompanied by high specific activity.

The saline solution of [^{11}C]NMS was prepared by the similar way as described above (Fig. 3) with minor modifications. The time course of radiochemical purity of [^{11}C]NMS were measured on [^{11}C]NMS in two series of solutions: 1)1 mL HPLC eluates used for the purification of [^{11}C]NMS (CH_3CN : 0.03 M-CH_3COONa : CH_3COOH / 100 : 100 : 1) and 2)1 mL [^{11}C]NMS saline solutions for i.v. injection (prepared from the purified [^{11}C]NMS solution by evaporating the solvent, dissolving it in saline and filtrating the solution through a 0.22 um Milex filter), containing a)10 mg KI(hydroxyl radical scavenger), b)no additives and c)10 mg $NaNO_3$ (hydrated electron scavenger), respectively. The solutions were allowed to decay in sealed vials and analyzed at irregular time intervals by radio-HPLC (column; Finepak SIL C_{18} T 4.6 mm dia. x 250 mm, eluent; CH_3CN/0.03M CH_3COONH_4/CH_3COOH (100/100/1), flow rate; 3 mL/min, UV 254 nm). Further information about the compound generated by radiolysis was obtained with LC/MS system(HP1090L/HP5988A, Yokogawa, Tokyo, Japan). Analytical conditions were as follows; column and eluent; same as above, flow rate; 1 mL/min, mass scan range; 180 - 500.

Fig.4 shows the radiochromatogram and mass spectra of the [^{11}C]NMS in saline (0.6 GBq/ml and 31 GBq/umol at EOS). The percent of ^{11}C-labelled unknown product was observed to be 9.1 % and increased with time. From the results of mass spectra, the unknown product was assumed to be the compound generated by the replacement of hydrogen atom on NMS(Mw=409) by hydroxyl group.

Fig.5 shows the dependency of radiochemical purity of [^{11}C]NMS on time and additives. It was observed that the radiochemical purity of [^{11}C]NMS remained constant throughout the experiments in the solutions containing 1 % of potassium iodide(a and A), expected to scavenge hydroxyl radicals generated by the radiolysis of water,. On the other hand, the purity of the [^{11}C]NMS solution of 1 % sodium nitrate (c and C, hydrated electron scavenger) decreased more rapidly than that without additives(b and B). From these results, it seems that hydroxyl radicals generated by radiolysis of water play a very important role in the decomposition of [^{11}C]NMS and that they have to be scavenged for the synthesis of [^{11}C]NMS with high specific activity and high radiochemical purity. This assumption may explain the slow progress of the decomposition in the solution of HPLC eluate(a,b,c) which may act as weak hydroxyl radical scavenger. In the A, B and C solutions, radiochemical purities were very low (84-93 %), even at early time from EOS. This may be caused mainly during solvent elimination in the dispensation process since the [^{11}C]NMS solution is concentrated during the process and acetonitrile evaporates at first. Ethanol and Polysolvate-80 (emulsifier, three alcoholic OH groups are contained in one molecule) was added into the [^{11}C]NMS solution before and after solvent elimination (final concentration: ethanol 0.8 vol.%, Polysolvate-80 1.5 vol.%)

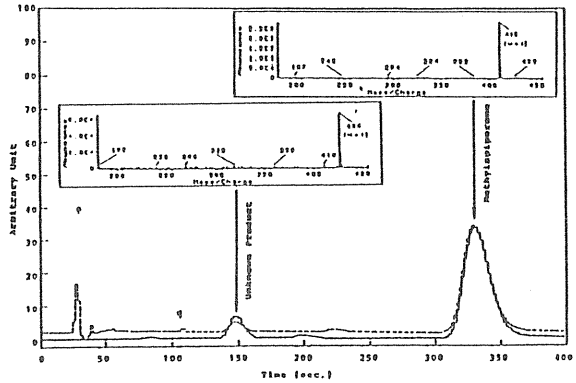

Fig.4 Radiochromatogram and mass spectra of ^{11}C-NMS solution

Mass spectra were reproduced from the result obtained with the LC/MS system. solid line; radioactivity output from Na[I?I] detector, broken line u.v. absorption output at 254 nm, ^{11}C activity and specific activity at EOS; 5.7 GBq/10 ml and 31 GBq/umol, column; Finepak SIL C_{18}T(4.6 x 250 mm), eluent; CH_3CN/0.03M CH_3COONH_4/CH_3COOH(100/100/1), flow rate; 3 ml/min, mass range; 180 - 500 for positive ion.

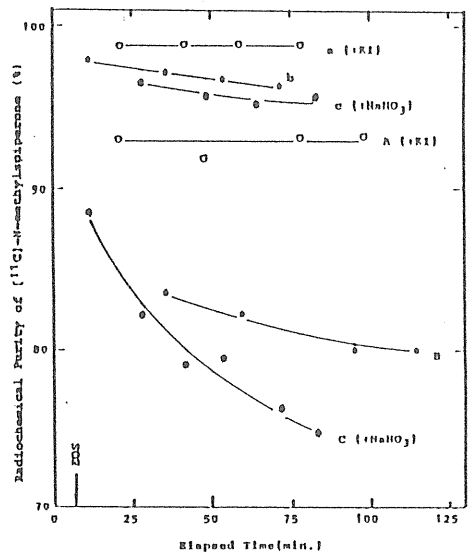

Fig.5 Radiochemical purity of ^{11}C-NMS vs. elapsed time from the end of purification by HPLC.

sample a-c; prepared by adding respective substances in 1 ml HPLC eluates containing 0.4 GBq of ^{11}C-NMS(at the end of purification). sample A-C; prepared by evaporating the solvent of ^{11}C-NMS fraction (residue of ^{11}C-NMS used in the preparation of above a-c), dissolving it in saline, filtrating the solution through 0.22 um filter and then adding respective substances in the filtrates (0.3 GBq of ^{11}C-NMS in 1 ml saline solutions at EOS). a and A; containing 10 mg KI, b and B; no additives, c and C; containing 10 mg $NaNO_3$, specific activity; 35 GBq/umol at EOS.

for suppression of radiolytic decomposition of [^{11}C]NMS and increase of filtration efficiency through a 0.22 um Millex filter. On 47 routine productions after the above improvements, 2.7 +/- 1.7 GBq of [^{11}C]NMS aqueous solutions have been produced at 98.3 +/- 1.0 % radiochemical purity and 37 +/- 18 GBq/umol specific activity (at EOS).

From the above results and discussions, it may be concluded that the saline solution of [^{11}C]NMS decomposes by the reaction with hydroxyl radical generated by the radiolysis of water and that the radiolysis can be suppressed by adding the hydroxyl radical scavenger such as ethanol and potassium iodide.

ATTEMPTS TO ACHIEVE HIGHER SPECIFIC ACTIVITY

Radiotracers with higher specific activity may be obtained by 1)irradiating the target at higher beam current, 2)using the nuclear reactions with larger cross section (^{13}C(p,n)^{13}N, ^{18}O(p,n)^{18}F reactions, etc.), 3)decreasing the carrier amount coming from impurities (^{11}C: using pure N_2 gas target without CO and CO_2 and purified THF solution of LAH without carbonate. ^{13}N: using small amount of pure water without NH_3 and NO_x^-. ^{18}F: using small amount of $H_2{}^{18}O$ and avoiding the use of Teflon tubing or vessels.), 4)designing a new synthetic route where the probability of isotopic dilution is less (use of [^{11}C]CN instead of [^{11}C]CH_3I and [^{18}F]F instead of [^{18}F]F_2), 5)enriching the desired isotope by several methods such as a capillary gaschromatography, a laser technique and a electromagnetic technique. Up to now, the above 1) - 4) have been attempted mainly to obtain radiopharmaceuticals with higher specific activity.

Berger(1983) succeeded to obtain [^{11}C]CH_4 with specific activity of 11,000GBq/umol by capillary gas chromatography at very low temperature (-208 C) on a hydrated soft glass column (Chrompack, i.d. 0.25 mm, length 200 m), using a helium nitrogen mixture (2.5 % N_2 in He) as the eluent. The apparatus and chromatogram are shown in Fig.6. The following subjects have to be solved for the routine production of ^{11}C-labelled radiopharmaceuticals with the technique, that is, increasing the injectable amount of $^{11}CH_4$ (+ $^{12}CH_4$) and effective conversion of [^{11}C]CH_4 into a more reactive precursor ([^{11}C]CH_3I or [^{11}C]HCHO) without isotopic dilution.

Laser technique has been applied to enrich the stable isotopes such as ^{2}H and ^{13}C (Arai S., 1985) using a CO_2 laser. Search of working substances suitable for isotopic enrichment and further labelling process seems to be most important for the technique to be applied in the preparation of short lived radiopharmaceuticals with hish specific activity.

Manser (1989) succeeded to separate ^{81}Rb($T_{1/2}$ = 4.6 h) with an efficiency of >85 % from other isotopes at the depletion factors of 0.2 - 1.5 x 10^5 (^{82m}Rb), 0.6 - 4 x 10^5 (^{83}Rb) and 1.5 - 9 x 10^5 (^{84}Rb), using electromagnetic isotope separator. This technique may be applied to the other short-lived isotope enrichments with small modifications in the injection port of the electromagnetic separator.

For the application of above techniques to the automatic synthesis of short-lived radiotracers, following modifications should be done, i.e., 1)considerable reduction in time required for isotopic enrichment, 2)miniaturization of the equipments to install inside a hot cell, 3)connection to a automatic synthesizer, etc.

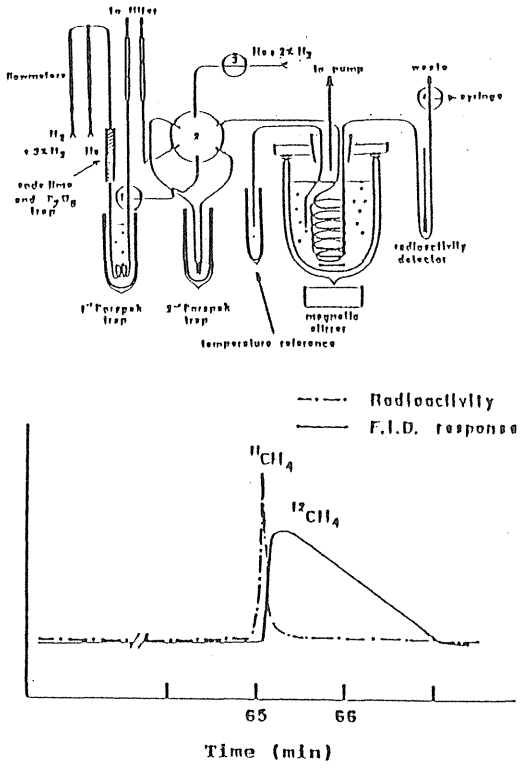

Fig.6 Isotopic separation of $^{11}CH_4$ from $^{12}CH_4$ (Berger, 1983)

ACKNOWLEDGMENT

The authors wish to thank Dr.Y. Kasida, Dr.T. Yamasaki and Dr. Y. Tateno for fruitful discussions and also Mr.K. Tamate for his support in the production of radiopharmaceuticals. Special thanks are also given to the cyclotron crew of NIRS for their excellent support.

References

Arai S., Ishikawa Y., Oyama T., The Review of Laser Engineering, 13, 707, 1985.

Banks. W., Tewson T.J., Digenis G., 7th Int. Symp. on Radiopharm. Chem., pp 69, 1988

Berger G., Prenant C., Sastre J. and Comar D., Int. J. Appl. Radiat. Isot., 34, 1525, 1983

Berger G., Maziere M., Knipper R., Prenant C. and Comar D., Int. J. Appl. Radiat. Isot., 30, 393, 1979

Berger G., Maziere M., Prenant C. and Comar D., Int. J. Appl. Radiat. Isot., 31, 577, 1980

Bergman J., Aho K., Haaparanta M., Reissel A. and Solin O., 7th Int. Symp. on Radiopharm. Chem. pp 143, 1988

Christman D.R., Finn R.D., Karlstrom K.I. and Wolf A.P., Int. J. App. Radiat. Isot., 26, 435, 1975

Crouzel C., Langstrom B., Pike V.W. and Coenen H.H., Appl. Radiat. Isot., 38, 601, 1987

Davis M.E., Akera T., Brody T.M. and Watson L., Proc. Natl. Acad. Sci. USA. 74, 5764, 1977

Diksic M. and Jolly D., 7th Int. Symp. on Radiopharm. Chem., pp 204, 1988

Fowler J.S., Arnett C.D., Wolf A.P., MacGregor R.R., Norton E.F. and Findley A.M., J. Nucl. Med. 23, 437, 1982

Gerozissis K., Rougeot C. and Dray F., Eur. J. Pharmacology., 121, 159, 1986

Hamacher K., Coenen H.H. and Stoecklin G., 6th Int. Symp. on Radiopharm. Chem., pp 15, 1986

Hanser A., Appl. Radiat. Isot., 40, 309, 1989

Iwata R., Ido T., Saji H., Suzuki K., Yoshikawa K., Tamate K. and Kasida K., Int. J. Appl. Radiat. Isot., 30, 194, 1979

Kilbourn M.R., Brodack J.W., Chi D.Y., Dence C.S., Jerabek P.A., Katzenellenbogen J.A., Patrick T.B. and Welch M.J., 6th Int. Symp. on Radiopharm. Chem., pp66, 1986

Lambrecht R.H.D., Slegers G., Mannens G. and Claeys A., ibid., pp 84, 1986

Langstrom B, Antoni G., Gullberg P., Halldin C., Nagren K., Rimland A. and Svard H., Appl. Radiat. Isot. 37, 1141, 1986

MacGregor R.R., Schlyer D.J., Fowler J.S., Wolf A.P. and Shiue C-Y. J. Nucl. Med. 28, 60, 1987

Suzuki K., Inoue O., Hashimoto K., Yamasaki T., Kuchiki M. and Tamate K., Int. J. Appl. Radiat. Isot. 36, 971, 1985

Suzuki K., Inoue O., Tamate K. and Mikado F., Appl. Radiat. Isot., in press.

August 1989

〈研　究〉

Comparative Studies on Various Iterative Image Reconstruction Algorithms for Emission Tomography

Hideo MURAYAMA*1, Eiichi TANAKA*1*2 and Norimasa NOHARA*1

Abstract: Several iterative reconstruction methods appropriate for emission tomography are compared in regard to the rate of convergence and image quality, by using the noise-free and noisy projection sets generated from a mathematical phantom using a computer. Two modified versions of the simultaneous iterative reconstrunction technique (SIRT) method are introduced as the additive SIRT (ASIRT) and the multiplicative SIRT (MSIRT). The MSIRT method is analogous to the iterative space reconstruction algorithm (ISRA). Simulation studies proved that the MSIRT method has faster convergence and better image quality than the ISRA method. It is suggested that, though the expectation maximization (EM) method gives good estimates for the same noisy projection set among all the methods reported here, the fast methods such as the filtered iterative reconstruction algorithm (FIRA) and the conjugate gradient method in weighted version (CONGRW) are good candidates for practical image reconstruction.

INTRODUCTION

Recently, iterative reconstruction methods have received considerable attention for their use in emission computed tomography (ECT), especially in positron emission tomography (PET) which is rapidly emerging as a versatile diagnostic tool in nuclear medicine. Compared to analytical reconstruction methods such as the convolution backprojection (CONVO) method [1] and the Fourier transform method [2], iterative methods have advantages in that they are tolerant to incomplete sampling of projection data, and that it is easy to incorporate a priori information about the emission distribution, such as non-negativity, etc. They are also promising methods for a stationary PET system with fine spatial resolution and high sensitivity using a three dimensional detector arrangement, in which undesirable gaps among the detector banks are inevitable or the finite distance between the adjacent detector elements restricts the spatial resolution of the image over the intrinsic detector resolution [3, 4].

It has been almost 15 years since Gilbert introduced the simultaneous interative Recon-

*1 Division of Physics, National Institute of Radiological Sciences [9-1, Anagawa-4-chome, Chiba-shi, 260 JAPAN]
*2 Hamamatu Photonics K.K.
(Received Sep. 2, 1988 and Accepted Oct. 7, 1988)
This work was supported in part by a grant from the Ministry of Education of Japan.

Key words: Image reconstruction, iterative method,emission computed tomography, positron emission tomography

struction technique (SIRT) method [5], and Goitein proposed the gradient (GRADY) method [6, 7] based on iterative least squares techniques. The conjugate gradient (CONGR) method [7, 8] was also developed in order to accelerate the rate of convergence. In the last five years, the expectation maximization algorithm (EM) method [9, 10], introduced by Shepp and Vardi [11], has been studied extensively by a number of investigators [12-31] because it is based on the realistic assumption that photon counts follow a Poisson process. The virtues of the EM method are not only that convergence to the maximum likelihood estimate can be proven theoretically, but also that automatic inclusion of non-negativity constraints and preservation of total image counts in every iteration are possible. Since its convergence rate is low, modified versions of the EM method have been developed by several authors [18, 19, 21, 23, 24].

One simple method is to reduce the number of views in the initial iteration steps. Another modification is to double or triple the size of the EM step while still proceeding in the EM direction. Lewitt et al [18] and Kaufman [24] suggested accelerated algorithms in which the changes to the images are multiplied at each iteration by an over-relaxation parameter. They obtained about three times faster speed of convergence. From a different approach, Tanaka [34] proposed the filtered iterative reconstruction algorithm (FIRA) method which is based on a modified EM algorithm. This enhances the convergence speed dramatically and improves the frequency response.

In spite of the virtues of the EM method, it is well known [11, 14, 15, 28] that reconstructed images with the EM method become noisy and have large distortions near the edges as iterations proceed beyond a certain point. In order to suppress both the noise and edge artifacts, improved versions of the EM method have recently been proposed to include constraints with a penalty function [23, 31] or to use a method of sieves [15, 16, 22]. Verklerov and Llacer [30] introduced a stopping rule of iterations for the EM method based on statistical hypothesis testing.

As an alternative to the EM algorithm, the image space reconstruction algorithm (ISRA) method has been proposed by Daube-Witherspoon and Muehllehner [32, 35]. In terms of asymptotic theory, the ISRA method provides an image which is not as good as the maximum likelihood in terms of precision [33], but is advantageous since it reduces the size of large, sparsely populated arrays of projection data by backprojecting them directly into a more compact image matrix. The ISRA method is a promising tool particularly for volume imaging, namely, three-dimensional image reconstruction.

The purpose of this paper is to present comparisons among several iterative reconstruction methods for both their algorithms and properties of convergence, from computer simulation studies, and to provide useful information to choose a method for practical use. The FIRA method as a fast algorithm is investigated, comparing with the CONGR method. Two modified versions of the SIRT method, which are called ASIRT and MSIRT, are also introduced in this paper.

METHOD

1. Reconstruction methods

We assume that a set of I measurements y_i $(1 \leq i \leq I)$ are available, where y_i is the number

of events counted in the i-th projection. The basic problem is to estimate the emission density x_j $(1 \leq j \leq J)$ from the measurements, where j is a source pixel in a set of J elements. A set of the J emission densities x_j defines an image vector $\mathbf{x}$. Let us denote the normalized probability that an event emitted from pixel j is assigned to projection i by a_{ij}. Then for each j,

$$\sum_{i=1}^{I} a_{ij} = 1. \tag{1}$$

In this paper, it is assumed that the effects of scattering and attenuation of photons are negligible, and the a_{ij} are known from the geometry. A set of I elements z_i $(1 \leq i \leq I)$ are the expected values of y_i, where

$$z_i = \sum_{j=1}^{J} a_{ij} x_j. \tag{2}$$

1) GRADY method [6, 7]

This method generates a sequence of sets of estimates $x_j^{(n)}$, where the index n specifies the iteration, according to the following step. For each $n=0, 1, \cdots\cdots$, and for each j $(1 \leqq j \leqq J)$,

$$x_j^{(n+1)} = x_j^{(n)} + \beta^{(n)} \Delta x_j^{(n)}, \tag{3}$$

$$\Delta x_j^{(n)} = \sum_{i=1}^{I} (y_i - z_i^{(n)}) a_{ij} / \sum_{i=1}^{I} (a_{ij}/\sigma_i)^2,$$

where $\Delta x_j^{(n)}$ is an error image at pixel x_j at the n-th iteration, and $z_i^{(n)}$ is the expected value of y_i, namely,

$$z_i^{(n)} = \sum_{j=1}^{J} a_{ij} x_j^{(n)}. \tag{4}$$

In eq. (3), $\beta^{(n)}$ is a damping factor which is determined so as to minimize the difference between the measured projections y_i and the estimated projections z_i in a least squares sense. The function to be minimized is

$$\chi^2(\mathbf{x}^{(n)}) = \sum_{i=1}^{I} (y_i - z_i^{(n)})^2 / \sigma_i^2, \tag{5}$$

where σ_i is the uncertainty with which y_i is measured, and $\mathbf{x}^{(n)}$ represents the image vector with J components, $x_j^{(n)}$. In this method, we chose $\sigma_i = 1$ for all i.

2) CONGR method [7, 8]

This method is similar to the GRADY method except that the convergence is improved by making an error image vector in each step of iteration orthogonal to those in the previous steps. While the first step is taken to be the same as in the GRADY method given by eq.(3), the succeeding steps are given by

$$x_j^{(n+1)} = x_j^{(n)} + \beta^{(n)} \Delta x_j^{(n)}, \tag{6}$$

$$\Delta x_j^{(n)} = \sum_{i=1}^{I} (y_i - z_i^{(n)}) a_{ij} / \sum_{i=1}^{I} (a_{ij}/\sigma_i)^2 - \gamma^{(n)} \Delta x_j^{(n-1)},$$

where $\gamma^{(n)}$ is determined so as to make all steps of iteration orthogonal in the sense that,

$$\sum_{i=1}^{I} \left(\sum_{j=1}^{J} a_{ij} \Delta x_j^{(k)} \right) \cdot \left(\sum_{j=1}^{J} a_{ij} \Delta x_j^{(m)} \right) / \sigma_i^2 = 0,$$

for all $k \neq m$, and $\beta^{(n)}$ plays the same role as the damping factor in the GRADY method. In the CONGR method, we chose $\sigma_i = 1$ for all i.

3) **CONGRW method** [7, 8]

This method is a special case of the weighted least squares method and is run using the same algorithm, as given by eq. (6), except that the choice of σ_i is different from the CONGR method. In the CONGRW method, σ_i is given by

$$\sigma_i = \begin{cases} y_i & \text{if } y_i > 0 \\ 1 & \text{if } y_i = 0. \end{cases}$$

4) **EM method** [11]

The iteration step for this method is given by

$$x_j^{(n+1)} = x_j^{(n)} \sum_{i=1}^{I} (a_{ij} y_i / z_i). \tag{7}$$

Equation (7) can be rewritten in the following additive form:

$$x_j^{(n+1)} = x_j^{(n)} + \Delta x_j^{(n)}, \tag{8}$$

$$\Delta x_j^{(n)} = \sum_{i=1}^{I} (y_i - z_i^{(n)}) a_{ij} x_j^{(n)} / \sum_{j=1}^{J} a_{ij} x_j^{(n)},$$

where eqs. (1) and (4) are used to transform eq. (7) into eq. (8).

5. **FIRA method** [21]

This is a method modified from the EM algorithm. Each iteration step is given by

$$x_j^{(n+1)} = \begin{cases} x_j^{(n)} C_j^{\alpha} \cdot U_j^{\beta / A_j} & \text{if } U_j \leq 1 \\ x_j^{(n)} \{C_j^{\alpha} + (U_j - 1) \cdot \beta / A_j\} & \text{if } U_j > 1, \end{cases} \tag{9}$$

where α and β are constants, and

$$C_j = \sum_{i=1}^{I} (y_i a_{ij}) / z_i^{(n)},$$

$$U_j = \sum_{i=1}^{I} [\{y_i a_{ij} (z_i^{(n)} * h)_s\} / \{z_i^{(n)} (y_i * h)_s\}],$$

$$A_j = (x_j + \rho) \sum_{i=1}^{I} [\{a_{ij} (z_i^{(n)} * h)_s\} / \{z_i^{(n)} (y_i * h)_s\}].$$

Here ρ is a small positive constant, and h is a low-pass filter, namely

$$h \equiv h(s) = (s^3 + 2s^2 + 3)^{-1} \ (-10 \leq s \leq 10), \tag{10}$$

where s is the bin number of the projections in the same view angle of the projection i. Two convolutions, $(z_i^{(n)} * h)_s$ and $(y_i * h)_s$, are performed on the sampling points on the s axis.

The total density of the reconstructed image is normalized to the total number of events at every iteration. For noisy data, the correction matrix U_j for the high frequency component is smoothed by a nine-point weighted filter (1 : 2 : 1 for the X and Y directions) before inserting it into eq. (9). In this study, we used the parameters $\alpha = 2$ and $\beta = 0.8$ in the first iteration, but the β value was halved in the following iterations.

6) **ISRA method** [32]

This method uses the following iteration step,

$$x_j^{(n+1)} = x_j^{(n)} \left(\sum_{i=1}^{I} y_i a_{ij} \right) / \left(\sum_{i=1}^{I} z_i^{(n)} a_{ij} \right). \tag{11}$$

Projection data are back-projected into image space, and the back-projected image is compared to an image produced by projections calculated from the corresponding iterative reconstruction image in each iteration.

The total density of the image is normalized to the total number of events at every

iteration.

7) **ASIRT method**

We introduce a new algorithm given by

$$x_j^{(n+1)} = \mathrm{Max}\,[x_j^{(n)} + \sum_{i=1}^{I}(y_i - z_i^{(n)})a_{ij}/b_i,\ 0], \tag{12}$$

where

$$b_i = \sum_{j=1}^{J} a_{ij}. \tag{13}$$

The total density of the image is normalized to the total number of events at every iteration. This algorithm is analogous to the additive form of the Gilbert's SIRT [5], which is described using components whose length is that of the i-th ray, and where the number of pixels lying along the particular i-th ray are substituted for a_{ij} and b_i in eq. (12). For this reason, the new method is called the additive simultaneous iterative reconstruction technique (ASIRT).

Compared with eq. (8) in the additive form of EM, eq. (12) is a similar expression except for the factor multipling the residual $(y_i - z_i^{(n)})$. In ASIRT the factor is proportional to a_{ij} and its normalization over all the J pixels, while in EM the factor is $a_{ij}x_j$ and its normalization. The former is a simplified algebraic expression of the latter.

8) **MSIRT method**

Another new algorithm is introduced by

$$x_j^{(n+1)} = x_j^{(n)} \sum_{i=1}^{I} (y_i a_{ij}/b_i) / \sum_{i=1}^{I}(z_i^{(n)} a_{ij}/b_i), \tag{14}$$

where b_i is given by eq. (13) and total density of the image is normalized to the total number of events at every iteration. This algorithm is analogous to the multiplicative form of Gilbert's SIRT [5], and it is therefore called the multiplicative simultaneous iterative reconstruction technique (MSIRT).

Equation (14) is a similar algebraic expression to eq. (11) in ISRA. At the backprojection stage, MSIRT uses a dividing factor, b_i, in order to correct the total detection probability for each i-th projection, but ISRA neglects this factor. This algorithm is derived by minimizing the least-squares distance measures between y_i and z_i as in [33]. The quantity to be minimized with respect to the (x_j) is

$$\sum_{i=1}^{I} w_i\,(y_i - \sum_{j=1}^{J} a_{ij}x_j)^2, \tag{15}$$

where the w_i's are weighting factors. If we denote the vector (y_i) by $\mathbf{y}$, the $I \times J$ matrix (a_{ij}) by [A], and the diagonal matrix (w_i) by [W], then this can be written as

$$(\mathbf{y} - [A]\mathbf{x})^T [W](\mathbf{y} - [A]\mathbf{x}), \tag{16}$$

where T denotes transpose.

The least squares estimates, $\hat{\mathbf{x}}$ of $\mathbf{x}$ are obtained by solving

$$[A]^T[W][A]\hat{\mathbf{x}} = [A]^T[W]\mathbf{y} \tag{17}$$

The link with the MSIRT can be made by noting that the j-th equation in (17) is written

$$\sum_{i=1}^{I} a_{ij}w_i(\sum_{r=1}^{J} a_{ir}x_r) = \sum_{i=1}^{I} y_i a_{ij} w_i, \tag{18}$$

or

$$1=\sum_{i=1}^{I}(y_i a_{ij} w_i)/\{\sum_{i=1}^{I}(\sum_{r=1}^{J} a_{ir}x_r)a_{ij}w_i\}. \quad (19)$$

Multiplication of both sides by x_j provides the following equation

$$x_j^{(n+1)}=x_j^{(n)}(\sum_{i=1}^{I} y_i a_{ij} w_i)/(\sum_{i=1}^{I} z_i^{(n)} a_{ij} w_i). \quad (20)$$

The weighting factor (w_i) should be chosen to be about the same size for all the components in expression (15). If all the components of $\mathbf{x}$ are equal, then we should choose

$$w_i=1/\sum_{j=1}^{J} a_{ij}. \quad (21)$$

This introduces the MSIRT algorithm. The above assumption is reasonable when we choose a uniformly distributed source for the initial guess of $\mathbf{x}$. The ISRA algorithm is also derived from the same equation, (20), for the case that $w_i=1$ for all i.

2. Simulated data

The mathematical simulation phantom as shown in **Fig. 1 A** was generated by computer. **Fig. 1 B** shows the emission density distribution. The mathematical phantom is digitized in a 64×64 matrix and the emission density x_j is unifrom within a square pixel j. We restricted the reconstruction region to a circle inscribed in a 64×64 square, and chose equispaced projections in which rays are prarallel lines with uniform spacing of the same side of a pixel.

A "true" noise-free image was prepared for the simulation study. Corresponding to the true image vector $\mathbf{T}$, a set of noise-free projection data y_i's was calculated analytically for 240 equally spaced angles over 180° from the following equation. For each i ($1\leq i\leq I$),

$$Y_i=\sum_{j=1}^{J} a_{ij}T_j, \quad (22)$$

where T_j is the j-th component of the true image vector $\mathbf{T}$, $J=3228$ and $I=68\times240$. A set of noisy projection data was also obtained by generating pseudo-random numbers from a Poisson distribution with a mean equal to the noise-free value of Y_i.

In the following simulation study, we used the three sets of projection data based on the same phantom: the first was the noise-free data with a total count of 1×10^6, the second was the noisy data with a total count of 1×10^6, and the third was the noisy data with a total count of 2×10^5. By using the Shepp-Logan convolution method [1], the reconstructed images shown in **Figs. 1 C, D and E** were obtained form the first, second and third projection data sets, respectively.

In this study, all the iterative reconstruction procedures were started from a uniform disk, namely the initial set of estimates $x_j^{(0)}$ is given by

$$x_j^{(0)}=\sum_{i=1}^{I} y_i/J, \text{ for all j.} \quad (23)$$

No constraints or a priori information were used in any of the reconstruction methods in order to clearly show differences between the algorithms.

Three functions were defined as measures of the goodness of the estimated image. The first was the mean absolute error, $m(\mathbf{x})$, of the image defined by

$$m(\mathbf{x})=\sum_{j=1}^{J}|x_j-T_j|/\sum_{j=1}^{J}T_j. \quad (24)$$

The second was the square of residual norm, $N^2(\mathbf{x})$, of the projection data defined by

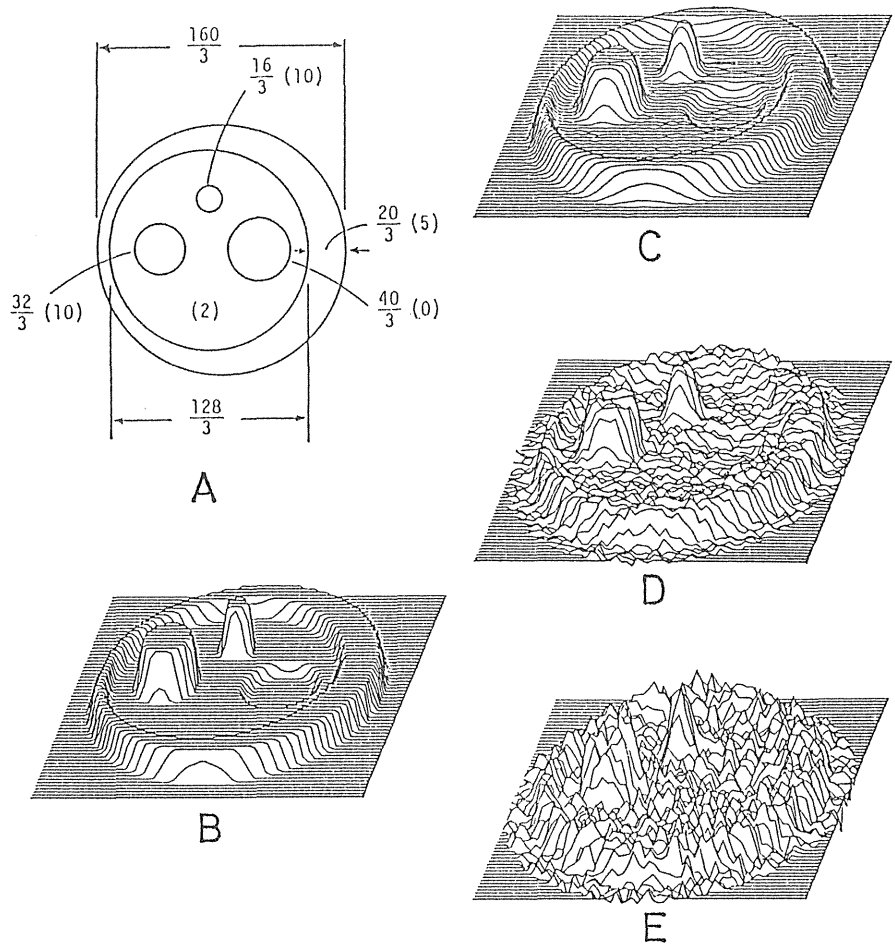

Fig. 1 The mathematical phantom used in the simulation (A), and its image (B). The values in front of the parentheses are diameters or distances in units of pixel width, and the values in parentheses are relative emission densities. Images C, D and E are reconstructed with the convolution backprojection (CONVO) method for the three sets of projection data; the noise-free data, and the two noisy data sets with the total counts of 1×10^6 and 2×10^5, respectively. These images are normalized by their total counts.

$$N^2(\mathbf{x})=\sum_{i=1}^{I}(y_i-z_i)^2. \tag{25}$$

The third was the log likelihood function $1(\mathbf{x})$, defined by

$$1(\mathbf{x})=\sum_{i=1}^{I}(y_i \log z_i-z_i). \tag{26}$$

The function $m(\mathbf{x})$ provides a measure of "source convergence", $N^2(\mathbf{x})$ provides a measure of "projection convergence" in the sense of mean square error and $1(\mathbf{x})$ indicates how closely the reconstructed image approaches the maximum likelihood estimate. Simulation studies allow the evaluation of $m(\mathbf{x})$ by the direct comparison of reconstructed image with the true source distribution, but in practice, the other two functions only are available because the true image is usually unknown.

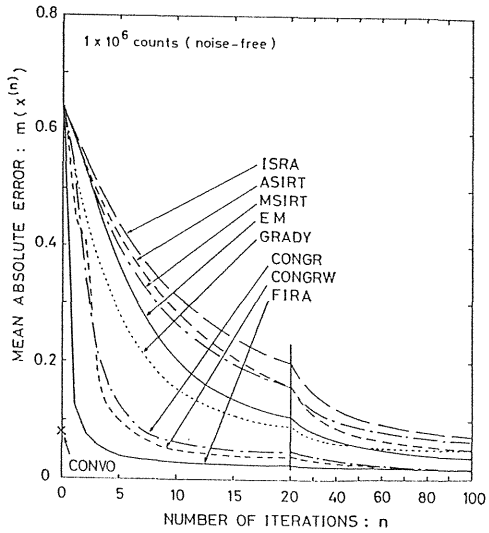

Fig. 2 Plots of the mean absolute error m ($\mathbf{x}^{(n)}$) as a function of the iteration number n, for the noise-free projection set. The point marked on the ordinate shows the value of m($\mathbf{x}$) for the CONVO image.

RESULTS AND DISCUSSION

1. Convergence for noise-free data

First of all, reconstruction was performed using noise-free projection set to demonstrate the dependence of rate of convergence on the reconstruction method. **Fig. 2** shows plots of the mean absolute error m($\mathbf{x}^{(n)}$) as a function of the number of interations n, for the first 100 iterations with the eight different methods. The value of m($\mathbf{x}$) for the CONVO image (**Fig. 1 C**) is marked by "x" on the ordinate of **Fig. 2**.

Plots of the square of residual norm $N^2(\mathbf{x}^{(n)})$ and the log likelihood $1(\mathbf{x}^{(n)})$ are shown in **Figs. 3 and 4**, respectively. It can be seen that, as the number of iteration increases, m($\mathbf{x}^{(n)}$) and $N^2(\mathbf{x}^{(n)})$ decrease monotonically, and $1(\mathbf{x}^{(n)})$ increases monotonically. **Fig. 5** shows the reconstructed images at 20 iterations with all methods. As compared with the CONVO image, FIRA, CONGRW and CONGR yield superior images, while GRADY and EM provide almost the same image quality, and ASIRT, MSIRT and ISRA provide inferior images. We found that by the 100-th iteration the images of all methods are close enough to the true image shown in **Fig. 1 B**.

In order to evaluate the rate of convergence quantitatively, we introduced three CONVO equivalent iteration numbers n(m), $n(N^2)$ and n(1), which give the closest reconstruction images to the CONVO image by measures of the mean absolute error, the square of residual norm and the log likelihood, respectively. **Table 1** lists the CONVO equivalent iteration numbers for all the methods reported here. The fastest convergence was obtained with FIRA and the second fastest with CONGRW. The slowest is ISRA. The EM method is faster than ASIRT, while ISRA is slower than MSIRT.

Compared with GRADY, EM is inferior in terms of both n(m) and $n(N^2)$, but superior

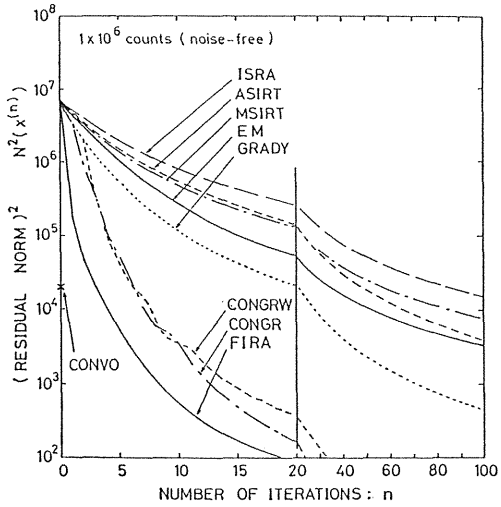

Fig. 3 Plots of the square of residual norm $N^2(\mathbf{x}^{(n)})$ as a function of the iteration number n for the noise-free projection set. The point marked on the ordinate shows the value of $N^2(\mathbf{x})$ for the CONVO image.

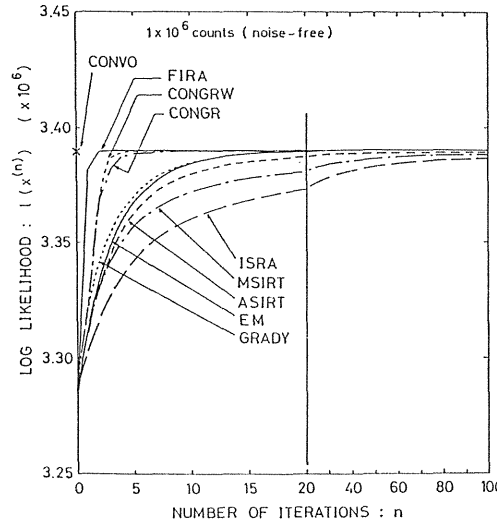

Fig. 4 Plots of the log likelihood $l(\mathbf{x}^{(n)})$ as a function of the iteration number n for the noise-free projection set. The point marked on the ordinate shows the value of $l(\mathbf{x})$ for the CONVO image.

in terms of n(1); the value of n(1) is about a half of $n(N^2)$ for EM, but n(1) is nearly equal to $n(N^2)$ for GRADY. This reflects the fact that the EM algorithm is designed to pursue the maximum likelihood estimate. That is, EM incorporates larger weights on the matching of projection data with low counts as compared with GRADY. The value of $N^2(\mathbf{x})$ is affected by the difference between measured and estimated projections with equal weight as given by eq. (25), while the matching of the low count data seriously affects the

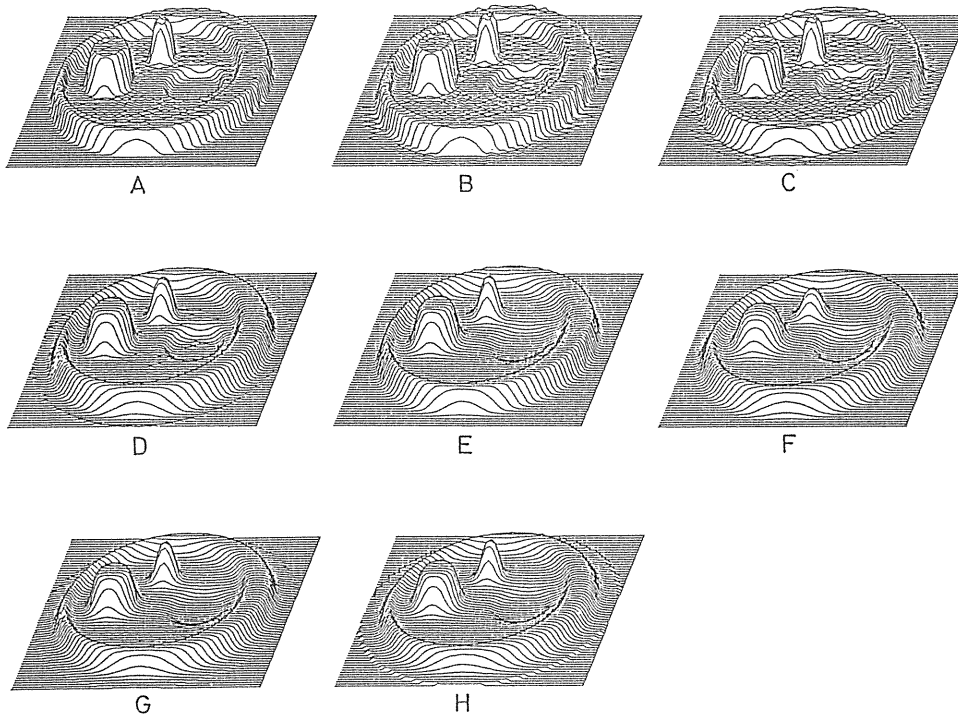

Fig. 5 Reconstructed images at 20 iterations with FIRA (A), CONGRW (B), CONGR (C), GRADY (D), EM (E), ASIRT (F), MSIRT (G) and ISRA (H), for the noise-free projection set.

Table 1 Comparison of the CONVO equivalent iteration numbers n(m), n(N^2) and n(1), where the reconstructed image is closest to the CONVO image in **Fig. 1 C**, by measure of the mean absolute error, the square of residual norm and the log likelihood.

Method	CONVO equivalent iteration number		
	n (m)	n (N^2)	n (1)
FIRA	2	3	2
CONGRW	6	6	4
CONGR	8	6	6
GRADY	25	21	20
EM	31	35	19
ASIRT	46	48	35
MSIRT	62	57	>100
ISRA	82	86	>100

value of n(1) due to the terms of log z_i in eq. (26). For the same reason, both MSIRT and ISRA provide much larger values of n(1) than the values of n(m) and n(N^2) when compared to EM.

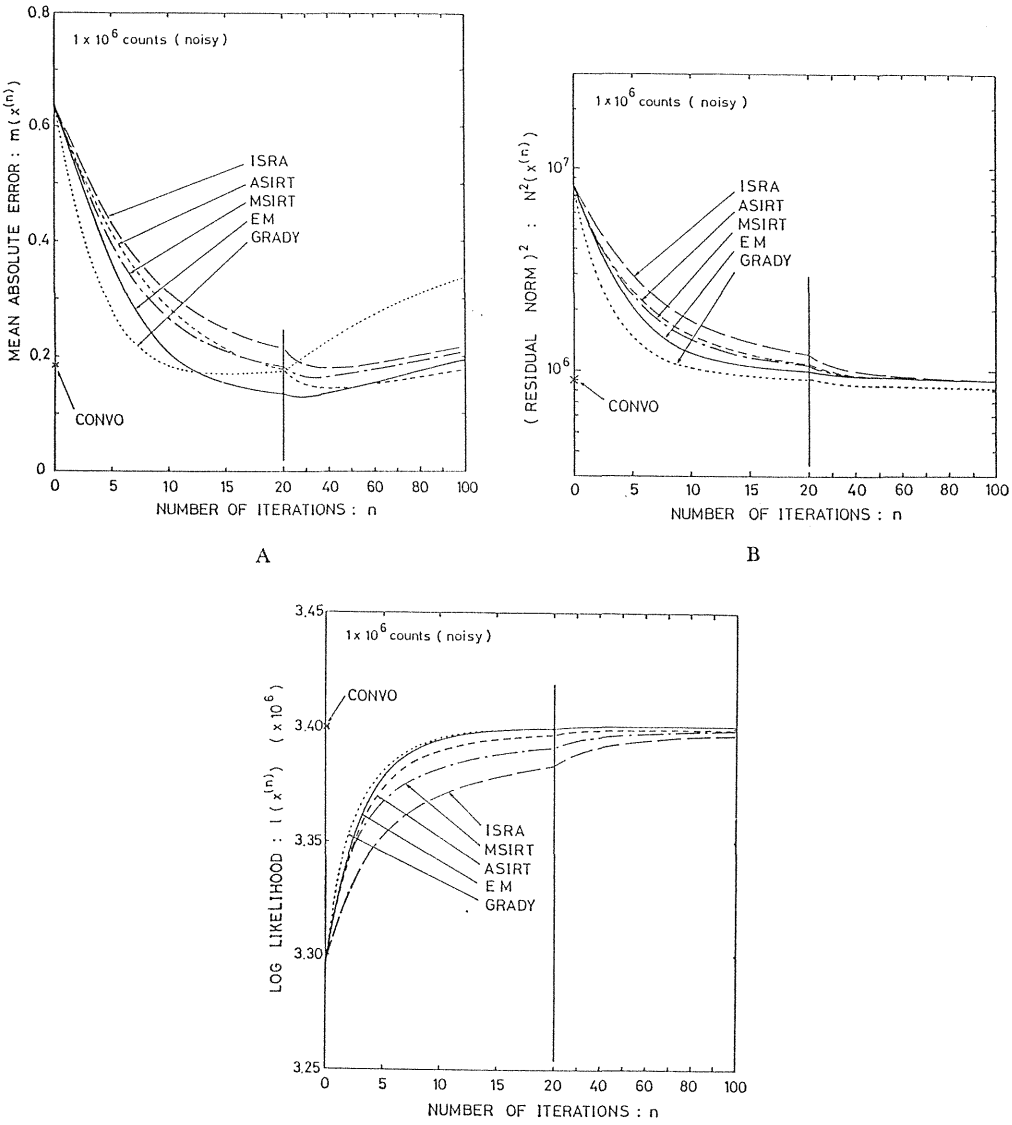

Fig. 6 Plots of (A) the mean absolute error $m(\mathbf{x}^{(n)})$, (B) the square of residual norm $N^2(\mathbf{x}^{(n)})$, and (C) the log likelihood $1(\mathbf{x}^{(n)})$, respectively, as a function of iteration number n for the noisy projection set with the total count of 1×10^6.

2. Convergence of slow methods for noisy data

In this section, we shall be concerned with the five slow methods of GRADY, EM, ASIRT, MSIRT and ISRA only, in order to avoid complexity in the comparative discussion. The others, FIRA, CONGRW and CONGR, will be discussed in the next section. In order to examine the effects of statistical noise on the rate of convergence, the reconstruction was performed for the noisy projection set with a total count of 1×10^6. **Figs. 6 A, B, and C** show plots of the mean absolute error $m(\mathbf{x}^{(n)})$, the square of the residual norm $N^2(\mathbf{x}^{(n)})$ and the log likelihood $1(\mathbf{x}^{(n)})$, respectively, for the first 100 iterations. The values of $m(\mathbf{x})$,

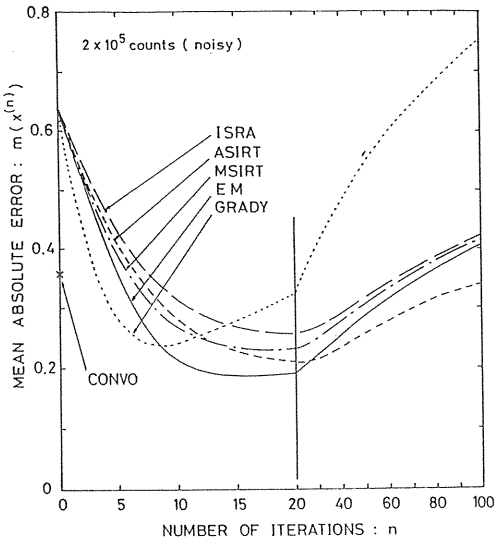

A

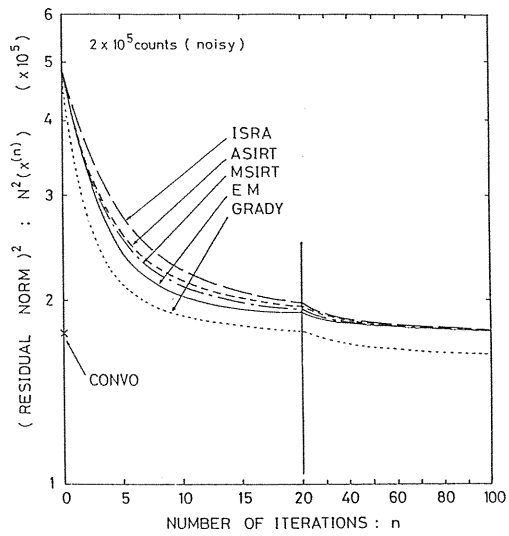

B

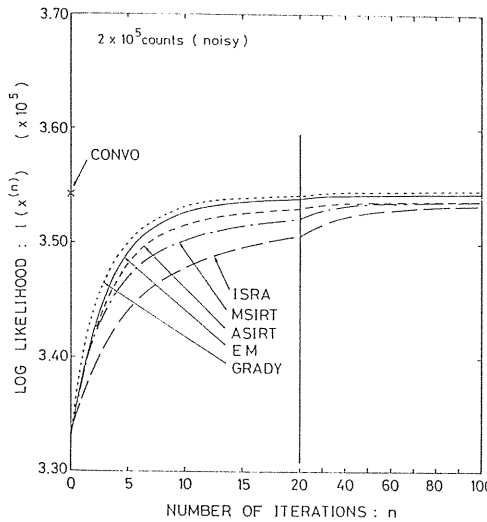

C

Fig. 7 Plots of (A) the mean absolute error $m(\mathbf{x}^{(n)})$, (B) the square of residual norm $N^2(\mathbf{x}^{(n)})$, and (C) the log likelihood $1(\mathbf{x}^{(n)})$, respectively, as a function of iteration number n for the noisy projection set with the total count of 2×10^5.

$N^2(\mathbf{x})$ and $1(\mathbf{x})$ for the CONVO image (**Fig. 1 D**) are marked by "x" on the ordinates of the corresponding plots.

Although the values of $m(\mathbf{x}^{(n)})$ approach zero for noise-free data, **Fig. 6 A** demonstrates that noise in the projection data prevents this and causes the values to increase after a certain number of iterations regardless to the recontruction method. By contrast, the values of $N^2(\mathbf{x}^{(n)})$ in **Fig. 6 B** and $1(\mathbf{x}^{(n)})$ in **Fig. 6 C** do not change their monotonical behavior, similar to the plots of **Fig. 3 and 4**. The plots of $1(\mathbf{x}^{(n)})$ have almost the same shape as the plots of **Fig. 4**. This implies that the relative values of $1(\mathbf{x}^{(n)})$ are insensitive to

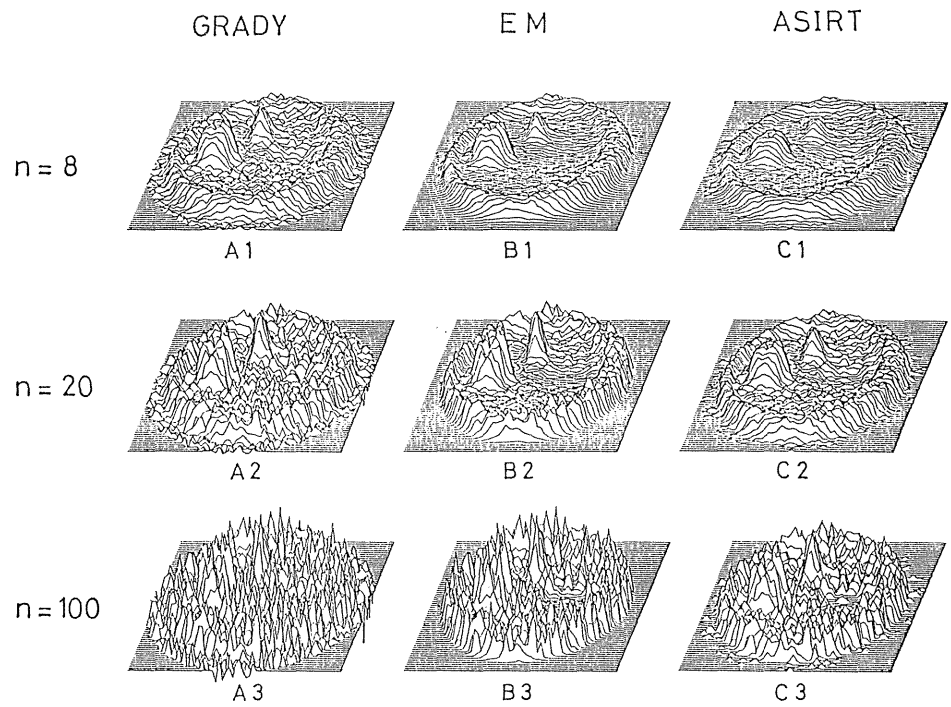

Fig. 8 Reconstructed images at 8, 20 and 100 iterations with GRADY (A 1, A 2, A3), EM (B 1, B 2, B 3), and ASIRT (C 1, C 2, C 3), for the noisy projection set with the total count of 2×10^5. The top, middle and bottom images were obtained at iteration numbers of n=8, 20 and 100, respectively.

existence of noise in the projection data.

To demonstrate a noisier situation, we ran the methods for 100 iterations, using another noisy projection set with the total count of 2×10^5. The resulting plots of $m(\mathbf{x}^{(n)})$, $N^2(\mathbf{x}^{(n)})$ and $1(\mathbf{x}^{(n)})$ are shown in **Figs. 7 A, B and C**, respectively. For all the methods, the minimum values of $m(\mathbf{x}^{(n)})$ in **Fig. 7 A** are obtained at a smaller number of iterations than in **Fig. 6 A**. The monotonical behavior of the functions $N^2(\mathbf{x}^{(n)})$ and $1(\mathbf{x}^{(n)})$ does not change in **Figs. 7 B and C**.

Fig. 8 illustrates the reconstructed images obtained from the noisy projection set with 2×10^5 counts at 8, 20 and 100 iterations with the GRADY, EM and ASIRT methods. All the bird's-eye view images at 100 iterations demonstrate "noise artifacts", and the reconstructed images differ from the true image at high iteration numbers. From this, it is apparent that both the functions $1(\mathbf{x})$ and $N^2(\mathbf{x})$ are not good measures to obtain desirable reconstruction with noisy data.

Outside the boundary of the phantom in **Fig. 8**, GRADY introduces noise enhancement even at low iterations, due to the lack of non-negativity constraints, and ASIRT produces dot-like artifacts due to the non-linear operation carried out in order to remove negative image density. EM produces much less noise due to the automatic non-negativity constraints. One remarkable result from **Figs. 6 A and 7 A** is that EM provides the smallest value of $m(\mathbf{x})$ among all the methods for the same noisy projection set. The minimum value of $m(\mathbf{x}^{(n)})$ for EM is 0.129 at n=28 for 1×10^6 counts, and 0.188 at n=16 for 2×10^5 counts.

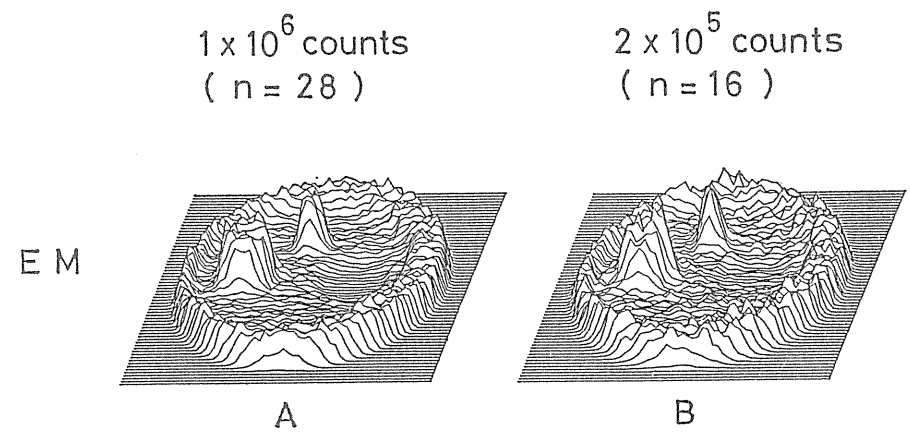

Fig. 9 Reconstructed images at 28 iterations with EM for the noisy projection set with the total count of 1×10^6 (A), and at 16 iterations with 2×10^5 (B).

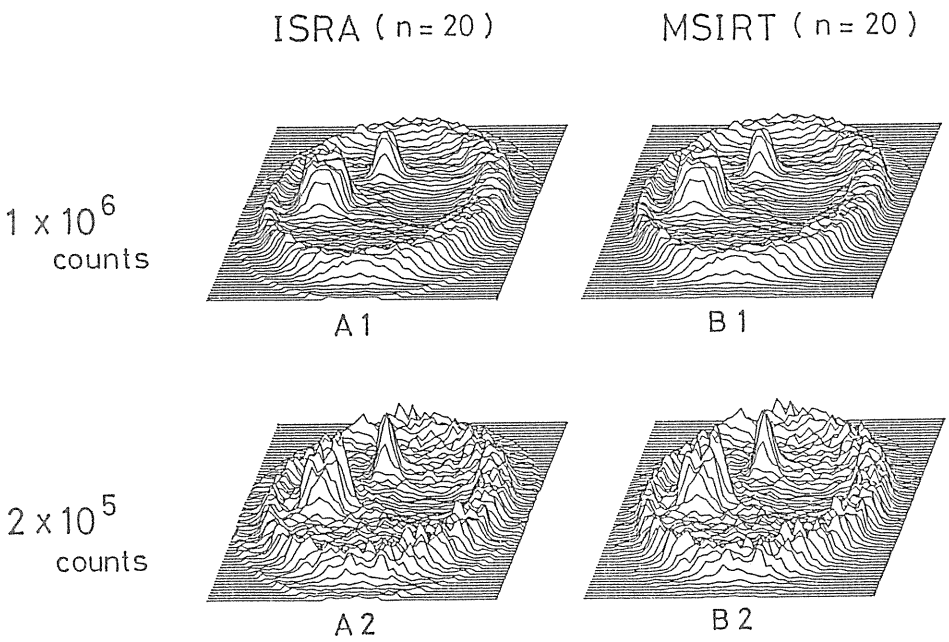

Fig. 10 Reconstructed images at 20 iterations with ISRA (A 1, A 2), and MSIRT (B 1, B 2). The top and bottom images were obtained by using the noisy projection sets with total counts of 1×10^6 and 2×10^5, respectively.

The corresponding reconstructed images are shown in **Figs. 9 A and B.**

Fig. 10 illustrates the reconstructed images at 20 iterations with ISRA and MSIRT for the noisy projection sets with total counts of 1×10^6 and 2×10^5. The MSIRT method has almost the same recovery rate of spatial resolution and the same noise properties as ISRA. The only difference between the two methods is that, outside the object, MSIRT has faster recovery than ISRA. This difference gives an insight into the reason why the minimum value of $m(\mathbf{x})$ for MSIRT is smaller than that for ISRA, as shown in both **Figs. 6 A and 7 A.** Thus, we can expect that MSIRT provides better images as compared with ISRA for

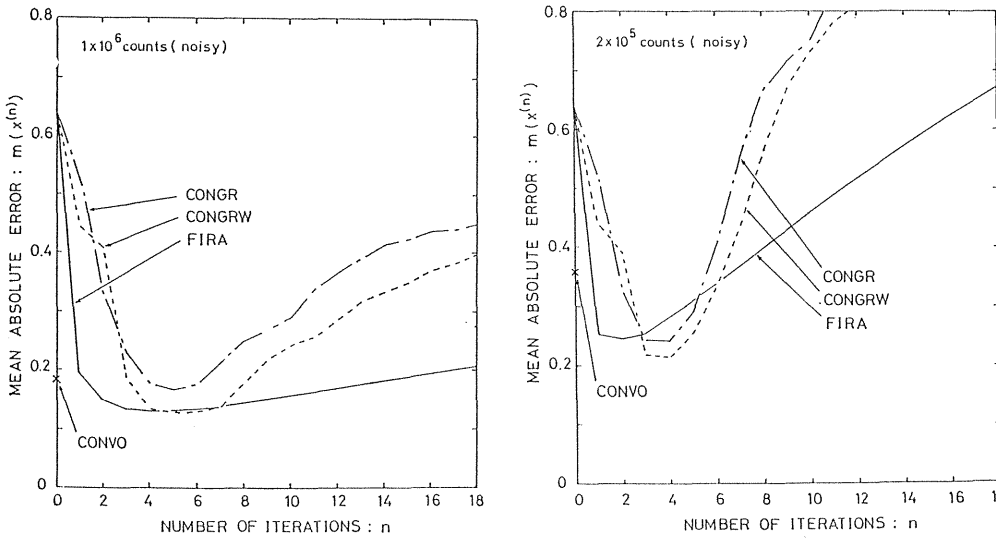

Fig. 11 Plots of the mean absolute error $m(\mathbf{x}^{(n)})$ as a function of iteration number n for the noisy projection sets with total counts of 1×10^6 (A) and 2×10^5 (B).

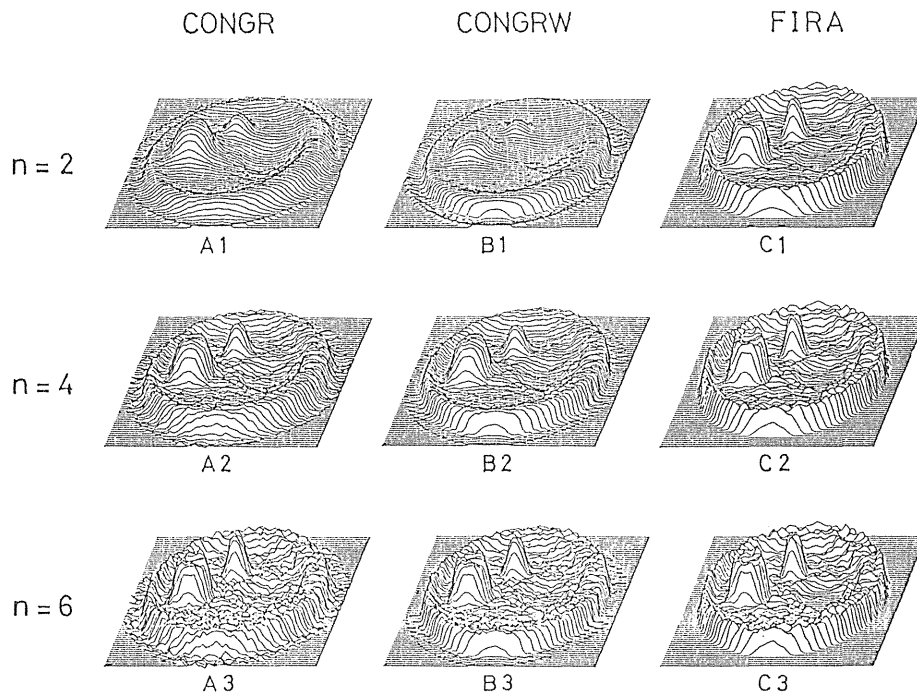

Fig. 12 Reconstructed images at 2, 4 and 6 iterations with CONGR (A 1, A 2, A 3), CONGRW (B 1, B 2, B 3) and FIRA (C 1, C 2, C 3), for the noisy projection set with the total count of 1×10^6. The top, middle and bottom images were obtained at iteration numbers of n=2, 4 and 6, respectively.

the same noisy projection set.

3. Convergence of the fast methods for noisy data

In this section, the three fast methods of FIRA, CONGRW and CONGR are compared.

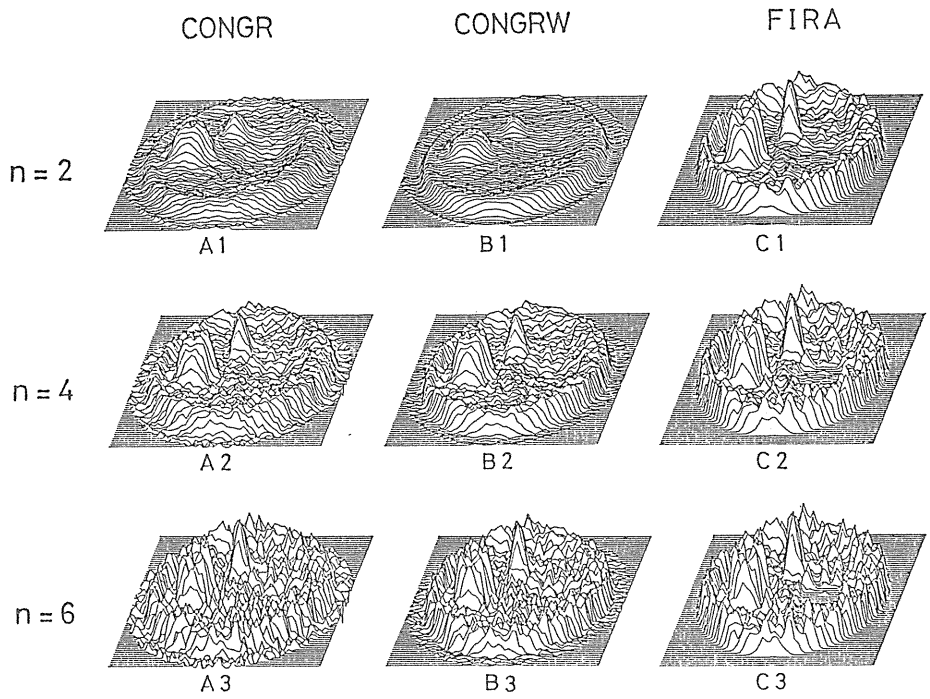

Fig. 13 Reconstructed images at 2, 4 and 6 iterations with CONGR (A 1, A 2, A3), CONGRW (B 1, B 2, B 3) and FIRA (C 1, C 2, C3), using the noisy projection set with a total count of 2×10^5. The top, middle and bottom images were obtained at iteration numbers of n=2, 4 and 6, respectively.

Figs. 11 A and B show plots of the mean absolute error $m(\mathbf{x}^{(n)})$ for the first 18 iterations using the noisy projection sets with the total counts of 1×10^6 and 2×10^5, respectively. These plots demonstrate the fast convergence of FIRA for the noisy data as well as for the noise-free data. This is because the frequency response of the iterative correction is significantly improved by incorporating adequate high frequency enhancement in the FIRA reconstruction. A suitable number of iterations may be from 2 to 4. In addition, FIRA proved to be more stable, based on the values of $m(\mathbf{x}^{(n)})$, when iterating after the minimum value had been reached, compared with CONGR and CONGRW. This is because FIRA uses a selective filter function such as eq. (10), with which the convergence of each frequency component is controlled.

Figs. 12 and 13 illustrate the reconstructed images at 2, 4 and 6 iterations with the three methods for the two noisy projection sets. It can be seen that FIRA produces better images at a few iterations. The image of C 1 with FIRA at n=2 provides a similar recovery of resolution as the image of B 3 with CONGRW at n=6, while the former image produces less noise than the latter. This is because the automatic non-negativity constraints involved in FIRA effectively suppress the noise enhancement in areas of low image density, in a similar way to EM. From the above comparison, we conclude that FIRA is a good candidate for the image reconstruction of ECT data, in practice.

From **Figs. 11 A and B**, it is seen that CONGRW has a smaller minimum value of $m(\mathbf{x}^{(n)})$ than CONGR, while the minimum values for both methods are obtained at almost

the same iteration number. A comparison of the reconstructed images with CONGR and CONGRW in **Figs. 12 and 13** shows that CONGRW is superior to CONGR due to the suppression of the noise in areas outside the object. This is because CONGRW achieves better matching of projection data with low counts than that with high counts by virtue of the weighted least squares, with which the low counts are assigned large weights to the minimizing function given by eq. (5).

The image quality for the fast methods is not pariticularly worse than that for the slow methods. From **Fig. 11 A**, the minimum value of $m(\mathbf{x}^{(n)})$ with CONGRW is 0.130 for 1×10^6 counts, which is very close to the corresponding value (0.129) with EM from **Fig. 6 A**. The CONGRW method seems to be practical because the minimum value of $m(\mathbf{x}^{(n)})$ is achieved at $n=5$ iterations, which is about 6 times faster compared with $n=28$ iterations with EM. For 2×10^5 counts, however, the minimum value of $m(\mathbf{x}^{(n)})$ with CONGRW becomes larger than EM. Compared with the image of EM shown in **Fig. 9 B**, the image of CONGRW in **Fig. 13 B 2** is inferior especially in areas of low image density. This is due to the excess enhancement of the high-frequency component of statistical noise, although the reconstructed images are sharpened too much at early iterations. For the FIRA method, we have the freedom to select the parameters α, β and the filter h(s) in eq. (9), so as to minimize degradation of the image quality. Further studies on FIRA will be reported elsewhere [34].

CONCLUSION

For a noise-free projection set, all the methods reported here provide stable convegence; that is, the three functions, $m(\mathbf{x})$, $N^2(\mathbf{x})$ and $1(\mathbf{x})$, approach their final values monotonically as the iterations proceed. The three CONVO equivalent iteration numbers, $n(m)$, $n(N^2)$ and $n(1)$ were used to evaluate the rate of convergence. From these quantitative comparisons, the fastest convergence can be obtained with the FIRA method.

Discrepancies in the values of $n(N^2)$ and $n(1)$ are observed with some methods; namely, FIRA, CONGRW, EM and ASIRT give smaller values of $n(1)$ than $n(N^2)$, while MSIRT and ISRA give larger values of $n(1)$. This is because the former methods incorporate larger weights for matching low count projections than for high count projections, compared to the latter methods. The former methods are superior in terms of noise enhancement in the area outside the object.

We introduced the MSIRT method as a candidate for the reconstruction of volume images. This is a modified algorithm of Gilbert's SIRT and has a similar algebraic expression to ISRA. It was shown that MSIRT provides faster convergence and better image quality than ISRA, especially in the area outside the object.

In practical use, the FIRA method is a good choice due to its fastest convergence, its low noise on the images with the automatic non-negativity constraints, and comparatively stable image quality for iterations after the optimum at 2-4 iterations. The CONGRW method is also useful in some practical cases because it provides adequate images at several iteration numbers.

ACKNOWLEDGEMENT

The authors wish to thank T. Tomitani, M. Yamamoto of NIRS and H. Toyama of Tokyo Metropolitan Institute of Gerontology for their useful discussions. We wish to express appreciation to K. Fukuhisa of NIRS for his technical assitance.

REFERENCES

[1] Shepp LA, Logan BF: Fourier reconstruction of a head section. IEEE Trans Nucl Sci **NS-21**: 21-43, 1974

[2] Mersereau RM: Direct Fourier transform techniques in 3-D image reconstruction. Comput Biol Med **6**: 247-258, 1976

[3] Meuhllehner G, Karp JS: A method for reconstructing images from data obtained with a hexagonal bar positron camera. IEEE Trans Med Imag **MI-4**: 134-138, 1985

[4] Tanaka E, Nohara N, Tomitani T et al: Stationary positron emission tomography and its image reconstruction. IEEE Trans Med Imag **MI-5**: 199-206, 1986

[5] Gilbert P: Iterative methods for the three-dimensional reconstruction for an object from projections. J Theor Biol **36**: 105-117, 1972

[6] Goitein M: Three-dimensional density recosntruction from a series of two-dimensional projections. Nucl Instr Meth **101**: 509-518, 1972

[7] Huesman R, Gullberg GT, Greenbey WL, et al: RECLBL library user's manual; Donner algorithms for reconstruction tomography. Publication PUB-214, Lawrence Berkeley Laboratory, 1977

[8] Budinger TF, Gullberg GT, Huesman RH: Emission Computed Tomography. In: Image reconstruction from projection; Implementation and application, Herman GT (ed.), New York, Spring-Verlag, pp. 147-246, 1979

[9] Rockmore AJ, Macovski A: A maximum likelihood approach to emission image reconstruction from projections. IEEE trans Nucl Sci **NS-23**: 1428-1432, 1976

[10] Rockmore AJ, Macovski A: A maximum likelihood approach to transmission image reconstruction from projections. IEEE Trans Nucl Sci **NS-24**: 1929-1935, 1977

[11] Shepp LA, Vardi Y: Maximum likelihood reconstruction for emission tomography. IEEE Trans Med Imag **MI-1**: 113-122, 1982

[12] Lange K, Carson R: EM reconstruction algorithms for emission and transmission tomography. J Comput Assist Tomogr **8**: 306-316, 1984

[13] Shepp LA, Vardi Y, Ra JB et al: Maximum likelihood PET with real data. IEEE Trans Nucl Sci **NS-31**: 910-913, 1984

[14] Vardi Y, Shepp LA, Kaufman L: A statistical model for positron emission tomography. J Amer Statist Assoc **80**: 8-37, 1985

[15] Snyder DL, Miller MI: The use of sieves to stabilize images produced with the EM alogrithm for emission tomography. IEEE Trans Nucl Sci **NS-32**: 3864-3872, 1985

[16] Miller MI, Snyder DL, Moore SM: An evaluation of the use of sieves for producing estimates of radioactivity distributions with the EM algorithm for PET. IEEE Trans Nucl Sci **NS-33**: 492-495, 1986

[17] Carson RE: A maximum likelihood method for region-of-interest evaluation in emission tomography. J Comput Assit Tomogr **10**: 654-663, 1986

[18] Lewitt RM, Muehllehner G: Accelerated iterative reconstruction for positron emission tomography based on the EM algorithm for maximum likelihood estimation. IEEE Trans Med Imag **MI-5**: 16-22, 1986

[19] Tanaka E, Nohara N, Tomitani T, Yamamoto M: Utilization of non-negativity constraints in reconstruction of emission tomograms. In: Information Processing Medical Imaging, Bacharach SL (ed.), Dordrecht, Martinus Nijhoff Publishers, pp. 379-393, 1986

[20] Tanaka E: Recent progress on single photon and positron emission tomography—from

detectors to algorithms—. IEEE Trans Nucl Sci **NS-34**: 313-320, 1987

[21] Tanaka E: A fast reconstruction algorithm for stationary positron emission tomography based on a modified EM algorithm. IEEE Trans Med Imag **MI-6**: 98-105, 1987

[22] Snyder DL, Miller MI, Thomas LJ Jr: Noise and edges artifacts in maximum-likelihood reconstructions for emission tomography. IEEE Trans Med Imag **MI-6**: 228-238, 1987

[23] Lange K, Bahn M, Little R: A theoretical study of some maximum likelihood algorithms for emission and transmission tomography. IEEE Trans Med Img **MI-6**: 106-114, 1987

[24] Kaufman L: Implementing and accelerating the EM algorithm for positron emission tomography. IEEE Trans Med Imag **MI-6**: 37-51, 1987

[25] Floyd CE Jr, Jaszczak RJ, Coleman RE: Convergence of the maximum likelihood reconstruction algorithm for emission computed tomography. Phys Med Biol **32**: 463-476, 1987

[26] Floyd CE Jr., Jaszczak RJ, Coleman RE: Maximum likelihood reconstruction for SPECT with Monte Carlo modeling: asymptotic behavior. IEEE Trans Nucl Sci. **NS-34**: 285-287, 1987

[27] Murayama H, Tanaka E, Nohara N, et al: A comparison of several iterative reconstruction methods for ECT. Jap J Nucl Med **24**: 797-807, 1987

[28] Llacer J, Andreae S, Verklerov E et al: Towards a practical implementation of the MLE algorithm for positron emission tomography. IEEE Trans Nucl Sci **NS-33**: 468-477, 1986

[29] Llacer J, Verklerov E, Hoffman EJ: On the convergenece of the maximum likelihood estimator method of tomographyic image reconstruction. LBL-21800, 1986

[30] Verklerov E, Llacer J: Stopping rule for the MLE algorithm based on statistical hypothesis testing. IEEE Trans Med Imag **MI-6**: 313-319, 1986

[31] Levitan E, Herman GT: A maximum of a posteriori probability expectation maximization algorithm for image reconstruction in emission tomography. IEEE Trans Med Img **MI-6**: 185-192, 1987

[32] Daube-Witherspoon ME, Muehllehner G: An interative image space reconstruction algorithm suitable for volume ECT. IEEE Trans Med Imag **MI-5**: 61-66, 1986

[33] Titterington DM: On the iterative image space reconstruction algorithm suitable for volume ECT. IEEE Trans Med Imag **MI-6**: 52-56, 1987

[34] Tanaka E: A filtered iterative reconstruction algorithm for positron emission tomography. In: Information Processing in Medical Imaging, de Graaf CN, Viergever MA (ed.), New York, Plenum Publishing Corp., pp. 217-234, 1988

[35] Daube-Witherspoon ME, Muehllehner G: Treatment of axial data in three-dimensional PET. J Nucl Med **28**: 1717-1724, 1987

* * *

CT Image Reconstruction from Incomplete Projection Data

Takehiro Tomitani, Norimasa Nohara and Hideo Murayama
Division of Physics, National Institute of Radiological Sciences

Introduction

In National Institute of Radiological Sciences, construction of heavy ion accelerator for radiation therapy is in progress. The merit of heavy ion therapy over electron/photon therapy lies in good dose localization. To make full use of it, accurate measurement of dose distribution is necessary. Direct measurement of dose distribution is possible by use of positron emitting radioactive beams,[1] e.g., ^{11}C, a product of stripping reaction through matter from ^{12}C. Distribution of the end points of the beams can be measured with positron emission tomography. However, there must be an entrance opening for ion beams and the projection data corresponding to the opening is lacking, and thus we are forced to solve CT image reconstruction from incomplete projection data.

Several algorithms have been reported, such as coordinate transform technique,[2] estimation maximization algorithm,[3] projection space iteration,[4] and constrained Fourier space method.[5] The last method was tested because of simplicity and economy in computation time, since FFT can be done efficiently with an array processor.

Principle

Suppose a point source on the image plane located at (ρ,ϕ) in polar coordinates. Its projection, $p(t,\theta)$, and Fourier transform with respect to t, $P(T,\theta)$, are

$$p(t,\theta) = \delta(t - \rho\cos(\phi - \theta)), \qquad P(T,\theta) = \exp\{i\rho T\cos(\phi - \theta)\}.$$

Fourier expansion of $P(T,\theta)$ is

$$P_k(T) = \frac{1}{2\pi}\int_0^{2\pi} P(T,\theta)\ \exp\{-ik\theta\}d\theta = \frac{1}{2\pi}\int_0^{2\pi} \exp\{i\rho T\cos(\phi - \theta) - ik\theta\}\ d\theta = J_k(\rho T),$$

which distributes almost like $(\rho T)^k$ near the origin of the coordinates and signals are rarely seen in Δ- region,[6] as seen in the middle row in Fig.1. True image information is confined to the outside of Δ-region. This property comes from the sinusoidal nature of the projection data. While, in the case of incomplete projection, the projection is not sinogramic and considerable amount of frequency components leak into Δ-region. By cutting components in Δ-region along with low-pass filter, only sinogramic components can be restored from incomplete projection data.

Algorithm

The algorithm based on the above principle is summarized below.

1) Perform 2-dimensional Fourier transform on the incomplete projection.
2) Cut out frequency components in Δ-region (and apply low-pass filter).
3) Perform 2-dimensional inverse Fourier transform.
4) Pad the resultant signals into the missing portion of the measured projection data.
5) Go to 1).

Note here that the measured projection data is defined in the angular range $(0,\pi)$, while Fourier expansion is defined in the range $(0,2\pi)$. Therefore, after Fourier transform with respect to t, conversion of the data from the range $(0,\pi)$ to the range $(0,2\pi)$ is necessary.

Computer Simulation

To test the algorithm, a simple elliptic disk was use, in which 1/6 of the detectors are lacking and projection data are deficient by about 60° which correspond to about 1/3 of the whole projection. The opening of 1/6 of the whole ring is considered large enough to allow the heavy ion beams to enter into the object. The results are shown in Fig. 1. In the figure, only a half part of the power spectrum of the projection is shown because of symmetry. It can be seen in Fig. 1 that spurious components in the power spectrum of incomplete data overlaps with that of signal only at high lateral frequencies, which suggests that low-pass filter is effective to restore low frequency components of missing data. In fact, it is effective up to a few iterations. After low frequency components have been restored, one must not use it in further iteration steps, since it limits the band width. Also, low-pass filter along angular frequency would work as well, but this was not implemented in this experiments, because Δ-

filtering works efficiently. However, if the object has more complex structure, then Δ-filtering perhaps will not work so efficiently and we would need low-pass angular filter.

Conclusions

Characteristics found in this experiments are 1) total counts are preserved through Δ-filtering, 2) after Δ-filtering, part of the signals spreads into the missing region on the sinogram and the intensity of the region where data is available decreased, 3) by inserting the measured data into the filtered data, total counts gradually increases as iteration proceeds, 4) interpolation of the missing region prior to the iteration enhances the restoration, but artifacts may occur and may not be advantageous, 5) low pass filter works efficiently up to a few iterations, but it degrades spatial resolution after a few iterations and should be removed, 6) the convergence speed drops after several iterations and the projection data recovers slowly. It might be advisable to use other iteration methods such as Estimation-Maximization algorithm after most of low frequency components are restored.

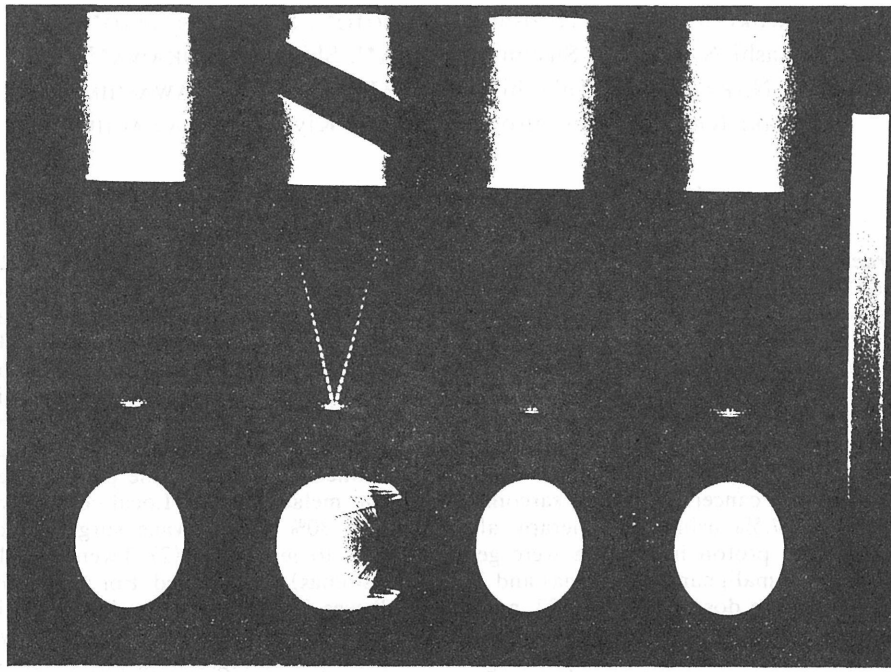

Figure 1. Results of computer simulation. The complete projection data, the incomplete projection data, the restored projection data after 5 iterations and that after 10 iterations are shown from the right side to the left side on the top row. The corresponding 2-D Fourier power spectrum are shown on the middle row and the corresponding images are shown on the bottom row.

References

1. J.Llacer, "Positron Emission Medical Measurements with Accelerated Radioactive Ion Beams," LBL-23454,
2. T. Inoue, "Image reconstruction with limited view angle projections," in Proc. Int. Workshop on Phys. and Eng. in Med. Imaging, Pacific Grove, CA Mar. 1982.
3. G. Muehllehner, J.S. Karp and A.Guvenis, "A method for Reconstruction Images from Data Obtained with a Hexagonal Bar Positron Camera," IEEE Trans. Med. Img., ML-4, 134-138, 1985.
4. J.H. Kim, K.Y. Kwak, S.B. Park and Z.H. Cho, "Projection Space Iteration Reconstruction-Reprojection," IEEE, Trans. Med. Img., ML-4, 139-143. 1985.
5. J.S. Karp, G. Muellehner and R.M. Lewitt,"Constrained Fourier Space Method for Compensation of Missing Data in Emission Computed Tomography," IEEE Trans. Med. Img., MI-7, 21-25, 1988.
6. P.R. Edholm, R.M.Lewitt and B. Lindholm, "Novel Properties of the Fourier Decomposition of the Sinogram," Proc. Soc. Photo-Opt. Instrum. Eng., 671, 8-16, 1986.

J. Jpn. Soc. Ther. Radiol. Oncol. 1: 145-153, 1989

放医研医用サイクロトロンによる陽子線治療

森田 新六*1, 恒元 博*1, 佐藤 真一郎*1, 中野 隆史*1,
久保田 進*1, 古川 重夫*2, 中村 譲*2, 平岡 武*3, 川島 勝弘*3,
金井 達明*4, 遠藤 真広*4, 河内 清光*4

PROTON RADIOTHERAPY BY NIRS MEDICAL CYCLOTRON

Shinroku MORITA*1, Hiroshi TSUNEMOTO*1, Shinichiro SATO*1,
Takashi NAKANO*1, Susumu KUBOTA*1, Shigeo FURUKAWA*2,
Yuzuru NAKAMURA*2, Takeshi HIRAOKA*3, Katsuhiro KAWASHIMA*3,
Tatsuaki KANAI*4, Masahiro ENDO*4 and Kiyomitsu KAWACHI*4

(*Received 6 April 1989, accepted 16 May 1989*)

Abstract Clinical trials on proton radiotherapy began in November, 1979 at NIRS-Chiba. Proton beams have a highly defined dose distribution, resulting in no radiation exposure beyond the beam range and very little side scatter. Since a 70 MeV proton beam penetrates about 38 mm through aqueous environments, only superficial tumors and ocular neoplasms are indicated for treatment with this radiotherapy. To optimize the dose distribution, the most important factors to consider are correct positioning, reproducibility of the clinical set up, and immobilization during irradiation. For treatment, fixed horizontal or vertical beams are used. Over the past 9 years, a total of 59 patients have been treated, and some preliminary clinical results have been obtained: (1) Thirty-nine patients were treated for skin cancer, soft tissue sarcoma, malignant melanoma, etc. Local control was achieved in 67.5% using radiotherapy alone, and in 30% with salvage surgery. Skin reactions after proton irradiation were generally mild to moderate. (2) Twenty ocular neoplasms (17 malignant melanomas and 3 retinoblastomas) were treated. For melanoma, average radiation dose was TDF 137, and the result was 1 complete regression, 7 partial regressions, and 2 enucleations due to glaucoma. For retionblastoma, average dose was TDF 77, and the result was 2 complete regressions and 1 partial regression. There were no severe radiation-related complications.

Key words: Radiotherapy, Proton, Superficial tumor, Ocular melanoma, Retinoblastoma

緒　言

がんの放射線治療では治療と障害の兼ね合いが重要である．局所治癒率を高めて，正常組織の放射線障害を抑えるために，多くの治療法が試みられているが，陽子線治療もその一つといえる．

陽子線治療の特長は優れた線量分布を生かした治療にある．陽子線の特性は(1)加速エネルギーに従った生体内での定まった飛程．(2)速度又はエネルギーが小さい程，その単位長さ当りのエネルギーの損失の割合は大きい．この(1)と(2)の要因による深部線量分布の基本型は，入射面近くの平担形と，飛程の終端近くで急激に立

放射線医学総合研究所*1 病院部, *2 臨床研究部, *3 物理研究部, *4 医用重粒子線研究部 (〒260 千葉県千葉市穴川4-9-1)
*1 Division of Hospital, *2 Division of Clinical Research, *3 Division of Physics, *4 Division of Accelerator Research, National Institute of Radiological Sciences (NIRS), 4-9-1, Anagawa, Chiba-shi, Chiba 260, Japan.

ち上がるピーク部 (bragg peak) である．(3)少ない側方散乱，これは入射荷電粒子の重さが重い程直進性が強くなることに起因し，X線・γ線・電子線・中性子線には認められない．(4)均等な線量分布，これは小線源治療時の線量分布では得られない．

これらの特徴が腫瘍へのビームの集中で，照射線量を著しく増加させて，局所制御率を高め，しかも周辺正常組織の放射線障害を低めることを可能にした．

一方，放医研の 70 MeV 陽子線の LET (Linear Energy Transfer) は 1～数 KeV/μm なので，速中性子線にある高 LET の生物効果は望めない．

陽子線による癌治療は Wilson (1946)[1] にはじまり，その後ローレンス・バークレイ研究所 (LBL) の下垂体腫瘍治療 (1954)，ボストン (1959)，ウプサラ (1962)，ソ連のデュブナ・モスクワ (1967) でそれぞれ治療が開始されている[2]．日本でも放医研 (1979)，筑波大学粒子線医科学センター (1983) で開始された[3]．

現在の放医研医用サイクロトロンの加速エネルギーは 70 MeV で，ビームの深達は 40 ミリ弱であり，適応症例は制限されている．症例数が少なく，しかも他の放射線で治療可能な場合が多かったが，しかし今回報告する基礎的な物理学的・生物学的研究，治療計画や照射術式に関する臨床的研究，患者治療経験は次の高エネルギー重イオン粒子線治療につながる貴重なものであった．

基 礎 研 究

(1) 線量分布

70 MeV 陽子線の深部線量分布は水中で 37 ミリの深さに bragg peak を有し，平均飛程は 38 ミリである．ピーク巾は 3.3 ミリなので，実際の臨床応用では飛程調整器 (Range modulator) でピーク巾を拡げて，腫瘍の深さ方向の厚さに対応しなければならない．4×4 平方センチの照射野の中心軸上の，水中での深部線量分布と，30 ミリ Range modulator での spread out bragg peak (SOBP) の分布曲線を Fig. 1 に示す[4]

(2) スポット走査式とワブラー方式

放医研での陽子線照射術式は spot scanning 方式[5,6] と Wobbler 方式 (拡大ビーム法)[7] である．前者は治療部位での 1×1 平方センチのスポットビームを上下左右の電磁石でスキャンさ

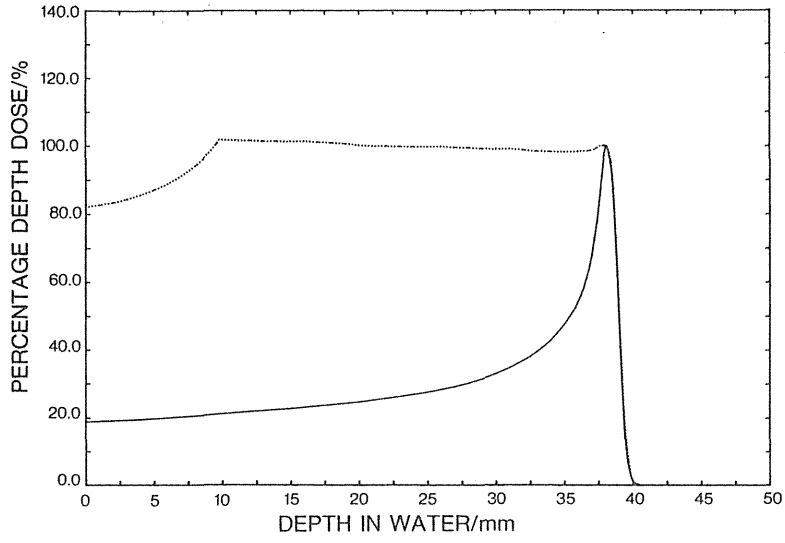

Fig. 1. Depth dose distribution of 70 MeV proton beam in water for unmodulated beam (solid curve) and spread out Bragg peak (dotted curve). Field size; 4×4 cm², 30 mm Range modulator. (Hiraoka, T., 1982)

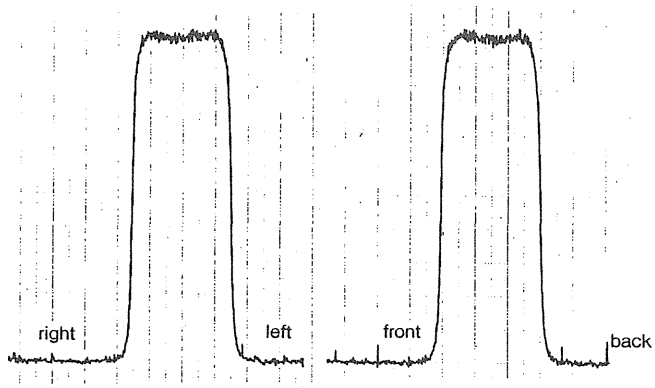

Fig. 2. Sharp dose distribution of collimated proton beam. 15mm diameter collimator was used for ocular tumor. There was no side scatter in left and right or front and back. (Hiraoka, T.,1986)

せることにより，打ち抜き照射，重複照射など線量の加減を含んだ不整形照射野を自由に得ることができる．照射野は1×1から20×20平方センチまで設定できた．後者は散乱体を用いてビームを10センチ直径以上に拡大して，一様な照射野を作る方法である．この場合，大きな照射野を得ようとすると数個の厚い散乱体が必要となり，また散乱体から照射位置まで長い距離を置かねばならず，エネルギーの損失が大きい欠点がある．Wobbler法は少ない散乱体で広い照射野を得るための方法で，エネルギーの損失は少ない．散乱したビームを一つの半径で回転させ(一重ワブラー法)，高い線量率のビームを短時間で照射できる方法を用いた．照射面で約140ミリ直径の照射野を得るには，金0.1ミリ厚の散乱体が必要だが，これによるビーム飛程の減少は約1ミリであり，ほとんど問題にならない．

照射野は多葉コリメーターや照射筒で，更に細かく整形された．

(3)RBE (Relative Biological Effectiveness) の検討

(i)培養細胞（支那ハムスター卵巣細胞）

Do値の比較で，RBEは対200 KVP X線で0.89，対Co-60γ線で1.2であった[8]．また陽子線の線量分布の相関性の実験では，ビーム飛程内およびSOBP内で，細胞は極めて安定した細胞致死効果が得られ，物理学的線量分布と生物効果はよく一致した．

(ii)マウスのNFSa腫瘍

マウス肺内転移減少率の比較では，対Co-60γ線で1.00～1.14であった[9]．

(4)装置の概要

水平ビームポートと垂直ビームポートが用いられた．水平ではスポット・スキャン法，垂直ではワブラー法が用いられているが，どちらもRange modulator(所定の厚さと角度を持つ，階段状の屋根型の羽根を回転させる）でSOBPを形成した．

ビーム飛程の調節にはRange shiftorやボーラスを用いた．Range shiftorは0.25～16ミリ厚のアルミ板を組合せる．腫瘍の深部側の形状に合わせた飛程の調整にはボーラスが適している．

多葉コリメーターや照射筒で照射野を細かく整形するが，これはRange modulatorやshiftorから出る散乱線を除去し，シャープなビームを形成するのに役立つ．Fig. 2に照射筒を用いた場合の線量分布図を示す．これは眼球腫瘍の照射に用いた．

臨床的研究

(1)治療の手順

患者は他施設で悪性腫瘍と診断されて，陽子線照射の目的で紹介された．

(i)X線CTで腫瘍の局在，周辺正常組織の組成，CT値，critical organとの関連を診断する．

ビームの通過部位の組織組成の違いで飛程が異なってくるので，補正する必要があるが，現在迄の症例は全て均一組成内のものであった．
(ii)腫瘍を含んだ部位の体位固定用発泡スチロール製固定具，ボーラス，シェル等の作成．
(iii)シェル，ボーラス，固定具を装着し，治療体位でのX線CT検査．画像より腫瘍とボーラスの位置関係，ボーラス厚，critical organ 遮蔽のためのブロックの位置設定を診断した．水平または垂直固定一門ビームに照準を合わせるため，患部の回転可能な半円筒型の固定具が試作された．
(iv)医師，技師，物理，生物の各担当者による治療打合せ会で治療の適否を最終決定し，照射線量配合を決定した．
(v)照射の直前にX線CTで諸条件を再確認した．2回目以降でもX線CTでの再確認は行った．

実際にビームがターゲットに確実に当ったかどうかの確認は，治療ビームでのProton graphyが撮れないだけに難しい．照射による腫瘍の変化，皮膚，粘膜反応などで判断したが，重要なことは，治療計画の正確な再現性である．

(2) ボーラス材質の検討

ボーラス材質の条件は，(i)質量が水に近く(組織と等価，CT値：5前後)，(ii)均一，(iii)透明(レザー光線を通す)，(iv)再現性，保存性，加工性良好，(v)皮膚面への密着性良好，(vi)清潔，(vii)経済的，などである[11,12]．寒天(CT値28)，水ボーラス，水性ゲルボーラスが実用された．水ボーラスは患者固定用シェルを利用して，2枚のアクリル板の間に箱をつくり，任意の厚さの水の層を調節できる．水性ゲルボーラスはアセトアセチル化水溶性高分子化合物とその架橋剤と水とを混合する．密度は1 g/cm³に近く，ゲル化時間は約4分，透明性，弾力性が良い．

(3) 患者の固定

陽子線の優れた線量分布の特長を生かすには照射中のターゲットの固定が確実でなければならない．患者の生理的運動（呼吸，心搏）に対応する照射技術はまだ研究段階であるが，体動は抑えて，確実な再現性を確保しなければならない．

アクリル板と棒で患部の入る囲いをつくり，ポリウレタン発泡剤で体の周囲を固める型を作った．頭頸部の場合はこれにマスクを加えた．マスクにはボーラスやブロックを装着する機能を附加した．

眼球腫瘍の場合は眼球の固定に加え，ビームラインから水晶体をはずすための眼球の回転・偏位が必要であった．成人の場合は患者が理解力があり，治療に協力的で，しかも照射時間が約10秒間（10 Gy）なので，両眼で一点（赤印や小光源）を凝視させる方法をとった．照射中の眼球の動きのチェックはテレビモニターで行い，全例動きのないことを確認した．小児の場合は全身麻酔施行下での眼球の回転・偏位・固定が必要で，軟コンタクトレンズ様吸着盤を試作して使用した．

(4) 照射線量

陽子線で照射容積を著しく少なくでき，周辺正常組織の障害を著しく軽減できれば，照射線量は従来の耐容線量を著しく超えることが可能となる．

現在のマシンタイムは週1回なので，1回大線量，少分割照射法を用いた．基本的線量配分は，TD 40 Gy/4回/4週（TDF 120）で，1回線量10 Gyは照射野，腫瘍の放射線感受性，患者の状態などの因子で，20%前後増減した．TDF（Time Dose Fractionation）100（1800 ret）が皮膚の耐容線量なので，これを超えた線量配分である．線量率は90〜100 Gy毎分，照射時間はスポットスキャン法で約5分，ワブラー法で約10秒であった．尚照射方法が少分割法でしかも速中性子線，電子線，X線などとの混合照射の場合も含まれているので，照射線量を標準照射法の場合と比較する目的で，TDF法を用いて目安とした．

対　象

(1) 症例

昭和54年10月から63年12月迄の9年間に59症例（60部位）の治療を行った．3ケ月児より84歳までの，男28例（平均年齢56歳），女

31例（平均50歳）．62年10月までは汎用照射室の水平ビーム(45例)，以降は地下照射室の垂直ビーム（14例）を用いた．対象疾患は加速エネルギーの関係で浅在性の皮膚・皮下腫瘍であったが，最近は眼球腫瘍が中心であった．

(2) 浅在腫瘍の症例

対象は体表より38ミリの深さまでで，均一組織内にある悪性腫瘍．39症例（40部位）の内訳は皮膚扁平上皮癌3，基底細胞癌3，耳下腺癌3，乳癌皮膚転移7，皮膚血管内皮腫2，肉腫7，悪性黒色腫9，転移性リンパ節6．根治照射22(55%)，姑息6(15%)，手術併用12(30%)．陽子線単独照射20(50%)，ブースト照射20(50%)．

照射線量は陽子線単独照射群の新鮮症例（9例）では，最大が眼瞼の悪性黒色腫例，24ミリ直径の照射野で，50 Gy/5回/5週（TDF 150），最小が頭部皮膚癌例，40×40平方ミリの照射野で，32 Gy/4回/4週（TDF 85）であった．9例の平均TDFは111.5であった．再発症例(7例)は，一般に線量が少なく，最大が乳癌再発例の26 Gy/2回/2週（TDF 106），最小は甲状腺癌のリンパ節転移例で，24 Gy/3回/3週（TDF 72）であり，平均TDFは89.2であった．

ブースト照射は中性子線，電子線，X・γ線の照射後に1～2回の追加照射をした場合で，悪性黒色腫などの放射線抵抗性癌が多かったので，一般的に線量が多く，最大は口腔癌の頚部リンパ節転移例でX線，中性子線，陽子線とつなげたTDF 160，最小は乳癌再発例の電子線，陽子線のTDF 81であった．平均は114.4であった．また照射終了後の手術摘出例も40%(8/20)にみられ，その平均照射線量はTDF 133.6であった．

(3) 眼球腫瘍の症例

眼球内腫瘍20例(脈絡膜メラノーマ，メラノサィトーマと悪性黒色腫17例，網膜芽細胞腫3例)．陽子線単独照射で，直径10～30ミリ（20例の平均16ミリ)の真鍮性照射筒を用いての照射線量は，眼球悪性黒色腫で，最大52 Gy/4回/4週（TDF 186），最小40 Gy/5回/5週（TDF 110)，平均TDF 143.6，メラノサィトーマで平均TDF 85，網膜芽細胞腫で，34～28 Gy/4回/4週（TDF 93～71，平均78）であった．

成　績

(1) 浅在腫瘍

局所制御率は照射単独で67.5%（27/40)，これに手術併用を加えると97.5%（39/40）となった．腫瘍の残存は第1例目の皮膚扁平上皮癌再発例（中性子線，陽子線ブーストでTDF 80照射）のみであった．

皮膚の悪性黒色腫は9例だが，2例に照射のみで局所制御を得た（耳介の腫瘍に中性子線と陽子線ブーストTDF 140，眼瞼の腫瘍に単独で50 Gy/5回/5週，TDF 150)．この他にも手術切除標本に癌細胞を認めなかった1例（口唇，中性子線，陽子線ブーストでTDF 160)があった．しかし他の6例は切除標本に残存腫瘍を認めた（平均TDF 108)．5例は現在良好な経過をとっている．

照射による副作用として高度の障害が5例(12.5%）にみられたが，照射後再発例の再照射が3例（3例とも局所制御）含まれているので，全般的な放射線障害の程度は，線量の割には，軽度と考えた．これらの結果をTable 1にまとめた．なお照射後の経過は64%が良好で，死亡36%の内訳は転移57%，重複癌21%，老衰その他21%であった．

(2) 成績の小括

(ｉ)局所制御率は97.5%で，対象が浅在腫瘍なら当然の結果であった．

(ii)皮膚障害は照射線量の割には軽度であった．陽子線照射の特長と考える．

(iii)照射後再発例の再照射でも，少ない線量で局所制御を期待出来る症例があった．ただし高度の障害を覚悟しなければならない．

(iv)放射線抵抗性癌といわれている腫瘍では併用手術で残存腫瘍の切除が必要であった．

(3) 眼球内腫瘍

照射後の経過観察が最長3年なので，結論を出せる段階ではないが，現在迄の結果をTable 2に示した．眼球メラノーマに関しては腫瘍の完全縮小（CR）1(5.8%)，縮小中（PR）7(41%)，変化なし（NC）7(41%)，増大（PD）0，摘出手

Table 1. Clinical results of superficial tumor, treated with proton irradiation (1979-1988, NIRS)

Site	No. of pats.	Average TDF	Policies			Proton		Tumor response			Skin reaction		
			Radical	Palliativ	with Surgery	Alone	Boost	CR	PR	Salvage ope.	Mild	Moder-ate	Severe
Skin ca.	6	97.5	5	1	•	5	1	5	1	•	4	2	•
Malig. endothelioma	2	114.5	2	•	•	2	•	2	•	•	•	2	•
Parotid ca.	3	113.3	1	•	2	•	3	1	•	2	1	2	•
Skin meta. breast ca.	7	104.7	5	2	•	3	4	7	•	•	2	2	3
Soft tissue sarcoma	7	91	2	2	3	5	2	4	•	3	5	1	1
Malig. melanoma	9	122.1	2	•	7	3	6	2	•	7	3	6	•
Neck nodes meta.	6	126.6	5	1	•	2	4	6	•	•	3	2	1
Total (%)	40	109.5	22 (55)	6 (15)	12 (30)	20 (50)	20 (50)	27 (67.5)	1 (2.5)	12 (30)	18 (45)	17 (42.5)	5 (12.5)

Table 2. Proton irradiation for ocular malignancies (1985-1988, NIRS)

	No. of pats.	Average TDF	CR	PR	NC	PD	Salvage ope.	Cataract	Retina detachment
Melanoma (adult)	17	137	1	7	7	0	2*	0	0
Retino blastoma (child)	3	77.6	2	1**	0	0	0	0	0

*：due to neovascular glaucoma
**：boost treatment by photo coagulation

術 (Salvage ope) 2 (12%)，白内障 (cataract) 0，網膜剝離 (retina detachment) 0．CR の 1 例は 39 Gy/3 回/3 週 (TDF 140) を照射したが，腫瘍の縮小は速やかであった．腫瘍の組織判定が不可能なのは発生部位の性質上やむをえないが，臨床経過からみると悪性黒色腫以外のものである可能性が強い．一般に腫瘍の縮小は緩徐であった．

摘出例の 2 例は緑内障が原因であったが，1 例目は視神経乳頭部のメラノサィトーマ，TDF 80 (30 Cy/3 回/4 週) の照射で，照射後 6 ケ月目は視野，視力の改善が認められたが，視神経内の血管の障害のため 1 年目に網膜中心静脈閉塞様症状を呈し，新生血管性緑内障が生じた．摘出標本では視神経の血管内膜の肥厚が認められたが，腫瘍細胞は完全な壊死状態であり，陽子線が正確に照射された証拠となった．2 例目は腫瘍が内腔の半分近くを占める大きさだったため，60 Gy/5 回/7 週 (TDF 147) の照射にもかかわらず，腫瘍の縮小がなく，かえって緑内障を併発したため，6 ケ月後に摘出した．標本の腫瘍細胞は 70%までが変性していた．

照射野の皮膚反応 (眼瞼，睫毛) は軽度 5 例 (29%)，中等度 9 例 (53%)，高度 3 例 (18%) であったが，回復は照射野が小さいだけに速かであった．

網膜炎は小血管の障害として，浮腫，出血斑，浸出性反応として示される．線量差，個人差はあるが全例に認められた．これが患者の自覚症状 (視力や視野) に及ぼす影響は照射範囲が視

神経乳頭部や黄斑部に及ぶとき顕著になる．前述の摘出1例目のように，網膜中心静脈閉塞様症状を呈したものが3例あり，視力障害を示した．この場合網膜は酸素欠乏状態となり，それを解消するために新生血管が増加し，緑内障の原因となるが，予防的に光凝固療法で新生血管を潰せば緑内障は防げる．

腫瘍の崩壊のため硝子体の混濁例があったが，徐々に混濁が吸収されている．

水晶体の混濁（白内障）や網膜剝離は現在のところ1例もない．

網膜芽細胞腫の1例目は28 Gy/4回/4週（TDF 71）の照射であったが，乳頭部を挟んで存在した大（4 PD），小（2 PD）2個の腫瘍のうち，小は消失制御したが，大は残存再発した．しかしこれは光凝固で消失出来た．

考　察

陽子線照射の特徴は大線量照射をしても，障害が重篤にならない点にある．はたしてどれほどの線量まで照射可能だろうか，乾性皮膚反応を放射線による皮膚の耐容限界と定めて，これを指標にし，陽子線照射の皮膚の耐容線量を求めた[13,14]．毎週1回の照射スケジュールの場合，NSD（Nominal Standard Dose）とTDF（Time Dose and Fractionation Factor）を現わす公式は，

$$NSD\ (P) = D \cdot N^{-0.20} \cdot T^{-0.11}$$

$$TDFA\ (P) = 0.00198 \cdot n^{1.159} \cdot d^{1.45} \cdot t^{-0.59} \cdot (A/100)^{0.28}$$

となる．D総線量，N照射回数，T照射期間（日数），d一回線量，A照射野項．Nのべき数0.20はX線の標準値0.24より低く，速中性子線の0.11より大きい．

照射野の大きさによる影響はかなり大きいが，10×10平方センチの照射野の耐容線量は1回線量で8.15 Gy，総線量32.6 Gy（TDF≒90），照射野4×4だと1回線量で15.1 Gy，総線量60.7 Gy（TDF≒240）となる．

筑波大学粒子線医科学センターの陽子線治療トライアル[15]では，昭和58年4月より63年10月迄に133例の治療例があった．加速エネルギーが250 MeVで深在腫瘍が対象である．8ヶ月以上経過観察の64例の局所制御率は67%（43/64），後遺症は12.5%（8/64）と報告された．

日本での陽子線治療はまだ始まったばかりで，物理学的特徴や正確な照射技術の開発を臨床面で確めている段階である．今後はお互に協力して，陽子線治療の普及に努力しなければならない．

欧米では治療の歴史も古く，臨床研究が進んで対象疾患も絞られている[16]．即ち頭蓋底や脊椎に隣接している腫瘍（脊索腫や軟骨肉腫），下垂体腫瘍，動静脈奇型，および眼球メラノーマである．現在最も治療患者数の多いのは，ボストンのハーバード大シンクロ・サイクロトロンでのもので，1963年から4600に達している．内訳は眼球メラノーマ1065例，下垂体510例，動静脈奇型205例，の順である．眼球メラノーマは欧米では頻度の多い疾患で，眼球保存療法として陽子線照射が威力を発揮している．ボストンの治療[17]は照射線量70 CGyE（Cobalt Gy Equivalent）を5分割で，7～10日間に照射するという強烈なものだが，長期観察の128例の分析で，腫瘍の消失又は瘢痕化が12%，縮小が21%，ほとんどの腫瘍が徐々に縮小している．視力も20/200より良い状態の保存率が，照射後6ケ月で94%，以後徐々に減少して5年後で69%であるという．放射線障害で最もきびしいのは，新生血管増生による紅彩炎と緑内障であるが，15%にみられ，このうち約1/3に眼球摘出を行っている．白内障の発生は33%で，そのうち約1/3に水晶体摘出を行っている．

この成績と放医研の成績を比較することはまだ出来ないが，印象では腫瘍の完全消失がまだ無く（疑問の一例を除いて），これは照射線量の差によると考えている．今後は照射線量を増しても，安全に，確実に照射出来る治療技術を完成しなければならない．

視力の保存は，腫瘍が視神経乳頭部や黄斑部に近い場合はもっと悪い[18]．

小児網膜芽細胞腫の陽子線照射は世界で初めての試みであった．この腫瘍は放射線感受性が高いので，従来よりX線照射の適応であった．

最近は眼球の固定技術に進歩があり，正確な照射が可能であるが[19]，X線と陽子線の線量分布の違いは眼球腫瘍のみに限局して照射出来る陽子線に明らかな利点がある．

治療計画時および照射時に必要な全身麻酔の施行も，今迄の症例では副作用の発現もなく経過した．

以上放医研で行った陽子線治療の現在までの臨床結果をまとめたが，線量分布上の特性を生かした，大線量照射の高局所制御率と低障害発生率は単にむずかしい部位の照射のみならず，あらゆる部位において，現在のX線照射に代って治療を行うことができ，治療成績の向上が期待出来るものである．更に早期癌の治療にも威力を発揮すると考えられる．

(謝辞：陽子線照射の診療研究に御協力下さっている，国立がんセンター眼科，慈恵医大眼科，慶応大医眼科，千葉大医眼科及び麻酔科の諸先生方に深く感謝致します．

なおこの研究の一部は厚生省がん研究助成金，計画研究24，金子班の援助をうけた．)

文　献

1) Wilson, R. R.: Radiological use of fast protons. *Radiology* **47**: 487-491, 1946.
2) Boone, M. L. M., Lawrence, J. H., Connor, W. G. *et al.*: Introduction to the use of protons and heavy ions in radiation therapy: historical prespective. *Int. J. Radiat. Oncol. Biol. Phys.* **3**: 65-69, 1977.
3) Tsunemoto, H., Morita, S., Ishikawa, T. *et al.*: Proton therapy in Japan. *Radiation Research* **104**: S232-S243, 1985.
4) 平岡武: 高エネルギー陽子線の吸収線量の算定とその線量分布に関する研究．日医放会誌 **42**: 30－54, 1982.
5) Kanai, T., Kawachi K., Kumamoto, Y. *et al.*: Spot scanning system for proton radiotherapy. *Med. Phys.* **7**: 365-369, 1980.
6) 河内清光，金井達明，松沢秀夫 他: スポット走査法を用いた陽子線治療装置．日医放会誌 **42**: 467－475, 1982.
7) 金井達明，平岡武，野田豊 他: 垂直陽子線治療システムについて．放治システム研究 **5** (Suppl.): 88－91, 1988.
8) 大原弘，五日市ひろみ，安藤興一 他: 放医研70 MeV陽子線の細胞致死効果と他施設間相互比較．特別研究「粒子加速器の医学利用に関する調査研究」最終報告書NIRS-R-**10**: 142-145, 1984. 放医研．
9) 安藤興一，小池幸子，河内清光 他: 放医研および筑波大学治療用陽子線の生物学的効果比．日医放会誌 **45**: 531-535, 1985.
10) 久津谷譲，梅垣洋一郎: 生物学的等価線量の考え方と計算法．癌・放射線療法，癌の臨床別冊/新編．篠原出版．1978, pp 79-92.
11) Akanuma, A., Majima, H., Furukawa, S. *et al.*: Compensation techniques in NIRS proton beam radiotherapy. *Int. J. Radiat. Oncol. Biol. Phys.* **8**: 1629-1635, 1982.
12) 古川重夫，中村譲，平岡武 他: 陽子線治療用ボーラスの開発とその応用．放治システム研究 **4** (Suppl.): 136-139, 1987.
13) 佐方周防，恒元博，森田新六: 組織反応の評価法について．文部省がん特別研究Ⅰ，粒子線治療に関する基礎的研究，報告書．1987, pp. 92-97.
14) 恒元博，森田新六，佐方周防: 多分割照射法，放射線治療効果の評価．癌の臨床**33**: 1579-1589, 1987.
15) 北川俊夫: 深部臓器がんに対する陽子線治療．癌の臨床 **34**: 1839-1844, 1988.
16) Seymour, M. A., Munzenrider, J. E., Goitein, M. *et al.*: Progress in Low-LET heavy particle therapy: Intracranial and paracranial tumors and uveal melanomas. *Radiation Research* **104**: S219-S226, 1985.
17) Gragoudas, E. S., Seddon, J. M., Egan, K. M. *et al.*: Long-term results of proton beam irradiated uveal melanomas. *Ophthalmology* **94**: 349 353, 1987.
18) Seddon, J. M., Gragoudas, E. S., Egan, K. M. *et al.*: Uveal melanomas near the optic disc or fovea. Visual results after proton beam irradiation. *Ophthalmology* **94**: 354-361, 1987.
19) Harnett, A. N., Hungerford, J. L., Lambert, G. D. *et al.*: Improved external beam radiotherapy for the treatment of retinoblastoma. *The British J. of Radiology* **60**: 753-760, 1987.

要旨：陽子線照射の臨床トライアルは1979年の11月に開始された．陽子線ビームの特徴は優れた線量分布にある．即ちブラッグピークを越えて線量が行かないことと，側方散乱が極めて少ないことである．70 MeV陽子線の飛程は38ミリなので，浅在性腫瘍と眼球腫瘍が対象となり，過去9年間で，59症例が治療された．線量分布の利点を生かすには，正確な治療計画と再現性のあるセットアップ，照射中の患部の固定が最も大切な因子である．治療結果として1）39例の浅在性腫瘍では，陽子線単独で67.5%，手術との併用で30%，合計97.5%の局所制御を得た．皮膚反応は一般に軽度又は中等度であった．2)20例の眼球腫瘍(17例のメラノーマ，3例の網膜芽細胞腫)では，平均照射線量がメラノーマでTDF 137，網膜芽細胞腫で77であったが，前者ではCR 1, PR 7，摘出2，後者ではCR 2，PR 1，高度の放射線障害は認められていない，という結果であった．

悪性耳下腺腫瘍の速中性子線治療

森田　新六・恒元　　博（放射線医学総合研究所）

頭 頸 部 腫 瘍　Vol. 16　No.1 (1989) 別 刷

5. 悪性耳下腺腫瘍の速中性子線治療

森田　新六・恒元　博（放射線医学総合研究所）

緒　言

耳下腺腫瘍は全唾液腺腫瘍の80～85％を占め，そのうち20～30％が悪性である。ほとんど全ての症例が手術的治療をうけるが，その治療成績に影響を及ぼす因子は，1）多様性をもつ病理組織の悪性度，2）解剖学的な腫瘍の浸潤程度による手術の難易度，3）顔面神経の侵襲度を含む病期（T）分類，4）頸部リンパ節転移（N）分類などである。近年，手術療法は技術的に完成し，積極的に行うことで，局所制御率は上昇したとはいえ，悪性腫瘍のうちの約60％を占める悪性度の高い組織の腫瘍では50％をこえる局所再発率を示し[1-3]，しかも再手術後も再発を繰り返し，またその再発までの期間も数年の長期間になることが稀でない。従来の放射線治療は主として術後照射と再発症例の姑息照射に用いられてきた。Tu ら[4]は，術後照射例と手術単独例の比較で，術後照射で5年生存率の上昇した症例は，1）再発例，2）悪性度の高い例，3）進行期例，4）顔面神経麻痺例であるとした。また Guillamondegui ら[5]によると，術後照射の適応は，1）高度に悪性な腫瘍，2）筋・骨・皮膚・側頭下顎関節・神経・傍神経リンパ管に浸潤例，3）領域リンパ節転移例，4）再発例の切除後，5）深葉の腫瘍，6）手術後の残存腫瘍が大きな例，7）顔面神経に隣接した腫瘍であるという。因に悪性度の高い腫瘍の病理組織には，高度の mucoepidermoid ca., malignant mixed tumor, 扁平上皮癌，未分化癌，T3・T4 の腺癌が含まれている。

手術不能の進行期腫瘍に対する放射線治療の効果は良好とは云えない[6-8]。放射線感受性は全てが悪いわけではないが[9]，概して放射線抵抗性であり，局所制御率を向上させるための速中性子線治療に期待がかかってきた。

速中性子線の特徴はその優れた放射線生物学的効果にある。即ち，1）生物学的効果比（RBE, Relative Biological Effectiveness）はX線より高い，2）照射された細胞の亜致死障害からの回復を抑える力がつよい，3）細胞の分裂周期の感受性の変動に左右されにくい，4）酸素効果比（OER, Oxygen Enhancement Ratio）が低く，放射線抵抗性の原因の1つとされる低酸素分圧細胞を抑える力がつよい。

しかし，物理学的線量分布はコバルト60の分布とほぼ同等であり，しかも器械的ハンディキャップでコリメーターが固定で一方向のみの照射なので，線量を腫瘍に集中させるのが日常的には容易でない。従って，周辺臓器の放射線障害が制限因子となって照射線量に影響してくる。

現時点の速中性子線治療成績の分析では[10-12]，放射線障害の発生を気にしないで済む部位では優れた局所制御の効果が発揮されている反面，障害を気にする部位では照射線量を控え目にするため，効果が発揮されないという傾向が示されている。

耳下腺腫瘍は体表に近いので比較的容易に適切な線量分布を形成することが可能で，しかも比較的緩徐に発育増大する腫瘍が中性子線の RBE が特に高いという放射線生物学的データ[13]のあることを考えれば，中性子線治療の最も良い対象の1つであると云ってよい。

放医研医用サイクロトロンによる速中性子線治療は1975年に開始され，1988年末には1717例の進行期難治性癌と放射線抵抗性癌が治療された。そのうち頭頸部癌は約20％を占め，耳下腺悪性腫瘍は約2.5％であった。耳下腺腫瘍は症例数が少ないため，ランドマイズ・クリニカルトライアルは行えなかったが，今回その治療成績を検討し，文献的考察を加えて報告する。

〔I〕症　例

放医研病院で速中性子線治療をうけた大部分の患者は，他病院で適応性について選択をうけた後，紹介されてきた。

1975年11月から1988年12月までの12年間の44症例が対象となった。男女比は20対24，年齢分布は12歳から82歳，平均年齢は男55.2歳，女48.1歳。新鮮症例：6例（T2：1，T3：4，T4：1），予防的術後照射例（病歴に明らかな腫瘍残存の記載のない症例）：16例，残存術後照射例（断端陽性など残存の明らかな症例）：9例，再発例：13例。組織別分類では，1）Adenoid cystic ca.：11例，2）Malignant mixed ca.：9例，3）Adeno ca.（moderate diff.）：7例，4）Adeno ca.（poorly diff.）：6例，5）Mucoepidermoid ca.：5例，6）Acinic cell ca.：4例，7）その他：2例（表1）。

〔II〕照射方法

1）線量分布

速中性子線は医用サイクロトロンで30 MeV に加速された重水素をベリリュウムの厚い金属ターゲットに衝突させて得られる。線量分布はコバルト60γ線のそれと

表 1 Fast Neutron Radiotherapy for Malignant Parotid Tumors

(1976—1988, NIRS)

No. of patients:	44
Male: Female:	20 : 24
Age:	12—82
Previous treatment:	
1) None	6
(T2 : 1, T3 : 4, T4 : 1)	
2) Post ope. (prophylactic)	16
3) Post ope. (residual)	9
4) Recurrent	13
Histological classification:	
1) Adenoid cystic ca.	11
2) Malignant mixed ca.	9
3) Adeno ca. (moderate diff.)	7
4) Adeno ca. (poorly diff.)	6
5) Mucoepidermoid ca.	5
6) Acinic cell ca.	4
7) Others	2

ほぼ等しい。10×10cm の照射野, SSD=175cm, ファントム内の測定で表面より1cm下が100%領域, 5cm下が80%領域, 10cm 下が54%領域となる。側方散乱は5cm 下の2cm 外側で約10%である[4]。

2) 照射線量

速中性子線単独照射の基本線量配分は腫瘍線量 TD=1620 CGy／18回／6週(TDF 100)である。TDF(Time Dose Fractionation, 生物学的等価線量) は, 速中性子線とX線というように, RBE の異なる放射線を混ぜて治療するとき, 線量の評価に便利である。一般に根治照射では TDF 100～120, 術後照射では80～90, 術前照射では50～60が目標線量となる。今回の耳下腺腫瘍症例の平均 TDF は, a) 新鮮例の根治照射で109, b) 予防的術後照射で87.6, c) 残存術後照射で92.5, d) 再発例で90.0, 全体で92.2であった。線量分布を改善する目的で速中性子線照射の後に電子線または陽子線をブースト照射した症例があったが, この方法による最大線量照射例は TDF134 (速中性子線760CGY／8回＋電子線3600 CGY／12回＋陽子線800CGy／1回) であった。

〔III〕 治療成績

1) 局所制御と遠隔転移発生率

各症例群ごとに少なくとも6カ月以上経過観察した結果での局所制御率と遠隔転移発生率を示す。a) 新鮮症例：4／6 (67%) と2／6 (33%), b) 予防的術後照射例：13／16 (81%) と7／16 (44%), c) 残存術後照射例：8／9 (89%) と2／9 (22%), d) 再発例：3／13 (23%) と6／13 (46%), e) 合計：28／44 (64%) と17／44 (39%) (表2)。

病理組織別ではそれぞれ, a) Adenoid cystic ca.：10／11 (91%) と4／11 (36%), b) 低分化腺癌：5／6 (83%) と3／6 (50%), c) 中分化腺癌：5／7 (71%) と1／7 (14%), d) 悪性混合腫瘍：5／9 (56%) と4／9 (44%), e) mucoepidermoid ca.： 1／5 (20%) と1／5 (20%), f) Acinic cell ca.： 2／4 (50%) と2／4 (50%), g) その他：0／2と2／2 (表3)。

表 2 Fast Neutron Radiotherapy for Malignant Parotid Tumors Local Control & Metastatic Rates and Previous Treatment Methods

(1976—1988, NIRS)

	None	Post ope. (Prophylactic)	Post ope. (residual)	Recurrent	Total
Local control	4／6 (67%)	13／16 (81%)	8／9 (89%)	3／13 (23%)	28／44 (64%)
Distant meta	2／6 (33%)	7／16 (44%)	2／9 (22%)	6／13 (46%)	17／44 (39%)

表 3 Fast Neutron Radiotherapy for Malignant Parotid Tumors Local Control & Metastatic Rates and Histological Classification

(1976—1988, NIRS)

	Adenoid cystic	Adeno ca poorly diff.	Adeno ca moderate diff.	Malig. mixed	Mucoepider-moid	Acinic cell
Local control	10／11 (91%)	5／6 (83%)	5／7 (71%)	5／9 (56%)	1／5 (20%)	2／4 (50%)
Distant meta.	4／11 (36%)	3／6 (50%)	1／7 (14%)	4／9 (44%)	1／5 (20%)	2／4 (50%)

	Others	Total
Local control	0／0 (0%)	28／44 (64%)
Distant meta.	2／2 (100%)	17／44 (39%)

表 4 Fast Neutron Radiotherapy for Malignant Parotid Tumors Early Radiation Complication

(1976—1988, NIRS)

Grade	Category	No.	%
1	Not recognizable	8	18
2	Mild, No treatment required	14	32
3	Moderate, Temporary treatment required	17	39
4	Severe, Continuous treatment or surgical reconstruction required	5*	11
5	Life threatening or radiation induced cancer	0	0

*4 patients were recurrent cases, only one patient developed severe late complication

2) 遠隔転移部位及び死因の分析

a) 遠隔転移の部位別例数（重複）

肺：11例（5例生存中，2年～9年），骨：5例，脳：2例，リンパ節：1例。

b) 死因，局所再発：6例，局所再発と転移：5例，転移：7例，その他：3例（肝炎，肺炎，老衰各1）。

3) 放射線障害発生率

照射による皮膚，口腔粘膜の急性期の障害の程度を5段階に分けて検討した。a) 1度：障害なし，8例（18%），b) 2度：軽度，治療不要，14例（32%），c) 3度：中等度，一時的治療必要，17例（39%），d) 4度：高度，持続的治療または外科的処置必要，5例（11%），e) 5度：致死的または2次発癌，0例（0%）。高度の障害5例の内4例は再発症例であった。この内1例のみが高度の晩発性障害（骨壊死）に結びついた（表4）。

4) 照射線量と局所制御，障害発生の関連

各症例群における照射線量（TDF）と局所制御（白抜き），再発（黒ぬり），高度の放射線障害（二重）の関連を図1に示した。

5) 生存率

各症例群の生存曲線を Kaplan Meier 法で示した（図2）。

各群の5年生存率（標準偏差）は，a) 新鮮症例：60.0%（13.3%），b) 予防的術後照射例：63.9%（5.3%），c) 残存術後照射例：43.9%（51.7%），d) 再発例：21.4%（38.4%），e) 全体：52.9%（2.9%）であった。

考 察

耳下腺の悪性腫瘍は，今回の報告の症例数，12年間で44例が示す通り，頻度が少なく，しかも術後照射がその過半数を占めるものであったが，高 LET（Linear Energy Transfer）放射線治療の分野では最も効果の上がっている疾患の1つである[12]。

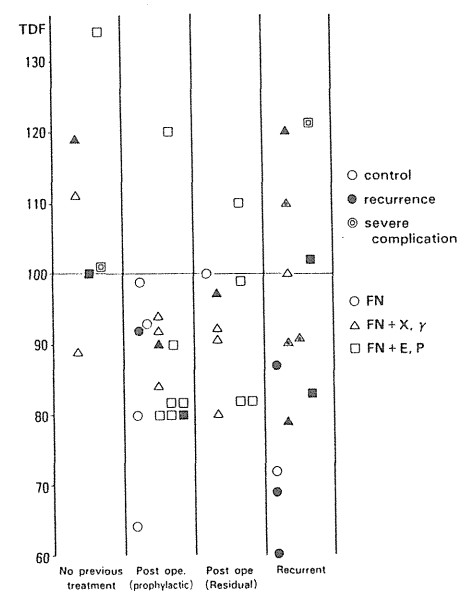

図 1 Radiation Dose and Results

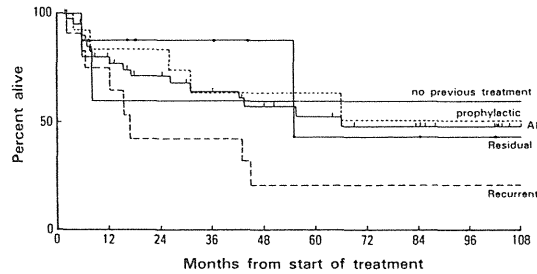

図 2 Survival, Parotid Gland Tumors, treated with Fast Neutrons

(1976—1988, NIRS)

速中性子線が耳下腺悪性腫瘍に効果的であることが Battermann ら[13]によって放射線生物学的に確められている。Adenocystic ca. の肺転移巣を用いて速中性子線と Co-60γ 線の効果を比較，RBE が1回照射で5.7，分割照射で8.0とした。比較的緩徐に発育する腫瘍に対して中性子線がより効果的に働くことを示したもので，他の一般の腫瘍の RBE が2.5～4.0であることを考えればこの値は高い。

臨床治療の結果もこれを裏付けている[15-17]。Griffin ら[17]の世界各施設からの報告のまとめによれば，唾液腺悪性腫瘍の予防的術後照射例を除いた手術不能例と再発例の局所制御率は，速中性子線照射例で67%（194／289），X線，電子線，あるいは放射性同位元素刺入治療例で24%（61／254）であった。今回の放医研の成績を同様の症例群で検討すると54%（15／28）であった。再発例の成績が若干悪かったためにこの成績になったと考える。

Hammersmith 病院の Catterall[15] は，1560 CGY 12回／4週（TDF 99）のスケジュールで，再発例を含む58例のT4症例を治療し，72%の局所制御を得た。新鮮症例の5年局所制御率は80%で，再発症例は35%であった。またこの時の障害発生は全体で14%で，再発例では21%であった。放医研の成績は新鮮6例の局所制御率が66%，再発例は23%（13例）であり，障害発生は問題となる高度の例で新鮮例16%（1／6），再発例で31%（4/ 13）であった。

今回の症例でも術後照射例の44%は2回以上手術をうけていた。再発を繰り返すのが特徴の1つであるが，再発を予防する意味での術後照射の必要性は認められている。Matsuba ら[3]は，悪性度の高い腫瘍の局所制御率は，手術単独で25%，再手術後で73%であるのに対し，術後照射例は80%であったと述べている。Sullivan ら[2]も手術単独で68%，術後照射を加えると86%，Barthne ら[7]は手術単独で53%，術後照射で66%，Fu ら[6]は手術単独46%，術後照射86%，また術後断端陽性症例は手術単独で14%，術後照射で69%（Tran[18]）。このように術後照射は前述のような適応症例に行えば有用である。放医研の症例にはX線照射例は無いが，速中性子線の術後照射例は予防的例81%，断端陽性を含む残存例で89%であった。

多様性のある病理組織別の悪性度の差によって予後が大きく左右される。Spiro ら[19]は acinic cell や low grade mucoepidermoid ca. は85%が10年生存するが，high grade mucoepidermoid ca や malignant mixed tumor，腺癌，adenoid cystic ca. は44～50%，扁平上皮癌は30%以下であると発表している。むろんこれらは手術主体の治療法の結果なので，高度悪性癌や低分化 mucoepidermaid ca. は臨床的に進行期症例が多く，adenoid cystic ca. や高分化 mucoepidermoid ca, acinic cell ca. には進行期例が少ない[7]という癌の進行期の差に大きく影響されている結果と考える。

速中性子線照射での病理組織別の局所制御率の差は，Catterall ら[15]が Adenoid cystic ca.: 76%, Adeno ca.: 82%, Mucoepidermoid ca.: 64%, Malignant mixed tumor: 67%, Griffin ら[17]が Adenoid cystic ca.: 88%, Mucoepidermoid ca.: 67%, Malignant mixed tumor: 100%, 低分化癌：75%と発表している。今回の放医研の成績では Adenoid cystic ca.: 91%, Adeno ca.: 77%, Malignantmixed tumor: 56%, Mucoepidermoid ca.: 20%であり，Mucoepidermoid ca. を除けばほぼ同等であった。病理組織別の差なく，平均して高い局所制御率が示されているのは速中性子線の特徴と考えられる。

最近，RTOG（アメリカ）／MRC（イギリス）のランドマイズ・クリニカルトライアルの結果が報告された[20]。2年以上の経過観察で，局所制御率は速中性子線：69%（9／13），X線：17%（2／12），2年生存率は速中性子線：62%，X線：25%であった。この結果は文献的集計の結果とほぼ等しいものであり，前述の放射線生物学的データを考慮すれば，結論として，速中性子線治療は手術不能，切除不能，再発の悪性唾液腺腫瘍に極めて有効であると述べている。

結　論

1）1975年11月より1988年12月までに44例の耳下腺悪性腫瘍の速中性子線治療を行った。

2）各症例群の局所制御率と遠隔転移発生率は，新鮮症例（n＝6）：67%と33%，予防的術後照射例（n＝16）：81%と44%，残存術後照射例（n＝9）：89%と22%，再発例（n＝13）：23%と46%であった。

3）放射線障害発生率は，急性期4度（高度）の障害で，5例（11%）であった。この内1例が晩発性の高度の障害に結びついた。

4）5年累積生存率は，新鮮症例：60%，予防的術後照射例：63.9%，残存術後照射例：43.9%，再発例：21.4%，全体：52.9%であった。

（この論文の要旨は第13回日本頭頸部腫瘍学会（大阪，1989）において発表した。）

文　献

1) Rossman, K. J.: The role of radiation therapy in the treatment of parotid carcinomas. Am. J. Roentgenol. 123: 492-499, 1975.
2) Sullivan, M. J., Breslin, K., McClatchey, K. D., et al.: Malignant parotid gland tumors: A retrospective study. Otolaryngology Head and Neck Surgery 97: 529-533, 1987.
3) Matsuba, H. M., Thawley, S.E., Devineni, V. R., et al.: High-grade malignancies of the parotid gland: Effective use of planned combined surgery and irradation. Laryngoscope 95: 1059-1063, 1985.
4) Tu, G., Hu. Y., Jiang, P., et al: The superiority of combined therapy (surgery and post operative irradiation) in parotid cancer. Arch Otolaryngol. 108: 710-713, 1982.
5) Guillamondegui, O. M., Byers, R. M., Luna, M. A., et al.: Aggressive surgery in treatment of parotid cancer: The role of adjunctive postoperative radiotherapy. Am. J. Rentgenol. 123: 49-54, 1975.
6) Fu, K. K., Leibel, S., Levine, M., et al.: Carcinoma of the major and minor Salivary glands: Analysis of treatment results and sites and causes of faliures. Cancer 40: 2882-2890, 1977.
7) Barthne, A., Kjellevolt, K., Kaalhus, O., et al.: Salivary gland malignant neoplasms: Treatment and prognosis. Int. J. Radiat. Oncol. Biol. Phys. 12:

747-754, 1986.
8) Elkon, D., Coleman, M., and Hendrickson, F.: Radiation therapy in the treatment of malignant salivary gland tumors. Cancer 41 : 502-506, 1978.
9) Shidnia, H., Hornback, N. B., Hamaker, R., et al.: Carcinoma of major salivary glands. Cancer 45 : 693-697, 1980.
10) 森田新六, 恒元　博, 青木芳朗, 他 : 高 LET 放射線治療の現況. 癌の臨床 33 : 1647-1654, 1987.
11) 恒元　博 : 速中性子線治療. 日本臨床 46 : 95-103, 1988.
12) Griffin, T. W., Wambersie, A., Laramore, G., et al.: High LET: Heary particle trials. Int. J. Radiat. Oncology Biol. Phys. 14 : S83-S92, 1988.
13) Battermann, J. J., Breuer, K., Hart, G. A., et al.: Observation on pulmonary metastasis in patients after single doses and multiple fractions of fast neutrons and cobalt-60 gamma rays. Europ. J. Cancer 17 : 539-548, 1981.
14) 星野一雄, 川島勝弘, 平岡　武, 他 : 放医研サイクロトロンからの速中性子線の線量分布. 日医放会誌 37 : 248-255, 1977.
15) Catterall, M., Errington, R. D.: The implication of improved treatment of malignant salivary gland tumors by fast neutron radiotherapy. Int. J. Radiation Oncology Biol. Phys. 13 : 1313-1318, 1987.
16) Henry, L. W., Blasko, J. C., Griffin T. W., et al.: Evaluation of fast neutron teletherapy for advanced carcinomas of the major salivary glands. Cancer 44 : 814-818, 1979.
17) Griffin, B. R., Laramore, G. E., Russell, K. J. et al.: Fast neutron radiotherapy for advanced malignant salivary gland tumors. Radiotherapy and Oncology 12 : 105-111, 1988.
18) Tran, L., Sadeghi, A., Hanson, D., et al.: Major salivary gland tumors: treatment results and prognostic factors. Laryngoscope 96 : 1139-1144, 1986.
19) Spiro, R. H., Armstrong, J., Harrison, L., et al.: Carcinoma of major salivary glands. Arch Otolaryngol Head Neck Surg. 115 : 316-321, 1989.
20) Griffin, T. W., Pajak, T. F., Laramore, G. E., et al. : Neutron vs photon irradiation of inoperable salivary gland tumors: Results of an RTOG-MRC cooperative randomized study. Int. J. Radiation Oncology Biol. Phys. 15 : 1085-1090, 1989.

Pigment Cell Research 2:372–3

Characteristics of Malignant Melanoma Cells in the Treatment With Fast Neutrons

HIROSHI TSUNEMOTO,[1] SHINROKU MORITA,[1] AND SHUNJI MORI[2]
National Institute of Radiological Sciences,[1] Chiba-shi, and School of Medicine, Gifu University, [2]Gifu-shi, Japan

The radioresistance of malignant melanoma cells has been explained by the wide shoulder of the dose-cell-survival curve of the cells exposed to photon beams. Fast neutrons, 30 MeV d-Be, were used to treat patients who had malignant melanoma in order to confirm the biological effects of high linear energy transfer (LET) radiation for tumor control.

Seventy-two patients suffering from malignant melanoma participated in the clinical trials with fast neutrons between November 1975 and December 1986. Of 72 patients, 45 had melanoma of the skin, 20 had melanoma of the head and neck, and seven had choroidal melanoma.

Five-year survival rate of the patients who had previously untreated melanoma of the skin was 61% and for patients who received postoperative irradiation, it was 35.7% whereas no patients who had recurrent tumor survived over 4 years. Of 22 patients who had melanoma of the skin, stage I, local control in four cases was achieved by irradiation alone, whereas local control was achieved in 17 of 18 patients who required salvage surgery after fast-neutron therapy. The results of pathological studies performed with specimens obtained from salvage surgery have shown that melanoma cells growing in intradermal tissue are radio-resistant, compared with cells growing in intraepidermal tissue. This might suggest that melanoma cells acquire radioresistance when the connective tissue is involved.

Five-year survival rate of the patients who had locally advanced melanoma of the head and neck, previously untreated, was 15.4%. Radiation therapy with accelerated protons was suitable for patients suffering from choroidal melanoma.

Key words: High LET radiations, Malignant melanoma, Radiation therapy

INTRODUCTION

Patients suffering from malignant melanoma have been preferentially treated with surgical procedures, because melanoma has been found to be markedly radioresistant. Although the features of malignant melanoma cells have not been fully elucidated in biological studies, it has been suggested that malignant melanoma is radioresistant, because the cells markedly repair sublethal damage of irradiation and that when fast neutrons characterized by high linear energy transfer (LET) were used the repair capability of the irradiated cells would be controlled. With regard to fast-neutron therapy, preliminary studies with 2.8-MeV d-Be neutrons performed at the National Institute of Radiological Sciences (NIRS) showed that of 23 patients who had malignant melanoma 10 demonstrated marked response to fast neutrons without unacceptable complications [Tsunemoto, 1986].

MATERIALS AND METHODS

One thousand four hundred ninety-seven patients participated in the clinical trials with fast neutrons between November 1975 and December 1986. Of the 1,497 patients, 72 had malignant melanoma. Forty-five of these 72 patients were suffering from melanoma of the skin, of whom 24 had previously untreated melanoma, eight required postoperative irradiation, and 13 had recurrent tumor that had developed after surgical procedures. There were 20 patients who had malignant melanoma of the head and neck, of whom 16 had previously untreated tumor and four had recurrent tumor. Choroidal melanoma was seen in seven patients who

Address reprint requests to Hiroshi Tsunemoto, National Institute of Radiological Sciences, 9-1, Anawaga 4-chome, Chiba-shi 260, Japan.
Received August 23, 1988; accepted September 21, 1988.

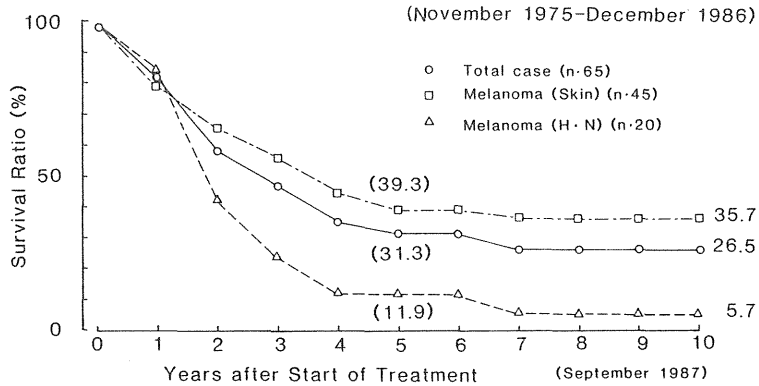

Fig. 1. Cumulative survival rates of patients suffering from malignant melanoma treated with 30-MeV d-Be neutrons (NIRS, November 1975–December 1986).

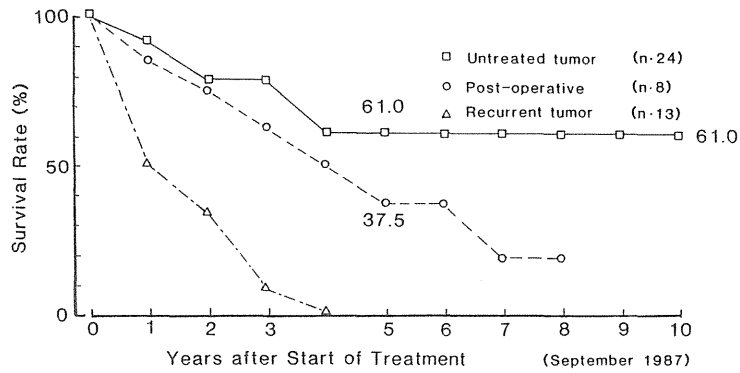

Fig. 2. Cumulative survival rates of patients suffering from cutaneous malignant melanoma treated with 30-MeV d-Be neutrons (NIRS, November 1975–December 1986).

TABLE 1. No. Patients Suffering From Malignant Melanoma Referred to Treatment With 30-MeV d-Be Neutrons (NIRS, November 1975–December 1986)

Site		No. patients
Skin		45
Previously untreated	24	
Postoperative recurrent tumor	8	
Recurrent	13	
Head and Neck		20
Previously untreated	16	
Recurrent	4	
Choroid		7
Total		72

were excluded from the evaluation because they were treated with 70 MeV protons (Table 1).

The treatments were performed with fast neutrons, which were produced by bombarding a thick beryllium target with 30-MeV deuterons accelerated by a cyclotron. Depth-dose curves of the beam for a 10 × 10-cm field at SSD 175 cm were equivalent to those of Tele-Cobalt gamma rays for a 10 × 10-cm field at SSD 80 cm. The dose rate measured in a tissue equivalent phantom was 42 cGy (n, γ)/min/30 μA for a 11.4 × 11.4-cm field at STD 200 cm. Gamma ray contamination was estimated to be less than 4% of the beam.

The patients who participated were usually treated with fast neutrons only, by which a total dose of 16.2 Gy was delivered in 18 fractions over 6 weeks as the standard (TDF 100). In the treatment of radioresistant cancers, such as malignant melanoma, doses equivalent to TDF 110–120 were required to achieve tumor control. Salvage surgery was prescribed for the patients who had uncontrolled tumor at the completion of irradiation.

RESULTS

Survival Rate and Local Control

Survival rates of patients who had malignant melanoma and were treated with fast neutrons are shown

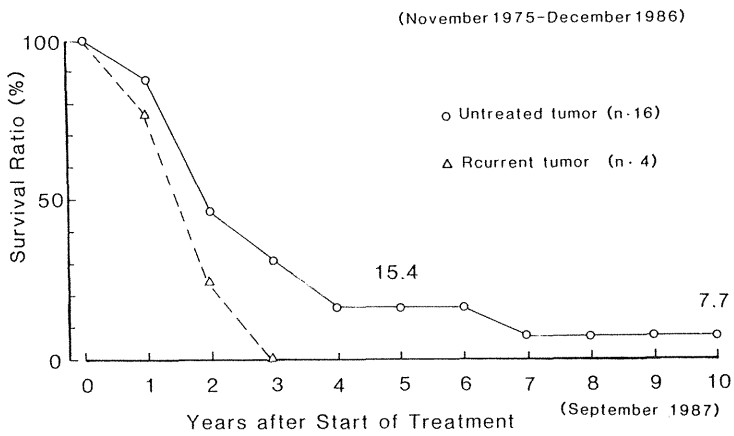

Fig. 3. Cumulative survival rates of patients suffering from malignant melanoma of the head and neck treated with 30-MeV d-Be neutrons (NIRS, November 1975–December 1986).

TABLE 2. Results of Treatment With 30-MeV d-Be Neutrons for Patients Suffering From Malignant Melanoma of Cutaneous Tissue (November 1975–December 1986, NIRS)

Site	No. patients	Response[a] CR	Response[a] PR (S · CR)	Moist reaction	Follow-up (September 1987) Months	Follow-up (September 1987) Dead
H and N	7	3	4 (4/4)	—	3–86	3
Leg (sole)	15	1	14 (13/13)	4	8–108	5
	22	4	18 (17/17)	4	3–108	8

[a]CR: complete regression, PR: partial regression, S · CR: CR with surgery.

in Figure 1. Five- and 10-year survival rates of patients who had either melanoma of the skin or the head and neck were 31.3 and 26.5%, respectively. In the treatment of patients with melanoma of the skin, the survival rates for 5 and 10 years were 39.3 and 35.7%, respectively. For patients who had melanoma of the head and neck, the survival rates were 11.9 and 5.7% at 5 and 10 years, respectively. Figure 2 shows the survival rates of patients who were suffering from cutaneous malignant melanoma treated with fast neutrons. In the treatment of 24 patients who had a previously untreated tumor, of whom 22 were in stage I and two in stage II, survival rates for both 5 and 10 years were 61%. The rate for patients who required postoperative irradiation was 37.5% at 5 years, whereas no patients with recurrent melanoma survived more than 5 years.

The survival rates of patients who had melanoma of the head and neck were 15.4% at 5 years and 5.5% at 10 years (Fig. 3). The reason why the survival rates of patients with melanoma of the head and neck were lower than those with melanoma of the skin are explained by the fact that patients with advanced tumors were referred to the clinical trials.

The status of local control of the tumor was evaluated in 22 patients who were suffering from stage I malignant melanoma of the skin. The results show that for seven patients who had melanoma of the head and neck, local control by irradiation alone was achieved for three of them and four showed local control when salvage surgery was also done. Of the 15 patients who had malignant melanoma of the extremities, 13 required salvage surgery in order to achieve local control, in which the surgical margin of the treatment could be minimized by means of radiation therapy with fast neutrons.

Moist desquamation was seen in four patients, whose reactions were managed by conservative treatment. Late reactions of normal tissues were acceptable (Table 2).

Characteristics of Malignant Melanoma

Radiosensitivity of malignant melanoma was evaluated by histopathological studies on specimens obtained by operation performed after completion of fast-neutron therapy. The 34 patients participating in this study were referred for fast-neutron therapy by the National Cancer Hospital, University of Gifu, and University of Kanazawa between 1970 and 1982. Of 34 patients, 20 had acral lentiginous melanoma (ALM) and 14 had nodular melanoma (NM). There were no patients suffering from either superficial spreading melanoma or lentigo maligna melanoma (Table 3). This supports the report that melanomas are likely to arise

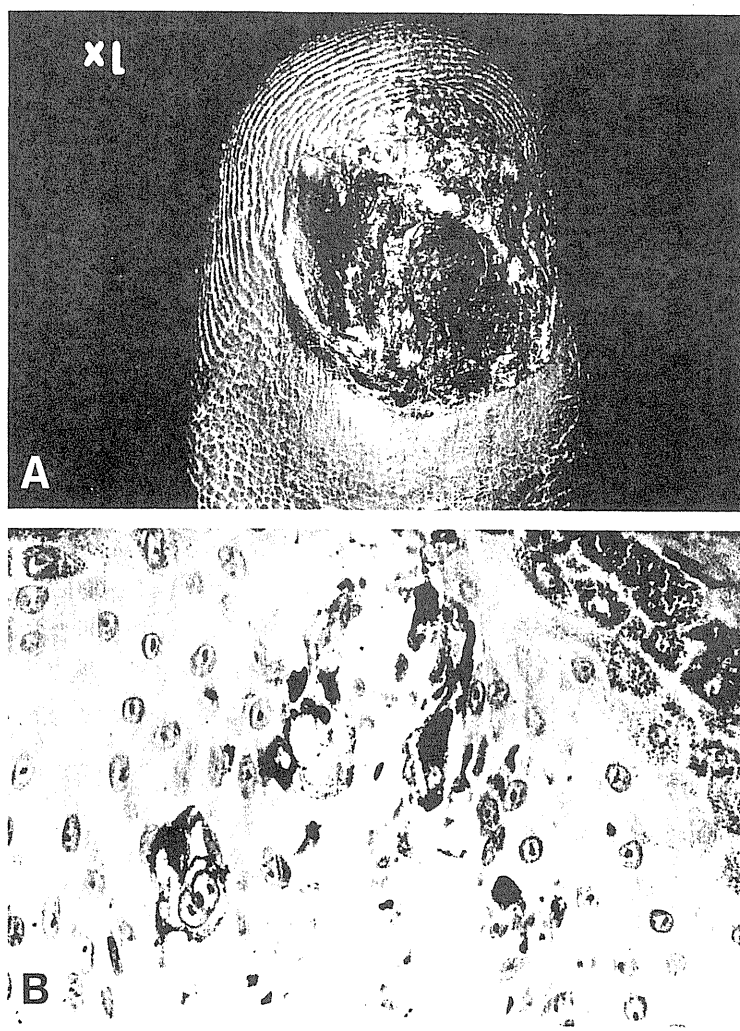

Fig. 4. This male patient, 68 years old, was suffering from a subungal melanoma on November 1980 and received fast-neutron therapy. Amputation of the forefinger was performed in January 1981 after irradiation of 17.7 Gy of fast neutrons delivered in 13 fractions in 31 days. The patient was still well without local recurrence and metastasis on September 1987. Photogram taken just after irradiation showed a marked effect of the irradiation (**A**) and the specimen obtained by surgery showed the intraepidermal tumor cells to be markedly degenerated (**B**).

TABLE 3. Clinico-pathological Classification of Malignant Melanoma Referred to Fast-neutron Therapy From the Institutions (1970–1982, NIRS)

	No. patients
Acral lentiginous melanoma (ALM)	20
Nodular melanoma (NM)	14
Superficial spreading melanoma	—
Lentigo maligna melanoma	—
	34

NCH and Universities of Gifu and Kanazawa (Mori, 1987).

TABLE 4. Results of Fast-neutron Therapy for Malignant Melanoma (1970–1982, NIRS)

	Effect[a]				
	CR	PR	MR	NC	
ALM	2 (25%)	3	12	2	1
NM	0 (29%)	4	5	3	2

[a]CR: complete response, PR: partial response, MR: minor response, NC: no change (Mori, 1987).

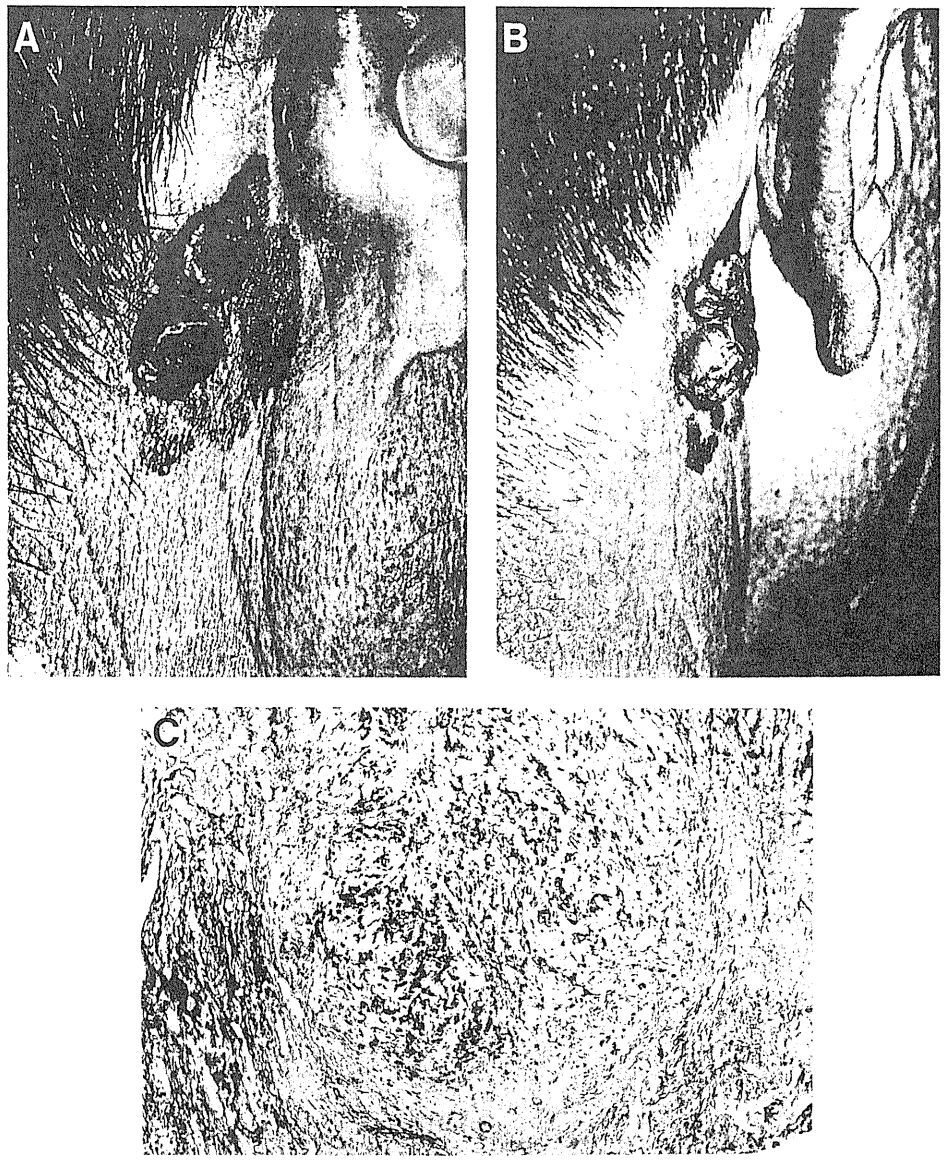

Fig. 5. The patient, 57 years old, had a nodular melanoma arising from the cutaneous tissue behind the ear on September 1980. Surgical removal of the tumor was performed on December 1980 after irradiation, where 20 Gy of protons were delivered to the target volume in two fractions following irradiation of 12 Gy of fast neutrons delivered in 25 days. The photograms, **A** and **B**, were taken before and after radiation therapy, respectively. Specimens obtained by salvage surgery showed degenerated tumor cells that were surrounded by a fibrotic tissue (**C**). The patient was still living without local recurrence in October 1987.

from the sole or oral cavity in Japanese, whereas melanomas are common in the regions exposed to the sun for patients in the European countries [Mori, 1973].

Patients referred to the clinical trials from 1970 to 1974 were treated with 2.8-MeV d-Be neutrons, for which the depth-dose curves were equivalent to those for 150-kV X-rays, whereas patients referred since 1975 were treated with 30-Mev d-Be neutrons when the cyclotron became available. The results show that of 20 patients suffering from ALM two achieved complete response of

TABLE 5. Effect of Fast Neutrons on Malignant Melanoma Cells Evaluated With Histological Specimens Obtained by Salvage Surgery (1970–1982, NIRS)

	Effects[a]
Intraepidermal melanoma cells	
Degeneration of cytoplasma	(+)–(++)
Degeneration of nucleus	(+)–(+++)
Intradermal melanoma cells	
Degeneration of cytoplasma	(−)–(+)
Degeneration of nucleus	(−)–(++)
Retraction of tumor mass	(−)–(+)

[a](+++): marked, (++): moderate, (+): low, (−): no change (Mori, 1987).

the tumor and three achieved partial response and that of ten patients who were suffering from NM none showed complete response of the tumor. Although there were no statistical differences between the results from the series with ALM and that with NM, NM seemed to be more radioresistant than was ALM (Table 4).

Studies performed with histological specimens have indicated that melanoma cells growing in intraepidermal tissue showed marked degeneration of the cytoplasma and nucleus, while the cytoplasma and nucleus of cells in the intradermal tissue showed no response or were slightly degenerated (Table 5). These results might suggest that malignant melanoma cells will acquire radioresistance when the cells grow into the intradermal tissue through the intraepidermal tissue (Figs. 4, 5).

Unfortunately, the relationship between radiosensitivity and histological appearance of malignant melanoma has not been confirmed, although malignant melanoma consisting of spindle cells seems to be radiosensitive compared with tumors classified as either epitheroid cell type or small cell type.

DISCUSSION

Studies with human malignant melanoma cells performed in vitro have indicated that the cells have a wide shoulder in the dose-cell-survival curve of the irradiated cells, which means that the cells are markedly able to repair their sublethal damage when treatment is scheduled with a conventional fractionation regime [Dewey, 1971]. Therefore, treatment with a large fraction of the doses has been recommended in treatment of patients who had malignant melanoma. The results of clinical trials for patients with malignant melanoma have indicated that when the treatment was performed using fraction sizes ranging from 4 to 8 Gy the rates of complete regression of the tumor have been improved, compared with the results of treatment obtained by using fractions under 4 Gy [Hornsey, 1978; Overgaad, 1986; Konefal et al., 1987]. Although the radioresistance of malignant melanoma seemed to be explained by the wide shoulder the fact that malignant melanoma cells in culture have not shown any marked additional resistance to radiation damage compared with cells derived from normal tissue still remains as a problem to be studied [Barranco et al., 1971]. As to the radioresistance of malignant melanoma cells in vivo, it was suggested that, because the growing fraction of the cells was found to be small in malignant melanoma and a large portion of the cells are keeping the cell cycle in "GO," malignant melanoma are protected from irradiation and behave as radioresistant, while malignant melanoma cells in culture are growing in an exponential phase and behave radiosensitively.

On the other hand, when radical treatment for the patients who have malignant melanoma is concerned, clinical appearance of the tumor has to be considered in managing the disease and in deciding the most appropriate treatment in order to preserve the function of the patients. The results of clinical trials performed with 30-MeV d-Be neutrons have shown that nodular melanoma is radioresistant, even to irradiation by fast neutrons and that the radioresistance of nodular melanoma can be partly explained by the fact that the cells of nodular melanoma tend to grow into the intradermal tissue, whereas acral lentiginous melanoma cells had a tendency to grow in the intraepidermal tissue and showed a response to fast neutrons compared to nodular melanoma cells.

It was emphasized that the features of radioresistance of malignant melanoma have to be confirmed by studies pursuing the interaction between cells of malignant melanoma and cells of the intradermal tissues.

CONCLUSIONS

The response of malignant melanoma to radiation was evaluated with special reference to fast neutrons. The results of the studies are summarized as follows:

1. The response of malignant melanoma was found to be dependent on the clinical appearance of the tumor, since nodular melanoma seemed to be more resistant to radiation compared with acral lentiginous melanoma even when fast neutrons were used.
2. Histological studies indicated that malignant melanoma cells growing in intraepidermal tissue showed a response to fast neutrons and that cells growing in intradermal tissue through the intraepidermal tissue were radioresistant.
3. Preoperative irradiation is recommended in the treatment of malignant melanoma in order to minimize the surgical margin and to improve local control rate of the tumor.

It was concluded that high LET radiation is suitable for treating malignant melanoma, in which the cells are markedly able to repair sublethal damage from irradiation [Thomson et al., 1975] and that the response of malignant melanoma cells to radiation has to be evaluated with reference to consideration based on clinical pathology.

REFERENCES

Barranco, S.C., M.M. Romsdahl, and R.M. Humphrey (1971) The radiation response of human malignant melanoma cells grown in vitro. Cancer Res., 31:830–833.

Dewey, D.L. (1971) The radiosensitivity of melanoma cells in culture. Br. J. Radiol., 44:816–817.

Hornsey, S. (1978) The relationship between total dose, number of fractions and fraction size in the response of malignant melanoma in patients. Br. J. Radiol., 51:905–909.

Konefal, J.B., B. Emami, and M.V. Pilepich (1987) Malignant melanoma; Analysis of dose fractionation in radiation therapy. Radiology, 167:607–610.

Mori, W. (1973) Geographic pathology of malignant melanoma in Japan. Pigment cell, 1:246–254.

Overgaad, J. (1986) The role of radiotherapy in recurrent and metastatic malignant melanoma. Int. J. Radiat. Oncol. Biol. Phys., 12:867–872.

Thomson, L.F., A.R. Smith, and R.M. Humphrey (1975) The response of a human melanoma cell line to high LET radiation. Radiology, 117:155–158.

Tsunemoto, H. (1986) Present status of the research project on medical application of the heavy particle beams and the purpose of the workshop. In: Proceedings of International Workshop on the NIRS Heavy Particle Medical Accelerator, Tsunemoto, H. et al., eds. NIRS, Japan, pp. 1–11.

Strahlentherapie und Onkologie

Zeitschrift für Radioonkologie,
Strahlenbiologie, Strahlenphysik

Sonderdruck

Present status of fast neutron therapy in Asian countries

H. Tsunemoto, S. Morita, S. Satoh, Y. Iino[1], Yul Yoo[2]

National Institute of Radiological Sciences, Chibashi, Japan, Institute of Medical Science[1], University of Tokyo, Tokyo, Japan, and Korea Cancer Center Hospital[2], Seoul, Korea

The present status of the treatment with fast neutrons performed in Asian countries is reviewed and the experiences with respect to the radiobiological indications are presentated and discussed. There are three facilities under operation, the National Insitute of Radiological Sciences (NIRS) in Chiba, the Institute of Medical Science (IMS) in Tokyo and the Korea Cancer Center Hospital (KCCH) in Seoul. The clinical experiences can be summarized as follows: Fast neutrons are the treatment of choice for carcinoma of the salivary gland, Pancoast tumor of the lung, osteosarcoma, soft tissue sarcoma and malignant melanoma. Provided the isodose planning can be improved, it seems that also squamous cell carcinoma of the head and neck and esophagus, adenocarcinoma of the lung, stage I and prostatic adenocarcinoma can be benefit from neutron therapy. The same holds for malignant meningioma, while the benefit for glioblastoma multiforme has not yet been confirmed. Studies are going on for the treatment of other cancers and for evaluating the possible role of neutron therapy in combination with surgery.

Der derzeitige Stand der Neutronentherapie in Asien

Über den derzeitgen Stand der Neutronentherapie in Asien wird berichtet und die Erfahrungen im Hinblick auf die radiologische Indikation dargestellt und diskutiert. Es gibt zur Zeit drei laufende Anlagen in Asien, nämlich das National Institute of Radiological Sciences (NIRS) in Chiba, das Institute of Medical Science (IMS) in Tokio und das Korea Cancer Center Hospital (KCCH) in Seoul. Die klinischen Erfahrungen können wie folgt zusammengefaßt werden: Schnelle Neutronen sind die Methode der Wahl für Schleimdrüsenkarzinome, Pancoast-Tumoren der Lunge, Osteosarkome, Weichteilsarkome und maligne Melanome. Bei verbesserter Dosisplanung scheinen sich auch noch Plattenepithelkarzinome im HNO-Bereich und frühe Adenokarzinome der Lunge sowie der Prostata zu eignen. Günstig dürfte die Neutronentherapie auch noch für maligne Meningiome sein, während ein Vorteil bei der Bestrahlung von multiformen Glioblastomen noch nicht erwiesen ist. Klinische Studien werden zur Zeit für die Therapie weiterer Tumoren und zur Klärung der möglichen Rolle der Neutronentherapie in Kombination mit der Tumorchirurgie durchgeführt.

Introduction

There are three facilities for fast neutron therapy in Asian countries; the National Institute of Radiological Sciences (NIRS), Chiba, Institute of Medical Science (IMS), Tokyo, and Korea Cancer Center Hospital (KCCH), Seoul. On November 1975, NIRS started clinical trials with fast neutrons, while the trials began at IMS on November 1976. A new project study was organized at KCCH, where the trials with a modern equipment for fast neutron therapy started on October 1986. In Table 1, the characteristics of the beams used in the clinical trials and the number of patients participated are summarized.

The present status of the treatment with fast neutrons performed in Asian countries is reviewed and the indications for fast neutron therapy are discussed.

I. National Institute of Radiological Sciences

1. Irradiation technique

Vertical beams were used for clinical trials with fast neutrons which were obtained by bombarding a thick Beryllium target with 30 MeV deuterons. The depth dose curves of the beam for 10×10 cm^2 field, at SSD 175 cm, were equivalent to those of telecobalt gamma rays measured in 10×10 cm^2 field, at SSD 80 cm. The dose rate (n, γ) in a tissue equivalent phantom was 42 cGy min^{-1} 30 μA^{-1} for 11.4×11.4 cm^2 field, at STD 200 cm. Gamma ray contamination was estimated to be less than 4% in the beam.

The patients who were suffering from locally advanced cancers as well as radioresistant cancers were treated either by fast neutrons only, mixed schedule or fast neutron boost. For fast neutrons only, a total dose of 1620

	Neutrons	Beams	Start treatment	Number of patients
NIRS*	d(30) + Be	Vertical	Nov. 1975	1498 (Dec. 1986)
IMS**	d(14) + Be	Horizontal	Nov. 1976	402 (Sept. 1987)
K. C. C. H.***	P(50.5) + Be	Rotational	Oct. 1986	67 (Sept. 1987)

* National Institute of Radiological Sciences, Chiba. ** Institute for Medical Science, Tokyo. *** Korea Cancer Center Hospital, Seoul

Table 1. Fast neutrons using for clinical trials in Asian countries.

	Number of patients	Complete regression	Complication
Locally advanced Carcinoma	5	3 (60.0 %)	1
Postoperative radiotherapy	14	14 (100 %)	1
Radiotherapy for recurrence	16	10 (62.5 %)	2
Total	35	27 (77.0 %)	4

Table 2. Results of clinical trials with fast neutrons for the patients suffering from carcinoma of the parotid gland (NIRS). (April 1987)

cGy was delivered in 18 fractions in six weeks as the standard (TDF 100). In the treatment with mixed schedule, the irradiation was performed with neutrons (72 cGy) on Tuesday and Friday, and with photons (170 cGy) on Monday and Thursday. Radical irradiation was performed with the doses equivalent to TDF 100 to 120, while the doses equivalent to TDF 80 were delivered to the target volume for postoperative irradiation.

Surgery was designed to remove cancers within two and three weeks following preoperative irradiation performed with fast neutrons equivalent to TDF 60.

2. Results

A total number of 1497 patients were treated with fast neutrons between November 1975 and December 1986. Neutrons were mainly given as a radical treatment, and patients who had radioresistant cancers were preferentially treated with fast neutrons only, while, for the cancers of head and neck, lung and brain, fast neutrons were given as boost following photon beam irradiation at doses of 30 to 40 Gy.

Mixed schedule was the treatment of choice for the patients who had carcinoma of the uterine cervix (Figure 1). Preliminary studies indicate that five year survival rate was 31.9 % for stage III cancers and 20.1 % for stage IV cancers.

a) Carcinoma of the larynx

The patients who had carcinoma of the larynx were treated with neutron boost after photon treatment at doses of 30 to 40 Gy. The total doses delivered were equivalent to TDF 120. The results showed that fast neutrons were effective to treat carcinoma of the supraglottis. 13 patients were treated with fast neutrons, eleven (84 %) achieved local control, while local control was achieved in only 25 of 100 patients (25 %) after photon irradiation. There was no definite difference in local control between fast neutrons and photons for carcinoma of the glottis and subglottis [7].

Therefore, a randomized study has been conducted to confirm the superiority of fast neutrons on carcinoma of the larynx.

b) Carcinoma of the parotid gland

35 patients were treated with neutrons from 1975 to 1986: 27 had local control. Among five patients who had inoperable cancer, three achieved local control. Among 16 patients who had recurrent cancer after radical parotidectomy, ten (62.5 %) had local control. Post-operative irradiation was prescribed for 14 patients, none of them developed recurrence. Moist desquamation of the skin developed in four patients, and required only conservative treatment (Table 2). Five year survival rates of the patients who had either inoperable cancer or recurrent tumor were 30 % or 60 %, respectively. The survival rate was 58.2 % for the patients who received post-operative irradiation. The cause of death of the patients who received fast neutron therapy was distant metastasis.

c) Carcinoma of the lung

Fast neutron therapy was prescribed for 74 patients suffering from carcinoma of the lung between 1975 and 1984. The results showed that adenocarcinoma of the

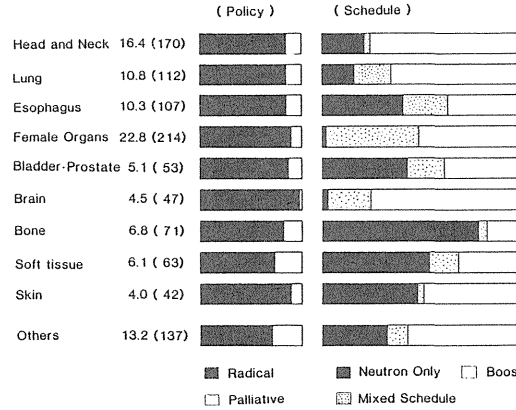

Figure 1. Treatment policy and schedule for fast neutron therapy performed at NIRS.

Stage	Number of patients	Age (mean)	TDF (mean)	Alive	Dead	Months of surviving	Cumulative 5 year survival rate (%)
III	11	62	115	3	8	21.2	36.3
IV	10	62.6	108	1	9	8.7	10.0
Total	21	62.2	112	4	17	14.6	23.2

Table 3. Results of clinical trials with fast neutrons for the patients suffering from Pancoast tumor of the lung (NIRS) [5].

Modalities	No. of cases	Complete regression (%)
F–N	34	15 (44.1)
Mixed schedule	20	7 (35.0)
Boost therapy	14	8 (57.1)
Photon	81	24 (29.6)

Table 4. Results of clinical trials fast neutrons for the patients suffering from carcinoma of the esophagus (NIRS) [2].

lung in early stage and Pancoast tumor of the lung are indications for fast neutron therapy. For seven patients with adenocarcinoma of the lung, stage I, the cumulative five year survival rate after neutron therapy was 52%, which was almost the same as after radical surgery. Cumulative five year survival rate of the 21 patients who had Pancoast tumor and participated to the clinical trials was 23.2%. For the patients, stage III, the cumulative five year survival was 36.3%, while it was 10.0% for stage IV. Neutron doses equivalent to TDF 110 were delivered to the target volume without unacceptable complications (Table 3) [5].

d) Carcinoma of the esophagus

99 patients suffering from carcinoma of the esophagus were treated with fast neutrons between 1976 and 1983. Among then, 34 had radical irradiation with either mixed schedule or fast neutron boost. Doses equivalent to TDF 90 to 120 were delivered to the target volume.

Among the 34 patients who received fast neutron therapy, 15 achieved local control of the tumor (44.1%), whereas 24 out of 81 patients treated with photons had local control (29.6%) (Table 4). Another study suggested that the results were strongly dependent on the extent of the lesion of the esophagus. When the lesions were smaller than 8 cm in length, local control rate after fast neutrons was 50% (13/26), which was superior than the rate of 41.5% (17/41) obtained with photons. However, when the lesions were longer than 8 cm, local control rates after fast neutrons or photons irradiation were 28.6% (2/7) or 25.9% (7/27), respectively. Therefore, it was recommended to evaluate the results of the treatment for patients with tumor of the esophagus smaller than 8 cm, in order to confirm the superiority of fast neutrons [2].

Five year survival rate for the patients who received the planned postoperative irradiation with fast neutrons was 16.7%, while all patients who had photon beam therapy died within 24 months.

e) Carcinoma of the uterine cervix

98 patients with squamous cell carcinoma of the uterine cervix, stage IIIb, entered in clinical trials from 1975 to 1983. 45 were treated with mixed schedule and 53 with photons only. The whole pelvis was irradiated by two opposed fields with a mixed schedule, three times a week with photons and twice a week with fast neutrons. The total doses were equivalent to 50 to 55 Gy of photons delivered in five to 5.5 weeks. All patients received intracavitary therapy with a remote afterloading high dose rate intracavitary system (RALS). The treatment was performed in two fractions with one week interval during the last two weeks of external irradiation; doses of 11 to 13 Gy were delivered at point A.

Local control rate was 73% (33/45) after mixed schedule and 66% (35/53) after photons. Although the local control rate for tumor of small size was improved in the neutron series (83%; 19/23) compared with photon beam series (65%; 17/26), no significant difference was observed in the survival rates. The cumulative five year survival was 49% in both series.

These results suggest that, in order to confirm the superiority of fast neutrons for carcinoma of the uterine cervix, the patients entering the clinical trials should be selected, since involvement of the para-aortic lymph nodes is common for patients with stage IIIb cancers. This view was supported by the results obtained for patients who had recurrent tumor in the pelvis due to carcinoma of the uterine cervix. Among 39 patients who had recurrent tumor in the pelvis and received fast neutron therapy, five year survival rate was 20.5%, while it was smaller than 10% after photon irradiation.

f) Carcinoma of the urinary bladder

Preoperative irradiation was prescribed for carcinoma of the urinary bladder. 49 patients participated to the clinical trials between 1976 and 1986, of whom 20 received fast neutron therapy and 29 had photon beam irradiation. Surgery was performed within two to three weeks after the irradiation, where the doses equivalent to TDF 60 were delivered with either fast neutron only or photon beams. The results evaluated for the patients staged T2 or T3, without metastasis, showed that five year survival rate for 13 patients who received fast neutrons was 82 % and was 76 % for 15 patients who had photon beam irradiation.

A complication was seen in one patient after fast neutron irradiation: dysfunction of the kidneys due to obstruction of the urethra.

g) Carcinoma of the prostate

47 patients were referred to the clinical trials with fast neutrons from University of Chiba between 1976 and 1986. Among them, 36 were treated with fast neutrons only and eleven with photons. Doses equivalent to TDF 100 were prescribed for either fast neutrons or photons.

Local control rates were evaluated for the patients staged A2, B and C, at three years after completion of the treatment: they reached 100 %, 60 % and 52 % for the patients staged A2, B and C, respectively (Figure 2).

Some complications appeared in the fast neutron series: stricture of the urethra, deformity of the penis and ulcer of the skin. There was no complication in the photon series.

Cumulative five year survival rate of the patients treated with fast neutrons were 50 %. All patients, staged A or B, are still surviving without no evidence of evolutive cancer.

h) Osteosarcoma

The patients suffering from osteosarcoma were treated with fast neutrons combined with chemotherapy from 1975 to 1981. The drugs for chemotherapy were injected through a femoral artery prior to irradiation, and, thereafter, fast neutrons equivalent to TDF 100 to 120 were delivered to the target volume.

Since 1981, the policy of the treatment has been modified to preserve the leg, because the late effects of the

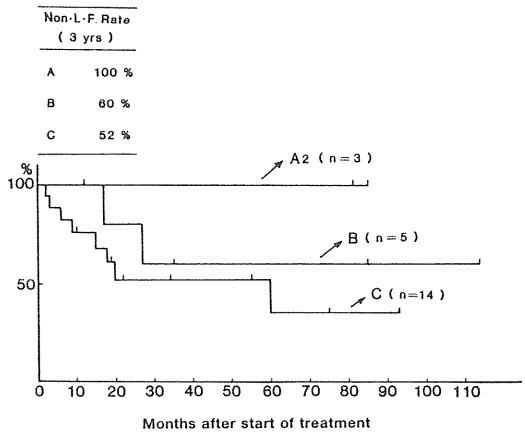

Figure 2. Local control rates of carcinoma of the prostate treated with fast neutrons (NIRS).

normal tissues were found to be more severe than expected to make prothesis. The treatment was modified as follows:

1. The patients who had the lesions ranging 1/3 to 1/4 long of the femur were selected for fast neutrons.

2. The doses equivalent to TDF 80 were delivered with fast neutrons only.

54 patients with osteosarcoma were treated with fast neutrons between 1975 and 1983. The results evaluated in 48 patients who received radical radiation therapy showed that five year survival rate was 67 % after fast neutron therapy, which was better than that rate of 19 % obtained with photon beam therapy. When the results were evaluated for the patients received limb salvage

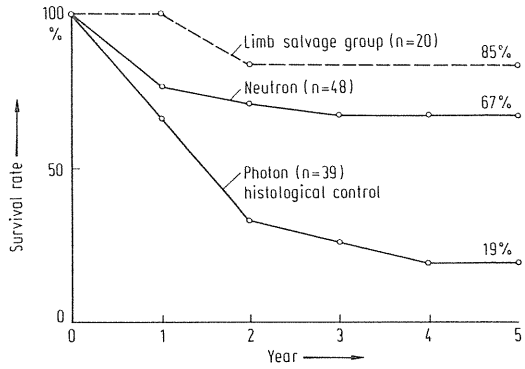

Figure 3. Cumulative survival rates of the patients suffering from osteosarcoma treated with either fast neutrons or photons [6].

operation, the five year survival rate was found to be 85% (Figure 3) [6].

i) Soft tissue sarcoma

Between 1975 and 1983, 84 patients suffering from soft tissue sarcoma were treated with fast neutrons. Of 82 patients, 22 were treated with radiation only, 16 received preoperative irradiation and 36 were treated with radiation therapy following various surgical procedures. Cumulative five year survival rate for the patients treated with radiation only was 20%. These patients had an advanced disease. For the patients who received pre-, or postoperative irradiation, the cumulative survival rates were 77.1% or 69.8%, respectively (Figure 4) [3].

Preoperative irradiation was found to be of value in the treatment of soft tissue sarcoma in order to minimize surgical margin of the treatment and to preserve the function of the tissues. The doses of fast neutrons equivalent to TDF 60 were acceptable to perform surgery and to control local recurrence.

j) Malignant melanoma

Fast neutron therapy was performed for 65 patients who were suffering from malignant melanoma. 45 had melanoma of the skin and 20 had melanoma of the head and neck. Cumulative ten year survival rates were 35.7% for the patients with skin melanoma and 5.7% for those with head and neck melanoma.

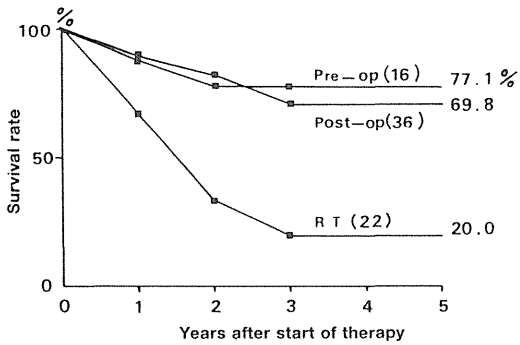

Figure 4. Cumulative survival rates of the patients suffering from soft tissue sarcoma treated with either fast neutrons or photons [3].

Of 45 patients with skin melanoma, 24 had previously untreated tumor, eight required postoperative irradiation and 13 had recurrent tumor after surgical procedures. Cumulative five year survival rate was 61% for the patients who had previously untreated tumor and 37.5% for those receiving postoperative irradiation, while no patients with recurrent tumor survived over three years.

An evaluation performed for the patients who had melanoma of the skin, stage I, indicates that preoperative irradiation is of value to control tumor and to minimize surgical margin. Among the 22 patients evaluated, four achieved local control with radiation alone and 17 have had local control after surgical procedures. Moist desquamation developed in four patients treated by conservative modalities (Table 5).

k) Malignant brain tumor

Malignant brain tumors were treated with either mixed schedule or fast neutron boost, for which a total gamma dose equivalent of 55 Gy was delivered to the target volume. For boost irradiation, fast neutrons equivalent to 15 to 20 Gy of photon beams were delivered to the target volume by using a shrinking field after 40 Gy of photon beam irradiation.

Among the 45 patients, with malignant brain tumor and receiving fast neutron therapy, 15 had astrocytoma, grade III, and 22 had astrocytoma, grade IV. The results showed that cumulative five year survival rates for the patients with astrocytoma grade III or IV were 36% or 16%, respectively. The results of fast neutron therapy for the patients, grade IV, seemed to be better than the results accumulated in the Brain Registry in Japan, where five year survival rate of the patients who had astrocytoma, grade IV, was 9.8% [1].

Site	No. patients	Response CR*	PR** (S · CR)***	Moist reaction	Follow-up months	dead
H & N	7	3	4 (4/4)	–	3–86	3
Leg (sole)	15	1	14 (13/13)	4	8–108	5
	22	4	18 (17/17)	4	3–108	8

* CR = complete regression, ** PR = partial regression, *** S · CR = complete regression with surgery.

Table 5. Results of clinical trials with fast neutrons for the patients suffering from malignant melanoma of the skin, stage I. November 1975 – December 1986 (NIRS). (September 1987)

Malignant meningioma was found to be an indication for fast neutron therapy.

II. Institute of Medical Science

1. Irradiation technique

At the Institute of Medical Science (IMS), clinical trials with fast neutrons started on November 1976.

A horizontal beam line was used for the clinical trials with fast neutrons produced by bombarding a thick beryllium target with 14 MeV deuterons accelerated by a cyclotron. The measurements performed for 10 × 10 cm^2 field at SSD 150 cm, indicate that the 50 % isodose is located at 8 cm in depth in a tissue equivalent phantom. The dose rate was 20 Gy · min^{-1} for a beam current of 50 μA.

The fast neutron beams are available every Monday and Friday. When fast neutrons only were used, 120 Gy were delivered every Monday and Friday. When mixed schedule was use, 80 cGy of fast neutrons were delivered on Monday and Friday, and 540 cGy of photons were delivered in three fractions between Monday and Friday. The treatment was usually performed in six weeks and a total dose equivalent to TDF 100 was delivered to the target volume. When the tumours seemed to be radio-resistant to photon beams, boost irradiation with fast neutrons was prescribed and 120 cGy of fast neutrons were given in two sessions each week.

2. Results

402 patients received 14 MeV d-Be neutrons at IMS between November 1976 and September 1987.

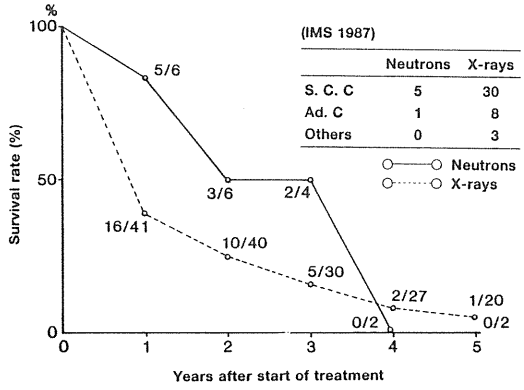

Figure 5. Survival rates patients suffering from carcinoma of the lung, stage II, treated with either fast neutrons or photons (IMS).

A non-randomized clinical trial was performed for the patients suffering from carcinoma of the lung. Out of 118 patients, 62 received radical treatment with fast neutrons. A group of 132 patients who received photon beam therapy was used as historical control. Preliminary results showed that, for the patients suffering from carcinoma of the lung, stage II, survival rate was better than for the series receiving photon beam irradiation, while for the patients, stage III or IV, treated with either photons or fast neutrons, the survival was almost the same (Figure 5).

On the other hand, the results evaluated for 16 patients with Pancoast tumour showed that mean survival after fast neutron therapy was 10.6 months, while the patients treated with photon beams died within five months after the treatment.

III. Korea Cancer Center Hospital

1. Irradiation technique

Studies with fast neutrons are carried out, at the Korea Cancer Center Hospital, using a machine, which is capable to make rotational irradiation. The fast neutron beams used in the clinical trials were produced by bombarding a thick beryllium target with 50.5 MeV protons, accelerated by a cyclotron made by Scanditronix, Sweden. The depth dose curves for a 10 × 10 cm^2 field, at SAD = 150 cm, are similar to that of 6 MV X-rays and the 50 % isodose lies at 14.3 cm in depth in a tissue-equivalent phantom. The current dose rate was 50 cGy · min^{-1}, at SAD = 150 cm.

Three modalities were used for clinical trials: fast neutrons only, mixed schedule and fast neutron boost. In the treatment with fast neutron only, 140 to 180 cGy of fast neutrons were given two to three times per week, and the total doses prescribed to the target volume were 16 to 22 Gy. For mixed schedule, a total dose equivalent to 50 to 70 Gy of photons was delivered using the following fractionation scheme: 80 cGy with fast neutrons twice weekly and 180 cGy with photons three times weekly.

2. Results

67 patients who were suffering from either locally advanced cancers or radioresistant cancers referred to clinical trials between October 1986 and September 1987. Out of 67 patients, 23 had a carcinoma of the head and neck, twelve a sarcoma, eleven a carcinoma of the salivary gland, six a carcinoma of the prostate, five a

Complete regression		
> 90 %	= 50 %	< 20 %
Salivary gland	Sarcoma	Head and neck
Prostate	Miscellaneous	
Advanced breast		

Table 6. Preliminary results of fast neutron therapy performed at the Korea Cancer Center Hospital (KCCH). (September 1987)

carcinoma of the breast and ten suffered from miscellaneous cancers.

Preliminary study showed that the cancers of the salivary gland and prostate and advanced breast cancer are indications for fast neutron therapy: a complete regression of the tumour was achieved in 90 % of the patients (Table 6).

Discussion and conclusion

Studies performed at various institutions throughout the world including Asian countries have shown that tumours, characterized by a slow growth rate, a poor reoxygenation, or a marked repair capability, are good indications for high-LET radiation therapy.

The indications for fast neutrons evaluated by the studies performed in the Asian countries are summarized in Table 7. Fast neutrons are the treatment of choice for carcinoma of the salivary gland, Pancoast tumor of the lung, osteosarcoma, soft tissue sarcoma and malignant melanoma. The studies also suggest that, with improved dose distribution for minimizing the exposure to the surrounding normal tissues, fast neutrons (high-LET radiations) could bring a benefit for squamous cell carcinoma of the head and neck and esophagus, adenocarcinoma of the lung, stage I, and prostatic adenocarcinoma. Malignant meningioma could be effectively treated with fast neutrons, while the benefit or fast neutrons has not yet been confirmed for glioblastoma multiforme. Further studies are still required to confirm the benefit of fast neutrons in the treatment of carcinoma of the pancreas and of the urinary bladder.

Clinical trials have to be performed in order to confirm the role of fast neutrons in cancer therapy, combination with surgery.

References

1. Aoki, Y.: Fast neutron radiotherapy for malignant brain tumor. Radiol. Med. 4 (1984), 107–111.
2. Ishikawa, T., Y. Aoki, S. Morita, T. Arai, H. Tsunemoto: Evaluation of fast neutron therapy for carcinoma of the esophagus. US-Japan Cooperative Cancer Research Program "Advances and New Techniques in Radiation Oncology Research", Seattle, Washington, May 2–4, 1984.
3. Ishikawa, T., S. Morita, H. Tsunemoto: Fast neutron therapy for soft tissue sarcoma. In: Annual report, April 1982 – March 1983 (NIRS-22). NIRS, Japan 1983, p. 61.
4. Morita, S., T. Arai, T. Ishikawa, H. Tsunemoto, K. Fukuhisa: Clinical experience of fast neutron therapy for carcinoma of the uterine cervix. Int. J. Radiat. Oncol. Biol. Phys. 11 (1985), 1439–1455.
5. Morita, S., H. Tsunemoto, T. Arai, T. Ishikawa: Fast neutron therapy for carcinoma of the lung at NIRS. In: Final report "Medical Application of Particle Accelerator" April 1979 – March 1983. NIRS, Japan 1984, p. 12–18.
6. Takada, N., E. Hodaka, T. Umeda, T. Kawahara, S. Takezaki: Treatment of bone and soft part sarcoma with special reference to the role of fast neutron therapy. In: Final report "Medical Application of Particle Accelerator" April 1979 – March 1983. NIRS, Japan 1984, p. 37–43.
7. Tsunemoto, H., S. Morita, Y. Aoki, T. Arai, T. Ishikawa, S. Kamata: Fast neutron therapy at NIRS. In: Kärcher, K. H. (ed.): Progress in radio-oncology III. International Club for Radio-Oncology (ICRO), Austria, 1987, p. 184–188.

	Radiotherpy only	Preoperative radiotherapy	Postoperative radiotherapy
Brain astrocytoma	–	–	O
meningioma	–	–	O
glioblastoma	–	–	–
Head and neck	O	–	–
Salivary gland	O	–	O
Lung: adenocarcinoma	O	–	–
Pancoast tumor	O	–	–
Esophagus	O	O	O
Pancreas	–	–	–
Uterine cervix	O	–	–
Prostate	O	–	–
Urinary bladder	–	–	–
Osteosarcoma	O	O	–
Soft tissue sarcoma	O	O	–
Melanoma	O	O	–

Table 7. Indications for fast neutron therapy according to the results of clinical trials at NIRS.
O = requiring improvement of dose localization.

Pigment Cell Research 2:365–369 (1989)

Estimation of Absorbed Dose in the Covering Skin of Human Melanoma Treated by Neutron Capture Therapy

HIROSHI FUKUDA,[1] TOORU KOBAYASHI,[2] JUNICHI HIRATSUKA,[3] HIROSHI KARASHIMA,[4] CHIHIRO HONDA,[5] KEIZOU YAMAMURA,[5] MASAMITU ICHIHASHI,[5] KEIJI KANDA,[2] AND YUTAKA MISHIMA[5]

[1]Division of Clinical Research, National Institute of Radiological Sciences, Chiba 260, [2]Kyoto University Reactor Institute, Osaka 590-04, [3]Department of Radiology, Kawasaki Medical School, Matsushima Kurashiki 701-01, [4]Department of Radiology, Hyogo Prefectural Cancer Center, and [5]Department of Dermatology, Kobe University School of Medicine, Kobe 650, Japan

A patient with malignant melanoma was treated by thermal neutron capture therapy using ^{10}B-paraboronophenylalanine. The compound was injected subcutaneously into ten locations in the tumor-surrounding skin, and the patient was then irradiated with thermal neutrons from the Musashi Reactor at reactor power of 100 KW and neutron flux of 1.2×10^9 n/cm^2/s. Total absorbed dose to the skin was 11.7–12.5 Gy in the radiation field. The dose equivalents of these doses were estimated as 21.5 and 24.4 Sv, respectively. Early skin reaction after irradiation was checked from day 1 to day 60. The maximum and mean skin scores were 2.0 and 1.5, respectively, and the therapy was safely completed as far as skin reaction was concerned. Some factors influencing the absorbed dose and dose equivalent to the skin are discussed.

Key words: Skin reaction, Melanoma, BNCT

INTRODUCTION

Skin-absorbed dose is important in any radiotherapy, including boron-neutron capture therapy (BNCT), because we must eradicate tumors with minimum damage to normal skin. More than 30 years ago, several patients were treated by BNCT at Brookhaven National Laboratory [Farr et al.,1954]. Moderate or severe dermatitis developed in these patients (in spite of low neutron fluences), because of extremely high ^{10}B-concentrations in the blood and a high contamination with primary gamma-rays [Archambeau, 1970]. Kanda et al. [1975] improved the beam quality of the Kyoto University Reactor by reducing the primary gamma-rays. The same modification was also made at the Musashi Reactor. These reactors were then suitable for biological and medical purposes. Furthermore, new tumor-seeking ^{10}B-compounds were developed. These compounds showed a specific accumulation in the tumor with good tumor:blood ratios and a specific killing effect of malignant melanoma was shown in both in vitro [Nakanishi et al., 1980; Ichihashi et al., 1982] and in vivo systems [Mishima et al., 1985]. These improvements encouraged us to begin clinical trials.

A patient with malignant melanoma was recently treated by BNCT at the Musashi Reactor. We describe the evolution and time course of the early skin reactions of this patient. These reactions were compared with those produced by X-rays, and dose equivalent to the capture therapy was estimated.

MATERIALS AND METHODS

Patient

At the end of November, 1985, a 66-year-old male patient came to Kobe University Hospital because of a pigmented nodule around the nail of the right big toe. The nodule was diagnosed as malignant melanoma, and his big toe was resected. In 1987, 14 months after the operation, a subcutaneous tumor in the right occipital region was observed and was diagnosed by X-CT as skull metastasis of malignant melanoma. It daily increased in size in spite of interferon treatment. Surgical treatment was impossible because the tumor had invaded the internal plate of the skull and venous sinus. We decided to treat this patient by BNCT.

Address reprint requests to Dr. Hiroshi Fukuda, Division of Clinical Research, National Institute of Radiological Sciences, 4-9-1 Anagawa, Chiba 260, Japan.
Received August 23, 1988; accepted September 21, 1988.

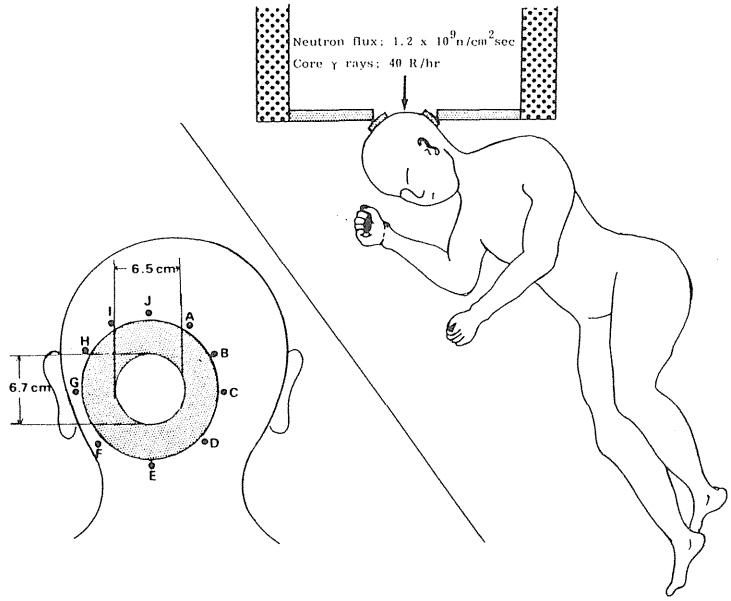

Fig. 1. Schema of irradiation port and collimation system at the Musashi Reactor. The primary collimator was a flexible sheet of LiF reinforced by LiF tile. The secondary collimator, attached to the patient's head, was also a flexible sheet of LiF. The radiation field was an ellipse of 6.5 × 6.7 cm. ^{10}B-paraboronophenylalanine (640 mg) in 2 ml saline was injected subcutaneously 20 and 6 hours before irradiation into the normal skin surrounding the tumor (A–J). The patient was irradiated under general anesthesia for 139 min by a thermal neutron flux of 1.2 × 10^9 n/cm^2/s and primary gamma-ray dose rate of 40–50 rad/min at the top of the head.

Neutron Irradiation and ^{10}B-Administration

The Musashi Reactor was used as the neutron source. The reactor has a neutron flux of 1.0–1.2 × 10^9 n/cm^2/s at the collimator surface and a primary gamma-ray dose rate of 40–50 rad/min. Six hundred and forty milligrams of ^{10}B-paraboronophenylalanine hydrochloride (^{10}B-BPA·HCl) in 2 ml saline were injected subcutaneously into each of ten locations in the tumor-surrounding skin 5 cm from the tumor margin. The injections were administered 20 hours and 6 hours before neutron irradiation, resulting in a total administered dose of 12.8 g (482 mg ^{10}B). The patient was irradiated under general anesthesia for 139 min at 9 reactor power of 100 KW (Fig. 1). The patient's hair was cut a few days before irradiation in order to fix the collimator with the skin and to observe the skin reaction.

Dosimetry and Estimation of Absorbed Dose

The neutron fluences were measured by gold wire or foil and gamma-rays by thermoluminescence dosimeter (TLD) of $MgSiO_4$(Tb). Absorbed dose to the skin was the sum of gamma-radiations from ^{1}H(n,γ)^{2}H reaction and primary gamma-rays, and from high-LET radiations of ^{14}N(n,p)^{14}C and ^{10}B(n,α)^{7}Li reactions. The former was measured directly by TLD and the latter was calculated by multiplying the thermal neutron fluences by the conversion factor. The concentration of ^{10}B in the skin was estimated by prompt gamma-ray analysis [Kobayashi and Kanda, 1983] carried out under the same conditions as the treatment. ^{10}B concentration in the blood before, during, and after the therapy was chemically determined.

Skin Reaction

Skin reaction of the tumor-covering skin in the radiation field was checked from day 1 to day 60 of the treatment. The skin scoring system developed by Aizawa [1973] (Table 1) was used for grading the dermatitis.

RESULTS

Absorbed Dose Estimation

Figure 2 shows the distribution of neutron fluences at the skin surface. The maximum and mean fluences in the radiation field were 9.37 and 9.05 × 10^{12}/cm^2, respectively. Neutron fluence decreased sharply from the edge of the LiF collimator and was one-tenth of the maximum at 1 cm inside the collimator edge. Figure 3 shows ^{10}B distribution in the skin estimated by prompt gamma-ray analysis. The concentration was very high

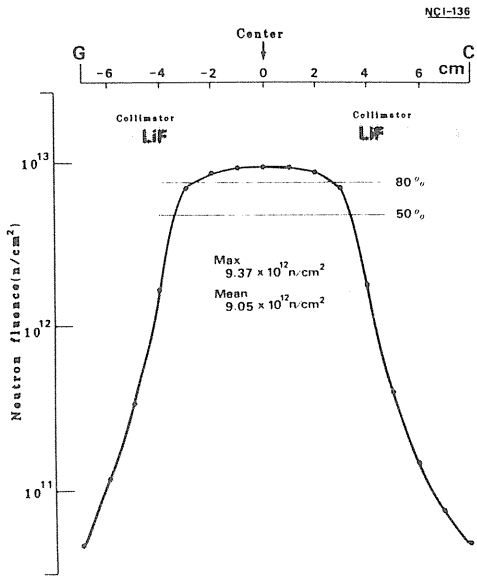

Fig. 2. Neutron fluences at the skin surface. The neutron fluences decreased sharply from the edge of the collimator. Maximum and mean fluences in the radiation field were 9.37 and 9.05 × 10^{12} n/cm^2, respectively.

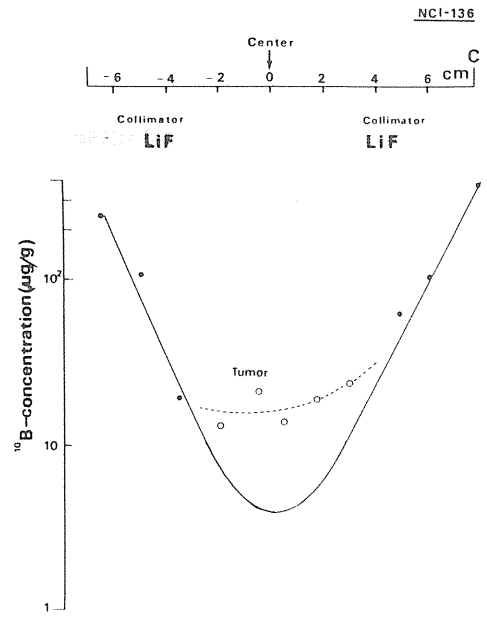

Fig. 3. Distribution of ^{10}B-concentration in the skin and the tumor. The values were estimated by prompt gamma-ray analysis. The concentration in the tumor-covering skin was estimated by extending the concentration curve in the surrounding normal skin to the center of the field. ●, ^{10}B-concentration in the skin; ○, in the tumor.

TABLE 1. Skin Reaction Scoring System (Early reaction)*

Score	Finding			
0.5	Doubt of difference from normal skin			
1.0	Slight reddening			
1.5	Definite reddening			
2.0	Severe reddening or dry desquamation (+)			
2.5	Dry desquamation (++)			
3.0–5.0	Moist desquamation			
	Area (A)	±	+	++
	$A \leqq \frac{1}{3}$	3.0	3.5	4.0
	$\frac{1}{3}A < \frac{2}{3}$	3.5	4.0	4.5
	$A \geqq \frac{2}{3}$	4.0	4.5	5.0

*From Aizawa, 1973.

TABLE 2. Absorbed dose in the Skin Surface by Thermal Neutron Beam

Radiation	Rad/min	Percentage
Primary-γ	0.83	14.1
Capture-γ[a]	3.12	52.9
^{14}N(n,p)^{14}C	1.95	33.0
Total	5.90	100

[a]From ^{1}H(n,γ)^{2}H reaction in the body and supporting materials for irradiation.

at the injection site (200–300 μg/g) and decreased linearly toward the center of the radiation field. ^{10}B concentration in the tumor was 15–25 μg/g. The concentration in tumor-covering skin was estimated by extending the concentration curve for the surrounding normal skin; it was 3 μg/g in the center of the field and 10 μg/g at the edge of the collimator.

Table 2 shows human absorbed dose from the thermal neutron beam at the skin surface. Besides this dose, the absorbed dose from ^{10}B(n,α)^{7}Li was added. ^{10}B concentration is a function of the distance from injected points, as shown in Figure 3. Figure 4 shows total absorbed dose distribution in the skin, including absorbed dose from ^{10}B. Maximum and mean absorbed doses in the skin were 12.5 and 11.7 Gy, respectively. Dose equivalents (Sievert) of these absorbed doses were obtained as 24.4 and 21.5 Sv respectively, by assuming that the RBE of the ^{10}B(n,α)^{7}Li and ^{14}N(n,p)^{14}C reactions was 2.5.

Skin Reaction

A few days after irradiation, slight reddening developed in the irradiated skin. It increased in degree and reached a maximum at day 20, subsiding during the following week. Pigmentation and fine scale developed after day 20, reached a maximum at day 30, and then

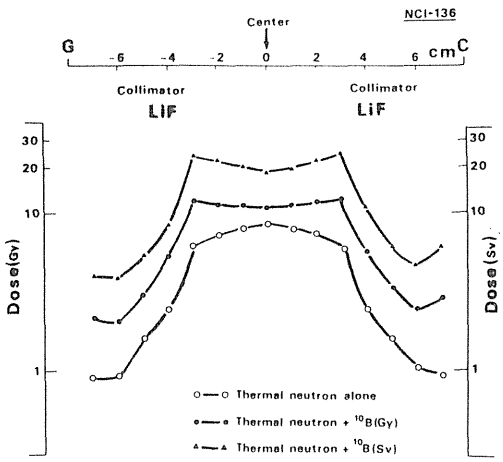

Fig. 4. Absorbed dose (Gy) and dose equivalent (Sv) to the skin. ○, absorbed dose by thermal neutron alone (without ^{10}B); ●, absorbed dose when ^{10}B was distributed in the skin as in Figure 3; ▲, dose equivalent (Sv) by assuming that RBE of the ^{14}N(n,p)^{14}C and ^{10}B(n,α)^{7}Li reactions was 2.5.

subsided. The skin was almost normal after day 50. Figure 5 shows the degree and time course of early skin reaction scored on a scale. Maximum and mean reaction scores were 2.0 and 1.5, respectively.

DISCUSSION

The observed maximum and mean skin reaction scores of 2.0 and 1.5, respectively, means that the therapy was completed within safety limits. Blood concentration of ^{10}B remained at 1.1–1.5 μg/g during the irradiation. This is one of the reasons our patient suffered less skin damage. In previous BNCT, ^{10}B concentrations in the blood were estimated to be 20–30 μg/g. Although ^{10}B measurements were not taken for the treated patients, the same dose administration to swine yielded 20–30 μg/g of ^{10}B in the blood [Archambeau, 1971].

These skin reactions were comparable with the reaction in humans after a single irradiation of 12.5 Gy X-rays or 4.54 Gy fast neutrons [Field et al., 1976]. Twenty Gy (Sv) of X-rays produced maximum and mean skin reaction of 2.5 and 1.8, respectively, in C3H mice [Baba, 1985]. In our patient, maximum and mean skin absorbed doses in the radiation field were 12.4 Gy and 11.7 Gy, respectively. Dose equivalents of these doses were estimated as 24.4 and 21.5 Sv, respectively, by assuming that the RBE of the ^{10}B(n,α)^{7}Li and ^{14}N(n,p)^{14}C reactions was 2.5. Therefore, there will have been some overestimation of our calculated dose equivalent.

There are at least four explanations for this finding: 1) the RBE of high-LET reactions is less than 2.5; 2) ^{10}B concentration is lower than we estimated; 3) nonhomogeneous distribution of ^{10}B in the skin may result in less damage being caused to the target cells of the skin; and 4) effect of low dose rate (4 rad/min for gamma-rays). However, we have treated only one case and further clinical experience is necessary for a final conclusion.

ACKNOWLEDGMENTS

The authors thank Dr. Aizawa, Dr. Nozaki, and Dr. Matsumoto for arranging for the medical irradiation with the Musashi Reactor. We also wish to thank Dr. Obara and his anesthetic team for excellent control of the patient's condition, and Mr. Ono for technical assistance.

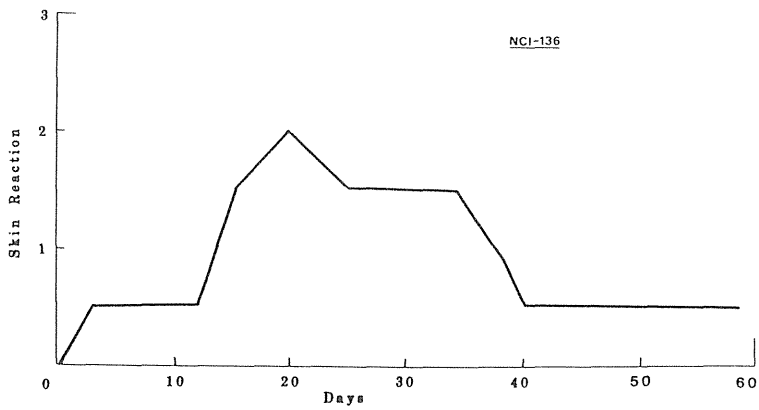

Fig. 5. Early skin reaction of the patient treated by boron neutron capture therapy. The scoring system shown in Table 1 was used. Maximum and mean scores were 2.0 and 1.5, respectively.

REFERENCES

Aizawa, H. (1973) Relative biological effectiveness of fast neutrons, observed in the skin reaction of mice, after single or fractionated irradiation. Nippon Acta Radiologica, 33:602–616.

Archambeau, J.O. (1970) The effect of increasing exposures of the $^{10}B(n,\alpha)^{7}Li$ reaction on the skin of man. Radiology, 94:179–187.

Archambeau, J.O., R.G. Fairchild, and H.J. Brenneris (1971) The response of the skin of swine to increasing absorbed doses of radiation from a thermal neutron beam, a degraded fission neutron beam, and the $^{10}B(n,\alpha)^{7}Li$ reaction. Radiat. Res., 45:145–165.

Baba H. (1985) Biological effects of charged particles. In: Basic Research on Radiotherapy With Charged Particles. Supported by a grand-in-aid for cancer research from the Ministry of Education, Science and Culture, Japan, pp. 52–56.

Farr, L.E., W.H. Sweet, J.S. Robertson, et al. (1954) Neutron capture therapy with boron in the treatment of glioblastoma multiforme. Am. J. Roentgenol., 71:279–293.

Field, S.B., R.L. Morgan, and R. Morrison (1976) The response of human skin irradiation with X-rays or fast neutrons. Int. J. Radiat. Oncol. Biol. Phys., 1:481–486.

Ichihashi, M., T. Nakanishi, and Y. Mishima (1982) Specific killing effect of ^{10}B-para-boronophenylalanine in thermal neutron capture of malignant melanoma: In vitro radiobiological evaluation. J. Invest. Dermatol., 78:215–218.

Kanda, K., T. Kobayashi, K. Ono, et al. (1975) Elimination of gamma rays from a thermal neutron field for medical and biological purposes. In: Biomedical Dosimetry. International Atomic Energy Agency, Vienna, pp. 205–223.

Kobayashi, T., and K. Kanda (1983) Microanalysis of ppm-order ^{10}B concentration in tissue for neutron capture therapy by prompt gamma-ray spectrometry. Nucl. Inst. Method, 204:525–531.

Mishima, Y., M. Ichihashi, T. Nakanishi, et al. (1985) Cure of malignant melanoma by single thermal neutron capture treatment using melanoma-seeking compounds: ^{10}B/melanogenesis interaction to in vitro/in vivo radiobiological analysis to preclinical studies. Kyoto University Reactor Institute-Technical Report 260:1–13.

Nakanishi, T., M. Ichihashi, Y. Mishima, et al. (1980) Thermal neutron capture reaction of malignant melanoma: In vitro radiobiological analysis. Int. J. Radiat. Biol., 37:573–580.

重粒子線治療システムの構想

遠藤真広

IMAGE TECHNOLOGY & INFORMATION DISPLAY

映像情報 MEDICAL

VOL.21 NO.19 〈387〉 1989

重粒子線治療システムの構想

●放射線医学総合研究所
医用重粒子線研究部
遠藤真広

1. はじめに

放射線医学総合研究所（放医研）では，1993年度の臨床試行開始をめざして，がん治療のための重粒子線加速器を建設中である[1]。この計画はヘリウムからアルゴンまでの原子核を核子あたり最高800MeVまで加速して人体に照射し，重粒子線の持つ優れた線量分布と生物学的効果によりがん治療成績の向上をはかることを目的としている。現在，重粒子線によるがん治療は，世界でも米国のローレンス・バークレイ研究所（LBL）で素粒子物理研究用の加速器を転用して行われているのみである。放医研の装置は完成すれば，世界で唯一の医学専用重粒子線加速器となり，がん治療の臨床研究や放射線物理・生物学の研究に重要な役割を果たすと期待され，国の内外からその完成が熱望されている。

重粒子線治療を実施するにあたっては，重粒子線加速器を完成させるのは勿論であるが，なお未知の点が多い重粒子線の物理学的・生物学的特性を良く把握し，またその特性を十分に活用するような治療システムを構築する必要がある。重粒子線加速器や重粒子線の物理学的・生物学的特性の詳細は他に譲り，ここでは治療システムについて著者らが現在，考えていることを中心に述べ諸賢の御批判をあおぎたい。

2. 重粒子線がん治療装置（HIMAC）

図1は現在，建設中の重粒子線加速器の概念図を示したものである。この装置は正式には重粒子線がん治療装置と呼ばれ，またHIMACという愛称がつけられている。この愛称は英語名 Heavy Ion Accelerator in Chiba を略したものである。

図に示すように本装置はイオン源，RFQとアルバレ型の2つのリニアックからなる前段加速器，上下2段のシンクロトロン，高エネルギービーム輸送系，物理・汎用照射系，2次ビーム照射系，生物照射系及び治療照射系より構成される。また，治療照射室は(A)垂直照射専用，(B)水平・垂直照射両用，(C)水平照射専用の3室からなる。

シンクロトロンを2段構成としたのは，医療用としての柔軟性をもたせるためである。原則として垂直ビームは上リングより，水平ビームは下リングより供給されるため，①照射室間のビーム切換の迅速化，②B室における水平・垂直同時照射が可能となる。また，③2つのリ

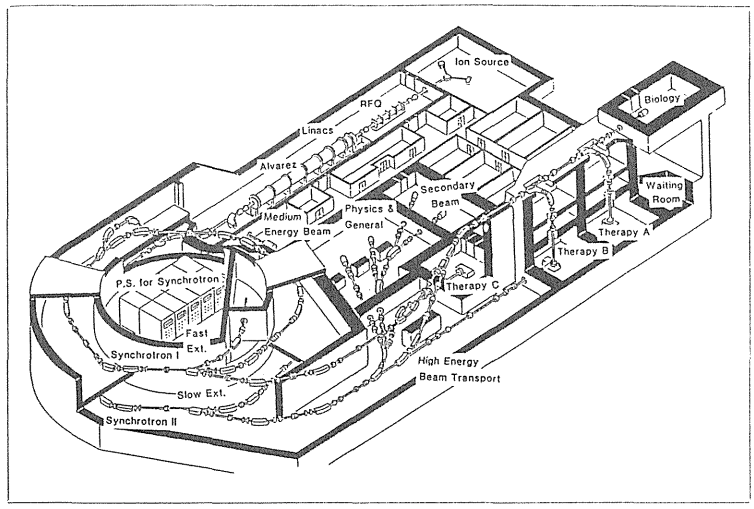

図1　重粒子線がん治療装置（HIMAC）の概念図

ングのビームを合流させることも可能で，強度と duty factor を2倍にできる。さらに，将来計画としては一方のリングを蓄積リングに改造することにより，シンクロトロンで大強度を得るのが困難なより重い核種や2次ビームを貯え利用することも考えている。

表1は HIMAC の基本性能をまとめたものである。表にみるように，加速可能な核種は He (Z=2) から Ar (Z=18) までである。このうち，イオン源の技術と利用面の要請から He(Z=2)，C(Z=6)，Ne(Z=10)，Si (Z=14)，Ar(Z=18) が利用の中心になると予想されている。加速エネルギーは核子あたり 100－800MeV である。しかし，全ての核種をこのエネルギー範囲にわたって加速するわけではなく，軽い核の加速エネルギーは小さく，重い核の加速エネルギーは大きい。これは放射線遮蔽の関係で水中飛程を30cmに制限しているからである。

ビーム強度は He, C に対しては治療位置（アイソセンター）で 5Gy/min/l の線量率が得られるように設定されている。Ne に対しては 2.5Gy/min/l の線量率であるが，これは Ne の RBE が大きいことを考慮したもので，生物学的な等価線量としては He,C とほぼ同じ程度である。Si, Ar に対してはイオン源技術が未開拓なため，線量率を一桁下げたものを仕様としている。

表2は治療照射室A，B，Cの概略仕様を示したものである。表に示すように，B照射室は主として軀幹部の治療を行うことを想定しているのに対し，A，C 照射室はそれに加えて頭頸部への精密照射をも行えるように考えられている。治療照射室の設計の詳細は別に報告されよう。

3. 治療の手順

HIMAC でどのような疾患を治療するかは大いに議論のあるところであるが，LBL では次のようなものを対象として治療している。

表2 照射室の仕様

	A	B	C
照射の方向	垂直	垂直／水平	水平
ビーム径	50,100,150,220mm	100,150,220mm	50,100,150,220mm
ビーム均一度	±2%	±2%	±2%
水中飛程(最大)	300mm	300mm	300mm
アイソセンター高さ	1250mm	1250mm	1250mm
ビームエネルギー(最大)	600MeV/n	600MeV/n(垂直) 800MeV/n(水平)	800MeV/n
治療体位	臥位	臥位	臥位／座位
コリメータ	患者コリメータ	マルチリーフ,患者	患者コリメータ
対象	頭頸部,軀幹部	軀幹部	頭頸部

表1 HIMAC の性能

加速核種	He, C, Ne, Si, Ar	
加速エネルギー	100－800 MeV/n	
水中飛程	30cm（最大）	
ビーム強度（治療受入れ）	He	1.1×10^{10} PPS
	C	1.8×10^{9}
	Ne	3.1×10^{8}
	Si	4.0×10^{7}
	Ar	2.4×10^{7}

He, C	5Gy/min/ℓ （アイソセンター）
Ne	2.5Gy/min/ℓ
Si, Ar	0.5Gy/min/ℓ

1)主として重粒子線の線量分布の良さを利用する疾患群：頭蓋底部及び脊髄近傍の腫瘍，眼球内腫瘍，脳の動静脈奇形，脳下垂体腺腫

2)主として重粒子線の生物学的効果を利用する疾患群：頭頸部の非偏平上皮癌（腺癌など），表在性の骨軟部腫瘍

3)線量分布と生物学的効果を利用する疾患群：前立腺癌，膵癌，食道癌，肺癌，脳腫瘍

これらのうちのいくつかは，治療成績の点でも光子治療をはるかに上回ることが証されつつある[2)]。しかし，重粒子線の適応はこれらに留まるものではなく，臨床トライアルの開始までに十分な検討を行い，適応疾患を決める必要があろう。

どのような疾患を治療対象として選択するにせよ，重粒子線の特徴を十分に生かすためには，利用可能な全ての臨床診断と画像診断の結果にもとづき最適な治療計画を行い，それにもとずき治療を確実に実施する必要がある。また，やり直しのきかない臨床トライアルの治療効果や障害について解析するために，種々のデータをきちんと管理していかねばならない。つまり，重粒子線治療では従来の放射線治療の過程をより厳格に実施する必要がある。

図2は，我々が現在，考えている重粒子線治療の手順をフローチャートとして示したものである。患者は他院で部位及び組織診断が確定していることが図のフローチャートに入る前提となる。第1回の治療会議では，それらの情報をもとに治療体位，固定法，治療ビーム（イオン）の種類を決め，また治療前作業のスケジューリングを行う。

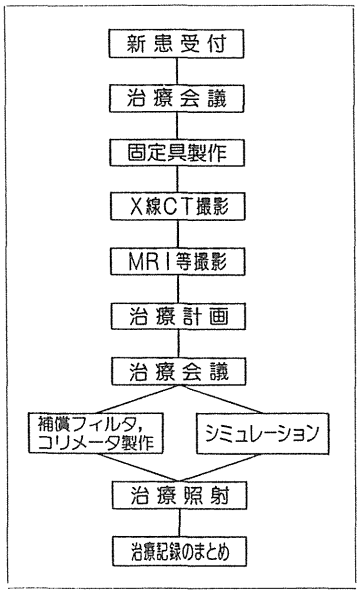

図2　重粒子線治療の手順

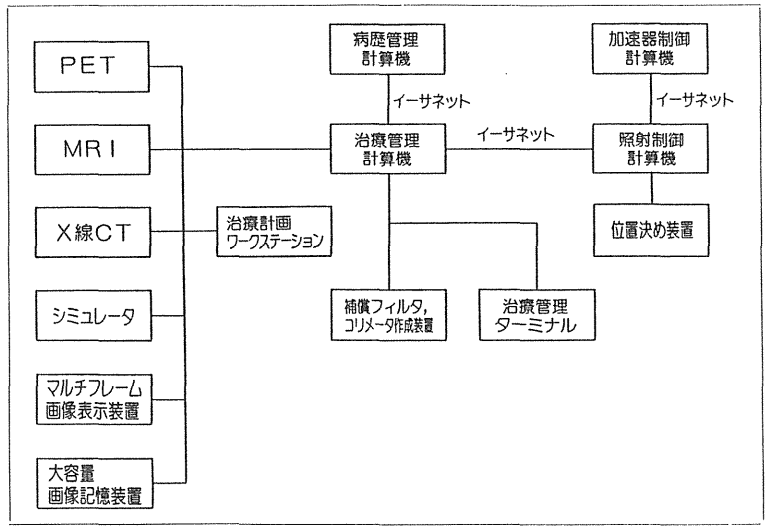

図3　重粒子線治療システム

治療前作業としては第一に患者毎に固定具を製作する。患者固定は重粒子線治療の重要な研究分野であり，その良し悪しが重粒子線治療の成功を左右する場合がしばしばある。現在，他の精度に見合った再現性を持つ固定法についての検討を行っている。

次に患者に固定具を装着し治療と同じ体位でX線CTの撮影を行う。がん病巣の進展範囲の診断については，X線CT以外にもMRIなど画像診断の技術が非常に進歩していて，治療システムにはこれらを取り込む必要がある。しかし，線量分布を計算するには重粒子線の体内飛程を電子密度から求める必要があり，これはCT値から換算される。この意味でX線CT撮影は重粒子線治療に不可欠な要件である。なお，治療計画用X線CT装置は診断用装置と異なる仕様が予想されるが，まだ十分に検討されているとはいえないので本稿からは割愛したい。

他の画像診断(MRI/SやPETなど)は，X線CTで病巣の進展範囲，重要臓器の範囲などが明確にならない場合や腫瘍の性状（特にhigh LETに対するレスポンス）を詳しく知りたい場合に追加される。MRIは特に前者の場合に，MRSやPETは後者の場合に情報を加えることが期待されている。

以上のような準備のもとに治療計画を行う。治療計画は広義には第1回治療会議と治療照射の間の全ての作業を指すわけであるが，狭義には標的容積を決め，またそれに対する照射ビームの方向，形状，線量配分を決めることをいう。後者の意味での治療計画には3次元画像データを対話式に扱かうことが不可欠であり強力な計算機支援が要求される。

第2回治療会議では治療計画を関係者により協議し，問題が無ければ承認する。また，加速器の運転スケジュールを参照しながら，治療照射スケジュールを決定する。図に示されている補償フィルタと患者コリメータは治療計画通りに重粒子ビームを整形するためのものであり，治療会議後，治療照射の開始までに速やかに製作される。シミュレーションは，X線CTで決められた治療計画を実際の治療機の座標系に移しチェックする操作であり，専用のシミュレータにより行われる。

治療照射では，治療計画通りに患者に重粒子ビームを照射する。ここでは標的に精度良く重粒子線をいわば命中させる必要があり，このためには重粒子ビームの整形に加えて，患者の固定と位置決めが重要である。最後に，新患受付から治療照射に至る過程で発生するデータは画像を含めて二度と得られない貴重なものである。これらは治療終了後に要約され，患者の追跡データと合せて永久に保存され後の解析に利用される。

4.　治療システムの概要

HIMACの治療システムでは以上のような治療の流れが，正確かつ円滑に行われねばならない。また，治療システムはHIMAC本体（加速器）システムと整合性を持つ必要があり，さらにシステムのversion upが容易に行われることが望ましい。これらの点を考慮して，図3

に示すようなシステムを構築することを目標とした。現在はそれに付随するさまざまな問題点を検討している段階である。

図に示すように HIMAC の治療システムの特徴は，

1) 各機器がネットワークにより接続されオンライン処理が行われる。

2) 記録用も含めデータは全てデジタルのものを用いる。

という点にある。

これらのうち，2)に述べたデータを全てデジタル的に取り扱うという考えはより基本的であり，1)のオンライン・ネットワーク化はこれから必然的に生まれてきている。図3の左側は病巣診断と治療計画を行うためのサブシステムを示している。PET, MRI, X線CTなどの画像診断装置において病巣を含む領域の3次元画像が発生し，図のネットワークを介して治療計画のワークステーションに転送される。治療計画のワークステーションとしては，最近，次第に使用されるようになってきたスーパー・グラフィック・ワークステーションを想定している。ワークステーション上で標的容積の決定や3次元線量計算，それにもとづく照射ビームの方向，形状，線量配分の決定などが対話式に行われる。マルチフレーム画像表示装置は治療会議で用いられるものであり，治療計画の結果得られた線量分布図などが表示される。シミュレータはシミュレーションを行うための装置であり，位置決め用の参照画像が撮像される。大容量画像記憶装置は，病巣診断と治療計画，さらには治療照射を含む治療の全過程で発生する画像データを記憶しておくためのものである。なお，以上に述べた図3のサブシステムは，現在，開発が進んでいるPACS (医用画像管理システム) と共通する要素が多く，この部分の設計にはPACSの標準的なものをできるだけ取り入れることを考えている。特に伝送路として何を採用するかはシステム成功の大きな鍵であり，現在，標準とされているイーサネットより1桁以上，高速のものの出現を期待している。

治療管理計算機は治療計画の結果得られる治療パラメータ（ビームのエネルギー，粒子の種類，線量，コリメータの開度など）と位置決め用の画像を HIMAC（実際には照射制御計算機）に転送したり，さまざまな治療データの管理，治療スケジュールの管理などを行う。また，補償フィルターやコリメータの作成装置を制御するのにも用いられる。さらに，病歴管理計算機とのデータのやり取りも行う。HIMAC 側では，照射制御計算機からのデータにもとづき加速器制御計算機が加速器の運転を制御する。位置決めの装置では位置決め用の画像を参照しながら，後に述べる方法で患者の位置決めを行う。病歴管理計算機，治療管理計算機，照射制御計算機及び加速器制御計算機間のデータ転送はイーサネットを介して行う。

以上が HIMAC 治療システムの概要であるが，以下の節ではその要となる標的容積の決定，治療計画，治療照射，病歴管理についてさらに詳しく述べる。

5. 標的容積の決定

標的容積を決定することは，一般のがんの放射線治療においても最重要なことの一つであるが，重粒子線治療では死活的な意味を持つ。すなわち，標的容積に容易に線量を集中できることが重粒子線治療の最大の長所であるが，もしも標的容積を誤って小さく決めるならば，照射されない部分からの再発は避けられず，最大の長所が最大の欠点に変わってしまう。しかし，標的の過小評価を恐れて必要以上に大きな標的を作ることも，重粒子線治療の価値を著しく損なうことになる。したがって，必要にして十分な標的容積を決定せねばならないが，これは現在の進歩した画像診断技術をもってしても容易ではない。

図3に示すように，HIMAC の治療システムでは，PET, MRI, X線CTの3つの機器を主な手段として病巣診断を行うことを計画している。実際には MRI とX線CTが標的決定の主要な武器であり，これらにより主病巣の範囲は比較的容易に決定されよう。しかし，リンパ節への小さい転移やがん細胞の微細な侵潤をこれらの装置で描出するのは不可能とはいえないまでも非常に困難である。標的決定にはこれらの点に関する医師の臨床判断がこれまで以上に要求されよう。

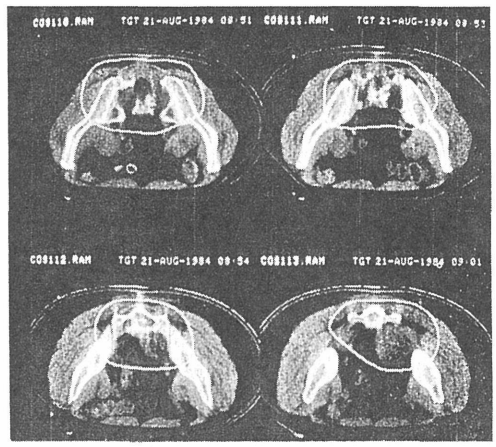

図4 標的容積の決定

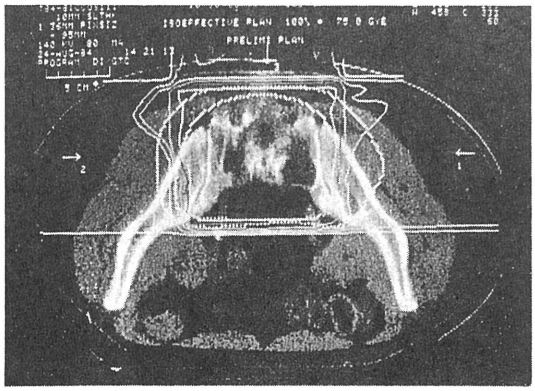

図5　線量分布の表示

標的容積の決定は実際には，図4に示すように，治療計画ワークステーション上に断層画像を表示し，輪郭を1枚1枚，対話式に入力することにより行われる。大きな標的を決定するには，数十枚の断層画像に対してこの操作を繰り返す必要がある。これは非常に時間がかかることであり，3次元画像技術の応用により簡略化できないかと考えている。また，複数の画像モダリティ間の位置合わせや情報の移転（例えばMRIで決定した標的容積をX線CTに移すなど）を容易に行う技術の開発も必要である。

6. 治療計画

標的容積の決定に引き続いて，それに隣接する重要臓器の範囲を決定する。ここで，重要臓器とは放射線感受性が高く，またその障害が生命に直接危険をおよぼしたり，quality of life を著しく損なう恐れのある臓器をいう。図4の骨盤部の治療の場合には，膀胱および直腸がそれに相当する。重要臓器も標的容積と同様に，ワークステーション上に表示された断層画像に輪郭を入力していくことにより決定される。

また，この段階で次の節で述べる治療照射時の位置決め操作に必要なランドマークも画像上に入力される。ランドマークは骨のエッジや手術用のクリップなどであり，X線CTだけではなく位置決め時に撮影されるX線テレビ画像にも描出される必要がある。ランドマークは治療計画で決められた照射法を，治療照射時に正確に実現するためのものである。

治療計画の次の段階は，重要臓器への照射を避けて標的に線量を集中する照射の方向と線量配分を決め，それにもとづき3次元線量分布を計算することである。照射方向は，必ずしも断層面と平行（いわゆる coplanar）な場合に限らず，non-coplanar な場合についても検討する必要がある。non-coplanar を含む治療計画においては，重要臓器と標的容積の重なり具合を立体的に観察する必要があり，3次元グラフィックスの強力な支援が必要となろう[3]。

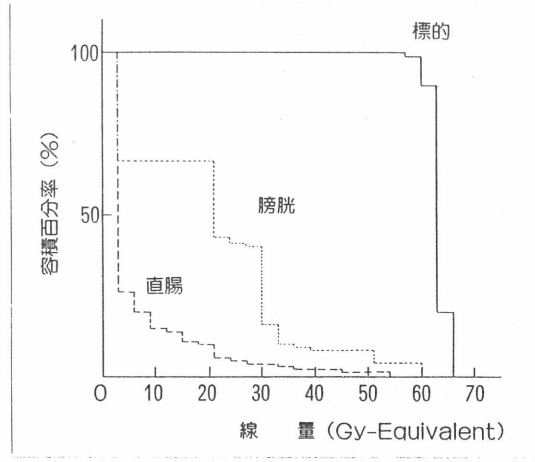

図6　dose-volume（線量—容積）ヒストグラム
骨盤部治療の場合

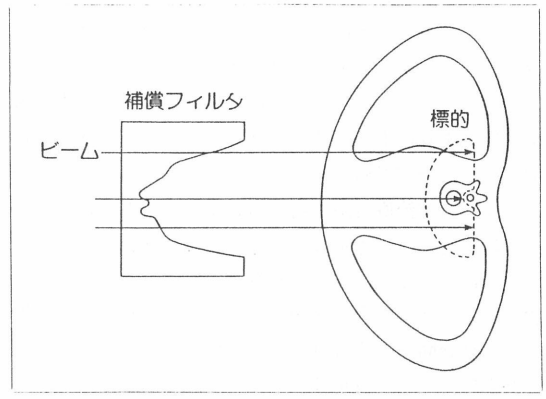

図7　補償フィルタの原理

治療計画のこの段階は，満足できる線量分布が得られるまで繰り返し実施する必要がある。計算された線量分布は，図5に示すように断層像に重畳して表示され，それを観察することで治療計画の適否が判断される。しかし，3次元治療計画では，観察すべき断層像の数が多いこと，また non-coplanar 治療計画では断層像での線量分布はしばしば理解しにくい形状をとることなどの理由により，線量分布図以外の指標も必要である。現在，そのような指標として図6に示すような dose-volume（線量—容積）ヒストグラムが推奨されている。dose-volume ヒストグラムの利用法は必ずしも確定していないが，重要臓器についてのヒストグラムからその障害発生率を推

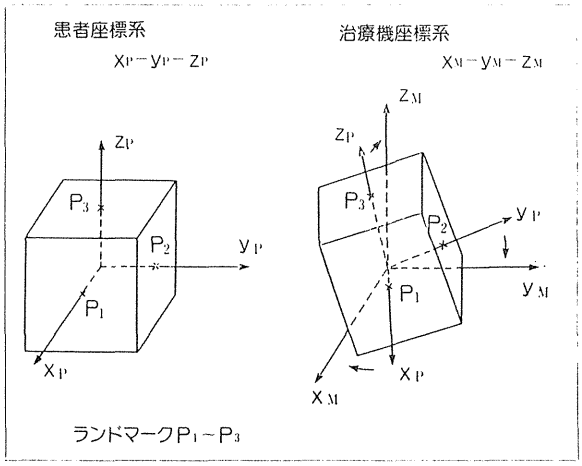

図8　ランドマーク法による位置決め

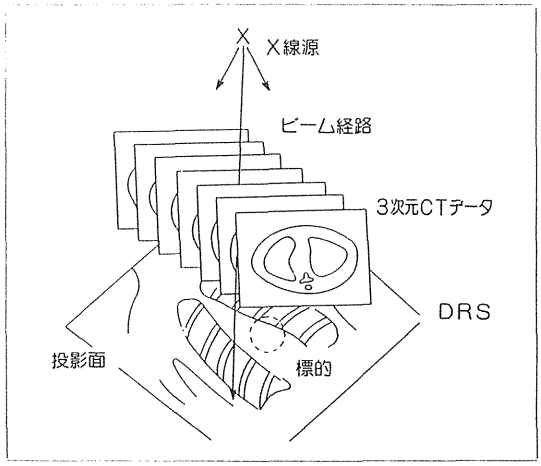

図9　DRS の原理

定する研究が行われている。我々も，このような定量的指標により，治療計画の適否を判定することをこのシステムを開発する一つの目的としたいと考えている。

線量分布計算と同時に，ビームのパラメータ（ビームの飛程，拡大ピーク幅）も計算される。また，標的に線量を集中する手段として，図7に示すような補償フィルタを用いる。これは入射皮膚面から腫瘍後縁までのビーム経路の実効長が異なるのを補正するためのもので，線量分布計算の過程で設計（ビームに垂直な平面での補償フィルタの厚さを求めること）が行われる。さらに，標的に線量を集中するためには，ビームを横方向に絞ることも必要であり，コリメータ輪郭として標的のビーム方向投影の輪郭を用いる。このように，ビームのパラメータやコリメータと補償フィルタの設計パラメータが治療計画の結果，得られることになり，これらは治療管理計算機を経て，HIMAC 本体または補償フィルタ・コリメータ作成機に送られる。

なお，治療計画においては，3次元のX線CTデータを照射方向から投影した，いわゆるデジタル合成シミュレーション (digital reconstruction simulationgraphy—DRS) 画像も計算される[4]が，これは次節の治療照射時の患者位置決めと密接に関係するのでそこでまとめて述べることにする。

7. 治療照射

治療照射は一般に数回～数十回に分割して行われるので，治療計画通りに再現性良く実施するためには，患者の固定についての特別な配慮と新しい位置決め法の開発が必要と考えられる。患者の固定については現在，いくつか検討中であるが，この稿からは省略したい。

患者の位置決めは，通常の放射線治療では皮膚面のマークに照射野を示すライトビームのエッジを合わせることにより行われる。しかし，この方法には1)皮膚マークを付けるときの誤差，2)皮膚の伸び縮みの影響，3)身体の傾き，ねじれなどいくつかの誤差要因が存在し，必ずしも，現在，我々が考えている高精度の位置決めが可能とは考えられない。

そこで，我々は LBL や MGH など重粒子線治療を行っている施設の位置決め法（ランドマーク法ともいうべきもので，治療計画時に指定したランドマークのX線写真を利用して位置決めを行う）を発展させた，デジタルX線テレビによる位置決め法を採用することにした。この方法の概念は次のようなものである。すなわち，第一に治療時に患者を設定する際のずれを患者に固定された座標系と治療ポート（治療機）に固定された座標系間のずれと考える。そして，図8に示すように患者中に存在し空間的な関係が既知のランドマーク群 (P_1～P_n) の治療機座標を定め，患者座標系との差を計算する。この差は座標変換のパラメータとして与えられ，患者（実際には寝台）の移動量となる。ここで，ランドマークの患者座標は治療計画時に入力され，治療機座標はデジタルX線テレビの2方向撮影により求める。

ランドマーク座標をX線テレビ画像から決めるためには，ランドマークが既に入った画像を参照する必要がある。このためには，治療計画時にX線テレビ画像をシミュレートする画像を作成し，その上にランドマークを投影しておく。この画像が前節の最後に述べたデジタル合成シミュレーション (DRS) 画像であり，図9に示すよ

うに3次元CTデータを，X線ビームを模擬する経路にそって積分することにより得られる。イメージング法の一つと考えたときのDRSの特性を現在，検討中である。

また，DRS画像を用いても治療計画と実行治療の間のギャップは大きいことが予想されるので，実際の治療の前にシミュレーションを行い，寝台パラメータなどをあらかじめ決めておく。したがって，DRS画像が参照画像として用いられるのはシミュレーション時で，実行治療時にはシミュレーション画像（シミュレーション時に撮影されるX線テレビ画像）が用いられよう。

なお，患者位置決めの将来構想としてX線CTなど他のモダリティを用いた方法も検討しているが，3節で述べた治療の流れ全体を変更する可能性があり慎重に対処したいと考えている。

8. 病歴管理

重粒子線治療をclinical scienceの立場でみたとき，最も重要なことは何をどう治療するかという治療プロトコールの作成と，その結果得られるデータの解析評価とであろう。データ管理もそれに見合って考えられるべきである。治療プロトコールについての検討がまだ進んでいない現在，病歴管理の細かい議論はできない。

しかし，重粒子線治療は人類の貴重な経験といえるので，我々のしたことを後の人が，retrospectiveに再体験するのに十分なデータを残すべきであると著者は考えている。したがって，治療の全過程（図2のフローチャート参照）で発生するデータの主なもの（例えば，3次元治療計画データ，治療ビームのパラメータ，位置決め時に撮影するX線テレビ画像 etc）は要約した上，長期間保存されねばならない。これらは，他の医学データや予後追跡データとともに管理され，後の解析に用いられる。

このようなデータ管理の作業は，図3の治療管理計算機と病歴管理計算機の両方で行われることになるが，その役割分担はまだ検討されていない。これらは，治療プロトコールとその解析評価法の輪郭が明らかになったとき，それに即した形で決められることになろう。

9. おわりに

以上述べてきたようにHIMACの治療システムは，現在のところ必ずしも確立しているとはいえない多岐にわたる技術を統一するものであり，その完成までに多くの開発努力が要求される。例えば，要素技術としては，次のものについての検討を十分に行わねばならない。

1) デジタルX線テレビによる位置決め（ランドマーク法）
2) イメージング法としてのDRS
3) スーパー・グラフィック・ワークステーションを用いた3次元治療計画
4) 高速画像伝送路
5) 異種画像のフォーマットの統一
6) 異種画像の位置合せと情報の相互移転
7) 治療データベースの構築と病歴管理システムの結合
8) 治療計画用X線CT
9) 患者固定法
10) 補償フィルタ及び患者コリメータの高速作成法

また，システム化の際には業務の内容や量を十分に検討し，それに見合ったものを導入する必要があるが，これらについて把握しきれない現状では，システム設計の困難も予想される。さらに，ここで述べた構想の多くの部分は，現在のところ著者らの私見であり，必ずしも関係者の合意を得たものとはいえない。今後，この構想をたたき台として多くの人の意見により修正を加えることも必要であろう。しかし，HIMACという最高の治療機に対しては，それに見合った最高の治療システムを準備すべきであるというのが著者の信念であり，治療開始までには衆智を結集した最高のシステムを実現したいと願っている。読者諸賢におかれては，本稿を読んでの御感想，御批判を是非とも著者にお寄せいただきたい。

＜謝辞＞

常に御指導いただく放医研医用重粒子線研究部の平尾泰男部長，同病院部の恒元博部長に深い感謝の意を表します。また，ともにHIMACプロジェクトを遂行している放医研医用重粒子線研究部の諸氏に同様の意を表したいと思います。特に河内清光第3研究室長，金井達明主任研究官には，本稿に関するさまざまな点を議論していただきました。なお，本研究の一部はがん研究助成金赤沼班（63—24）の援助を受けた。

＜参考文献＞

1) K. Kawachi, T. Kanai, M. Endo et al : Radiation oncological facilities of the HIMAC. 日本放射線腫瘍学会誌 1：19—29, 1989.
2) A. M. Berson, J. R. Castro, P. Petti et al: Charged particle irradiation of chordoma and chondrosarcoma of the base of skull and cervical spine : The Lawrence Berkeley Laboratory experience. Int.J Radiation Oncology Biol.Phys. 15 : 559—565, 1988.
3) 遠藤真広：3次元画像処理の粒子線治療への応用。映像情報(M) 19：1073—1076, 1987.
4) 遠藤真広，河内清光，飯沼武：デジタル合成シミュレーション写真の作成法の検討。医用電子と生体工学 Vol. 27 suppl. pp. 46, 1989.

厚生省特定疾患運動失調症調査研究班

研究報告書　抜刷

多系統萎縮症における黒質病変のMRIによる検討

平山惠造　青墳章代　篠遠　仁
橋本隆裕　池平博夫　福田　寛
福田信男　舘野之男

平成元年度

多系統萎縮症における黒質病変のMRIによる検討

平山惠造* 青墳章代* 篠遠仁*
橋本隆裕** 池平博夫** 福田寛**
福田信男** 舘野之男**

はじめに

多系統萎縮症に属するオリーブ橋小脳萎縮症，Shy-Drager 症候群，線条体黒質変性症はいずれも黒質—線条体系路に病変を有し，パーキンソニズムをきたすことが知られている．今回我々は高磁場 MRI を用いて多系統萎縮症の黒質病変をパーキンソン病とともに検討した．

対象と方法

対象は，臨床的に診断されたオリーブ橋小脳萎縮症 6 例（46～71 歳，罹病期間 2 ～ 8 年），Shy-Drager 症候群 2 例（47，60 歳，罹病期間 5，7 年），線条体黒質変性症 5 例（48～68 歳，罹病期間 3 ～ 9 年），正常対照 8 例（59～72 歳）である．このほかに黒質に主病変を有するパーキンソン病 22 例（50～78 歳，罹病期間 1 ～11 年）を疾患対照として，同時に検討した．

装置は静磁場強度 1.5 Tesla の超伝導型 MRI (Gyroscan S15) を用い，パルス系列は繰り返し時間 2500 msec，エコー時間 40msec と，80msec の条件のスピンエコー法により T_2 強調画像を得た．最初に正中矢状断像で中脳下丘を通り脳幹軸に直交する面から＋10 度を原則として撮像面を設定し，スライス厚 5mm で基底核レベルまで 14 スライスの撮像を行った．次に，中脳水平断像において赤核の中心と大脳脚を通る直線上の信号強度をプロフィールに表し，低信号域を示す赤核と

図 1 正常対照例の中脳水平断像と信号強度のプロフィール SE 法（TR 2500ms/TE 40ms）

黒質網状層の間にある緻密層の等信号域のピークの半分の高さにおけるピークの幅を測定し，緻密層信号域の幅とした（図 1）．各疾患群及び正常対照群の黒質緻密層信号域の幅の平均と標準偏差をもとめ Student t-test で検定した．

結果

(1) 正常対照における緻密層信号域の幅は 4.28 mm (SD＝0.66) であり，疾患対照のパーキンソン病では 2.69mm (SD＝0.34) と有意な狭小化が認められた ($p<0.01$)．正常対照とパーキンソン病の代表例を 図 2，3 に示す．

またパーキンソン病では Yahr の重症度および罹病期間が進むにつれて，統計的に有意ではないものの，緻密層信号域の狭小化が強くなる傾向が認められた（図 4，5）．

(2) オリーブ橋小脳萎縮症では緻密層信号域の平均幅は 3.65mm (SD＝0.64) で，正常より若干狭小化がみられるが，パーキンソン病のような有

* 千葉大学医学部神経内科
** 放射線医学総合研究所臨床研究部

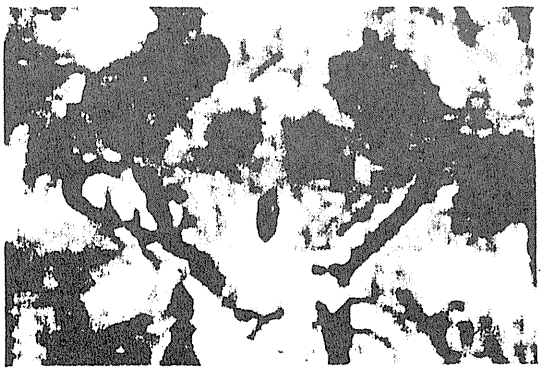

図 2　正常対照の中脳 MRI
（59 歳，男性）

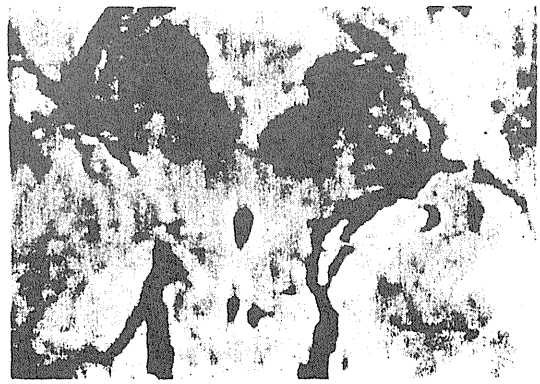

図 3　パーキンソン病の中脳 MRI
（経過 4 年，54 歳，男性）
緻密層信号域の著明な狭小化が認められる

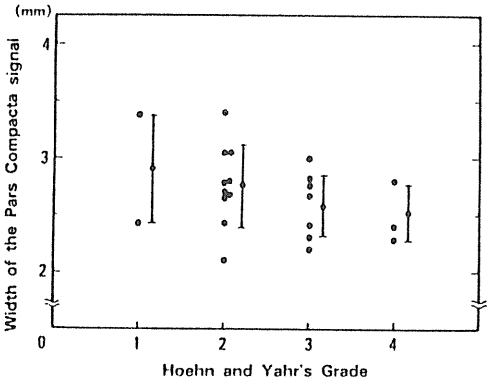

図 4　パーキンソン病における Yahr の重症度分類と緻密層信号域の幅との関係

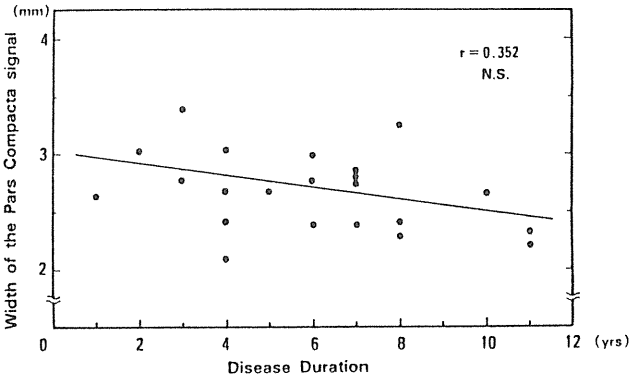

図 5　パーキンソン病における罹病期間と緻密層信号域の幅との関係

図 6　オリーブ橋小脳萎縮症の中脳 MRI
（経過 5 年，58 歳，男性）
緻密層信号域の狭小化は軽度である

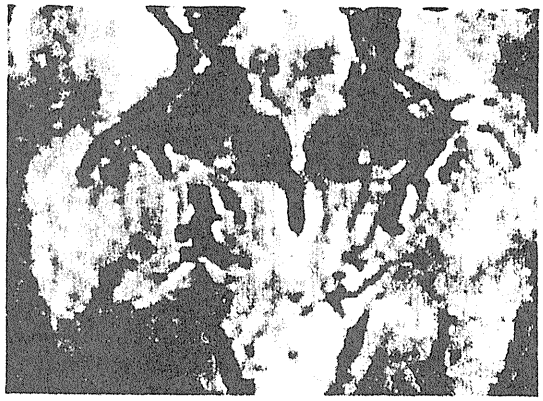

図 7　Shy-Drager 症候群の中脳 MRI
（経過 7 年，47 歳，女性）
緻密層信号域の狭小化が認められる

図 8　線条体黒質変性症の中脳 MRI
（経過4年，48歳，女性）
緻密層信号域の狭小化が認められる

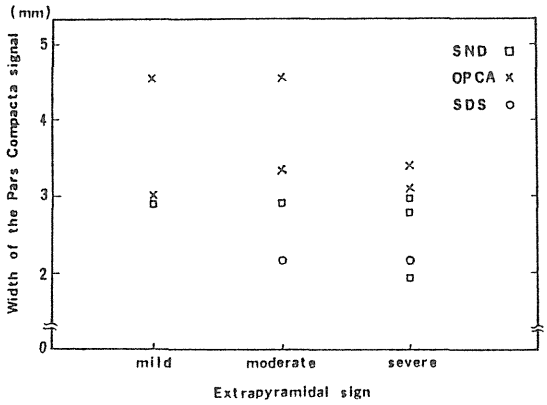

図10　多系統萎縮症における錐体外路症状と緻密層信号域の幅との関係

意な狭小化は認められなかった．

(3) Shy-Drager 症候群では緻密層信号域の平均幅は 2.15mm (SD＝0.01) で，2例共に狭小化が認められた．

(4) 線条体黒質変性症では緻密層信号域の幅は 2.70mm (SD＝0.55) と，パーキンソン病と同様に正常対照に比較して有意な狭小化が認められた ($p<0.01$)．

オリーブ橋小脳萎縮症，Shy-Drager 症候群および線条体黒質変性症の代表例を 図 6，7，8 に示す．また各疾患別の緻密層信号域の分布を図9に示す．

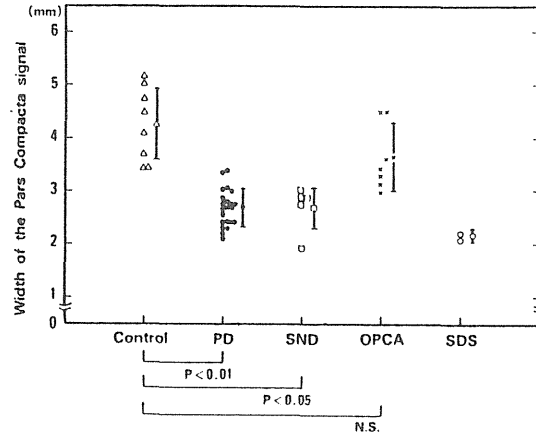

図 9　多系統萎縮症とパーキンソン病，正常対照の緻密層信号域の分布

(5) オリーブ橋小脳萎縮症，Shy-Drager 症候群，線条体黒質変性症の13例で錐体外路症状（筋固縮）を軽度，中等度，高度の3段階に分け，緻密層信号域の幅との関係を検討した．横軸に錐体外路症状の強さを，縦軸に緻密層信号域の幅をとると 図10のような分布を示し，統計的に有意ではないものの，錐体外路症状が高度になるにつれて黒質緻密層信号域の幅が小さくなる傾向がみられた．

考　察

MRI の T_2 強調 SE 法では正常脳で赤核，黒質網状層が低信号を示すことが知られており，この低信号は鉄の磁性体効果によると考えられている[1]．MRI 上の黒質の低信号域と解剖学的な組織との対応は議論のあるところであるが，パーキンソン病や線条体黒質変性症，Shy-Drager 症候群にみられた黒質の緻密層信号域の狭小化は，緻密層の萎縮あるいは緻密層の鉄沈着の増加を反映していると考えられる．

1986年，Duguid ら[2]，Braffmann ら[3]がパーキンソン病における黒質の緻密層信号域の狭小化を報告して以来，多系統萎縮症においても黒質の低信号域の拡大や被殻後外側の異常低信号が報告され[1,4,5]，これらの疾患に対する高磁場 MRI の有用性が明らかになってきているが，臨床症状や重症度，罹病期間との関係など詳細な検討を行っ

た報告はない．今回の検討で，線条体黒質変性症，Shy-Drager 症候群ではパーキンソン病と同様に比較的初期から緻密層信号域の狭小化が認められるのに対し，オリーブ橋小脳萎縮症では末期にいたる前までは緻密層信号域の幅が保たれていた．このことはオリーブ橋小脳萎縮症における黒質病変の進行過程に線条体黒質変性症や Shy-Drager 症候群とは差異があることを示唆している．また黒質の緻密層信号域の幅が多系統萎縮症の錐体外路症状の程度と軽度ながら対応があることからも，MRI で黒質の緻密層信号域の幅を測定することが多系統萎縮症の病態を理解する一助となると考えられた．

まとめ

高磁場 MRI により多系統萎縮症における黒質病変をパーキンソン病とともに検討した結果，緻密層信号域の幅は線条体黒質変性症，Shy-Drager 症候群ではパーキンソン病と同様に有意な狭小化が認められたが，オリーブ橋小脳萎縮症では比較的保たれていた．多系統萎縮症の 13 例で，錐体外路症状の程度が強くなるにつれて緻密層信号域の狭小化が強くなる傾向がみられた．

文献

1) Drayer BP, Burger P et al: Magnetic resonance imaging of brain iron. AJNR 7: 373, 1986.
2) Duguid JR, Paz RDL et al: Magnetic resonance imaging of the midbrain in Parkinson's disease. Ann Neurol 20: 744, 1986.
3) Braffmann BH, Grossman RI et al: MR Imaging of Parkinson Disease with Spin-Echo and Gradient-Echo Sequences. AJR 152: 159, 1989.
4) Pastakia B, Polinsky R et al: Multiple system atrophy (Shy-Drager syndrome): MR imaging. Radiology 159: 499, 1986.
5) Rutledge JN, Hilal SK et al: Study of movement disorders and brain iron by MR. AJNR 8: 397, 1987.

Abstract

MRI of the Midbrain in Multiple System Atrophy

by

Keizo Hirayama[1], Akiyo Aotsuka[1], Hitoshi Shinoto[1], Takahiro Hashimoto[2], Hiroo Ikehira[2], Hiroshi Fukuda[2], Nobuo Fukuda[2] and Yukio Tateno[2]

from

[1]Department of Neurology, Chiba University School of Medicine
[2]Division of Clinical Research, National Institute of Radiological Sciences

We studied 13 patients with multiple system atrophy (OPCA 6, SDS 2, SND 5), 22 patients with Parkinson's disease (PD) and 8 age matched controls by high field strength MRI.

The results were as follows.

1. The mean width of the pars compacta signal was 2.69mm (SD=0.34)in the PD group and 4.28mm (SD=0.66) in controls. The difference between the means was highly significant ($p<0.01$). There was a trend toward narrowing the width of pars compacta signal of substantia nigra as the Yahr's grade or disease duration progressed.
2. The mean width in the OPCA group was 3.65mm (SD=0.64), but the decrease was not significant.
3. The mean width in the SDS group was 2.15 mm(SD=0.14) and very narrow.
4. The mean width in the SND group was 2.70 mm (SD=0.39). Compared with that in controls, narrowing of the pars compacta signal was also significant in this group ($p<0.05$).

MR imaging with measurement of the width of the pars compacta is useful in understanding of the pathogenesis of multiple system atrophy and PD.

MRIによる心血管血流の可視化

今井　均，隈井俊彦，関谷政夫
内山明江，小林史朗，榊原　誠
今関安雄，渡辺　滋，増田善昭
稲垣義明，橋本隆裕，池平博夫
福田　寛，館野之男

日本バイオレオロジー学会誌（B＆R）別刷
第3巻　第4号　1989

総　説

MRIによる心血管血流の可視化

今井　均*　隈井俊彦*　関谷政夫*
内山明江*　小林史朗*　榊原　誠*
今関安雄*　渡辺　滋*　増田善昭*
稲垣義明*　橋本隆裕**　池平博夫**
福田　寛**　館野之男**

1. はじめに

MRI（magnetic resonace imaging）は近年，開発された新しい非侵襲的な画像診断方法であり[1]，心血管腔および血流を可視化することができる[2]。MRIによる血流診断の進歩は著しく，従来のスピンエコー（SE）法に加え，シネMRI法が臨床応用されている[3,4]。シネMRIはスピンエコー法より高速度の血流を高信号として描出し，弁逆流やシャント流を血流信号欠損像(flow void)として描出する[5-7]。この血流信号欠損像の成因は高速流や乱流と言われているが，まだ充分に検討されていない。

そこで，我々は，SE法とシネMRIのうちのFFE法(fast field echo)を使用し，MRIによる心血管系血流の評価を，狭窄実験および臨床的検討により行った。

2. 対象と方法

対象は実験では定常流による狭窄管モデルを使用し，臨床的には正常および各種心血管疾患患者の約780例を対象とした。装置は従来のSE法についてはピッカー社製（0.5テスラ），およびフィリップ社製（1.5テスラ）の超伝導装置を使用し，FFE法については後者を使用した。撮像条件はSE法では心拍同期（TE：エコー時間は30，60 msec），および心拍非同期（TEは24，30 msec，TR：パルス繰り返し時間は600 msec）を用い，FFE法ではTEは12-18 msec，フリップ角は45度を用いた。スライス幅は10mm（実験では9 mm），収集画像画素は128×128，平均加算回数は4回を用いた。心拍同期SE像およびFFE像では心電図のR波をトリガーにして，心拍同期を行っている。FFE像では速度や加速度による位相補正は行っていない。狭窄実験では狭窄部上流より，アルミ塗料を流しこみ，流れの可視化を行った。一部の例では，カラードップラー像と比較した。

Fig. 1に，狭窄モデルのシェーマを示す。透明なアクリルの長方形（内径40，高さ10，長さ900 mm）に幅2 mm，高さ10mmのスリットを作り，定常流ポンプにて狭窄部での流速が0から，この実験で得られた最大流速の98cm／secまで脱気した水道水を流した。信号強度は静止水のそれを対照とした。

3. 結　果

A．実験の結果

1)　アルミ塗料による可視化

Fig. 2は狭窄部の流速が42cm／secのとき，狭窄上流よりアルミ塗料を流した写真である。矢印方向の狭窄の下流において中心流（C），剝離領域（S），乱流領域（T）を認める。

2)　FFEとSE法の流速画像

Fig. 3の左はFFE法（TE14，TR600msec），右はSE法（TE30，TR600msec）で流速を上から下に向かい0から98cm／secまで変化させた像を示す。左側のFFE像では矢印の狭窄部の下流で中心流を98cm／secの流速まで白で示される高信号の部として認め，その到達距離は流速の増加とともに延長している。また，黒で示される無信号領域はモデル実験より乱流形成によると考えられ，流速の増加とともに無信号領域は拡張している。

*千葉大学医学部第3内科，**放射線医学総合研究所
〔〒280　千葉市亥鼻1－8－1〕

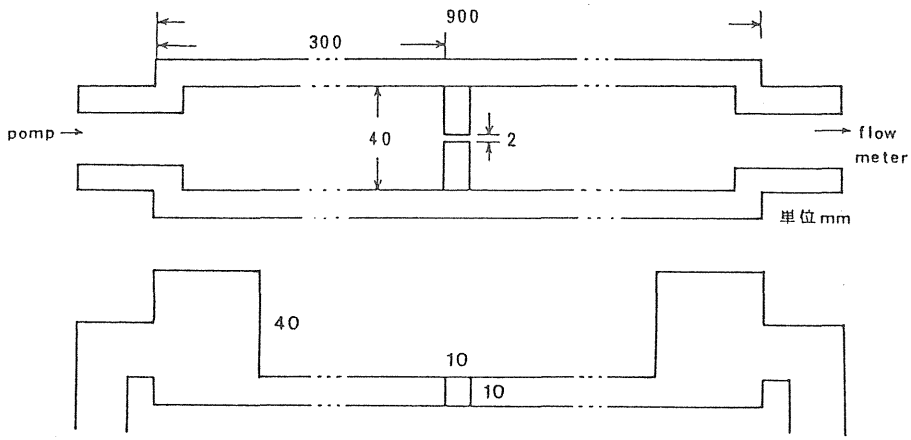

Fig. 1 狭窄モデルのシェーマ

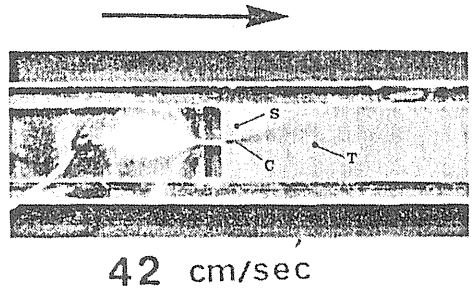

Fig. 2 アルミ塗料による流れの可視化

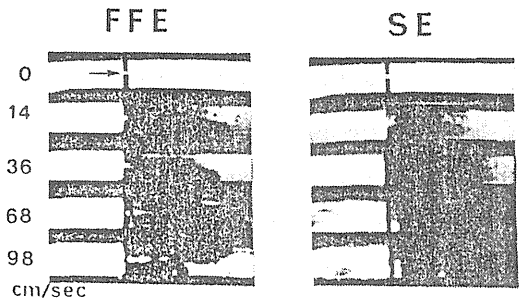

Fig. 3 FFEとSE法による狭窄モデルのMR像

また，流速の変化とともに，流れのパターンが変化しているため無信号領域の形は左右対称でない。一方，右側のSE像ではFFE像に比較し，中心流の発達は小さく，また黒で示される無信号領域もFFE像よりも広い範囲で存在している。

3) 流速と信号強度比の関係

流速と静止水との信号強度比の関係を模式的にグラフに表した(Fig. 4)。狭窄後の中心流はモデル実験より層流なので，層流の信号強度はFFE像

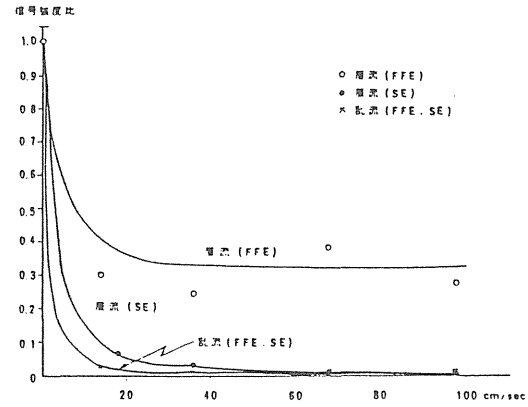

Fig. 4 流速と信号強度比の関係

では少なくとも約100cm／secまで，SE像では約30cm／secまで信号の存在が認められた。一方，乱流領域の信号は両者とも流速の増加とともに著明に減少している。また，SE像では血流の停滞する剝離領域には高信号(slow flow image)を認める。一方，FFE像ではこの剝離領域を含め乱流の存在するところでは無信号(flow void)となっている。

B．臨床の結果

1) 症例を呈示する。

症例1. 正常例の心拍同期SE像(Fig. 5)

正常例の心拍同期SE像で左上より90msec毎でR波より最大630msecまでの横断像である。左心内では収縮末期や拡張期に血流画像を認めるが，著明ではない。一方，下行大動脈では拡張末期に著明な血流信号を認め，収縮期に血流信号は減少している。

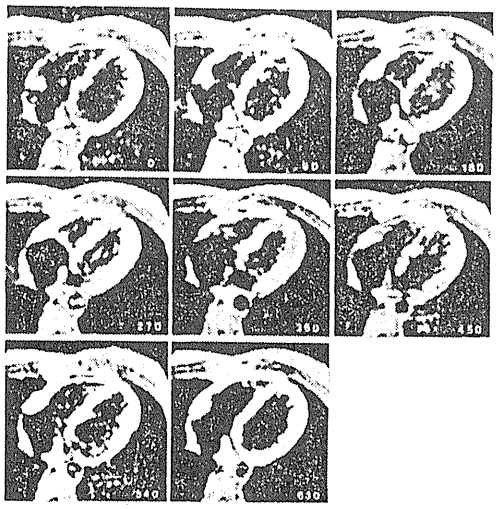

Fig. 5　正常例の心拍同期SE像。
左心腔内に収縮末期や拡張期に血流画像を認めるが，著明ではない。一方，下行大動脈に拡張末期では著明な血流信号を認め，収縮期に血流信号は低下している。

症例2.　正常例のFFE像（Fig. 6）

正常例のFFE像で，左上より，58msec毎でR波より最大533msecまでの左室から胸部大動脈にいたる斜断像である。左心内（V）や左房内（A）には全体に高信号の血流画像を認める。また，上行大動脈（A_o）の基部（矢印）や弓部では収縮早期に血流信号の減弱を認めるが，下行大動脈（D）には常時，高信号の血流画像を認める。

症例3.　陳旧性広範囲前壁心筋梗塞

Fig. 7Aは陳旧性広範囲前壁心筋梗塞例の心拍同期SE像の冠状断像である。左室瘤内に停滞した著明な高信号の血流画像を認める。このような，左室内に血流画像を著明に認める陳旧性心筋梗塞例の左室駆出率は著明に低下していた。

Fig. 7Bは同一症例のFFE像の左室長軸冠状断像である。左心尖部の瘤内と左室の基部には高信号の血流画像を認めるが，左室の中央部には帯状に血流信号減弱領域があり，これは左室の瘤内と瘤外の血流運動が異るために発生した渦流や乱流領域と推定された。

症例4.　僧帽弁逸脱症

Fig. 8は僧帽弁逸脱症のFFE像で矢状断の左室長軸である。収縮期に弁逆流が左室より僧帽弁の前尖側を通り左房の後壁まで達する血流信号の減弱領域として描出されている。また拡張初期に左室内に信号低下領域を認める。本症例はカラードップラー法により4度逆流を示す僧帽弁逸脱症（前尖）であった。

症例5.　大動脈解離（DeBakeyⅢb）

Fig. 9は大動脈解離例の胸部下行大動脈部の横

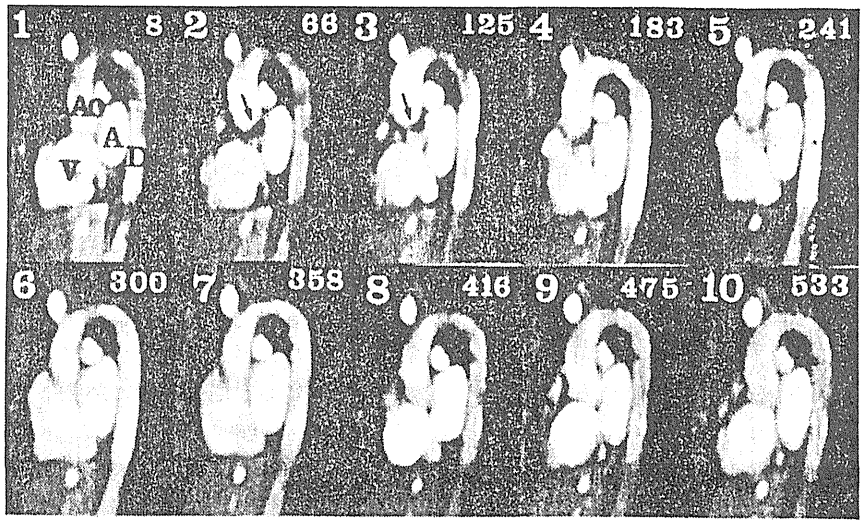

Fig. 6　正常例のFFE像。
心腔内には全画面で高信号の血流画像を認める。一方，上行大動脈の基部（矢印）や弓部では収縮期に血流信号の減弱を認めるが，下行大動脈には常時，高信号の血流画像を認める。

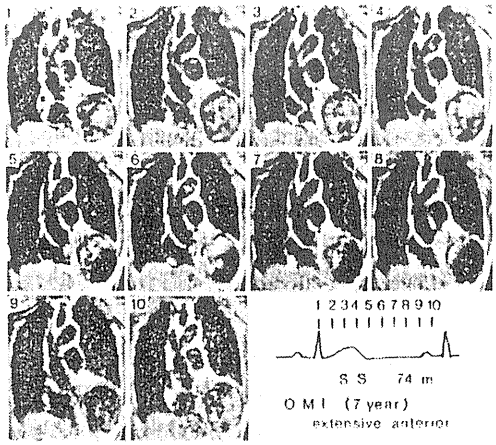

7A

Fig. 7 陳旧性広範囲前壁心筋梗塞。
7Aは心拍同期SE像の冠状断である。左室瘤内(LV)に停滞した著明な血流画像を認める。7Bは同一症例のFFE像の左室冠状断長軸像である。左心尖部の瘤内と左室の基部には高信号の血流画像を認めるが，左室の中央部には帯状に血流信号減弱領域を認める。

7B

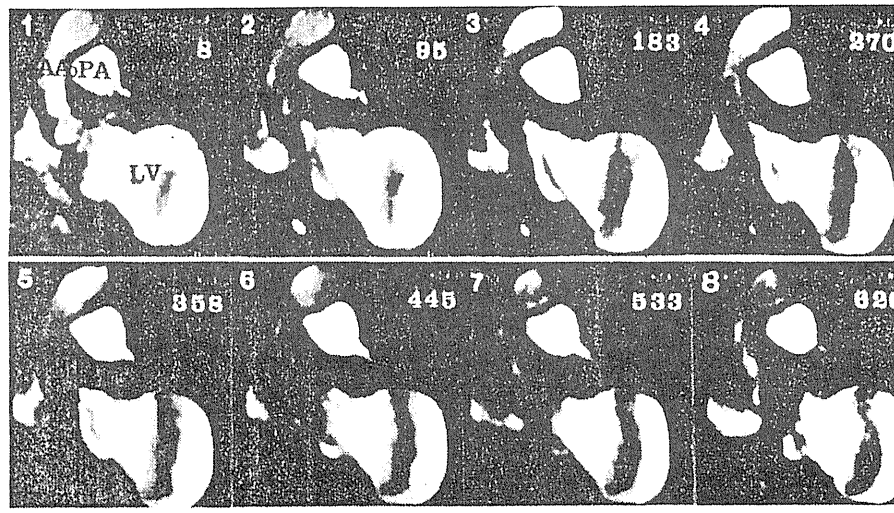

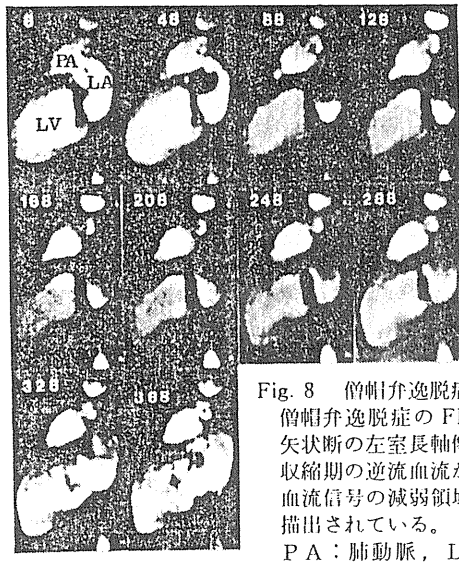

Fig. 8 僧帽弁逸脱症
僧帽弁逸脱症のFFE像で矢状断の左室長軸像である。収縮期の逆流血流が左房に血流信号の減弱領域として描出されている。
PA：肺動脈，LV：左室，LA：左房

断像である。一番右のシェーマで内腔の大きい方が偽腔(FL)，小さい方が真腔(TL)である。造影X-CTでは内側の高信号部が真腔，外側の低信号部が偽腔である。一方，SE像では真腔は無信号に偽腔は中等度信号になっているが，FFE像では反対に真腔が高信号に偽腔が中等度信号になっている。

2) FFEによる弁逆流重症度評価

FFEによる僧帽弁および大動脈弁逆流の程度をflow voidが左房および左室内に占める面積比であらわし，カラードップラーによる逆流の重症度と比較すると，Fig. 10のような良好な関係が認められた。

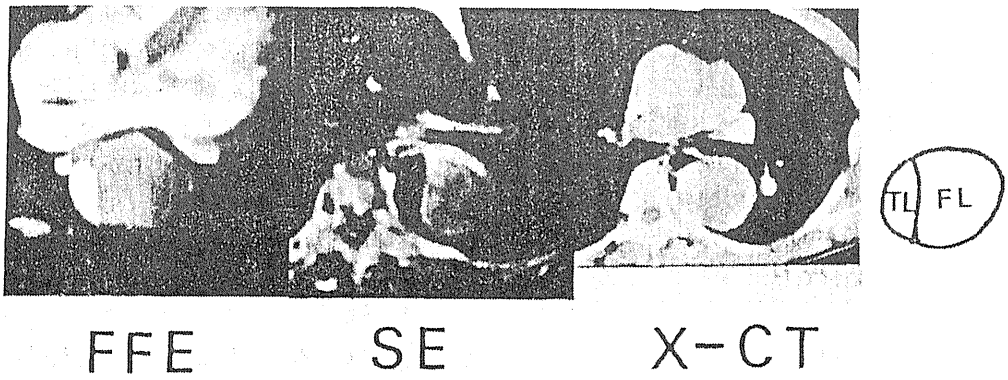

Fig. 9　大動脈解離（DeBakeyⅢb）。
大動脈解離例の胸部下行大動脈部の横断像である（左よりFFE, SE像，造影X-CT像）。造影X-CT像より内側の高CT値部が真腔，外側の低CT値部が偽腔である。SE像では真腔は無信号に偽腔は中等度信号になっているが，FFE像では反対に真腔が高信号に偽腔が中等度信号になっている。

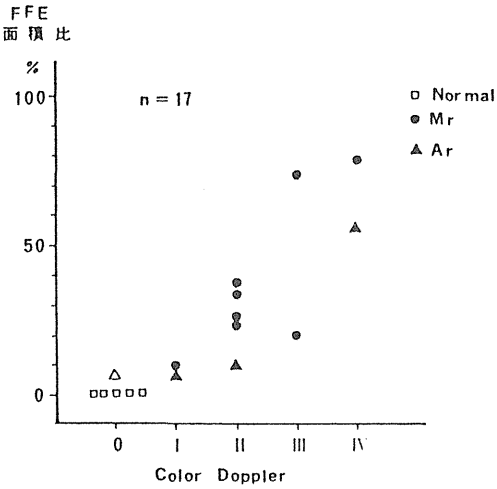

Fig. 10　FFE法と超音波Doppler法による弁逆流重症度評価の比較。
FFE法による弁逆流を無信号の面積比であらわし，超音波Doppler法による重症度と比較すると，図のような良好な関係が認められた。（Mr：僧帽弁閉鎖不全症，Ar：大動脈弁閉鎖不全症，△：Doppler法では逆流はないが，FFEでは左室流出路に無信号域の認められた例）

4. 考　案

1)　MRIの血流

MRIによる血流画像は振幅法と位相法とに分類でき，SE法は前者であり，FFE法は後者である[9]。一般に，MRIの血流信号は，流速，層流および乱流，T_2の位相のずれ，流れの方向などにより影響される。また，SE法では，スライス幅，パルス繰返し時間，エコー時間，T_1またはT_2値に影響され，一方，FFE法では血流信号は主としてパルス繰返し時間，エコー時間，に影響然され，T_1またはT_2値に影響されない[9]。流速と血流信号の関係では，SE法では（逆説増強が起こる流速は除いて）流速の増加とともに，その血流信号は低下する[10]。一方，FFE法では，血流信号は流速の増加とともに，その血流信号は低下するが，SEより血流信号の低下の程度は緩徐である。しかし，流速が増加すれば，乱流が発生しやすく，MRIによる血流信号の低下が流速によるものかどうかは判定しがたい。たとえば，加藤ら[11]はモデル実験のSE法では流速が約30cm／secまで，phase reforcusing法（位相補正後）では約50cm／secまで可視化できると報告しているが，関心領域が大きく，必ずしも層流と乱流を区別していない。

2)　当モデルの特徴

この狭窄モデルは内腔の高さ10mm，幅40mm，スリットの高さ10mm，幅2mmの2次元平面狭窄モデルであり，スライス幅9mmのMRIの水平段像は，この2次元平面内の血流動態をそのまま反映していると考えられた。流体として使用した水は，血液よりT_1値，T_2値は長く，また血流より粘性が低いため，血液より乱流になりやすく，流速98cm／secの時のレイノズ数は約1040であった。

3)　モデル実験の検討

一般に，定常流の狭窄直後の中心流は層流とい

われている[12]。今回の狭窄実験でも，アルミ塗料により，中心流，剥離領域，乱流領域が示された。

血流画像は狭窄直後の中心流が確認できたときに，血流画像の陽性所見とした。SE像では36cm／secまで中心流を確認できたが，FFE像では約1m／secまで確認できた。またその減衰曲線の低下は約1m／secでも緩徐があり，さらに速い流速でも可視化ができると類推された。

一方，乱流領域は速度の増加とともに著明に拡大し，血流信号は著明に減少した。

このことより，FFE像で見られる血流信号の低下は，すくなくとも1m／sec以下なら，主として，乱流のためと考えられた。乱流で信号低下の生じる理由はMRIのピクセル内の水素原子の位相がランダムであり，そのためMR信号を検出できないと考えられている[13]。また，SE像よりFFE像でより速い流速を画像化できるのは，主に，エコー時間(ET)が短いためと考えられる。

加速度により位相のずれが生ずるため，MR信号が減弱するといわれる[5]。狭窄直前の上流側の液体は狭窄口に吸込まれたため，加速流が生じる（アルミ塗料の実験でも示される）が，今回の実験では加速流による血流信号低下領域は観察されなかった。これは，加速領域が小さく，容積効果のため観察されなかった可能性はある。しかし，加速の程度により位相のずれが異なり，加速流でも血流信号低下を呈したり，しなかったりする可能性も否定できないと考えられた。

4) 臨床応用の検討

一般に，正常者の心腔は層流であり[14]，上行大動脈の基部は乱流を発生しやすく，弓部では湾曲のため速度分布が変化するが，上行大動脈の基部以後の大動脈はほぼ層流に近いと言われている[12]。また，正常者の大動脈の最大血流速度は約1.8m／secであり[12]，大動脈弁狭窄症で約6m／secまでと言われている[14]。

われわれは，すでに，SE像では心血管系の血流が生理的に停滞する部位や病的に停滞する部位で血流画像を認めることを報告している[15]。一方，今回の検討では，シネMRIでは正常者の心腔および上行大動脈の基部と弓部を除いた大動脈において，全心周期を通じて，中～高信号の血流信号を認めたが，上行大動脈基部や弓部では収縮期に血流信号の消失を認めた。また，疾患例では，弁逆流やシャント流，大動脈解離の偽腔内への流入血流が他の報告と同様に無信号領域として認められ，モデル実験より考えられるように，これは高速度や乱流のためと思われた．しかし，ASDの一部の例ではシャント流はかならずしも，信号消失として認められなかった。この理由は，ASDのような低圧系のシャント流は弁逆流より速度は遅く，乱流の発生が小であるためであり，実験結果とも合致すると考えられた。また，大動脈弁逆流例で逆流の無信号領域の中に小さな高信号の中心流を認めた例があった。この部位は層流でありかつ流速が最大となる部位であるので，弁逆流の無信号領域は高速流の領域より，主に，乱流領域を観察していると推定された。さらに，大動脈解離例について検討すると，SE法では血流の速い真腔は無信号，血流の遅い偽腔は弱～中等度信号であったが，FFE法では逆に，多数例で真腔では高信号，偽腔では無～弱信号であった。これは，真腔は偽腔より血流は速く，偽腔はエントリーからの流入血流のため真腔より乱流度が大であるためと考えられた。

以上，心血管系の血流診断にシネMRIはきわめて有用と考えられたが，その信号強度の解釈には，血流速度だけでなく，乱流等の要素を加味して考える必要があることを示している。

5. 結　論

MRIによる血流画像について狭窄モデルおよび臨床例を対象に検討した。

A．モデル実験

FFE法はSE法より速い流れ（すくなくとも約1m／sec）まで描出できたが，いずれの方法でも乱流領域は無信号として示された。

B．臨床例

1) SE法では，一般に，心血管腔は無～中等度信号であった。しかし，心筋梗塞，僧帽弁狭窄症，大動脈瘤および大動脈解離例で血流の停滞する部分に，著明な血流画像を認めた。

2) FFE法では心血管腔に血流画像を認めたが正常例では大動脈基部や弓部に病態では，弁逆流，シャント性疾患，大動脈解離のエントリー部など，高速流や乱流の発生しやすい部位に血流画

像の消失を認めた。

以上，MRIによる血流の可視化は種々の血流情報を提供し，今後臨床的に広い利用が期待される。

文　献

1. Pykett, I. L,, Newhouse, J.F., Buonanno, F. S., Brady, T. J., Goldman, M. R., Kistler, J. P. and Pohost, G. M. : Principles of nuclear magnetic resonance imaging. *Radiology*, 143, 157－168, 1982.
2. Kaufman, L., Crooks, L. E., Sheldon, P., Hricak, H., Herfkens, R. J. and Bank, W. : The potential impact of nuclear magnetic resonance imaging on cardiovascular diagnosis. *Circulation*, 67, 251－257, 1983.
3. Rumancik, W. M., Naidich, D. P., Chandra, R., Kowalski, H. M., McCauley, D. I., Megibow, A. J., Hernanz-Schulman, M. and Genieser, N. B. : Cardiovasucular Disease : Evaluation with MR phase imaging. *Radiology*, 166, 63－68, 1988.
4. Gao, J. H., Holland, S. K., and Gore, J. C. : Nuclear magnetic resonnance signal from flowing nuclei in rapid imaging using gradient echo. *Med Phys*, 15, 809－814, 1988.
5. Roos, A. D., Reichek, M., Axel, L. and Kressel, H. Y. : Cine MR imaging in aortic stenosis. *J. Comp Assi Tomo*, 13, 421－425, 1989.
6. Pflugfelder, P. W., Landzberg, J. S., Cassidy, M. M., Cheitlin M. D., Schiller, N. B., Auffermann, W. and Higgins, C. B. : Comparison of cine MR imaging with Doppler echocardiography for the evaluation of aortic regurgitation. *A. J. R.*, 152, 729－735, 1989.
7. Simpson, I, A., Chung, J. K., Class, R. F., Sahn, D. J., Sherman, F. S., and Hesselink, J. : Cine magnetic resonance imaging for evaluation of anotomy and flow relations in infants and children with coactation of the aorta. *Circulation*, 78, 142－148, 1988.
8. Schiebler, M., Axel, L., Reichek, N., Aurigemma, G., Yeager, P. D., Boging, K., and Kressel, H. : Correlation of cine MR. imaging with two-dimensional pulsed Doppler echocardiographyin valvular insufficiency. *J. Comput. Assisi. Tomogr.*, 11, 627－632, 1987.
9. Satoh, K. and Kuhara, S. : Basic aspect for measuring blood flow by MRI. *Jap. J. Mag.*, 7, 24－42, 1987.
10. Axel, L. : Blood flow effects in magnetic resonance imaging. *A. J. R.*, 143, 1157－1166, 1984.
11. Katoh, T., Sawada, S., Yoshida., Noguchi, Y., Tanaka, Y., Yamanouchi, Y., Shimojyo, M., Koito, H., Kubota, Y., Noguchi, T., Kaneda, R., Imazato, I. and Oyamada, K. : Phase reforcusing techniques in MRI — experimental study and clinical application —. *Jap. J. Mag.*, 9, 28－36, 1989.
12. 沖野　遙，菅原基晃，松尾裕英：心臓血管系の力学と基礎計測，講談社，1982, pp, 180, 186－207.
13. Bradley, W. G. and Waluch, J. V. : Blood flow : Magnetic resonance imaging. *Radiology*, 154, 443－450, 1985.
14. Hatle, L. and Angelson, B. : Doppler ultrasound in cardiology. physical principles and clinical applications. Philadelphia : Lea & Febiger, pp. 74－96, 1982.
15. Imai, H. Sakakibara, M., Sunami, U., Yoshida, K., Nishimoto, Y., Taguchi, K., Watanabe, S., Syukuya, M., Masuda, Y. and Inagaki, Y. : Flow imaging of the cardio vascular system using magnetic resonance imaging. *J. Cardiol,*, 18, 493－505, 1988.

Reprinted from

NUCLEAR MEDICINE AND BIOLOGY
INTERNATIONAL JOURNAL OF RADIATION
APPLICATIONS AND INSTRUMENTATION PART B

Vol. 16, *No.* 3, *pp.* 247–254

2-DEOXY-2-[^{18}F]FLUORO-D-GALACTOSE AS AN *IN VIVO* TRACER FOR IMAGING GALACTOSE METABOLISM IN TUMORS WITH POSITRON EMISSION TOMOGRAPHY

KIICHI ISHIWATA,[1] KEIICHIRO YAMAGUCHI,[2] MOTONOBU KAMEYAMA,[3] HIROSHI FUKUDA,[2] MASAO TADA,[2] TAIJU MATSUZAWA,[2] KENJI MURAISHI,[3] JUN ITOH,[3] KOICHIRO KAWASHIMA,[1] TOSHIHIRO TAKAHASHI[1] and TATSUO IDO[1]

[1]Division of Radiopharmaceutical Chemistry, Cyclotron and Radioisotope Center, Tohoku University, Aoba Aramaki, Sendai, 980, [2]The Research Institute for Tuberculosis and Cancer, Tohoku University and [3]Institute of Brain Diseases, Tohoku University School of Medicine, Sendai, Japan

PERGAMON PRESS PLC
OXFORD · NEW YORK · BEIJING · FRANKFURT
SÃO PAULO · SYDNEY · TOKYO · TORONTO
1989

Nucl. Med. Biol. Vol. 16, No. 3, pp. 247–254, 1989
Int. J. Radiat. Appl. Instrum. Part B
Printed in Great Britain.

0883-2897/89 $3.00 + 0.00

2-Deoxy-2-[^{18}F]fluoro-D-galactose as an *In Vivo* Tracer for Imaging Galactose Metabolism in Tumors with Positron Emission Tomography

KIICHI ISHIWATA,[1]* KEIICHIRO YAMAGUCHI,[2] MOTONOBU KAMEYAMA,[3] HIROSHI FUKUDA,[2] MASAO TADA,[2] TAIJU MATSUZAWA,[2] KENJI MURAISHI,[3] JUN ITOH,[3] KOICHIRO KAWASHIMA,[1] TOSHIHIRO TAKAHASHI[1] and TATSUO IDO[1]

[1]Division of Radiopharmaceutical Chemistry, Cyclotron and Radioisotope Center, Tohoku University, Aoba Aramaki, Sendai, 980, [2]The Research Institute for Tuberculosis and Cancer, Tohoku University and [3]Institute of Brain Diseases, Tohoku University School of Medicine, Sendai, Japan

(*Received* 17 *July* 1988)

The feasibility of 2-deoxy-2-[^{18}F]fluoro-D-galactose ([^{18}F]FdGal) for imaging galactose metabolism in tumors with positron emission tomography (PET), was investigated using two hepatomas, Yoshida sarcoma, or glioma in rats, and mouse mammary carcinoma. In hepatoma-bearing rats the highest uptake of [^{18}F]FdGal was observed in the liver followed by the kidney and tumor. The tumor uptake increased with time, and the high uptake ratios of tumor to organ were observed except for the liver and kidney. Tumor uptake was also measured in all tumors. As main metabolites in all tumors, [^{18}F]FdGal 1-phosphate and UDP-[^{18}F]FdGal were found by HPLC. Two hepatomas showed a slightly higher uptake and a larger percentage of UDP derivative than the other three tumors. By autoradiography the brain tumor was visualized clearly. These results indicate that [^{18}F]FdGal has potential as a tracer for imaging galactose metabolism in tumors with PET.

Introduction

Recent experimental and clinical studies of tumors using positron-emitting radiopharmaceuticals and PET have opened a new methodology in cancer diagnosis (Beaney, 1984). As metabolic substrates [^{11}C]glucose and 2-deoxy-2-[^{18}F]fluoro-D-glucose ([^{18}F]FDG) are useful for measuring glucose utilization (Beaney, 1984; Patronas *et al.*, 1985; Paul *et al.*, 1986; Joensuu and Ahonen, 1987; Di Chiro *et al.*, 1987), and ^{11}C-labeled L-amino acids for measuring amino acid utilization and/or protein synthesis rate (Beaney, 1984; Kubota *et al.*, 1985; Lilja *et al.*, 1985; Bustany *et al.*, 1986; Bergstron *et al.*, 1987; Bolster *et al.*, 1986). Fluorine-18-labeled pyrimidine is correlated to the nucleic acid metabolism (Abe *et al.*, 1985). Besides the metabolic substrates, several other positron-emitting tracers have been applied to tumor studies in connection with the altered transport or permeability of substrates through cell membrane of tumors (Beaney, 1984). Ligands for receptors in the tumors are another candidate (Brandes *et al.*, 1987). The use of several positron-emitting radiopharmaceuticals in tumor diagnosis with PET enables one to characterize the metabolic function of the tumors. Consequently it could be possible to measure the viability of tumor tissue before and after treatment and to estimate the validity of protocols of the treatment.

Flourine-18 labeled 2-deoxy-2-fluoro-D-galactose ([^{18}F]FdGal) has been developed for measuring galactose metabolism in the liver with positron emission tomography (PET) (Tada *et al.*, 1984, 1987; Fukuda *et al.*, 1985, 1986, 1987a, b, c; Matsuzawa *et al.*, 1985; Ishiwata *et al.*, 1988). The [^{18}F]FdGal is taken by the liver at the highest level, and is phosphorylated to 2-deoxy-2-[^{18}F]fluoro-D-galactose 1-phosphate ([^{18}F]-FdGal-1-P) by galactokinase. Compared to the metabolism of [^{18}F]FDG, which is trapped in the phosphate derivative in the tissue (Gallagher *et al.*, 1978), the different metabolic fate of the [^{18}F]FdGal is observed (Ishiwata *et al.*, 1988). The [^{18}F]-FdGal-1-P is further converted to UDP-2-deoxy-2-[^{18}F]fluoro-D-galactose (UDP-[^{18}F]FdGal) by UDP-

*Author for correspondence.

glucose:galactose-1-phosphate uridyltransferase. The trapping of [^{18}F]FdGal by the phosphate and uridylate forms are also observed in the brain, heart, spleen, lung, small intestine and kidney. The metabolism of [^{18}F]FdGal proceeds via the UDP-galactose synthetic pathway. The presence of enzymes concerning this pathway is confirmed in all animal tissues (Ballard, 1966; Noltman, 1972; Wallenfels and Weil, 1972). In the tissue the UDP-galactose is transferred to UDP-glucose by UDP-glucose 4-epimerase, and is introduced into the glucose metabolism. This pathway is expected to be predominant in the liver. In clinical studies with PET, a high accumulation of the [^{18}F]FdGal was observed in the normal liver, while the accumulation was much lower in the cirrhotic liver (Fukuda *et al.*, 1985, 1987c). Preliminarily, a high uptake of [^{18}F]FdGal was also measured in hepatocellular carcinoma with PET (Fukuda *et al.*, 1985, 1987c) and an experimental hepatoma (Matsuzawa *et al.*, 1985).

On the other hand, the UDP-galactose has a role as a galactose donor to oligosaccharide, glycoprotein and glycolipid. The significance of UDP-galactose in the glycoprotein synthesis in the cell membrane is indicated in tumors (Kalcker, 1965; Mitchell *et al.*, 1975). These findings prompted us to investigate further the tumor studies using [^{18}F]FdGal. In this paper we compare the tumor accumulation and metabolism of [^{18}F]FdGal in two experimental hepatomas in rats and three kinds of other tumors in rats or mice.

Materials and Methods

[^{18}F]FdGal was synthesized by the reaction of $CH_3COO^{18}F$ and tri-O-acetyl-D-galactal as described previously (Tada *et al.*, 1987; Ishiwata *et al.*, 1988).

Donryu rats with hepatoma, AH109A and AH272, and with Yoshida sarcoma, YS and C3H/He mice with mammary carcinoma, FM3A, were prepared as described previously (Ishiwata *et al.*, 1985). Wistar rats with brain tumor, glioma KEG-1 (Kaneko *et al.*, 1980), were prepared by the method of Tsurumi *et al.* (Tsurumi *et al.*, 1984). The KEG-1 tumor cells were also inoculated subcutaneously on the back of the same rats.

Tumor accumulation of [^{18}F]FdGal

Male Donryu rats with AH109A were injected with 30 μCi of [^{18}F]FdGal through a lateral tail vein. The rats were sacrificed by cervical dislocation at 10, 30, 60 and 120 min after injection. Blood was removed by heart puncture using a syringe. The tumor, brain, heart, lung, liver, kidney and muscle were dissected and washed with physiological saline. The tissues were counted for ^{18}F and weighed. The tissue uptake was expressed as differential absorption ratio (DAR), (counts of tissue/total injected counts) × (g body weight/g tissue), to correct the data for body weight of rats and mice.

Metabolic studies

For metabolic studies rats and mice were injected i.v. with [^{18}F]FdGal. The injected doses of [^{18}F]FdGal were 3–5 mCi and 0.6–1.5 mCi for rats and mice, respectively. The animals were sacrificed at 60 min after injection and the tumor uptake was measured as described as above. Analysis of metabolites was carried out by high-performance liquid chromatography (HPLC) as described in a previous paper (Ishiwata *et al.*, 1988). The tumor tissues were treated with $HClO_4$, and the metabolites in the acid-soluble fraction were analyzed by HPLC. An anion-exchange column, Radial-PAK SAX (Waters Associates), was used with 0.1 M sodium acetate, pH 4.1, containing 0.15 M NaCl as eluent.

Autoradiography of brain tumor

Wistar rats bearing KEG-1 tumor were sacrificed at 60 min after i.v. injection of 5 mCi [^{18}F]FdGal. The brain was removed, frozen on dry ice and cut into 40 μm-thick slices using an autocryotome. The slices were dried at 40°C on a hot-plate. An x-ray film (NMC-1, Eastman Kodak) was exposed on these slices and then developed. The same slice was stained with hematoxylin and eosin. Autoradiograms were scanned with a Chromoscan 3 (Joyce-Loeble). The data were digitized and the density of radioactivity in the region of interest was measured.

Results

The results of tissue distribution of [^{18}F]FdGal in AH109A-bearing rats are represented in Fig. 1. Blood clearance of radioactivity was rapid. The highest uptake was observed in the liver followed by the

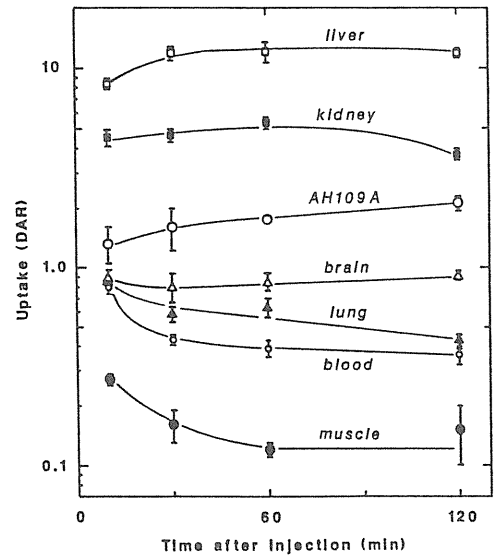

Fig. 1. Tissue distribution of radioactivity after i.v. injection of 2-deoxy-2-[^{18}F]fluoro-D-galactose in rats bearing AH109A tumor.

Table 1. Tumor accumulation and metabolites at 60 min after i.v. injection of 2-deoxy-2-[^{18}F]fluoro-D-galactose ([^{18}F]FdGal)

Tumor	No.	Uptake (DAR)	Metabolites* [^{18}F]FdGal (%)	[^{18}F]FdGal-1-P (%)	UDP-[^{18}F]FdGal (%)
AH109A	4	1.75 ± 0.12	7.2 ± 1.6	64.9 ± 2.1	17.4 ± 1.3
AH272	3	1.86 ± 0.21	7.2 ± 2.2	75.7 ± 3.6	14.8 ± 2.2
KEG-1	4	1.55 ± 0.41	9.4 ± 2.2	76.9 ± 3.6	9.1 ± 1.3[a,b]
YS	4	1.15 ± 0.30[b,b']	11.7 ± 4.1	80.5 ± 4.1	6.7 ± 3.8[a,b']
FM3A	3	1.40 ± 0.09[b,d']	3.0 ± 0.3	86.4 ± 1.2	9.4 ± 1.3[a,c']
Liver†			2.7 ± 0.1	36.4 ± 4.6	60.5 ± 3.2
Brain†			6.8 ± 0.5	76.9 ± 3.9	25.8 ± 0.6

*Percentage of each peak was normalized as total recovered ^{18}F to be 100%. Small amounts of unknown materials with smaller retention times than the [^{18}F]FdGal-1-P were detected.
†Reference: Ishiwata *et al.*, 1988.
Data indicate an average of three or four rats. Error is ±SD.
Student's *t*-test was carried out: [a]$P < 0.001$; [b]$P < 0.01$ (compared to AH109A); [b']$P < 0.01$; [c']$P < 0.02$; [d']$P < 0.05$ (compared to AH272).

kidney and AH109A tumor. The radioactivity increased with time in the liver and AH109A, and decreased in the lung and muscle. The uptake in the brain remained constant for 120 min. The uptake ratio of tumor to tissue increased with time, and the uptake ratios of tumor-to-brain, tumor-to-blood and tumor-to-muscle were 2.0, 4.4 and 15 at 60 min after injection.

In Table 1 the accumulation of [^{18}F]FdGal in five tumor tissues are summarized at 60 min after injection. To compare the data obtained from rats and mice, the uptake is corrected for body weight. Although the injected amounts of the [^{18}F]FdGal in the metabolic study were over 100 times higher than the amounts used in the tissue distribution study, the similar high uptake of radioactivity (DAR) was measured in the AH109A tumor. KEG-1, FM3A and YS tumor tissues showed a slightly lower accumulation than AH109A and AH272. Compared to the metabolism of [^{18}F]FdGal in the liver and brain, the different metabolic fate was observed. Figure 2 shows a radio-HPLC chromatogram of metabolites in the acid-soluble fraction of AH109A tissue. Five components were detected. The [^{18}F]FdGal, the peak *a*, has no retention time on an anion-exchange column. The peaks *d* and *e* were identified to be [^{18}F]FdGal-1-P and UDP-[^{18}F]FdGal, respectively. The peaks *b* and *c* were not identified. In the other four tumor lines the predominant metabolites were also [^{18}F]FdGal-1-P and UDP-[^{18}F]FdGal at 60 min after injection. The proportions of the main three components are also represented in Table 1. The summed percentage of minor components was 10.5, 2.3, 4.6, 1.1 and 1.2% for AH109A, AH272, KEG-1, YS and FM3A, respectively. The radioactivity in the acid-precipitable fraction was less than 1% of the total radioactivity in tumor tissue. The ratios of the uridylate form in tumor tissues is smaller than those in the liver and brain. In two hepatoma tissues the ratios of uridylate form were larger than in KEG-1, YS and FM3A tissues.

By autoradiography, the higher accumulation of radioactivity in KEG-1 tumor was clearly visualized from the surrounding brain tissue. Three cases are presented in Fig. 3. The density of radioactivity in several regions of tumor and normal brain was measured. The relative density in the regions was expressed as the ratio to the normal cortex. The results are summarized in Table 2. In the first case, Fig. 3(A), the high density of ^{18}F was coincident with the regions deeply stained with hematoxylin and eosin, and the different regional distribution in the tumor was recognized. No accumulation of ^{18}F was

Table 2. Regional distribution of radioactivity in brain section of rats with glioma, KEG-1, at 60 min after i.v. injection of 2-deoxy-2-[^{18}F]fluoro-D-galactose

Region	Relative density of ^{18}F* Case A	Case C	Case D
1 Cortex	1.00	1.00	1.00
2 Striatum	0.80		0.84
3 Amygdaloid cortex		0.74	
4 Hippocampus		0.75	
5 Thalamus		0.95	
6 Hypothalamus		0.73	
7 Corpus callosum		0.74	
8 Tumor region	1.49	1.70	1.40
9 Tumor region	1.47	1.65	1.36
10 Tumor region	1.22	1.54	1.21

*The relative density in the individual region is presented as the density in the cortex, region 1, to be 1.00.

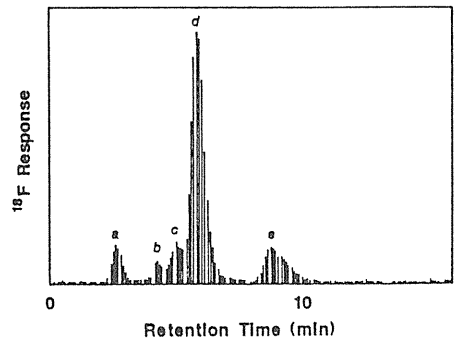

Fig. 2. High-performance liquid chromatography of ^{18}F-labeled metabolites in AH109A tumor tissue on a Radial-PAK SAX column after injection of 2-deoxy-2-[^{18}F] fluoro-D-galactose. The peaks *a*, *d* and *e* are identified to be [^{18}F]FdGal, [^{18}F]FdGal-1-P and UDP-[^{18}F]FdGal, respectively (Ishiwata *et al.*, 1988).

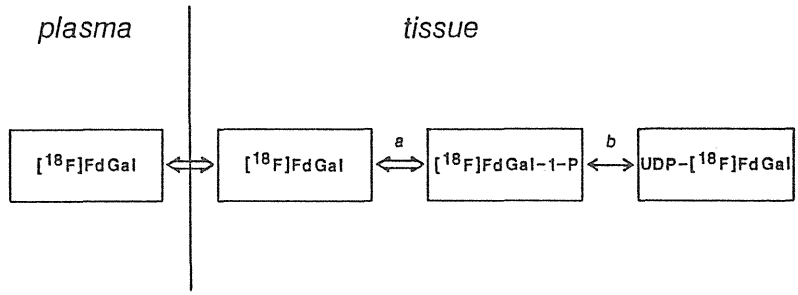

Fig. 4. Metabolic model of 2-deoxy-2-[^{18}F]fluoro-D-galactose in the liver, tumor and other tissues. *a*: galactokinase; *b*: UDP-glucose:galactose-1-phosphate uridyltransferase.

shown in the central necrotic region. In the other two cases without a necrotic region, the nonuniformity of the ^{18}F distribution in tumor was also observed. In the normal brain tissue a different regional distribution showed the highest density in the cortex. The uptake ratios of tumor to cortex were 1.21 to 1.70.

Discussion

Fluorine-18 labeled FdGal has been developed for the purpose of functional imaging of the liver with PET (Tada *et al.*, 1984, 1987; Fukuda *et al.*, 1985, 1986, 1987a, b, c; Matsuzawa *et al.*, 1985; Ishiwata *et al.*, 1988). In the liver and other tissues, the radioactivity is trapped by the phosphate and uridylate forms according to the galactose metabolic pathway, and further metabolism is inhibited substantially (Ishiwata *et al.*, 1988). In the liver the transfer of galactose into glucose metabolism by this UDP-galactose pathway may be a predominant metabolic pathway. On the other hand, this pathway is significant in the glycoprotein synthesis in the tumor cells (Kalcker, 1965; Mitchell *et al.*, 1975). In adult animals UDP-galactose is supplied by the interconversion of UDP-glucose to UDP-galactose. The reaction is catalyzed by UDP-galactose 4-epimerase, the activity of which is significantly enhanced in the hepatoma (Reutter and Bauer, 1978). From these points of view, the [^{18}F]FdGal was applied to several kinds of experimental tumors.

As indicated in the preliminary study using AH109A-bearing rats (Matsuzawa *et al.*, 1985), in all tumors investigated a high uptake of radioactivity was observed. The metabolism of [^{18}F]FdGal, summarized in Fig. 4, results in the trapping of [^{18}F]FdGal as the phosphate and uridylate forms as observed in the liver and other tissues (Ishiwata *et al.*, 1988). However, compared to the metabolism in the liver and brain, in the tumor tissue the phosphate form is a predominant metabolite, and the proportion of UDP-[^{18}F]FdGal is much smaller. The metabolism of [^{18}F]FdGal is possibly due to the presence of galactokinase and UDP-glucose:galactose-1-phosphate uridyltransferase. As minor unidentified metabolites, two components, peaks *b* and *c* in Fig. 2, were found. Peak *b* may correspond to a very small amount of unknown component in the liver (Ishiwata *et al.*, 1988). The finding of these metabolites indicates a complicated metabolism of the [^{18}F]FdGal in tumor tissue compared to the liver tissue. It is pointed out that the interconversion of UDP-[^{18}F]FdGal to UDP-[^{18}F]FDG is uncertain in our HPLC analysis as indicated in the previous paper (Ishiwata *et al.*, 1988), although the incorporation of [^{18}F]FdGal into macromolecules was substantially inhibited.

Among five tumors different characteristics were observed. Two hepatomas, AH109A and AH272, showed a slightly higher uptake than glioma, Yoshida sarcoma and mammary carcinoma. Also in these hepatomas the proportions of uridylate derivative were larger than in the other three tumors. These results may be explained as follows: the hepatoma has a high activity of galactose metabolism inherent in the host liver tissue. In the literature the galactokinase activity in Morris hepatoma was nearly equal to the activity in the host liver tissue, although both the concentration of UDP-galactose and the uridyltransferase activity were reduced to a fourth or to a half (Reutter and Bauer, 1978). It is possible that the PET study using [^{18}F]FdGal differentiates the hepatoma from other kinds of tumors. This expectation was demonstrated by the preliminary PET studies in patients with hepatocellular carcinoma (Fukuda *et al.*, 1987c). The application of [^{18}F]FdGal to hepatomas will be discussed in detail in another report. On the other hand, the uptake in KEG-1, FM3A and YS indicates that [^{18}F]FdGal is also suitable for the imaging of tumors other than hepatoma, especially when located in the regions of the head, neck and chest. The distinct regional distribution of radioactivity in KEG-1 by autoradiography [Fig. 3(A)] represents the image of galactose metabolism rather than the breakdown of the blood–brain barrier. The brain images may also reflect the regional activity of the galactose metabolism. Further investigations are required to find out whether the uptake and metabolism of [^{18}F]FdGal is correlated to the biological activities of glycoconjugate synthesis and/or galactosyl transfer.

For the quantitative measurement of galactose metabolism with PET, a metabolic model is shown in

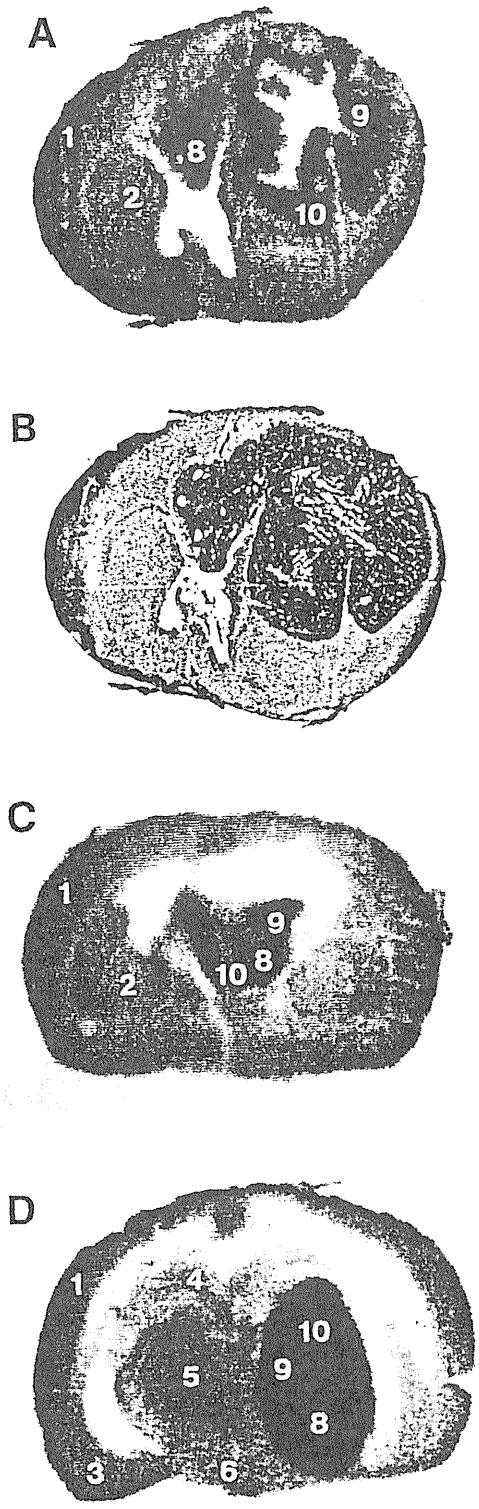

Fig. 3. Autoradiographic distribution of radioactivity in the coronal section of rat brain with KEG-1 tumor after injection of 2-deoxy-2-[^{18}F]fluoro-D-galactose. Figures (A), (C) and (D) present autoradiograms of the individual rat brain sections. (B) presents the hematoxyline-eosin staining of the same brain section used to obtain the autoradiogram in (A). The relative optical density in the regions 1 to 10 was measured, and the results are represented in Table 2.

Fig. 4. The pathway from [^{18}F]FdGal-1-P to UDP-[^{18}F]FdGal is significant in the liver. In tumor the contribution of this pathway is relatively small, while it is considerable in the hepatoma. Probably, the uptake of [^{18}F]FdGal in the tumors except for the hepatoma is mainly attributed to the activity of galactokinase, as the hexokinase is responsible for the accumulation of [^{18}F]FDG. The contribution of the pathway to minor metaoblites on the model is reasonably small based on the accuracy of PET.

In conclusion, uptake of [^{18}F]FdGal and the metabolic trapping of the phosphate and uridylate forms were confirmed in five tumor cell lines. Two hepatomas showed a higher uptake and a larger percentage of UDP derivative compared to the other three tumors. The [^{18}F]FdGal is promising as a tracer evaluating galactose metabolism for tumor diagnosis with PET.

Acknowledgements—This work was supported by a Grant-in-Aid for Cancer Research No. 62010034 from the Ministry of Education, Science and Culture, Japan. The authors are grateful to the cooperation of the staffs of Cyclotron and Radioisotope Center.

References

Abe, Y.; Matsuzawa, T.; Ito, M.; Fujiwara, T.; Yamaguchi, K.; Hatazawa, J.; Fukuda, H.; Kubota, K.; Sato, T.; Watanuki, S.; Ido, T.; Ishiwata, K.; Monma, M. Cancer detection with ^{18}F-5-fluorodeoxyuridine—A new cancer diagnostic agent reflecting the nucleic acid metabolism. *Jpn. J. Nucl. Med.* 22: 583–586; 1985 (in Japanese).

Ballard, F. J. Purification and properties of galactose kinase from pig liver. *Biochem. J.* 98: 347–352; 1966.

Beaney, R. P. Positron emission tomography in the study of human tumors. *Semin. Nucl. Med.* 14: 324–341; 1984.

Bergström, M.; Ericson, K.; Hagenfeldt, L.; Mosskin, M.; von Holst, H.; Norén, G.; Eriksson L.; Ehrin, E.; Johnström, P. PET study of methionine accumulation in glioma and normal brain tissue; Competition with branched chain amino acids. *J. Comput. Assist. Tomogr.* 11: 208–213; 1987.

Bolster, J. M.; Vaalburg, W.; Paans, A. M. J.; van Dijk, T. H.; Elsinga, P. H.; Zijlstra J. B.; Piers, D. A.; Mulder, N. H.; Woldring, M. G.; Wynberg, H. Carbon-11 labelled tyrosine to study tumor metabolism by positron emission tomography (PET). *Eur. J. Nucl. Med.* 12: 321–324; 1986.

Brandes, S. J.; Katzenellenbogen, J. A. Fundamental considerations in the design of fluorine-18 labeled progestins and androgens as imaging agents for receptor-positive tumors of the breast and prostate. *Nucl. Med. Biol.* 15: 53–67; 1987.

Bustany, P.; Chatel, M.; Derlon, J. M.; Darcel, F.; Sgouropoulos, P.; Soussaline, F.; Syrota, A. Brain tumor protein synthesis and histological grades: A study by positron emission tomography (PET) with C11-L-methionine. *J. Neuro-Oncol.* 3: 397–404; 1986.

Di Chiro, G.; Hatazawa, J.; Katz, D. A.; Rizzoli, H. V.; De Michele, D. J. Glucose utilization by intracranial meningiomas as an index of tumor aggressivity and probability of recurrence: A PET study. *Radiology* 164: 521–526; 1987.

Fukuda, H.; Yamaguchi, K.; Matsuzawa, T.; Abe, Y.; Yamada, K.; Yoshioka, S.; Ito, M.; Fujiwara, T.; Tada, M.; Watanuki, S.; Ido, T. Imaging of hepatoma with 2-deoxy-2-[^{18}F]fluoro-D-galactose by positron emission tomography. In: *Proceedings of the International Symposium on Current and Future Aspects of Cancer Diagnosis with Positron Emission Tomography (PET 85)*, Sendai, Japan, 1985; 24–27.

Fukuda, H.; Matsuzawa, T.; Tada, M.; Takahashi, T.; Ishiwata, K.; Yamada, K.; Abe, Y.; Yoshioka, S.; Sato, T.; Ido, T. 2-Deoxy-2-[^{18}F]fluoro-D-galactose: A new tracer for the measurement of galactose metabolism in the liver by positron emission tomography. *Eur. J. Nucl. Med.* 11: 444–448; 1986.

Fukuda, H.; Yamaguchi, K.; Matsuzawa, T.; Abe, Y.; Yamada, K.; Yoshioka, S.; Sato, T.; Tada, M.; Ogawa, Y.; Takahashi, T.; Ido, T. 2-Deoxy-2-(^{18}F)fluoro-D-galactose: A new tracer for the evaluation of liver function by PET. I. Evaluation of toxicity and radiation dose. *Jpn. J. Nucl. Med.* 24: 165–169; 1987a (in Japanese).

Fukuda, H.; Yamaguchi, K.; Matsuzawa, T.; Itoh, M.; Abe, Y.; Fujiwara, T.; Yamaguchi, T.; Miyazawa, H.; Kawai, H.; Matsui, H.; Ishiwata, K.; Ido, T. 2-Deoxy-2-[^{18}F] fluoro-D-galactose: A new probe for the evaluation of liver function by PET. II. A first clinical PET study of the liver in normal volunteers. *Jpn. J. Nucl. Med.* 24: 871–874; 1987b (in Japanese).

Fukuda, H.; Yamaguchi, K.; Matsuzawa, T.; Abe, Y.; Fujiwara, T.; Ito, M.; Tada, M.; Ido, T. Imaging hepatocellular carcinoma with 2-deoxy-2-[F-18]fluoro-D-galactose using PET. *J. Nucl. Med.* 28: 706; 1987c (Abstract).

Gallagher, B. M.; Fowler, J. S.; Gutterson, N. I.; MacGregor, R. R.; Wan, C.-N.; Wolf, A. P. Metabolic trapping as a principle of radiopharmaceutical design: Some factors responsible for the biodistribution of [^{18}F]2-deoxy-2-fluoro-D-glucose. *J. Nucl. Med.* 19: 1154–1161; 1978.

Ishiwata, K.; Ido, T.; Abe, Y.; Matsuzawa, T.; Murakami, M. Studies of ^{18}F-labeled pyrimidines III. Biochemical investigation of ^{18}F-labeled pyrimidines and comparison with ^{3}H-deoxythymidine in tumor-bearing rats and mice. *Eur. J. Nucl. Med.* 10: 39–44; 1985.

Ishiwata, K.; Ido, T.; Imahori, Y.; Yamaguchi, K.; Fukuda, H.; Tada, M.; Matsuzawa, T. Accumulation of 2-deoxy-2-[^{18}F]fluoro-D-galactose in the liver by phosphate and uridylate trapping. *Nucl. Med. Biol.* 15: 271–276; 1988.

Joensuu, H.; Ahonen, A. Imaging of metastases of thyroid carcinoma with fluorine-18 fluorodeoxyglucose. *J. Nucl. Med.* 28: 910–914; 1987.

Kalckar, H. M.; Galactose metabolism and cell "sociology". *Science* 150: 305–313; 1965.

Kaneko, S.; Abe, H.; Aida, T.; Tsuru, M.; Kodama, T.; Kobayashi, H. Experimental study of immunochemotherapy of brain tumors. Experimental brain tumor model and immunochemotherapy by a combination of PS-K and ACNU. *Neurol. Med. Chir. (Tokyo)* 20: 997–1105; 1980 (in Japanese).

Kubota, K.; Matsuzawa, T.; Ito, M.; Ito, K.; Fujiwara, T.; Abe, Y.; Yoshioka, S.; Fukuda, H.; Hatazawa, J.; Iwata, R.; Watanuki, S.; Ido, T. Lung tumor imaging by positron emission tomography using C-11 L-methionine. *J. Nucl. Med.* 26: 37–42; 1985.

Lilja, A.; Bergström, K.; Hartvig, P.; Spännare, B.; Halldin, C.; Lundqvist, H.; Långstrom, B. Dynamic study of supratentorial gliomas with L-methyl-^{11}C-methinine and positron emission tomography. *Am. J. Neuro. Rad.* 6: 505–514; 1985.

Matsuzawa, T.; Fukuda, H.; Abe, Y.; Fujiwara, T.; Yamaguchi, K.; Ito, M.; Kubota, K.; Hatazawa, J.; Ito, K.; Sato, T.; Fares, Y.; Watanuki, S.; Sugawara, Y.; Tada, M.; Komatsu, K.; Ido, T.; Iwata, T.; Ishiwata, K.; Takahashi, T.; Monma, M. Current and future aspects of cancer diagnosis with positron emission tomography: Biological and clinical aspects. In: *Proceedings of the International Symposium on Current and Future Aspects of Cancer Diagnosis with Positron Emission Tomography (PET 85)* Sendai, Japan, 1985; 1–23.

Mitchell, B.; Haigis, E.; Steinmann, B.: Gitzelmann. Reversal of UDP-galactose 4-epimerase deficiency of human leukocytes in culture. *Proc. Natl. Acad. Sci. USA* 72: 5026–5030; 1975.

Noltman, E. A. Aldose-ketose isomerases. In: Boyer, P. D., editor. *The Enzymes* 3rd edn, Vol. 6. New York: Academic Press; 1972: 271–352.

Patronas, M. J.; Di Chiro, G.; Kufta, C.; Bairamian, D.; Kornblith, P. L.; Simon, R.; Larson S. M. Prediction of survival in glioma patients by means of positron emission tomography. *J. Neurosurg.* 62: 816–822; 1985.

Paul, R.; Roeda, D.; Johansson, R.; Ahonen, A.; Haaparanta, M.; Solin, O.; Sipilä, H. Scintigraphy with [^{18}F]2-fluoro-2-deoxy-D-glucose of cancer patients. *Nucl. Med. Biol.* 13: 7–12; 1986.

Reutter, W.; Bauer, C. Terminal sugars in glycoconjugates: Metabolism of free and protein-bound L-fucose, N-acetylneuramic acid and D-galactose in liver and Morris hepatomas. *Adv. Exp. Med. Biol.* 92: 405–437; 1978.

Tada, M.; Matsuzawa, T.; Ohrui, H.; Fukuda, H.; Ido, T.; Takahashi, T.; Shinohara, M.; Komatsu, K. Synthesis of some 2-deoxy-2-fluoro[^{18}F]hexopyranoses, potential diagnostic imaging agents. *Heterocycles* 22: 565–568; 1984.

Tada, M.; Matsuzawa, T.; Yamaguchi, K.; Abe, Y.; Fukuda, H.; Itoh, M.; Sugiyama, H.; Ido, T.; Takahashi, T. Synthesis of ^{18}F-labeled 2-deoxy-2-fluoro-D-galactopyranoses using acetyl hypofluorite procedure. *Carbohydr. Res.* 161: 314–317; 1987.

Tsurumi, Y.; Kameyama, M.; Shirane, R.; Katakura, R.; Suzuki, J. The uptake of ACNU in the experimental brain tumor and the effect of induced hypertension. *CYRIC Annual Report (Tohoku University)* 1984: 217–219.

Wallenfels, K.; Weil, R. β-Galactosidase. In: Boyer, P. D., editor *The Enzymnes* 3rd Edn, Vol. 7. New York: Academic Press; 1972: 617–663.

平成元年度　第１回粒子線治療研究委員会

議　事　概　要

日　時：平成元年７月15日（土）10時30分～15時

場　所：霞山会館

出席者：恒元　博委員長，田崎瑛生，末桝恵一，入江五朗，　鎌田力三郎，辻井博彦，橋本省三，森田皓三，井上俊彦，春日　孟，坂本澄彦，鈴木紀夫，稲田哲雄，伊藤　彬，入江　実，梅垣洋一郎，川島勝弘，大原　弘，飯沼　武，青木芳朗，森田新六，近藤龍雄、各委員

説明者及びオブザーバー：平岡　武，安藤興一，丸山隆司，山崎統四郎，　坂下邦雄，久保田進，中村　譲，富谷武浩，河内清光，遠藤真広，中野隆史，野原功全，福田　寛，本間　清（以上放医研）

配布資料：1.粒子線治療研究委員会規程及び粒子線治療研究委員会名簿

2.特別研究「重粒子線によるがん治療法に関する調査研究」研究計画

議事概要

1．経過報告

a）委員長より、平成元年度から新たに特別研究「重粒子線によるがん治療法に関する調査研究」が実行されることになり、その内容が紹介され、併せて「重粒子線医療準備チーム」が編成され、臨床試行の実施体制を検討することになったことが報告された。

b）企画課長より、特別研究並びに重粒子線がん治療装置製作に関連する平成元年度の予算が紹介された。

2．研究計画

特別研究のグループリーダーより、平成元年度における研究計画が紹介された。

研究の成果は　平成２年３月に報告される予定である。

a）重粒子線治療のための物理・生物学的基礎研究：

放医研と理化学研究所との間で進められていた重粒子線の医学・生物学研究に関する共同研究契約が平成元年３月にまとまった。本年度には研究に必要な理研重イオンビームポートの整備が行われる予定である。理研のビームポートを用いて行われる物理・生物学研究の成果は、重粒子線照射に必要なデグレーダーの設計に役立てられる予定である。

b）重粒子線治療における核医学に関する基礎的研究：

ポジトロン標識リガンドを用いて放射線照射によるレセプターの機能変化を測定し、放射線損傷を定量的に評価することを再重点課題として研究が進められる。

c）重粒子線治療に関する臨床的研究：

速中性子線治療と陽子線治療の臨床成績を評価するとともに、dose-volume histogram 法に

よって組織が受ける放射線量を積算することにより、重粒子線治療の適応を線量分布の面から評価する方法を開発する研究が重点となる。

d）重粒子線治療の総合的調査研究：

臨床トライアルに必要な前臨床的基礎研究を総合調整して研究を効率化し、国内外の研究協力に関し、基本となる研究方針が討議される。

3．討　　議

研究計画に関して、

a.研究協力体制の制度化

b.速中性子線等粒子線が有効な症例の受け入れ体制

c.標的容積の診断方法

等につき充実した討議が行われた。

平成元年度第１回重粒子線がん治療装置
建設委員会議事概要

１．日　時　　平成元年10月17日（火）14：00～16：30

２．場　所　　放医研　第一会議室

３．出席者　　平尾委員長，恒元副委員長，高橋，永田，有澤，川島，松本，大原，小川，
佐藤（健），河内，黒沢（以上委員）
井上，山田（聰），遠藤，佐藤（幸）（以上オブザーバー）

４．配布資料

1）平成元年度 重粒子線がん治療装置建設委員会 委員名簿
2）昭和63年度 第１回重粒子線がん治療装置建設委員会議事概要
3）昭和63年度 第１回～第３回 加速器システム部会議事概要
4）昭和63年度 第１回治療システム部会議事概要
5）昭和63年度 第１回～第３回建屋建設部会議事概要
6）重粒子線がん治療装置建設スケジュール（案）

５.議事概要

(1) 委員長より、重粒子線がん治療装置建設委員会組織構成及び平成元年度委員について説明があった。

(2) 昭和63年度第１回議事概要の確認を行い、字句の修正を行って了承された。

(3) 重粒子線がん治療装置建設の状況報告

a）昭和63年度各部会の報告

① 昭和63年度第１回～第３回加速器システム部会について、山田（聰）氏より議事概要を基に説明があった。

② 昭和63年度第１回治療システム部会について、遠藤氏より議事概要を基に説明があった。

③ 昭和63年度第１回～第３回建屋建設部会について、佐藤（幸）氏より議事概要を基に説明があった。

④ 昭和63年度第１回及び第２回装置製作総合検討部会について、河内委員より議事概要を基に説明があった。

b)装置製作進捗状況の報告

① 入射器系については山田（聰）主任研究官より説明があった。その内容は、

・入射器系の製作は、第３タンクの組立がほぼ終了する段階にあり、他の機器の製作も順調に進行している。

・平成２年度中には製作を終了する計画であったが、予算の執行上、また建屋建設計

画との整合をはかるため、国庫債務負担の期限を1年延長する話が進められている。

・イオン源では、ＰＩＧイオン源のＲ＆Ｄでかなり良い結果を得ており、別途高原子番号Ｓｉ，Ａｒ等のイオン強度を上げるため、東大核研並びに東工大と共同で、ＥＣＲイオン源のＲ＆Ｄを進めている。

国庫債務負担の期間延長により、全体計画の遅れがないようにして欲しいと委員から要望があった。

② 主加速器については、佐藤（健）委員より説明があった。

・各コンポーネントの配置がほぼ固定してきており、担当の日立、東芝間で、数㎜程度の取り合い等を調整している段階である。

・Ｒ＆Ｄについては、昭和63年度発注のビーム入射試験装置で本体に組み込むべき一部が製作されている。

・電源等は、シンクロトロンの運転パターン等の検討を進め、必要電力量等がかなり詰まってきた。

・無効電力補償装置を含め、建屋電源設備と密接な関係があり、今後詳細な打合せを放医研、関東地建並びに現場の担当者間で進めることゝした。

③ビーム輸送系については、小川委員より説明があった。

・ビーム輸送系は、本年度から５年間の国庫債務負担で契約することになっているが、予算的に大きな開きがあったため遅れている。

・ビーム光学計算等の再検討を行い、電磁石の磁極間隔等を詰める等努力してきたが、未だ厳しい状況にある。

・冷却水系は、主加速器並びにビーム輸送系等の努力により多少縮小傾向にあり、当初計画より10数％つめた値で検討している。

④照射系については、河内委員より説明があった。

・照射系に関しては平成２年度の契約になるが、輸送系とも密接に関連してくる所があり、総合的に詰めを行っている。

・各種機器については、多葉コリメータ走査電磁石電源、患者位置決め装置等のＲ＆Ｄを始めている。

(4) 建屋建設の進捗状況

建屋建設の進捗状況については、建設スケジュール（案）に沿って高橋委員より説明があった。

・建屋建築工事は、基礎工事の内、土工事がほぼ終わりに達している。この後ステコンをし、防水を行い、耐圧盤工事が行われる。

・躯体工事が引き続き発注され、地下２階より順次工事が行われる。

・設備工事のうち電気工事は２社ＪＶ、通信工事は１社、また機械工事の内空調工事は２社ＪＶ、衛生工事は１社に発注すべく作業を進めている。

・全体として、スケジュールに沿って早目に進めるよう努力しているが、大幅に短縮することは難しい。

装置の工程表は問題なく実施可能かとの質問に対して、平成３年度末からの搬入・据付が一時期に集中している点が厳しい。平成５年度の臨床試行を実現させるためには、搬入開始時期が早まることが必要である旨が述べられた。

(5) その他

装置完成後の運営が円滑に行えるように、研究所としては、

1．重粒子線医療準備チーム

2．重粒子線がん治療装置運営保守検討委員会

を発足させ、中味の検討を始めている。

平成元年度第２回粒子線治療研究委員会

議　事　概　要

日　時　平成２年３月９日（金）13：00～16：00

場　所　東京ガーデンパレス

出席者　恒元委員長，田崎，溝江（入江代），柄川，浦橋（鎌田代），山下（橋本代），森田（皓），井上，春日，増田，鈴木，稲田，梅垣，入江（実），川島，大原，舘野，飯沼，森田（新），近藤　各委員

説明者及びオブザーバー

設楽（東大脳外），河内，金井，遠藤，丸山，富谷，山崎，安藤，宮本，中野，丑山，河合

配布資料

１．研究成果に関する資料

ａ．重粒子線治療のための物理・生物学に関する基礎的研究

ｂ．重粒子線治療における核医学に関する基礎的研究

ｃ．重粒子線治療に関する臨床的研究

ｄ．重粒子線がん治療研究の総合評価に関する調査

２．重粒子線治療ネットワーク会議（案）

議事概要

１．研究成果に関する報告

ａ．重粒子線治療に関する物理的研究の分野では、電離箱法によって吸収線量を評価する場合の精度の全不確定度は７％程度であることが確認された。

一方、放射線防護に関する研究は、ＬＢＬ、理化学研究所に出向いて実験を行い、基礎的データーが集積されている。

重粒子線治療の基礎研究を進めるために必要な理研ビームポートの整備は平成２年度後半のビーム利用を目標に進められている。

生物学的研究の分野では、ヒト由来の唾液腺腫瘍の放射線感受性、並びにカーボン、ヘリウムイオンによるＶ－７９細胞の放射線感受性に関する研究が進んでいる。

ｂ．放射線治療の効果と正常組織の損傷を in vivo の画像を用いて評価しようとする試みが核医学基礎研究グループの目標である。今年度は N-methylpiperidyl ester に ^{11}C 標識した薬剤等を用いて研究が行われた。

一方、ラジオアクティブビームを用いて行われる治療について、検出器のシュミレーション研究が行われている。

c．1989年12月までに速中性子線治療と陽子線治療を行った症例は、それぞれ1,805例と66例である。今年度に、パンスコースト腫瘍、耳下腺がん、悪性黒色腫の治療成績がそれぞれ分析された。

さらに、ＤＶＨ（dose volume histogram）法によって、線量分布の面から重粒子線治療の適応を追及する研究と、がんの標的容積を診断するための精度向上を目指す研究も進められた。

2．重粒子線がん治療装置の建設に必要な掘削工事が平成元年10月に終了したことと加速器の製作現況が紹介された。

3．重粒子線治療ネットワークの会議（案）が紹介され、重粒子線治療の進め方等について討議が行われた。

平成元年度第１回短寿命及び陽電子ＲＩの医学利用に関する研究委員会議事概要

日　時：平成元年10月12日（木）14：00～17：00

場　所：東京ガーデンパレス　華の間

出席者：（委員）、安東（（財）実験動物中央研究所）、黒沢（塩野義製薬）、野崎（北里大学）、葉杖（日本メディフィックス）、福田（日本大学）、増田（千葉大学）、町野（上智大学）、樫田（放医研）、野原（放医研）、松本（放医研）、山崎（放医研）、鈴木（近藤代理、放医研）

（オブザーバー）田中、伊藤、西尾、伊豫、福田、須原、井上、入江、玉手、遠藤、篠遠、加賀谷、米澤

配布資料：

1．臨床研究計画書
2．説明書および承諾書
3．サルＰＥＴ研究計画書（１）、（２）
4．短寿命委員会規定
5．短寿命委員会名簿

報告事項、その他：

1．山崎委員より、舘野委員長が出席できない旨報告があり、山崎委員が議長をつとめることとした。
2．山崎委員より、安東委員、町野委員、佐藤委員が今回から委員に加わったことが報告された。
3．山崎委員より、短寿命委員会規定の一部改正があったことが報告された。
4．山崎委員より放射薬剤の品質管理規準について、法改正などもあり、見直しを行っていること、次回の本委員会で、改正案の提出を考えているとの報告があった。

1．臨床研究計画および説明書・承諾書について

須原、山崎より、新規臨床研究計画について、研究の目的・内容および被験者への説明書・承諾書について説明があった。また、現在進行中の臨床研究課題についても、福田、須原、篠遠よりあらためて説明があった。

・増田委員より、心筋血流量測定の意義に関する補足説明があった。
・町野委員より、対象被験者の年令の範囲、責任能力の有無、検査中の被験者の観察の方法について質問があり、それぞれ回答があった。

以上の質疑応答の後、臨床研究計画が承認された。

2．サルＰＥＴ研究について

井上、入江より、サルを用いたＰＥＴ研究の目的、研究内容について説明があった。

・町野委員より、放射薬物剤を投与されたサルのその後の処置について質問があり、井上より飼育を続け再使用するとの回答があった。

・安東委員より、サルに対する注射法について助言があった。

以上の質疑応答の後、研究計画が承認された。

平成元年度第２回短寿命及び陽電子ＲＩの医学利用に関する研究委員会議事概要

日　時：平成２年３月22日（木）13：30～16：30

場　所：東京ガーデンパレス　須磨の間

出席者：委員長・舘野（放医研）

委員・安東（実中研）、大熊（国立神経・精神センター）、黒沢（塩野義製薬）、佐藤（千葉県立衛生短大）、寺尾（国立衛生試験所）、野崎（北里大学）、増田（千葉大学）、町野（上智大学）、飯沼（放医研）、樫田（放医研）、近藤（放医研）、野原（放医研）、山崎（放医研）

オブザーバー：田中（浜松ホトニクス）、伊藤、西尾、伊豫、福士、入江、福田、須原、鈴木、根本、篠遠（以上放医研）

配布資料：

1．サイクロトロン製造放射薬剤品質管理基準について
2．サイクロトロン製造放射薬剤品質管理基準（第２版、1981年）の一部改定および確認事項
3．新しい細菌試験法
4．新規臨床計画「11C-PK11195による脳腫瘍の診断および末梢臓器機能診断に関する研究」
5．研究計画の一部変更「ポジトロンＣＴを用いる薬物依存メカニズムの研究」
6．説明書・承諾書の一部変更「ドーパミンＤＩ受容体測定に関する説明書および承諾書」

舘野委員長の経過説明の後、以下の審議が行われた。

審議事項

1．　サイクロトロン製造放射薬剤品質管理基準の一部改定について

樫田委員より院内製剤の品質管理についての考え方、問題点について解説あり、ついで福士より新しい細菌試験法を採用したい旨の提案がなされた。寺尾委員より新試験法の原理、特徴、信頼性について質問があり、福士より説明があった。以上の質疑応答の後、提案が承認された。

鈴木より品質管理基準（第２版）通則11項及び14項に関する一部改定および1982年以降に追加された ^{11}C-標識放射薬剤についての品質管理基準の追記事項の提案がなされた。寺尾委員より、同一の装置を用いて複数の薬剤を製造する場合、前製造工程からの汚染の可能性について質問があった。鈴木より、最終製剤で検定を行うので問題はないとの回答があった。

以上の質疑応答の後、改定案が承認された。

2．　新規臨床研究計画について

福田より、^{11}C-PK11195を用いる新規臨床研究計画の内容および被験者への説明書・承認書について説明あった。大熊委員より被験者の「家族」の定義について質問があり、福田より、保護義務者になりうる者との回答があった。以上の質疑応答の後、本研究計画が承認された。

3．研究計画の一部変更について

西尾よりポジトロンＣＴを用いる薬物依存メカニズムの研究（平成元年度第１回会議承認）について研究計画の一部変更の提案がなされた。町野委員、大熊委員より研究計画の表現に一部不明確な部分があるとの指摘があり、一部手直しの上、承認することとした。

4．説明書・承諾書の一部変更について

須原より被験者に対する説明書・承諾書の表現の書き改めおよび形式の一部変更の提案がなされた。佐藤委員、大熊委員、安東委員、田中より参考意見、助言が述べられた後、変更が承認された。

報告事項

現在進行中の以下の臨床研究について経過報告がなされた。

1．頭部用高分解能ポジトロンＣＴ装置について（野原）

2．パーキンソン症候群でのドーパミン受容体測定（篠遠）

3．ポジトロンＣＴを用いる薬物依存メカニズムの研究（西尾）

4．正常者およびうつ病患者におけるドーパミンＤＩ受容体の測定（須原）

特別研究「重粒子線によるがん治療法に関する調査研究」
平成元年度　班員名簿

（班　　長）	恒　元　　博	病院部長
（副 班 長）	川　島　勝　弘	物理研究部長
	舘　野　之　男	臨床研究部長
	平　尾　泰　男	医用重粒子線研究部長
（顧　　問）	梅　垣　洋一郎	特別研究員
	樫　田　義　彦	〃
	田　中　栄　一	〃
	福　田　信　男	〃

1．重粒子線治療のための物理・生物学的基礎調査研究

（1）重粒子線の線量評価および線量分布に関する研究

平　岡　　武	物理研究部第２研究室長
川　島　勝　弘	物理研究部長
星　野　一　雄	物理研究部第２研究室
福　村　明　史	〃　　〃
白　貝　彰　宏	〃　第３研究室
喜多尾　憲　助	〃　第４研究室
中　村　　譲	臨床研究部第２研究室
古　川　重　夫	〃　第４研究室
河　内　清　光	医用重粒子線研究部第３研究室長
遠　藤　真　広	〃　第３研究室
金　井　達　明	〃　〃
中　野　隆　史	病院部医務課
佐　藤　眞一郎	〃　〃
坂　下　邦　雄	〃　〃

（2）重粒子線の初期過程および生物作用モデルに関する研究

丸　山　隆　司	物理研究部第３研究室長
星　野　一　雄	〃　第２研究室
山　口　　寛	〃　第３研究室
野　田　　豊	〃　〃
中　島　敏　之	〃　第４研究室長
大　原　　弘	障害基礎研究部第３研究室長
小　川　博　嗣	医用重粒子線研究部第１研究室長
佐　藤　幸　夫	〃　第１研究室
佐　藤　健　次	〃　第２研究室長
河　内　清　光	〃　第３研究室長
金　井　達　明	〃　第３研究室
隈　元　芳　一	技術部サイクロトロン管理課

根　井　　充	養成訓練部指導室

(3) 重粒子線治療関連機器に関する研究

河　内　清　光	医用重粒子線研究部第３研究室長
平　尾　泰　男	医用重粒子線研究部長
小　川　博　嗣	〃　第１研究室長
山　田　孝　信	〃　第１研究室
山　田　　聰	〃　〃
佐　藤　幸　夫	〃　〃
佐　藤　健　次	〃　第２研究室長
金　澤　光　隆	〃　第２研究室
遠　藤　真　広	〃　第３研究室
金　井　達　明	〃　〃
河　野　俊　之	〃　〃
平　岡　　武	物理研究部第２研究室長
福　村　明　史	〃　第２研究室
野　田　　豊	〃　第３研究室
中　村　　譲	臨床研究部第２研究室
森　田　新　六	病院部医務課長
久保田　　進	〃　医務課
中　野　隆　史	〃　〃
坂　下　邦　雄	〃　〃

(4) 重粒子線に対する細胞感受性および障害回復に関する研究

大　原　　弘	障害基礎研究部第３研究室長
坪　井　　篤	〃　第１研究室長
小　島　栄　一	〃　第１研究室
山　口　　寛	物理研究部第３研究室
松　本　信　二	薬理科学研究部第１研究室
青　木　芳　朗	障害臨床研究部長
大　山　ハルミ	障害臨床研究部第２研究室
金　井　達　明	医用重粒子線研究部第３研究室
根　井　　充	養成訓練部指導室

(5) 治療効果比の早期判定法に関する実験的・臨床的研究

安　藤　興　一	臨床研究部第４研究室長
福　田　　寛	〃　第３研究室長
古　川　重　夫	〃　第４研究室
小　池　幸　子	〃　〃
古　瀬　　健	生理病理研究部第２研究室
大　原　　弘	障害基礎研究部第３研究室長
松　本　恒　弥	技術部動植物管理課
松　下　　悟	〃　〃

上　島　久　正	養成訓練部指導室
宮　本　忠　昭	病院部医務課
向　井　　稔	〃　〃
久保田　　進	〃　〃
中　野　隆　史	〃　〃
佐　藤　眞一郎	〃　〃
岡　　邦　行	〃　検査課長

2．重粒子線治療における核医学に関する基礎的研究

(1) 標識薬剤の開発に関する研究

山　崎　統四郎	臨床研究部第１研究室長
入　江　俊　幸	〃　第１研究室
福　士　　清	〃　〃
井　上　　修	〃　〃
福　田　　寛	〃　第３研究室長
安　藤　興　一	〃　第４研究室長
鈴　木　和　年	技術部サイクロトロン管理課

(2) 高分解能ポジトロンＣＴに関する研究

野　原　功　全	物理研究部第１研究室長
富　谷　武　浩	〃　第１研究室
山　本　幹　男	〃　〃
村　山　秀　雄	〃　〃
山　崎　統四郎	臨床研究部第１研究室長
福　田　　寛	〃　第３研究室長
遠　藤　真　広	医用重粒子線研究部第３研究室

(3) ラジオアクティブビーム等の利用に関する調査研究

富　谷　武　浩	物理研究部第１研究室
野　原　功　全	〃　第１研究室長
山　本　幹　男	〃　第１研究室
村　山　秀　雄	〃　〃
山　田　　聰	医用重粒子線研究部第１研究室
佐　藤　幸　夫	〃　〃
金　井　達　明	〃　第３研究室

3．重粒子線治療に関する臨床的研究

(1) 重粒子線治療の評価法に関する研究

森　田　新　六	病院部医務課長
恒　元　　博	病院部長
宮　本　忠　昭	病院部医務課
向　井　　稔	〃　〃
久保田　　進	〃　〃
中　野　隆　史	〃　〃

佐藤眞一郎	病院部医務課
野本靖史	〃　〃
坂下邦雄	〃　〃
熊谷和正	〃　〃
柴山晃一	〃　〃
千尾武彦	〃　〃
平岡武	物理研究部第２研究室長
星野一雄	〃　第２研究室
福村明史	〃　〃
舘野之男	臨床研究部長
飯沼武	臨床研究部第２研究室長
中村譲	〃　第２研究室
安藤興一	〃　第４研究室長
古川重夫	〃　第４研究室
青木芳朗	障害臨床研究部長
河内清光	医用重粒子線研究部第３研究室長
遠藤真広	〃　第３研究室
金井達明	〃　〃
福久健二郎	技術部技術課

(2) 重粒子線治療システムの開発に関する研究

遠藤真広	医用重粒子線研究部第３研究室
河内清光	〃　第３研究室長
金井達明	〃　第３研究室
福村明史	物理研究部第２研究室
飯沼武	臨床研究部第２研究室長
中村譲	〃　第２研究室
福田寛	〃　第３研究室長
池平博夫	〃　第３研究室
古川重夫	〃　第４研究室
福久健二郎	技術部技術課
森田新六	病院部医務課長
久保田進	〃　医務課
中野隆史	〃　〃
佐藤眞一郎	〃　〃
坂下邦雄	〃　〃
熊谷和正	〃　〃
柴山晃一	〃　〃
千尾武彦	〃　〃

(3) ポジトロンＣＴ・ＭＲＩ等の臨床応用に関する研究

福田寛	臨床研究部第３研究室長

舘　野　之　男	臨床研究部長
山　崎　統四郎	臨床研究部第１研究室長
井　上　　修	〃　第１研究室
飯　沼　　武	〃　第２研究室長
池　平　博　夫	〃　第３研究室
青　木　芳　朗	障害臨床研究部長
遠　藤　真　広	医用重粒子線研究部第３研究室
鈴　木　和　年	技術部サイクロトロン管理課
中　野　隆　史	病院部医務課
久保田　　進	〃　〃
坂　下　邦　雄	〃　〃

4．重粒子線がん治療の総合的調査研究

(1) 重粒子線がん治療研究の総合評価に関する調査研究

川　島　勝　弘	物理研究部長
大　原　　弘	障害基礎研究部第３研究室長
舘　野　之　男	臨床研究部長
山　崎　統四郎	臨床研究部第１研究室長
飯　沼　　武	〃　第２研究室長
中　村　　譲	〃　第２研究室
平　尾　泰　男	医用重粒子線研究部長
恒　元　　博	病院部長
森　田　新　六	病院部医務課長

特別研究「重粒子線によるがん治療法に
関する調査研究」論文集　第１集
平成３年２月
千葉市穴川４－９－１
放射線医学総合研究所
Tel.0472-51-2111(代)